RÉPUBLIQUE FRANÇAISE
Liberté Égalité Fraternité

Université de Toulouse

Doctorat de l'Université de Toulouse

préparé à l'ISAE-SUPAERO

Développement d'une nouvelle méthode de conception avion adaptée à l'aile volante à hydrogène

---

Thèse présentée et soutenue, le 19 janvier 2026 par

Romain PARELLO

École doctorale
MEGEP - Mécanique, Energétique, Génie civil, Procédés

Spécialité
Génie mécanique, mécanique des matériaux

Unité de recherche
ISAE-ONERA EDyF Energétique et Dynamique des Fluides

Thèse dirigée par
Yves GOURINAT et Emmanuel BENARD

Composition du jury
Mme Annafederica URBANO, Présidente, ISAE-SUPAERO
M. Mark PRICE, Rapporteur, Queen's University Belfast
M. Frank THIELECKE, Rapporteur, Technische Universität Hamburg
M. Maurice HOOGREEF, Examinateur, TU Delft
M. Joaquim R.R.A. MARTINS, Examinateur, University of Michigan
M. Yves GOURINAT, Directeur de thèse, ISAE-SUPAERO
M. Emmanuel BENARD, Co-directeur de thèse, ISAE-SUPAERO

Membres invités
M. Sébastien DEFOORT, Co-encadrant, ONERA
M. Mickael LALLEMAND, Airbus

Remerciements

Après plus de trois années, cette thèse touche désormais à sa fin, et il est temps d'en faire le bilan. Ce furent trois années d'une aventure unique, qui m'a parfois semblé filer à toute vitesse, mais je mesure aujourd'hui le chemin parcouru depuis mes débuts. Et si je suis fier du travail accompli ainsi que des connaissances que j'ai acquises, je tiens aussi à remercier toutes les personnes qui ont contribué à cette thèse et qui ont fait de ces trois années une période dont je garderai un beau et précieux souvenir.

Tout d'abord, je voudrais remercier le professeur Frank Thielecke et le professeur Mark Price, qui ont tous deux accepté d'être les rapporteurs de ce manuscrit. Ils se sont investis en temps et en énergie pour en faire une analyse critique que j'ai grandement appréciée. Je remercie également AnnaFederica Urbano, Maurice Hoogreef, Joaquim R.R.A. Martins et Mickaël Lallemand, qui ont aussi pris part à mon jury de soutenance et ont ainsi pu apporter leur regard expérimenté sur mes travaux.

J'aimerais ensuite remercier mes encadrants à l'ONERA et à l'ISAE-SUPAERO. Merci donc à Sébastien Defoort, Emmanuel Bénard et Yves Gourinat, qui m'ont donné de précieux conseils tout au long de ces trois années. Merci également d'avoir cru en moi dès le début en me laissant une grande autonomie sur la direction que prenait cette thèse et en me soutenant dans les décisions que j'ai pu prendre.

Au-delà de mes encadrants, merci aussi à toutes les personnes à qui j'ai pu demander de l'aide et qui n'ont jamais hésité à me consacrer du temps. Je pense ainsi à Christophe David, Eric Nguyen Van ou Enrico Stragiotti, qui m'ont maintes fois sauvé la mise avec Python ou FAST-OAD et sans qui cette thèse aurait été deux fois plus difficile. Merci à Julie Gauvrit pour sa patience à m'expliquer le fonctionnement de CICAV et pour l'intérêt qu'elle a porté à mes travaux. Merci à Valentin Priasso pour sa collaboration sur la compilation du modèle structural de l'aile volante, qui n'a pas toujours été simple. Merci à Nathalie Bartoli, Paul Saves, Sylvain Dubreuil et Rémi Lafarge pour leurs explications sur les plans d'expériences (DOE) et l'optimisation bayésienne, ainsi que pour leurs outils mis à ma disposition. Merci enfin à Claire Dabin pour son aide indispensable dans toutes les missions que j'ai effectuées, et à Muriel Guibert, qui a tout fait pour que la fin de ma thèse et ma soutenance se passent au mieux.

Je n'oublie pas non plus tous les stagiaires et doctorants de l'ONERA ou de l'ISAE-SUPAERO que j'ai pu côtoyer pendant cette thèse. C'est principalement grâce à eux qu'il y a toujours eu une très bonne ambiance au bureau et que j'ai toujours eu plaisir à venir travailler le matin. Je salue notamment Sam, Rémy, Camille, Marie, Henoïk, Jonathan, Elton, Louison, Luiz, Armand, Gaston, Léa, Victor, Mauricio, Abdoulaye, Laura, Lucas L., Lucas M., Charles, Emmanuel, Hugo, Antoine, Coriolan, Enric, Haythem, Matisse, Marco, Alune, Jasper, Robert, Claire, Alex, Arnault, Paul Ier et Duc Anh. Je pense aussi aux artistes du deuxième étage, avec Thibault, toujours prêt à nous faire rire, Romain B., éternel second qui a raté une carrière dans la chanson, et Anouck, dont l'imagination en design d'avion ou en escalade me dépasse largement. Merci à Jason, qui m'a appris ce que c'est que d'être passionné par un jeu ou un instrument et qui m'a accompagné dans les longues formations de rédaction et de préparation à la soutenance. Merci à Gabriele de m'avoir accompagné dans mes conférences en Italie et pour nos discussions sur les avions à hydrogène (sans oublier les trains !). Merci à Inês, qui a prouvé que râler n'est pas un apanage des Français, mais sans qui je ne serais peut-être pas allé voir Mickey, ainsi qu'à Shon, qui nous a accompagnés dans ce voyage mémorable. Merci à Julien pour ses magnifiques vocalises à l'autre bout du couloir et grâce à qui je n'avais aucune chance d'oublier la fin de ma thèse. Et enfin, merci à Dider, le meilleur co-bureau de l'ONERA, de m'avoir supporté pendant près de deux ans avec le sourire, d'avoir écouté mes plaintes matinales contre le vent, la pluie ou les voitures, et d'avoir partagé avec moi les hauts (et les bas) de la conception d'avions avec FAST-OAD. Qui sait, peut-être que nos concepts voleront un jour... ou pas ! Quoi qu'il arrive, je garderai précieusement le souvenir de nos afterworks, karaokés, sessions EVA, soirées raclettes, escape games, déménagements sportifs, casseroulettes légendaires... et des quelques milliers de parties de tarot passées avec vous tous !

Au-delà de toutes les personnes déjà citées, je voudrais également remercier ma famille, à commencer par mes parents. Leur soutien indéfectible m'a toujours permis de suivre mes envies et de tracer mon propre chemin. Et si j'ai pu arriver à la fin de cette thèse, après plus de 25 ans dans le système scolaire, c'est en partie grâce à eux, à leurs conseils avisés et à leur confiance. Je tiens aussi à remercier ma sœur Océane, qui, malgré un parcours bien différent du mien, a toujours manifesté de l'intérêt pour mes travaux. Elle m'a offert des pauses bienvenues lors de voyages rares mais inoubliables, et m'a parfois aidé à voir les choses sous un angle nouveau. Enfin, j'ai aussi une grande pensée pour l'ensemble du reste de ma famille, qui, bien qu'éloignée géographiquement, a toujours été une base solide sur laquelle je pouvais compter.

Et enfin, et surtout, merci infiniment à Floriane, celle qui a partagé chaque instant de cette thèse à mes côtés. Dès le premier jour, où elle m'a accompagné à Toulouse pour l'entretien, jusqu'à la soutenance, dont elle a largement contribué au succès. Que ce soit dans les bons moments comme dans les moins bons, pour m'aider, me conseiller ou simplement me changer les idées, tu as toujours été là, sans compter. Une partie de cette thèse te revient, et j'ai hâte de voir ce que l'avenir nous réserve.

Abstract

The aviation industry's dependence on fossil fuels, coupled with its sustained growth, is intensifying the global climate crisis, which poses a significant threat to the sustainability of modern society. In response, the industry has committed to achieving carbon neutrality by 2050—an ambitious goal that demands disruptive innovation. Hydrogen-powered aircraft stand out as a promising zero-emission solution, as hydrogen emits no carbon in flight and can be produced using low-carbon electricity. However, its low energy density requires storing it as liquid hydrogen in large pressurized cryogenic tanks, which strongly affect aircraft architecture and often reduce overall performance of conventional tube-and-wing (T&W) aircraft. In contrast, the blended-wing-body (BWB) configuration offers a promising alternative for hydrogen integration, combining improved fuel efficiency with large internal volume for cryogenic tanks. Yet hydrogen-powered BWBs remain largely underexplored. This PhD thesis therefore develops an overall aircraft design (OAD) methodology tailored to the sizing of hydrogen-fueled BWB configurations.

This design method builds on FAST-OAD, the aircraft sizing tool developed by ISAE-SUPAERO and ONERA and implemented within NASA's OpenMDAO framework. To the conventional OAD structure, a cryogenic tank thermodynamic model is first added to estimate hydrogen losses due to liquid-hydrogen boil-off. A structure module, capable of sizing cylindrical tanks in compliance with CS-25 pressurized-vessel requirements, is then developed, enabling the design of hydrogen T&W aircraft. FAST-OAD is further extended to model BWB configurations, incorporating a flexible framework for defining hydrogen tank size, number, and placement. The hydrogen BWB design is then formulated as a multidisciplinary analysis and optimization problem with mixed variables, ensuring the aircraft's geometric feasibility and stability.

The new BWB design method's capabilities are demonstrated through a 37-variable design of experiment (DOE) for a medium-range aircraft incorporating 18,000 points, highlighting the critical impact of stability constraints. Following this, a specific hydrogen BWB design is optimized using the Bayesian optimizer SEGOMOE, with the number of design variables and constraints reduced based on the DOE findings. The resulting optimized hydrogen-powered BWB, larger than its kerosene counterpart due to stability-driven forward tank placement, consumes 12% more energy than a kerosene BWB. However, compared to hydrogen T&W design, despite a higher structural mass, its aerodynamic advantages cut energy use by 3%. Ultimately, its energy consumption slightly undercuts that of a kerosene T&W, underscoring both the concept's potential and the importance of refining its sizing methodology to advance sustainable aviation.

Résumé

La dépendance de l'aviation aux énergies fossiles, combinée à sa croissance continue, intensifie la crise climatique globale et pose un risque sérieux pour la durabilité des sociétés contemporaines. En réponse, le secteur s'est engagé à atteindre la neutralité carbone d'ici 2050 - un objectif ambitieux nécessitant des innovations radicales. Les avions à hydrogène représentent une solution prometteuse, l'hydrogène pouvant être produit à partir d'électricité bas carbone et n'émettant pas de CO_2 en vol. Cependant, sa faible densité énergétique impose un stockage sous forme liquide dans de grands réservoirs cryogéniques pressurisés, souvent pénalisant pour les configurations classiques à fuselage tubulaire (T&W). La configuration aile volante, aussi appelée blended-wing-body (BWB), constitue une alternative prometteuse pour l'intégration de l'hydrogène, alliant une meilleure efficacité énergétique à un volume interne important pour les réservoirs cryogéniques. Cependant, le concept d'aile volante à hydrogène reste peu étudié. Cette thèse de doctorat vise donc à développer une méthode de conception globale d'avion (OAD) spécifiquement adaptée au dimensionnement des configurations BWB à hydrogène.

Cette méthode s'appuie sur FAST-OAD, l'outil de conception avion développé par l'ISAE-SUPAERO et l'ONERA. À la structure OAD conventionnelle est d'abord ajoutée une modélisation thermodynamique des réservoirs cryogéniques, permettant d'estimer les pertes d'hydrogène dues à l'évaporation de l'hydrogène liquide dans les réservoirs. Un module structurel dimensionnant des réservoirs cylindriques conformes aux exigences CS-25 est ensuite développé, permettant la conception d'avions T&W à hydrogène. Une extension de FAST-OAD est ensuite développée pour modéliser les configurations BWB, offrant une paramétrisation très flexible du nombre, de la taille et du positionnement des réservoirs d'hydrogène. Le dimensionnement d'une aile volante à hydrogène est finalement formulé comme un problème d'analyse et d'optimisation multidisciplinaire à variables mixtes, garantissant à la fois la faisabilité géométrique et la stabilité de l'appareil.

Les performances de cette nouvelle méthode de conception sont illustrées par un plan d'expériences (DOE) à 37 variables pour un avion moyen-courrier, analysant plus de 18 000 designs et révélant l'impact critique des contraintes de stabilité. Par la suite, le dimensionnement d'une aile volante optimisée est réalisé à l'aide de l'optimiseur bayésien SEGOMOE, avec un nombre réduit de variables de conception et de contraintes basé sur les résultats du DOE. Le design résultant, plus volumineux que son équivalent kérosène en raison du positionnement vers l'avant des réservoirs dicté par la stabilité, présente une efficacité énergétique inférieure de 12% à celle du BWB à kérosène. Ses avantages aérodynamiques permettent cependant une réduction de 3% de la consommation énergétique et une division par deux de sa longueur comparée à un T&W à hydrogène. Au final, sa consommation énergétique est légèrement inférieure à celle d'un T&W kérosène, soulignant à la fois le potentiel d'aile volante à hydrogène et l'importance d'affiner sa méthodologie de conception pour réduire l'impact climatique de l'aviation.

Contents

Remerciements iii

Abstract v

Résumé vii

List of Figures xiii

List of Tables xviii

Acronyms xxi

Nomenclature xxv

Introduction 1

I Context and Research Strategy 5

I.1 The Environmental Crisis Pressuring Aviation to Reduce Its Climate Impact 9

I.2 Hydrogen Aircraft: a promising but disruptive technology to reach zero-emission aircraft . . . 16

I.3 Blended Wing Body: a revolutionary yet challenging concept promising to improve aircraft energy efficiency . . . 33

I.4 Hydrogen-Powered Blended Wing-Body Aircraft: An Emerging Synergy of Technologies that could enable low-emission flight . . . 46

I.5 Research strategy . . . 51

I.5.1 Literature Review synthesis and Research Objectives . . . 51

I.5.2 Disruptive Aircraft Design: A New Conceptual Paradigm Enabled by the FAST-OAD Sizing Tool . . . 52

I.5.3 Methodology and Development Choices . . . 56

II Development of a medium fidelity hydrogen tank thermodynamic model to estimate hydrogen boil-off **59**
II.1 Introduction . . . 63
II.2 State-of-the-Art of Thermodynamic Models of H2 Tanks in Aircraft . . . 65
II.2.1 Common Thermodynamic Framework for Tank Heat Inflow . . . 66
II.2.2 Review of Internal Thermodynamic State Evolution Models for Hydrogen Storage . . . 68
II.3 Enhanced Model for Estimating H2 Boil-Off in Aircraft Cryogenic Tanks . 72
II.3.1 Estimation of Heat Leak into a Hydrogen Tank Using an Enhanced Thermal Resistance Model . . . 72
II.3.1.1 Definition of heat flows involved in aircraft cryogenic tanks 72
II.3.1.2 Formulation of a System of Equations to Determine Convective Heat Exchange in Gaseous and Liquid Hydrogen Phases . . . 76
II.3.2 Derivation of a temporal equation system describing the evolution of the tank's internal state . . . 79
II.3.2.1 Fundamental Assumptions and Representation of the Tank Model . . . 80
II.3.2.2 Energy Conservation Analysis for the Bulk-Liquid Hydrogen Volume . . . 81
II.3.2.3 Energy Conservation Analysis for the Ullage Volume . . . 84
II.3.2.4 Energy Conservation Analysis for the Interface . . . 85
II.3.2.5 Governing System of Ordinary Differential Equations for Tank Thermodynamic State: Formulation and Comparative Analysis with Prior Studies . . . 86
II.3.3 Development of a methodology to estimate hydrogen loss during venting . . . 87
II.3.4 Hydrogen tank model implementation into FAST-OAD . . . 88
II.4 Conclusion and perspectives . . . 90

III Development of a hydrogen tank structural sizing methodology compliant with CS-25 regulations for tank mass estimation **93**
III.1 Introduction . . . 96
III.2 Hydrogen Tank structural sizing in literature . . . 97
III.3 Development of a methodology to size a hydrogen tank and its stiffening structure respecting the CS-25 guidelines . . . 102
III.3.1 Load Analysis for Hydrogen Tanks in Tube-and-Wing Aircraft Configurations . . . 103
III.3.2 Development of a Methodology for Pre-sizing Structural Elements of Pressurized and potentially Integral Hydrogen Tanks in Aircraft . 105
III.3.2.1 Step 1 : Determination of the tank's wall thickness . . . 105
III.3.2.2 Step 2: Optimization of Stringers and Frames Configuration to Prevent Buckling . . . 107
III.3.2.3 Step 3: Sizing of Stringer and Frame Cross-Sections . . . 107

III.4 Integration of the H2 Tank Weight Estimation Module into FAST-OAD . . 109
III.5 Conclusion and perspectives 110

IV Design Exploration of a Tube and Wing Hydrogen Aircraft through Parametric Studies 113
IV.1 Introduction 116
IV.2 Case Study Setup for the Design of a SMR Hydrogen Aircraft 117
IV.3 Evaluating FAST-OAD Hydrogen Aircraft Design Capabilities 118
IV.4 Parametric Analysis to Assess Sensitivity in H2 Aircraft Design 122
IV.4.1 Influence of tank insulation and design pressure 122
IV.4.2 Influence of fuselage width for integral tanks configurations 124
IV.4.3 Integral and non-integral tank trade-off 126
IV.4.4 Influence of a zero venting constraint during dormancy phase . . . 128
IV.5 Performance Comparison: Optimal H2 vs. Jet-A Aircraft Design 129
IV.5.1 Optimal Hydrogen Aircraft Design Selection Based on Parametric Analysis 129
IV.5.2 Sizing and Analysis of the identified optimal hydrogen aircraft design 130
IV.6 Conclusion 134

V Extending FAST-OAD for Hydrogen Blended Wing Body Sizing: A Framework for Flexible Tank Configuration Design 139
V.1 Introduction 142
V.2 Implementation of a FAST-OAD Extension for BWB Geometry Generation, Structural Sizing, and Stability Analysis Using the CICAV Framework 142
V.2.1 Description of the Geometry Module 143
V.2.2 Description of the Structure Module 144
V.2.3 Description of the Stability Module 146
V.2.4 Development of a New System Positioning Module 147
V.3 Development of a Hydrogen Tank Sizing and Positioning Framework for BWB 149
V.3.1 Development of a new Parametrization for Cylindrical Tank Integration into a BWB 149
V.3.1.1 Parametrization of Tank Number and Placement 150
V.3.1.2 Parametrization of Tank Geometry 152
V.3.1.3 Parametrization of Tank Spacing 153
V.3.2 Formulation of Design Space Constraints for Feasible and Optimal Hydrogen Blended Wing Body Configurations 155
V.3.2.1 Fuel Tank Volume Constraint 156
V.3.2.2 Geometric Constraints on Rear–Side Tank Intersections . 157
V.3.2.3 Tank Positioning Constraints Relative to Control Surfaces 158
V.3.2.4 Limitations on Tank Radius Imposed by Airframe Thickness 159
V.3.2.5 Static Margin Constraints for Aircraft Stability 160
V.4 Set-up of MDAO Framework in FAST-OAD for the Sizing of Hydrogen BWB 161
V.4.1 Specification of the Multidisciplinary Optimization Problem 161

V.4.2 Complete MDAO Framework for Hydrogen BWB Design 165
V.5 Conclusion 166

VI Demonstrating the Hydrogen Blended Wing Body Sizing Method in FAST-OAD: Design Exploration and Optimization of Short-to-Medium-Range Configurations 169
VI.1 Introduction 173
VI.2 Description of the case study 173
VI.2.1 Mission selection 173
VI.2.2 Specifications of Model Inputs and Configuration Assumptions . . . 174
VI.2.3 Design of reference aircraft 176
VI.3 First exploration of the design space through a DOE analysis 177
VI.3.1 Design Space Construction 177
VI.3.2 Analysis of Constraint Characteristics Across the DOE 179
VI.3.3 Analysis of Feasible Region Trends from the DOE 183
VI.4 Optimisation of Small-to-Medium-Range Hydrogen-BWB 189
VI.4.1 Establishing a Mixed-Variable Optimization Process 189
VI.4.2 Assessment of Iterative Optimization Behavior 192
VI.4.3 Evaluating the Performance and Key Design Features of an Optimized Hydrogen-Powered Blended Wing Body Aircraft for SMR missions 195
VI.4.3.1 Presentation of the optimized hydrogen powered Blended Wing Body design 195
VI.4.3.2 Evaluating Optimization Impact on Hydrogen **BWB** Performance and Attributes 198
VI.4.3.3 Potential of Hydrogen **BWB** Compared with Hydrogen and Jet-Fuel **T&W** Aircraft 205
VI.5 Conclusion 211

Conclusion and perspectives 215

Annexes 223
A.1 Production pathways for alternative aviation fuels 224
A.2 A Review of Materials for Cryogenic Hydrogen Storage: Properties and Challenges 225
A.3 Effect of Tank Dimensions on the Hydrogen **BWB** Feasible Design Space . 228

List of Figures

I.1 Near-linear relationship between cumulative CO_2eq emissions and the increase in global surface temperature [**3**] 9
I.2 Global CO_2 emissions from commercial aviation [**5**] 10
I.3 Crude oil production of the 16 main EU suppliers from 1950 to 2050 (projected post 2020 by the Shift Project). Source : Rystad Energy. Adapted from [**8**] 11
I.4 **LTAG** integrated scenario 3: aggressive decarbonization path [**9**] 12
I.5 Full life-cycle emission intensity for sustainable aviation fuels. Bars indicate the composition of the emission intensity (**ILUC** or **CLCA**) for a pathway. Points and solid line represent the full life-cycle emission intensity (sum of **ILUC** and **CLCA** values). Dotted line shows life-cycle emission intensity of petroleum-based jet fuels [**12**] 14
I.6 Comparison of bio-SAF supply and blend-in target for the future (2022)[**13**] 15
I.7 Liquid hydrogen tank concept of Silverstein and Hall [**17**]. Dimension : 25m long, 3m in diameter 17
I.8 Hydrogen reconaissance aircraft [**17**] 17
I.9 Supersonic hydrogen fighter [**17**] 17
I.10 Modified B-57 bomber used in the BEE project: (top) schematic view [**18**] and (bottom) real photo with hydrogen and helium tanks [**19**]. 18
I.11 Lockheed CL-400 reconnaissance aircraft prototype using liquid hydrogen (1955) [**16**] 19
I.12 Hydrogen-powered, double-deck commercial transport aircraft for a 400 passenger / 5500 nmi mission of G. D. Brewer[**24**] 20
I.13 Concept of aircraft engine with hydrogen-cooled bleed air [**24**] 20
I.14 Comparison of liquid hydrogen, liquid methane, and synthetic fuel aircraft on their gross weight and resource equivalent energy for different flight segments. Adapted from G. D. Brewer[**24**] 21

I.15 Fuselage cross section of Muehlbauer hydrogen cargo aircraft [**26**] 22
I.16 H2 refueling truck [**27**] 23
I.17 H2 refueling boom [**27**] 23
I.18 Relative energy consumption of hydrogen and jet-A transport aircraft[**27**] . 23
I.19 The hydrogen-fueled Tu-155 aircraft with one LH2-powered NK-88 engine[**29**] 24
I.20 Temperature characteristics of hydrogen combustion chambers [**32**] 25
I.21 Potential NOx Emissions reduction in hydrogen engine [**31**] 25
I.22 Aircraft configurations studied in the cryoplane project [**33**] 25
I.23 Energy consumption (top) and mass variation (bottom) of hydrogen-powered aircraft compared to kerosene-fueled aircraft, as projected in the Cryoplane project [**33**] 26
I.24 LH2-400 long-range aircraft concept of Maniaci [**38**] 28
I.25 Impact of hydrogen tank gravimetric efficiency on aircraft energy consumption depending on mission range [**46**] 31
I.26 Three hydrogen fueled aircraft concepts presented by Airbus in its Zero-e program 33
I.28 John Dunne's D-8 tailless aircraft concept [**61**] 34
I.27 Early aircraft concept of Penault "aéroplane" (left) [**60**], Ader's Eole (center) and Etrich's Glider (right) 34
I.29 The Delta 1 aircraft of Alexander Lippisch [**62**] 35
I.30 The Horten Ho 229 V3 being captured by U.S Force in its manufacturing plant (Source: Wikicommons) 35
I.31 Semi-flying wing aircraft developed by Northrop (Source : Smithsonian **NASA** Museum) 36
I.32 Northrop Xb-35 (top) and YB-49 (bottom) aircraft (Source: U.S. Air Force photo, Public Domain) 36
I.33 Northrop-Grumman B2 Spirit bomber (Source : US Air Force Website) . . 37
I.34 Early **BWB** concept envisonned at McDonnell Douglas in 1988 [**66**] . . . 38
I.35 Surface area comparison between conventional and **BWB** configurations through successive design stages [**66**] 38
I.36 Liebeck 800 passengers, double deck second generation **BWB** [**65**] 39
I.37 Comparison of inertial and lift distribution between a conventional configuration and the **BWB** [**66**] 40
I.38 Liebeck's proposed **BWB** aircraft family with shared structural components [**66**] 40
I.39 NASA Dryden engineer Gary Cosentino prepares the X-48B for flight. Source: NASA website, Credit: Tony Landis 41
I.40 H3.2 conceptual aircraft design of NASA for its N+3 program [**68**] 41
I.41 Conceptual **BWB** configurations developed in the 2000's: NACRE (top), **ACFA** (middle), SAX-40 (bottom) [**71**] 42
I.42 Airbus **MAVERIC** prototype aircraft (Source : AIRBUS) 42
I.43 The 6 control surfaces configurations proposed by Sgueglia [**99**] 44
I.44 C-type (left) and U-type flying wing concept of Martinez et al. [**102**] . . . 45

I.45 Concept of a hydrogen powered cargo **BWB** developped for the german greener freighter project[**110**] . . . 47
I.46 Three concept of the Airbus Zero-e project announced in 2020 . . . 48
I.47 Illustration of the hydrogen tank sizing methodology in a **BWB** of Karpuk et al.[**113**] . . . 49
I.48 Three tank arrangement in the hydrogen **BWB** tested by Di Summa [**114**] 49
I.49 Sensitivity analysis of the energy usage of hydrogen **BWB** and **T&W** aircraft to the gravimetric index [**115**] . . . 50
I.50 FAST-OAD multidisciplinary Analysis process [**120**] . . . 54
I.51 Illustration of the aerodynamic-structure discipline coupling in aircraft design within an **XDSM** graph . . . 54

II.1 Comparison of Gravimetric Index Values in LH2-Powered Aircraft studies (adapted from [**127**]) . . . 64
II.2 Tank zone breakdown breakdown by Winnefeld [**48**] . . . 68
II.3 Schematic representation of the seven control volumes in a hydrogen tank as modeled by NASA's TankSIM [**132**] . . . 70
II.4 Heat flows involved in a cryogenic hydrogen tank . . . 73
II.5 Evolution of the thermal conductivity of polyurethane and rohacell foam with temperature [**32**] . . . 74
II.6 Self-pressurizing hydrogen tank model . . . 80
II.7 Top-Down Representation of the Ullage-Liquid Hydrogen Interface Geometry at an Arbitrary Liquid Level . . . 82
II.8 Variation in Liquid Hydrogen Density as a Function of Temperature at 2 Bar . . . 84

III.1 Ellipsoid tank representation used by Winnefeld [**48**] . . . 99
III.2 Ellipsoid conical tank representation used by Silberhorn et al.[**47**] . . . 100
III.3 Artist impression of tank attachments options considered by Onorato in [**51**]100
III.4 Tanks CATIA model created by Gomez and Smith [**130**] . . . 101
III.5 Representation of a cylindrical hydrogen tank and its stiffening structure. . 102
III.6 Beam model of an aircraft . . . 104
III.7 Tank's section parametrization . . . 105
III.8 Example of a super stiffener's section . . . 108

IV.1 Design Mission Profile of a Medium-Range Hydrogen Aircraft . . . 118
IV.2 Design of Experiments: Impact of Tank Design Variables on a Tube-and-Wing Hydrogen Aircraft . . . 121
IV.3 Impact of maximal pressure differential and insulation thickness on tank efficiency [**158**] . . . 123
IV.4 Impact of maximal pressure differential on tank mass (insulation thickness fixed to 7 cm)[**158**] . . . 124
IV.5 Evolution of aircraft consumption, tank mass and tank gravimetric index with fuselage width [**158**] . . . 124

IV.6 Impact of fuselage width on aircraft operational empty weight and lift-to-drag ratio[**158**] . . . 125
IV.7 Evolution of hydrogen aircraft characteristics and performance of twin-aisle cabin configurations compared to a single-aisle . . . 126
IV.8 Impact of fuselage loads transmission to the tank on aircraft performance [**158**] . . . 127
IV.9 Impact of fuselage loads transmission on hydrogen tank mass [**158**] . . . 128
IV.10 Impact of Insulation Thickness on Hydrogen Loss During Dormancy and related Block Fuel Performance [**158**] . . . 129
IV.11 Planform comparison of Jet-A and hydrogen-powered **T&W** aircraft . . . 131
IV.12 Aerodynamic Polar Curves of Jet-A and hydrogen-powered **T&W** aircraft 132
IV.13 Drag Breakdown Comparison Between the Jet-A and the H2-Powered **T&W** aircraft at their average cruise lift-to-drag ratio. The drag of the H2 version was corrected by the ratio of surface area to compensate the different cruise CL . . . 132
IV.14 Evolution of key design performance of hydrogen aircraft compared to the jet-fuel aircraft . . . 133
IV.15 Cumulative Engine Energy Consumption: Hydrogen vs. Conventional Aircraft from Mission Start . . . 133
IV.16 Ullage Pressure Evolution in a Hydrogen Tank During Mission . . . 135
IV.17 Temporal Variation of Tank Temperature and Heat Transfer During Flight Hydrogen Aircraft Mission . . . 135

V.1 **BWB** geometry parametrization of **CICAV** which divide the wing in five segment[**105**] . . . 144
V.2 Primary structure contours on a typical BWB configuration planform (top view) [**107**] . . . 145
V.3 3D view of the bottom part of the primary structure of a BWB in CICAV with visible stiffeners . . . 146
V.4 Workflow for BWB stability analysis . . . 147
V.5 Side view of the landing gear longitudinal position on a blended wing body 148
V.6 Illustration of the range of possible tank configuration in a hydrogen BWB aircraft with four conceptual examples . . . 150
V.7 Examples of tank number parametrization . . . 151
V.8 Example of tank radius parametrization . . . 152
V.9 Example of tank length parametrization . . . 153
V.10 Illustration of rear and side row spacing parameters $\boldsymbol{S_{xrear}}$ and $\boldsymbol{S_{yside}}$ . . . 154
V.11 Illustration of the tank spacing parameters $\boldsymbol{S_{xside}}$ and $\boldsymbol{S_{yrear}}$ . . . 156
V.12 Example of hydrogen **BWB** configuration with tank overlap . . . 158
V.13 Illustration of the minimal tank-surface control distance constraint . . . 159
V.14 Constraint formulation for the side tank radius within the BWB airframe . 160
V.15 Constraint formulation for the rear tank radius within the BWB airframe . 160
V.16 Definition of a new design variable: ϵ_{p0} . . . 163
V.17 XDSM of the **MDAO** use for hydrogen **BWB** design . . . 167

VI.1 Aircraft Emissions and Fleet Composition by Segment and Operational Range [**163**] . . . 174
VI.2 Design mission profile for the hydrogen **BWB** . . . 175
VI.3 Distribution of aggregated constraints values across the **DoE**. Negative values for radius and distance constraints indicate violated constraints. . . . 182
VI.4 Distribution of fuel margin and static margin constraints values across the **DoE** . . . 183
VI.5 Minimum static margin distributions: full DOE vs feasible vs most efficient feasible designs . . . 183
VI.6 Twenty hydrogen **BWB** designs from the **DoE**, satisfying geometrical constraints and ranked by fuel efficiency (left to right, top to bottom) . . . 184
VI.7 Tank count distribution on the first rear row : Comparison Between Geometrically Feasible **DoE** Subset, Energy-Optimized feasible Configurations, and Stability-Optimized feasible Configurations . . . 185
VI.8 Tank count distribution in geometrically feasible DOE subset . . . 186
VI.9 Distribution of aircraft characteristics in the geometrically feasible DOE subset . . . 187
VI.10 Distribution of aircraft characteristics in the geometrically feasible DOE subset . . . 188
VI.11 Evolution from Near-Feasible (left) to Feasible Design (right) of the SMR Hydrogen BWB by expert adjustment . . . 192
VI.12 Convergence History of Objective and Constraints (Fuel and Static Margin) During Optimization . . . 193
VI.13 Convergence History of Geometrical Constraints During Optimization . . . 194
VI.14 3D Visualisation of the optimized hydrogen **BWB** design on OpenVSP . . . 196
VI.15 2D Visualisation of the optimized hydrogen **BWB** design . . . 196
VI.16 Evolution of Aircraft Center of Gravity and Static Margin During Fuel and Payload Loading for Multiple Tank Fueling Strategies (Small segments: fuel mass variation | Long segments: payload loading/unloading) . . . 197
VI.17 Comparison of 2D planform of conventional and hydrogen **BWB** . . . 199
VI.18 Aerodynamic polar curves of different **BWB** design . . . 199
VI.19 Drag Breakdown Comparison Between the Jet-A-Powered **BWB** and the H2-Powered **BWB** at their average cruise lift-to-drag ratio. The drag of the H2 version was corrected by the ratio of surface area to compensate the lower cruise CL . . . 200
VI.20 Comparative Analysis: Mission Profile, Lift-to-Drag Ratio, and Energy Consumption of Conventional vs. Hydrogen-Powered Blended Wing Body Aircraft . . . 201
VI.21 Transition Analysis: Changes in Characteristics and Performance from Jet-Fuel to Hydrogen **BWB** Through Optimization . . . 203
VI.22 Weight Distribution: Jet-Fuel vs. Hydrogen **BWB** Aircraft . . . 204
VI.23 Comparison of 2D planform of jet-fuel and hydrogen **BWB** with jet fuel and hydrogen powered **T&W** . . . 205
VI.24 Comparison of aerodynamic polar curves of **BWB** and **T&W** design . . . 206

VI.25 Comparative Analysis: Mission Profile, Lift-to-Drag Ratio, and Energy Consumption of Conventional **T&W** vs. **BWB** Aircraft 208
VI.26 Relative Performance and Characteristics of Jet-Fuel **BWB** and Hydrogen-Powered **T&W**/**BWB** Configurations Compared to a Conventional Jet-Fuel **T&W** 209
VI.27 Evaluation of the Performance of Hydrogen-Powered **BWB** Compared to Hydrogen-Powered **T&W** Configurations 209
VI.28 Fuel Consumption Breakdown by Mission Segment for Jet-Fuel and Hydrogen **T&W** and **BWB** 210
A.29 Schematic Overview of Alternative Aviation Fuel Pathways: From Biomass to Electric-Based Fuels [**174**] 224
A.30 Foam-based insulation [**32**], derived from Brewer [**24**] 226
A.31 Multi-layer insulation [**32**], derived from Brewer [**24**] 226
A.32 Advantages and disadvantages of various insulation methods (listed in order of increasing thermal insulation performance) [**176**] 227
A.33 Influence of Rear Tank Dimensions on Geometric Feasibility and Stability Constraints 228
A.34 Influence of Side Tank Dimensions on Geometric Feasibility and Stability Constraints 229

List of Tables

I.1 Discipline-Specific Modeling Approaches in FAST-OAD 55

III.1 Hydrogen tank sizing process inputs 110

IV.1 Tank model inputs 119
IV.2 Tank inputs DOE 120
IV.3 Technical Specifications of Hydrogen and Jet-Fuel Aircraft 136

VI.1 **BWB** sizing case inputs 176
VI.2 **DoE** design variable bounds 180
VI.3 **DoE** design variable hierarchical structure 181
VI.4 Design Variables and Bounds for the Optimization of a Hydrogen-Powered **BWB** Aircraft for **SMR** Missions 191
VI.5 Key Characteristics and Performance Metrics of Hydrogen- and Jet-Fuel-Powered Blended Wing Body Aircraft 202
VI.6 Key Characteristics and Performance Metrics of Hydrogen- and Jet-Fuel-Powered **BWB** and **T&W** Aircraft 207

Acronyms

ACFA Active Control for Flexible Aircraft.

BWB Blended Wing Body.

CFD Computational Fluid Dynamic.

CICAV Conception Intégrée d'une Configuration d'Aile Volante (Integrated Design of a BWB configuration).

CLCA Core Life Cycle Assessment.

CORSIA Carbon Offsetting and Reduction Scheme for International Aviation.

DoE Design of Experiment.

EQHHPP Euro Quebec Hydro Hydrogen Project.

FAST Future Aircraft Sizing Tool.

FAST-OAD Future Aircraft Sizing Tool for Overall Aircraft Design.

FE Finite Element.

FLOPS Flight Optimization System.

GMDSO GENUS Multi-variate Design Synthesis Optimization.

ICAO International Civil Aviation Organization.

ILUC Induced Land Use Change.

IZEA Integrated Zero Emission Aviation.

LHS Latin Hypercube Sampling.

LR Long-Range.

LTAG Long Term Aspirational Goal.

MAC Mean Aerodynamic Chord.

MAVERIC Model Aircraft for Validation and Experimentation of Robust Innovative Controls.

MDA Multi-Disciplinary Analysis.

MDAO Multi-Disciplinary Analysis and Optimization.

MDO Multidisciplinary Optimization.

MHTB Multipurpose Hydrogen test Bed.

MIT Massachusetts Institute of Technology.

MLI Multi-Layer Insulation.

MTOW Maximum Take Off Weight.

NACA National Advisory Committee for Aeronautics.

NASA National Aeronautics and Space Administration.

OAD Overall Aircraft Design.

ODE Ordinary Differential Equation.

OWE Overall Weight Empty.

PrADO Preliminary Aircraft Design and Optimization.

RPK Revenue Passenger Kilometer.

SAF Sustainable Aviation Fuel.

SEGOMOE Super Efficient Global Optimization Mixture Of Expert.

SFC Specific Fuel Consumption.

SLSQP Sequential Least Squares Programming.

SMR Small to Medium Range.

SMT Surrogate Modeling Toolbox.

T&W Tube and Wing.

TLARs Top Level Aircraft Requirements.

TOGW Take-Off Gross Weight.

VLM Vortex Lattice Method.

XDSM eXtended Design Structure Matrix.

Nomenclature

Symbol	Description	Unit
Aircraft		
η	Gravimetric index	-
C_D	Drag coefficient	-
C_L	Lift coefficient	-
α	Angle of attack	deg
M	Mach number	-
t/c	Thickness to chord ratio	-
SM	Static margin	%
h_{cabin}	Cabin height	m
c_{MAC}	Mean aerodynamic chord	m
$c_{m,L}$	Pitching moment coefficient	-
x_{cg}	Center of gravity along the x axis	m
x_{mlg}	Main landing gear longitudinal position	m
x_{nlg}	Nose landing gear longitudinal position	m
Thermal model		
R_{ext}	Thermal resistance of the tank external skin	$K.W^{-1}$
R_{ins}	Thermal resistance of the tank insulation	$K.W^{-1}$
R_{int}	Thermal resistance of the tank internal wall	$K.W^{-1}$
$h_{ext,conv}$	Thermal transfer coefficient for tank skin external convection	$W.K^{-1}.m^{-1}$
h_{int}	Thermal transfer coefficient for tank wall internal convection	$W.K^{-1}.m^{-1}$

Symbol	Description	Unit
$h_{ext,rad}$	Thermal transfer coefficient for tank skin external radiation	$W.K^{-1}.m^{-1}$
T_{skin}	Temperature tank skin	K
T_{wall}	Temperature tank wall	K
T_{atmos}	Temperature of the external atmosphere	K
$T_{recovery}$	Temperature in the fuselage boundary layer	K
T_{dp}	Temperature dew point	K
T_{sat}	Saturation temperature	K
T_g	Temperature ullage	K
T_l	Temperature liquid	K
T_m	Mean temperature	K
P_g	Pressure gas	Pa
ΔP_{max}	Maximum Pressure differential between tank interior and exterior	Pa
$\dot{m}_{fuel}$	Engine mass fuel flow	$kg.s^{-1}$
$\dot{m}_{boil}$	Mass flow of hydrogen boiling	$kg.s^{-1}$
$\dot{m}_v$	Mass flow of hydrogen evaporating of interface	$kg.s^{-1}$
$\dot{m}_{pres}$	Mass flow of hydrogen being artificially vaporized for pressurization	$kg.s^{-1}$
M_{H2}	Molar mass	$kg.mol^{-1}$
R	Molar gas constant	$J.mol^{-1}.K^{-1}$
ρ	Density	kg/m^3
σ	Stefan-Boltzmann constant	$kg.s^{-3}K^{-4}$
ϵ	Emittance	-
ν	Kinematic viscosity	$m^2.s^{-1}$
β	Isobaric expansion coefficient	K^{-1}
Nu	Nusselt number	-
Ra	Rayleigh number	-
Pr	Prandlt number	-
Gr	Grashof number	-
Re	Reynolds number	-
k	Thermal conductivity	$W.m^{-1}.K$
q	Heat flux	$W.m^{-2}$
$\dot{Q}$	Rate of heat flow	W
h_{in}	Specific enthalpy of incoming mass flow	$J.kg^{-1}$
h_{out}	Specific enthalpy of outgoing mass flow	$J.kg^{-1}$
h_{vap}	Specific enthalpy vaporization	$J.kg^{-1}$
c_p	Constant-pressure specific heat	$J.kg^{-1}.K^{-1}$
c_v	Constant-volume specific heat	$J.kg^{-1}.K^{-1}$
W	Work	W
t	Time	s
g	Gravitational acceleration constant on earth	$m.s^{-2}$
N_s	Number of reflective shield layer	

Symbol	Description	Unit
N^*	Density of reflective shield layer	cm^{-1}
E_{cv}	Energy control volume	J
U	Internal energy	J
u	Specific internal energy	$J.kg^{-1}$
FL	Filing Level	-
DL	Dry Level	-
L	Characteristic length	m
A	Area	m^2
V	Volume	m^2
$S_{interface}$	Interface surface	m^2
r_i	Tank inner radius	m
r_o	Tank outter radius	m
r_{tank}	Tank radius	m
d_{tank}	Tank diameter	m
h_d	Height tank bulkhead dome	m
e	Ellipse Eccentricity	m
mg_{tank}	Tank extra volume margin	%

Tank Structure model

r_{tank}	Tank structure radius	m
L_{tank}	Tank structure length	m
$t_{wall/barrel}$	Tank wall thickness, barrel section	m
$t_{wall/bulkhead}$	Tank wall thickness, bulkhead section	m
$t_{wall/bulkhead}$	Tank wall thickness, bulkhead section	m
E	Young Modulus	Pa
σ_a/σ_e	Elastic stress limit	Pa
σ_b	Break stress limit	Pa
σ_{VM}	Von Mises stress	Pa
$\epsilon_I, \epsilon_{II}, \epsilon_{III}$	Principal Strain	-
e_w	Weld efficiency	-
CG	Center of Gravity	m
n	Load factor	-
M_b	Bending Moment	$N.m$
$M_{torsion}$	Torsion Moment	$N.m$
T_z	Shear flow	Pa
I_z	Moment of inertia	$kg.m^{-2}$
a	Stringer pitch	m
b	Frame pitch	m
N_{strg}	Stringer number	
N_{frm}	Frame number	
$A_{superstrg}$	Super Stringer section	m^2
$A_{superfrm}$	Super Frame section	m^2

Symbol	Description	Unit
$m_{insulation}$	Insulation mass	kg
BWB geometric model		
y_{px}	Lateral position of the plan p_x	m
c_{p0}	Chord at plan p_0	m
ϵ_{p0}	Half of the difference between the available thickness and the cabin height at the central plan p_0	m
h_{max}	Maximum cabin height	m
Max_{side}	Maximum number of side tank row	-
Max_{rear}	Maximum number of rear tank row	-
$Max_{tank/srow}$	Maximum number of tank per side row	-
N_{side}	Number of side tank	-
N_{rear}	Number of rear tank	-
R_{side}	Radius of side tank	m
R_{rear}	Radius of rear tank	m
L_{side}	Length of side tank	m
L_{rear}	Length of rear tank	m
S_{xside}	Longitudinal spacing between side tank	m
S_{xrear}	Longitudinal spacing between rear tank row	m
S_{yside}	Lateral spacing between side tank row	m
S_{yrear}	Lateral spacing between rear tank	m
$A_{overlap}$	Sum of projected area of tank overlap	m^2
$a_{i,j}$	Projected area of jth tank on the ith side row	m^2
a_k	Projected area of the outermost rear tank on k^{th} rear row	m^2
$a_{k,ij}$	Intersecting area of a_k and $a_{i,j}$	m^2
$d_{xr,1i}$	Longitudinal distance between the outermost rear tank bulkhead dome on the ith row and control surface	m
$d_{xr,2i}$	Longitudinal distance between the outermost rear tank barrel corner on the ith row and control surface	m
d_{xsi}	longitudinal distance between tank the aft top dome of the most aft tank on the ith row and the trailing control surfaces	m
$h_{sfront,ij}$	Height between the intrados and the extrados at the front barrel end of the jth tank on the ith side row	m
$h_{srear,ij}$	Height between the intrados and the extrados at the rear barrel end of the jth tank on the ith side row	m
$h_{r,ij}$	Available height between the intrados and the extrados for the jth tank on the ith rear row	m

Introduction

Over the past two centuries, humanity's impact on the environment has grown exponentially, leading scientists to designate this era as the Anthropocene. The Earth's ecosystems—upon which modern human societies have developed—are now undergoing rapid and unprecedented changes, often described as a series of interconnected crises. These transformations are occurring at a pace far exceeding the natural capacity for adaptation, threatening the sustainability of current societal models and planetary systems. Without decisive action, the stability of these systems—and thus the conditions that support contemporary human civilization—could be severely compromised.
Among these crises, climate change stands as one of the most urgent challenges, driven by the global rise in atmospheric temperatures. In 2015, 196 countries signed the Paris Agreement, pledging to limit global warming to 2^oC—a threshold beyond which the current model of human society may no longer be sustainable. Since climate change is primarily driven by the increased radiative forcing of the atmosphere, meeting this target requires a drastic reduction in emissions of the three primary greenhouse gases: carbon dioxide (CO_2), methane (CH_4), and nitrogen oxides (NO_x).

In this global context, the aviation sector accounts for 2–3% of global CO_2 emissions, yet its contribution rises to 5–6% of the increase in radiative forcing when non-CO_2 effects—primarily NO_x emissions and contrails—are considered. This share is projected to grow in the coming decades, as air traffic continues to expand while other emitting sectors decarbonize more rapidly. As part of the global push toward sustainability, aviation must actively contribute to emission reduction efforts, leading the **International Civil Aviation Organization (ICAO)** to declare in 2022 that the sector must achieve climate neutrality by 2050. To meet this ambitious target, the aviation industry is focusing on developing more fuel-efficient aircraft while transitioning to decarbonized energy sources. While **Sustainable Aviation Fuel (SAF)** offers a short-term solution, its scalability and environmental benefits are still debated. Hydrogen, produced with clean electricity, stands out as a zero-emission long-term alternative, capable of powering gas turbines or fuel cells without emitting CO_2.

Designing a hydrogen-powered aircraft, however, presents significant technical challenges. Hydrogen gas has an extremely low volumetric energy density, making liquefaction essential to obtain a practical storage volume for any aircraft beyond the regional category. Even in liquid form, however, hydrogen still requires roughly four times the volume of conventional kerosene (while regional aircraft might manage with very high-pressure gaseous tanks, the associated weight penalties are prohibitive for larger aircraft). This also introduces the need for cryogenic storage (given hydrogen's boiling point of 20 K) and pressurized tanks, which profoundly impacts aircraft design. Consequently, hydrogen tank integration must be considered as early as the pre-conceptual design phase. Numerous studies have proposed new aircraft design methodologies tailored to hydrogen-powered **Tube and Wing (T&W)** configurations. These studies show that while hydrogen's high specific energy reduces fuel mass, the need for large tanks and major airframe modifications to accommodate them can degrade aircraft performance—especially in energy efficiency, payload capacity, and range.

One promising approach to overcome these challenges and facilitate hydrogen integration is to transition to entirely new aircraft configurations, such as the **Blended Wing Body (BWB)** architecture. In this design, the entire fuselage contributes to lift generation, offering improved fuel efficiency—as demonstrated in previous studies on Blended Wing Body (BWB) configurations—compared to conventional **T&W** aircraft, as well as a large internal volume suitable for accommodating voluminous hydrogen fuel tanks, a feature emphasized in research on hydrogen-powered aircraft. Despite its potential, the hydrogen-powered BWB concept remains understudied, with little research dedicated to this specific configuration. Given its significant departure from conventional kerosene-based **T&W** designs, traditional conceptual aircraft design methods—often relying on historical data—are inapplicable. To determine whether this concept could or should play a role in the aviation industry's efforts to reduce its environmental impact, a key research question emerges: **How can a new methodology be developed to accurately size a hydrogen-powered Blended Wing Body aircraft and rigorously assess its performance at the conceptual design stage?** Addressing this question is the primary objective of this thesis, whose work was divided in 6 steps.

Chapter 1 provides a comprehensive literature review on the subject. It begins by outlining the current environmental crisis, its causes, and potential consequences, before focusing on the aviation sector's role and its strategies for mitigation. The chapter then explores key innovative technologies, starting with hydrogen-powered aircraft. It traces the evolution of the concept—from early prototypes to recent research—highlighting efforts to develop design methodologies and assess performance. While studies suggest hydrogen aircraft are feasible, they also underscore persistent technological and economic challenges, particularly the integration of hydrogen tanks as the primary technical hurdle. A third section reviews Blended Wing Body aircraft, a concept dating back over a century. Despite its proven fuel efficiency, industrial, safety, and economic barriers have delayed its commercialization. The chapter concludes by examining the limited existing research on hydrogen-powered BWB aircraft, which, though promising in early studies, remains constrained by narrow design exploration and low-fidelity modeling. Finally, the

chapter explains how this context shapes the research strategy of this thesis.

Chapter 2 presents the development of a medium-fidelity analytical model designed to estimate hydrogen losses in an onboard cryogenic tank during the pre-conceptual aircraft design phase. It starts with a review of existing thermal and fluid dynamic modeling methods for cryogenic hydrogen tanks, highlighting gaps in self-pressurization fidelity in traditional homogeneous models while drawing inspiration from spacecraft industry approaches. The chapter introduces a novel thermodynamic model using an enhanced electrical resistance analogy to estimate heat flux into the tank's liquid and gaseous phases. By segmenting the tank into multiple sections, each analyzed individually, the model captures localized thermal variations, improving accuracy. A three-control-volume self-pressurization model—independently simulating the bulk liquid, ullage, and their interface—is then proposed, moving beyond conventional homogeneous models. Inspired by space industry practices, this approach provides a computationally efficient yet robust framework for predicting the tank's thermodynamic evolution, particularly its internal pressure dynamics, during flight. Finally, the model is integrated into the FAST-OAD aircraft design tool, enabling an assessment of cryogenic fuel storage boil-off losses, and facilitating critical trade-offs between insulation, weight, and efficiency.

Chapter 3 extends the thermodynamic model by introducing a CS-25-compliant structural sizing methodology for hydrogen tanks, integrated into FAST-OAD to estimate tank mass. Since liquid hydrogen requires large, pressurized storage volumes—unlike kerosene tanks—its structural mass must be considered early in design for accurate performance evaluations. After reviewing existing methods and their limitations in terms of certification compliance or modeling fidelity (high-fidelity finite-element analyses being unsuitable at this stage due to their prohibitive computational cost), this chapter introduces a new analytical methodology for sizing cylindrical cryogenic tanks with hemispherical or semi-elliptical bulkheads. It comprises four main steps: determining the loads applied to the tank (for the **T&W** configuration), calculating the required wall thickness, selecting the appropriate number of stiffeners, and finally sizing their cross-sections. For integral tanks, loads are computed using a simplified beam model, while non-integral tanks rely on a user-defined load transmission factor. The sizing process ensures compliance with CS-25 regulations, optimizing wall thickness and stiffener configurations to prevent buckling and elastic deformation under operational loads. Finally, the chapter details total tank mass computation, concluding with its integration into the FAST-OAD aircraft sizing tool.

After integrating a thermodynamic model to estimate hydrogen boil-off losses and a structural sizing methodology for hydrogen tanks into FAST-OAD, Chapter 4 demonstrates the enhanced capability of the tool to design hydrogen-powered **T&W** aircraft. The chapter also aims to determine optimal tank parameters, which will serve as a foundation for the conceptual design of a hydrogen-powered Blended Wing Body (BWB) aircraft. The analysis begins with a design test case: a hydrogen-powered single-aisle aircraft configured for a typical **Small to Medium Range (SMR)** mission. A design of experiments is conducted, successfully sizing hundreds of hydrogen-powered aircraft to evaluate the impact of critical tank design variables on both tank and aircraft performance. The findings inform parametric trade-off studies, assessing the interplay between key variables—such as insulation thickness, pressure differential, dormancy duration, and

tank configuration—and their effects on fuel efficiency, tank mass, and boil-off. Finally, an optimized hydrogen-powered aircraft configuration is identified, sized, and compared to a conventional jet-fuel aircraft, offering valuable insights into the performance and design characteristics of hydrogen-powered aviation.

Chapter 5 expands FAST-OAD to enable the design of hydrogen-powered **BWB** aircraft, incorporating a framework for flexible tank configurations. The chapter begins by adapting FAST-OAD's geometric and structural models with **BWB**-specific modules, extracted from previous work conducted at onera (**Conception Intégrée d'une Configuration d'Aile Volante (Integrated Design of a BWB configuration) (CICAV)**), while also introducing new functionalities, including a stability analysis module for evaluating static margin and optimized modules for engine and landing gear placement. The chapter then introduces a framework for hydrogen-powered flying-wing design, featuring a novel parameterization to define the number, position, and geometry of cylindrical hydrogen tanks within the airframe. Geometric and stability constraints are established to ensure aircraft feasibility. To address the complexity of the design space, the traditional Multidisciplinary Analysis approach in FAST-OAD is advanced to a Multidisciplinary Design Analysis and Optimization (MDAO) framework, enabling a systematic exploration of solutions to identify optimized and feasible **BWB** designs that meet all technical and operational requirements.

Chapter 6 demonstrates the capabilities of the enhanced **Multi-Disciplinary Analysis and Optimization (MDAO)** design methodology integrated in FASt-OAD by applying it to the conceptual design of a short-to-medium-range hydrogen-powered **BWB** aircraft. First, the design case study is defined, including the **SMR** mission and the set-up of key design parameters. Next, a design space for the hydrogen **BWB** is constructed and explored through a large-scale **Design of Experiment (DoE)**, leveraging high-performance computing at ONERA. The **DoE** is analysed to provide statistical insights into feasible and efficient aircraft architectures. The analysis highlights that the minimum static margin constraint imposes the most significant limitation, while other constraints can be safely simplified or omitted to streamline the process. Finally, the insights from the **DoE** are used to simplify the optimization problem, enabling a full optimization of the hydrogen **BWB** using the Bayesian Optimizer **Super Efficient Global Optimization Mixture Of Expert (SEGOMOE)**. The optimized design is then compared to conventional jet-fuel **BWB** and **T&W** configurations (both hydrogen- and jet-fuel-powered) to assess energy efficiency, architectural advantages, and the potential of the **BWB** for aviation's energy transition.

This dissertation concludes with a comprehensive review of the conducted work, summarizing the key results, and then outlines perspectives for future developments to further refine or expand the hydrogen-powered blended wing body design methodology.

CHAPTER I

Context and Research Strategy

Résumé

Ce premier chapitre de thèse a pour but de poser le cadre général du problème traité dans cette étude. Il commence par exposer le contexte actuel de crise environnementale, dont l'une des manifestations les plus pressantes est le changement climatique. Ce dernier pourrait en effet fortement déstabiliser les sociétés humaines s'il dépasse leur limite d'adaptabilité, estimée autour de 2°C par le Groupe d'experts intergouvernemental sur l'évolution du climat (GIEC). Or, le transport aérien, dont l'impact sur le climat est déjà significatif, voit son empreinte appelée à s'aggraver avec la croissance exponentielle du trafic prévue dans les décennies à venir. Pour réduire son impact, celui-ci mise sur l'amélioration technologique des aéronefs, visant à réduire leur consommation et leurs émissions, mais aussi sur l'utilisation de carburants décarbonés. Cependant, les gains en efficacité des configurations conventionnelles atteignent aujourd'hui leurs limites, tandis que les carburants aériens durables (SAF), actuellement envisagés comme une solution majeure, se heurtent à des contraintes de disponibilité limitée et à une réduction d'impact en cycle de vie encore insuffisante. Pour atteindre l'objectif de neutralité carbone, des innovations disruptives s'avèrent donc indispensables.

L'utilisation d'hydrogène comme source d'énergie en vol ainsi que l'adoption d'une configuration de type aile volante sont identifiées comme des solutions crédibles répondant à ces objectifs. Une revue détaillée de l'historique de ces deux concepts est donc menée, complétée par une analyse approfondie de l'état de l'art académique sur le sujet.

Concernant l'avion à hydrogène, il apparait que le concept est étudié depuis des dé-

cennies et que plusieurs prototypes ont déjà volé dans le passé, ce qui suggère que le concept est techniquement envisageable. La principale difficulté identifiée est le stockage du carburant à bord : en raison de sa faible densité énergétique volumique, l'hydrogène doit être liquéfié à 20 K (-253°C) pour que la quantité nécessaire pour un vol représente un volume raisonnable. Même dans ces conditions, le volume requis reste environ quatre fois supérieur à celui nécessaire pour stocker une énergie équivalente sous forme de kérosène. Les réservoirs d'un avion à hydrogène doivent donc être à la fois cryogéniques et pressurisés, non seulement pour maintenir l'hydrogène à l'état liquide, mais aussi pour limiter les pertes par évaporation — un phénomène inévitable, très marqué si l'isolation thermique est insuffisante. Cette double exigence rend les réservoirs lourds et encombrants, le résultat d'un compromis délicat entre isolation et masse. Ces contraintes impactent profondément l'architecture de l'avion, ainsi que ses performances globales. Par conséquent, la modélisation du réservoir d'hydrogène et l'étude de son intégration doivent être abordées dès la phase de pré-conception, lors de laquelle l'architecture préliminaire de l'avion est définie pour répondre aux exigences opérationnelles tout en identifiant les compromis optimaux. Plusieurs études ont donc proposé des méthodes de conception multidisciplinaire incluant le dimensionnement des réservoirs d'hydrogène pour évaluer différents concepts d'avions. Si ces travaux confirment la faisabilité et l'intérêt environnemental du concept, les performances estimées varient sensiblement selon les hypothèses et modèles. Des modèles plus précis sont donc nécessaires pour réduire ces incertitudes et affiner les prédictions.

Le concept d'aile volante intégrée (ou Blended Wing Body) est une configuration étudiée depuis plusieurs décennies également, avec un exemple opérationnel dans le domaine militaire : le bombardier B-2. La définition moderne de ce type d'appareil dans une utilisation commerciale, formalisée dans les années 2000, met en avant des améliorations aérodynamiques et structurelles majeures, notamment grâce à l'absence d'empennage, ce qui se traduit par une efficacité accrue. Ces avantages ont été confirmés par de nombreuses études, bien que cette configuration pose encore des défis importants en matière de contrôle en vol et d'évacuation d'urgence.

Bien que les avions à hydrogène et les configurations **BWB** offrent des avantages significatifs, les défis techniques mais aussi économiques et industriels qu'ils soulèvent ont jusqu'à présent freiné leur développement concret. Cependant, la configuration **BWB** présente des atouts structurels qui pourraient faciliter l'intégration de l'hydrogène : sa faible consommation énergétique réduit les besoins en carburant, tandis que son volume interne généreux offre un espace optimal pour loger des réservoirs cryogéniques. Dans un contexte de transition climatique, ce concept suscite un intérêt croissant, bien que les études disponibles restent rares.

Les quelques travaux identifiés confirment le potentiel technique et environnemental de cette approche, mais se limitent souvent à des analyses préliminaires sans optimisation poussée de l'architecture d'une aile volante à hydrogène.

Dans ce contexte, l'objectif de cette thèse est donc d'approfondir les recherches sur l'aile volante à hydrogène, notamment en développeant une méthode permettant de les

dimensionner et d'évaluer leurs performances. Pour cela il faudra développer un modèle de réservoirs d'hydrogène cryogénique, d'un niveau de fidélité supérieur à celui de la littérature, capable d'estimer la masse des réservoirs et les pertes par évaporation (boil-off) au cours d'une mission. Ce modèle devra être intégré au logiciel de conception avion FAST-OAD, co-développé par l'ONERA et l'ISAE-SUPAERO.

FAST-OAD sera ensuite été étendu pour permettre le dimensionnement de configurations de type **BWB**. Une paramétrisation flexible de l'agencement des réservoirs au sein d'un avion **BWB** à hydrogène est visée, afin d'offrir la possibilité d'explorer un large éventail de configurations. Cette approche permettrait d'identifier les architectures optimales et d'en évaluer les performances.

Contents of this Chapter

I.1 The Environmental Crisis Pressuring Aviation to Reduce Its Climate Impact 9
I.2 Hydrogen Aircraft: a promising but disruptive technology to reach zero-emission aircraft . . . 16
I.3 Blended Wing Body: a revolutionary yet challenging concept promising to improve aircraft energy efficiency . . . 33
I.4 Hydrogen-Powered Blended Wing-Body Aircraft: An Emerging Synergy of Technologies that could enable low-emission flight . . . 46
I.5 Research strategy . . . 51
I.5.1 Literature Review synthesis and Research Objectives . . . 51
I.5.2 Disruptive Aircraft Design: A New Conceptual Paradigm Enabled by the FAST-OAD Sizing Tool . . . 52
I.5.3 Methodology and Development Choices . . . 56

I.1 The Environmental Crisis Pressuring Aviation to Reduce Its Climate Footprint

In recent years, the accelerating degradation of Earth's ecosystems has become increasingly apparent, as evidenced by climate change, biodiversity loss, environmental pollution, and the depletion of natural resources. Collectively, these challenges represent substantial threats to the well-being and long-term sustainability of human societies, necessitating careful consideration and coordinated action. At the moment, climate change is probably the most well-known of these issues, and as stated in the IPCC's Sixth Assessment Report[**1**], it is primarily the result of human activities. The climate is indeed affected by human emissions of different gases, mostly carbon dioxide (CO_2), methane, and nitrogen oxide, that increase the greenhouse effect on earth, warming its atmosphere and oceans. During the last decade (2014-2023), the average temperature on earth was already around 1.2°C [**2**] above preindustrial level.

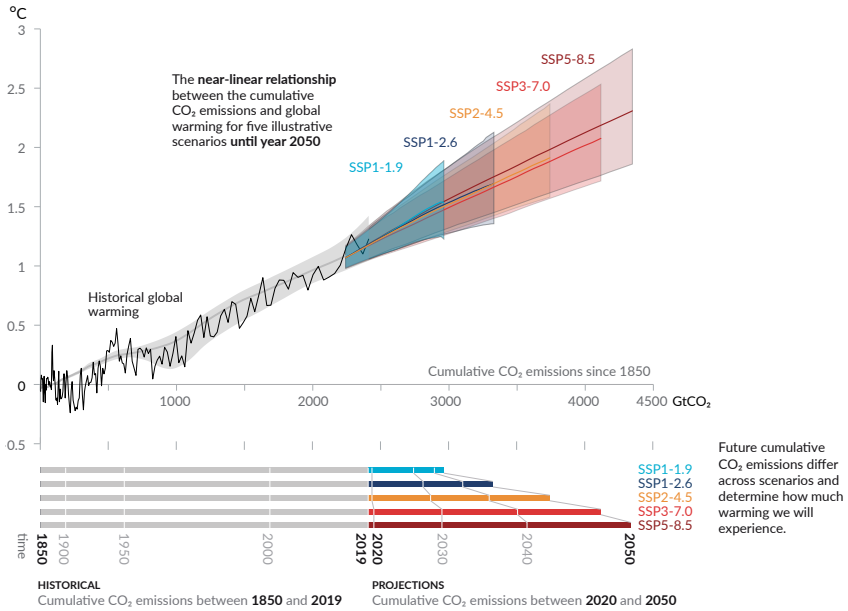

Figure I.1: Near-linear relationship between cumulative CO_2eq emissions and the increase in global surface temperature [**3**]

In 2015, countries around the globe signed the Paris Agreement, promising to cut their greenhouse gases emissions to stay below a 2°C increase on earth by 2100. This target was established to avoid a future where ecosystems and human societies face such profound transformations due to climate change that their capabilities to adapt are surpassed. As illustrated by the various future climate evolution scenarios assessed by the IPCC in Figure I.1, the global temperature rise exhibits an almost linear relationship with the cumulative emissions of greenhouse gases. Consequently, limiting global warming to 2°C necessitates establishing a maximum threshold for cumulative carbon-equivalent emissions that must not be exceeded. In his last summary for policymaker of its sixth assessment report [**3**], the IPCC estimates that to have at least a 50% chance of limiting the global warming to 2°C, the remaining carbon budget was around 1350 $GtCO_2eq$ (900 $GTCO_2eq$ for a 83%

chance) at the beginning of the 2020's. This budget is to be compared to the 59 ± 6.6 $GTCO_2eq$ emitted in 2019 [**4**], which means that at current trend the entire budget will be consummed in 15 to 25 years.

In this global context, the aviation industry contributes also to the radiative forcing on earth. Due to its reliance on fossil fuel in the form of kerosene, it is directly responsible for around 1 $GtCO_2eq$ in 2019 [**4**].Figure **I.2** presents the breakdown of emissions associated with the aviation sector. Overall, aviation contributes approximately 2.4% of global carbon emissions and 11% of emissions from the transport sector. Passenger air travel accounts for the vast majority—around 80%—of aviation emissions, with roughly two-thirds of that stemming from international flights, while the remaining third is attributed to domestic operations. The emissions are however equally distributed between short-haul (<1500 nmi), medium and long-haul flight (>4000nmi).

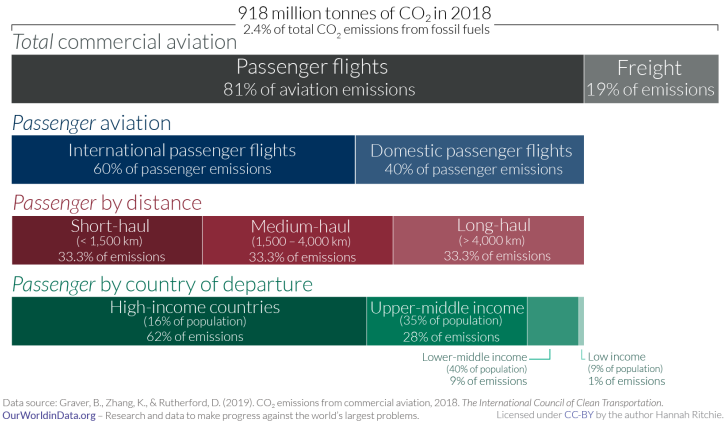

Figure I.2: Global CO_2 emissions from commercial aviation [**5**]

If the total emissions of air travel might appear to be a small percentage, they are comparable in magnitude to those of other major sectors such as maritime shipping, cement production or waste management [**4**]. Ultimately, no single economic sector dominates global emissions, making aviation's contribution significant in the broader context of climate mitigation efforts. Several others important facts must also be taken into account:

- Carbon dioxide emissions are not the sole, and potentially not the primary, means by which aircraft contribute to climate change. Lee and al. [**6**] stated indeed that the aviation sector is responsible for 2-3% of the global CO_2 emissions but of potentially 5-6% of the radiative forcing on earth when non-CO_2 effect are included.These non-CO_2 effects primarily arise from NO_x emissions and contrail formation. In the upper atmosphere, NO_x emissions act as catalysts in chemical reactions involving ozone (O_3) and methane (CH_4), altering their concentrations and contributing to global warming. Meanwhile, contrails form under specific temperature and pressure conditions in Ice-Supersaturated Regions (ISSRs), where ice crystals nucleate around soot particles emitted in aircraft exhaust. These contrails can persist in the stratosphere and may further promote the formation of cirrus clouds, which exert a net positive radiative forcing—particularly at night—thereby amplifying climate warming. However, the formation of contrails is highly dependent on local atmospheric conditions and weather patterns, making their occurrence difficult to predict

or quantify accurately. Consequently, significant uncertainty persists regarding the exact magnitude of radiative forcing attributable to contrails.

- Even just considering the CO_2 emissions, it is widely acknowledged that aviation is a hard-to-decarbonize sector. Although it currently represents only approximately 2.4% of global emissions, the aviation sector has been one of the fastest-growing sectors in terms of carbon emissions over the past decade, with a growth rate still accelerating - averaging nearly 4% per year between 2010 and 2019, compared to 2.5% annually in earlier periods [**4**]. Given a projected traffic growth rate of approximately 3.5% annually and the likelihood that other sectors will decarbonize more rapidly, aviation's share of global greenhouse gas emissions could increase significantly in the coming years. If left unchecked, a sustained traffic growth rate of 3.5% per year [**7**]—despite an expected average annual energy efficiency improvement of 1.3% [**4**] —could still result in approximately 200 $GtCO_2$ emissions by 2100 ($\sum_{i=0}^{75}(1.035-0.013)^i = 195\ GtCO_2$)—representing 15–20% of the remaining carbon budget compatible with the Paris Agreement targets.

- As illustrated in Figure I.2, the majority of air passengers come from high-income socio-economic groups, meaning that a relatively small portion of the global population contributes disproportionately to climate impacts through air travel. Within the framework of a fair ecological transition, this disparity risks being perceived as unfair, potentially fueling resentment among lower-income populations. Should the aviation sector fail to address its emissions independently, these groups may legitimately demand that prioritized action—whether through policy interventions or reductions in overall air traffic—be taken to curb the sector's climate impact.

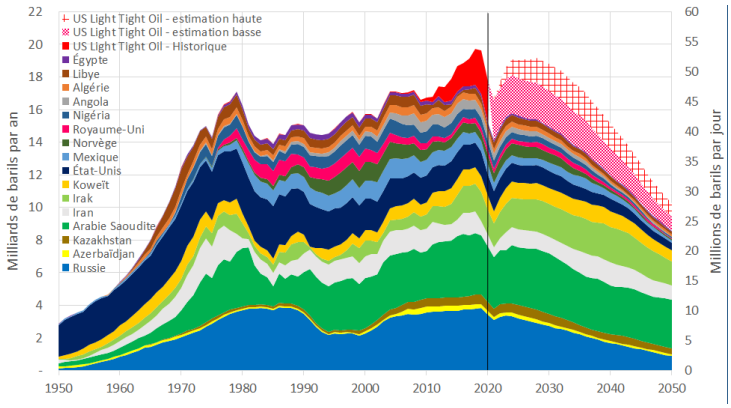

Figure I.3: Crude oil production of the 16 main EU suppliers from 1950 to 2050 (projected post 2020 by the Shift Project). Source : Rystad Energy. Adapted from [**8**]

- Even setting aside the climate crisis, the aviation industry's near-total dependence on fossil-based kerosene—a finite and non-renewable resource—poses a fundamental challenge to its long-term sustainability. Over the medium to long term, the growth, or even the maintenance, of air travel at current levels is inherently constrained by the availability of this resource. This constraint may become particularly

acute in regions with limited natural oil reserves or production capacity. Figure I.3, based on data from Rystad Energy analysed by the Shift Project [**8**], illustrates projected crude oil production trends for the 16 primary suppliers to the European Union—most of which are also the world's largest oil producers—up to 2050. The projections indicate a decline in production beginning in the 2030s, with output potentially halving by 2050. Given the European Union's increasing competition with emerging economies for oil supplies, the decline in available fuel for Europe could accelerate even further. Developing alternatives to fossil fuels is therefore not only essential for the long-term viability of air travel but for the sustainability of all transport sectors.

In response to this situation, the **ICAO**—the UN agency responsible for regulating international civil aviation standards and policies—declared in 2022 that the aviation sector must achieve climate neutrality by 2050. Figure I.4 illustrates ICAO's most ambitious roadmap to mitigate aviation's climate impact. Like most air travel decarbonization scenarios, this plan relies on four key levers to reduce emissions:

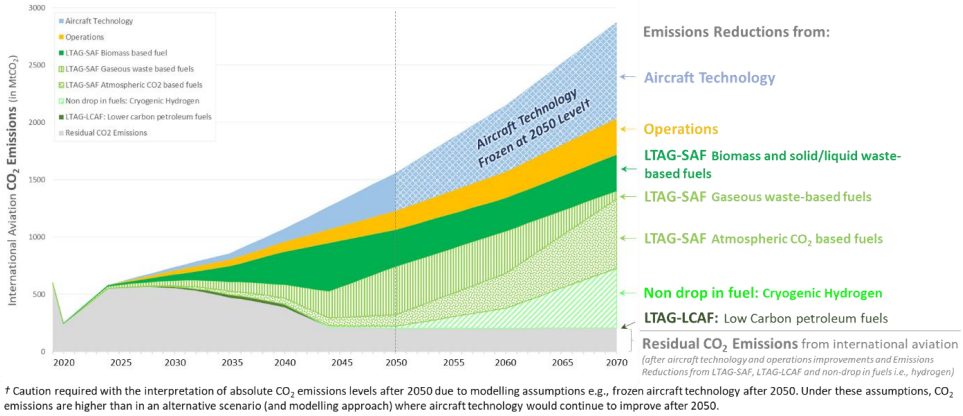

Figure I.4: **Long Term Aspirational Goal (LTAG)** integrated scenario 3: aggressive decarbonization path [**9**]

- Producing more energy-efficient aircraft: as aircraft emit carbon by burning kerosene (Jet A), aircraft that consume less fuel automatically release less CO_2 in the same order of magnitude. This is the strategy most aircraft manufacturer have been following until now as more efficient aircraft are also more economically interesting. The fuel consumption of aircraft per passenger-mile have been divided several time since the beginning of air travel but this benefit was more than compensated by the growth in traffic [**6**]. In the aggressive long term aspiration goal scenario of **ICAO** depicted in figure **I.4** this lever (in blue) account for 21% of the total carbon reduction by 2050. This category includes all technological advancements aimed at reducing fuel consumption, ranging from incremental improvements—such as lighter materials and more aerodynamic wing profiles—to disruptive innovations like open-fan engines or new configurations like lifting fuselages or structurally braced wing aircraft that enable higher aspect ratios.

- More efficient aircraft operations: another way to reduce emissions is to optimize the operations of aircraft. This includes for example optimizing flight paths to have the shortest routes possible, operating on continuous cruise climb and continuous descend or avoiding aircraft loitering for landing clearance as much as possible. It also encompasses reducing emissions on the ground where aircraft engine are especially inefficient with single-engine taxiing or electric taxiing for example. In most scenarios like the **LTAG** this represent around 10% of emissions saving.

These first two decarbonization levers together account for one-third of the pathway to net zero in ICAO's plan. However, as in the past, their potential to reduce emissions is insufficient to just offset the increase in emissions driven by growing air traffic. Furthermore, even highly efficient aircraft will still require energy to operate, meaning that achieving net-zero emissions ultimately depends on decarbonizing the energy source used by aircraft. This can be done in two different way, which are the last two levers of decarbonization:

- Replacing fossil jet fuel by **SAF**: SAF, also known as biofuel or electrofuel, are fuels that are really similar to current kerosene in their chemical composition. As such it is relatively easy to use them in current jet engines (they are also called "drop-in" fuel), but they still emit carbon while burning. Their benefit for the environment appears when looking at their life-cycle analysis. SAFs are indeed either produced from biomass or by combining atmospheric CO_2 with hydrogen in a chemical reaction to recreate hydrocarbon chains (electrofuel). A detailed review of all production pathways for these alternative aviation fuels is provided in the annex (Figure A.29). As the carbon released during combustion of these fuels originates from the atmosphere—for the biofuel case, the plant absorbs the carbon by photosynthesis during its growth—their use is supposedly carbon neutral.

  In **ICAO**'s **LTAG** biofuel (in solid green in figure I.4) are the main way of decarbonization in the short-to-medium term. As of 2025, seven different biofuel production pathways have been certified by **ICAO** that meet sustainability criteria defined under **Carbon Offsetting and Reduction Scheme for International Aviation (CORSIA)**[**10**]- ICAO's global carbon offsetting scheme aimed at capping and reducing CO_2 emissions from international aviation to 2020 levels. These SAFs are already being blended into current jet fuel supplies, making them the most readily scalable solution for aviation decarbonization. As such, the aerospace industry is heavily relying on them in their decarbonization plans.

  However, current SAF use remains limited to just a few percent of total aviation fuel, and there are significant challenges and controversies to large-scale adoption. One of the main constraints is the limited availability of sustainable biomass, as diverting it for fuel production can compete with land, water, and other resources essential for food production. Cultivating biofuel feedstocks may reduce agricultural capacity, drive deforestation to recover lost farmland, and result in **Induced Land Use Change (ILUC)**, all of which contribute additional emissions. Moreover, biofuel production often requires large quantities of water, as well as fertilizers and pesticides, exacerbating environmental and climate impacts [**11**].

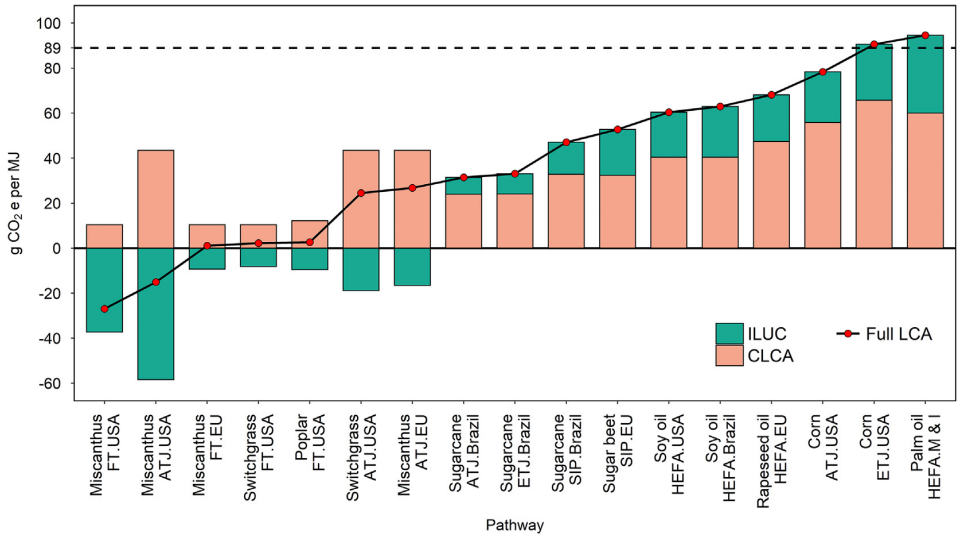

Figure I.5: Full life-cycle emission intensity for sustainable aviation fuels. Bars indicate the composition of the emission intensity (**ILUC** or **Core Life Cycle Assessment (CLCA)**) for a pathway. Points and solid line represent the full life-cycle emission intensity (sum of **ILUC** and **CLCA** values). Dotted line shows life-cycle emission intensity of petroleum-based jet fuels [**12**]

Figure I.5 further illustrates that not all biofuels offer the same climate benefits. For example, SAFs produced from palm oil via the HEFA process can have life-cycle emissions around 60 gCO_2eq/MJ—only about a 30% reduction compared to conventional kerosene (89 gCO_2eq/MJ). When **ILUC** emissions are taken into account, some SAFs may even have a higher carbon footprint than fossil-based jet fuel. **ILUC** is thus a critical factor in accurately assessing the true emission reduction potential of SAFs.

To mitigate these issues, CORSIA restricts eligible feedstocks primarily to waste and agricultural residues. Nevertheless, the availability of these resources in sufficient quantity remains a major challenge—particularly as other sectors, such as shipping, also compete for the same limited supply. Figure **I.6** shows that while initial SAF blending targets are relatively achievable, future goals are at risk due to the limited availability of sustainable feedstocks [**13**].

A way to get pass the feedstock problem of biofuel is to go towards e-fuels, or Power-to-liquid SAF. Those fuels are indeed synthetized by combining hydrogen with CO_2 and don't necessitate feedstock. However, for this pathway to be truly carbon-neutral, the hydrogen must be generated using low-emission methods—typically through electrolysis powered by decarbonized electricity. Additionally, the source of CO_2 is critical: to ensure climate benefits, it must either come from direct air capture (also powered by clean electricity) or from industrial processes that combust renewable feedstocks. Since hydrogen production, CO_2 capture, and the subsequent fuel synthesis processes (such as Fischer–Tropsch or methanol synthesis) are all energy-intensive and often operate with moderate conversion efficiencies, the overall energy efficiency of e-fuels remains relatively low—around 30% [**14**]. This pathway there-

fore requires large amounts of renewable electricity, and its technological maturity is still not fully proven at commercial scale.

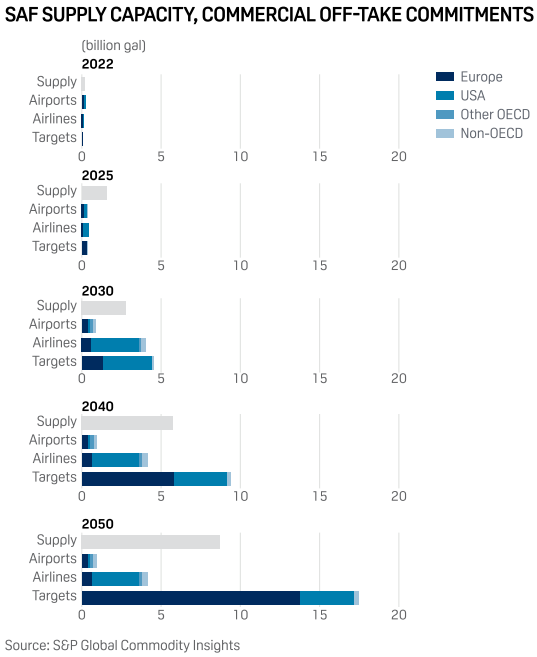

Figure I.6: Comparison of bio-SAF supply and blend-in target for the future (2022)[**13**]

- Using hydrogen aircraft: In the long term, hydrogen-powered aviation is considered one of the most promising pathways for fully decarbonizing flight. Hydrogen can be used in a gas turbine or in a fuel cell to produce electricity that powers electric motors, and in both cases it does not emit CO_2. If hydrogen is produced sustainably—primarily through electrolysis using decarbonized electricity, which is currently the main considered pathway—it could enable net-zero aviation, although other clean production pathways are under development and may also emerge in the future. Compared to Power-to-Liquid SAF, this approach avoids the need for carbon capture and a secondary fuel synthesis process, potentially offering higher well-to-wake energy efficiency. However, significant technological, safety, and economic challenges limit its potential to substantially reduce aviation emissions in the near future. Moreover, for hydrogen aircraft to become a viable solution, an entirely new infrastructure and broader "hydrogen economy" must be established. This transformation extends well beyond the aerospace sector and depends heavily on developments in the energy industry, political decisions, and long-term economic strategies.

These four pathways to climate-neutral aviation are not mutually exclusive and will likely need to be combined to achieve ICAO's 2050 goals. Many of the most advanced aircraft concepts presented in the recent literature already combine sustainable energy sources with improved energy efficiency. From a medium- to long-term perspective focused on aggressive decarbonization, two particularly promising developments are hydrogen-powered aircraft and the adoption of innovative aircraft configuration designs such as the **BWB**. The following chapters will explore these two concepts in greater detail.

I.2 Hydrogen Aircraft: a promising but disruptive technology to reach zero-emission aircraft

The potential of hydrogen as an aviation fuel has gained renewed interest in recent years as a promising solution to mitigate the environmental impact of air travel. However, the exploration of hydrogen-powered aircraft is not a recent idea; its origins trace back over a century, driven by early concerns about the long-term availability of oil or the perceived superiority of hydrogen as an energy carrier. Consequently, a significant portion of the studies reviewed in this chapter dates from earlier periods. Nevertheless, this section endeavors to provide a comprehensive historical overview of the hydrogen aircraft concept, as many of these early works laid foundational insights that remain pertinent to contemporary research.

The concept of hydrogen-powered aircraft first emerged in the early 20th century, as researchers sought viable alternatives to gasoline and kerosene for aviation propulsion. Meyer [**15**] noted already in 1923 that pure hydrogen offers one of the highest energy densities by mass, making it an exceptionally lightweight fuel. However, he also highlighted that its practical application was hindered by the large storage volume and the heavy tanks required to contain it.

In 1942, thermodynamicist F. Simon of Oxford University suggested to Robert Kerley—then the leading aviation fuel expert with the U.S. Air Force and at **National Advisory Committee for Aeronautics (NACA)** (the precursor to **National Aeronautics and Space Administration (NASA)**)—that hydrogen could be used as an aircraft fuel. Kerley's skeptical response, humorously delivered in a tongue-in-cheek poem urging Simon to "shut off all this goddamn fuss"[**16**], reflected the impracticality of hydrogen for piston engines and the considerable challenges of producing and handling liquid hydrogen at the time.

However, with the advent of jet propulsion after World War II, hydrogen regained attention. Herrick L. Johnston at Ohio State University's Cryogenics Laboratory began studying hydrogen combustion [**16**]. While aircraft of that era lacked the internal volume to store sufficient cryogenic fuel, the growing interest in hydrogen propulsion for rocket drove significant advances in the production and handling of liquid hydrogen.

By the early 1950s, hydrogen's suitability for high-altitude flight—due to its ability to combust at low temperatures and pressures and its exceptionally high heating value—sparked renewed military interest. In 1951, Hugh M. Henneberry of **NACA**'s Lewis Flight Propulsion Laboratory remarked that "if tactical considerations predicate flight at extreme high altitudes, liquid hydrogen must be considered as a possible fuel"[**16**].

This idea advanced further in 1954 when Abe Silverstein, associate director at the Lewis Laboratory, recognized that high-altitude aircraft require large wings for lift—thus offering ample internal volume for storing low-density hydrogen. Together with analyst Eldon Hall, Silverstein wrote a report outlining both the advantages and engineering challenges of hydrogen-powered aircraft. The key advantages included improved engine efficiency and weight due to hydrogen's high heat of combustion, potentially enabling aircraft to reach ceilings of 80 000 feet (24 500 m), far beyond the JP-4 fuel limit of

21,000 feet and **NACA**'s 30,000-foot target. The primary challenge remained storage, which they addressed by proposing a hydrogen tank design inspired by long-range missile architecture (illustrated in Figure **I.7**), which consists of a long insulated cylindrical tank to hold the internal pressure.

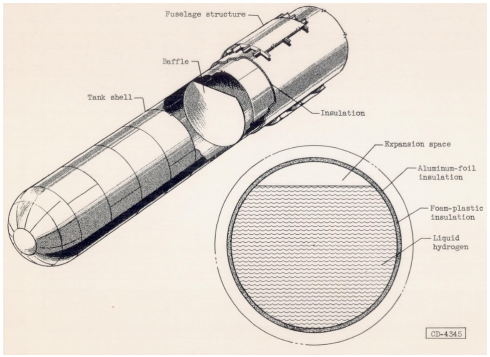

Figure I.7: Liquid hydrogen tank concept of Silverstein and Hall [**17**]. Dimension : 25m long, 3m in diameter

With this tank concept, they designed three aircraft: a subsonic bomber, a subsonic reconnaissance aircraft, and a supersonic fighter. The latter two are illustrated in Figures **I.8** and **I.9**. Notably, in the reconnaissance aircraft, nearly the entire internal volume is dedicated to hydrogen storage.

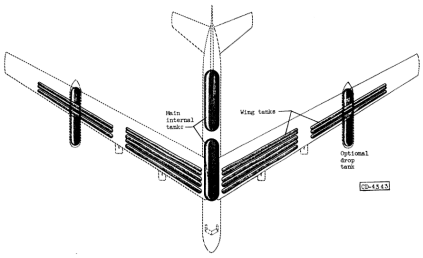

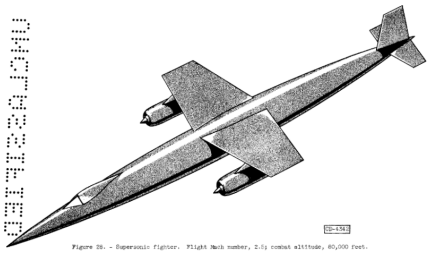

Figure I.8: Hydrogen reconaissance aircraft Figure I.9: Supersonic hydrogen fighter [**17**] [**17**]

This report led to a massive research program on hydrogen-fueled aircraft encouraged by Silverstein, which explored various aspects including hydrogen combustion, fuel properties, cryogenic materials, pumps, tanks, and engine adaptations. These efforts culminated in the BEE Project, where a B-57 aircraft was modified to operate with one of its engines powered by hydrogen, as shown in Figure **I.10**. In February 1957, the team successfully transitioned one engine from JP-4 to hydrogen during cruise flight at 50,000 feet, maintaining hydrogen operation for approximately twenty minutes. The hydrogen was stored in a pressurized tank mounted under the left wing, with helium used for pressurization from a separate tank under the right wing. Before combustion, the hydrogen was vaporized using a ram-air heat exchanger. The modified engine was capable of running on either fuel—or even both simultaneously—with minimal modifications [**18**]. This experiment also addressed several key questions related to hydrogen-powered aircraft. It demonstrated, for example, that liquid hydrogen could be rapidly and safely jettisoned in case of emergency and confirmed the necessity of purging the hydrogen fuel lines—using helium in this case—before operation. Furthermore, it showed that the hydrogen boiling

rate inside the tank matched closely that observed in static tests during flight, although significant deviations were observed during taxiing due to fuel sloshing within the tank [**16**]. In subsequent flights, it was further demonstrated that a liquid hydrogen pump could be used instead of the helium pressurization system to feed the engine [**19**]. This allowed for a reduction in the maximum required tank pressure, allowing the use of lighter tank structures, resulting in a significant overall weight savings.

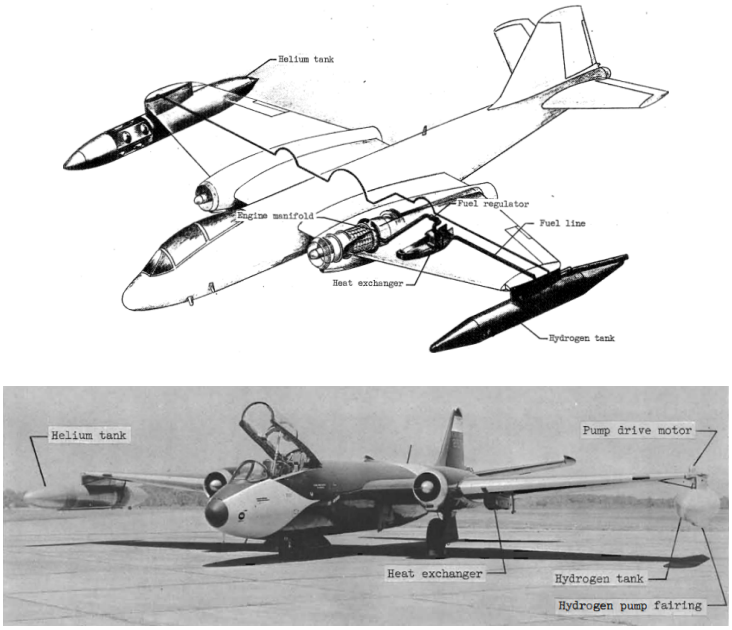

Figure I.10: Modified B-57 bomber used in the BEE project: (top) schematic view [**18**] and (bottom) real photo with hydrogen and helium tanks [**19**].

In parallel to this main experiment, others studies at **NACA** explored hydrogen engines for Mach 4 aircraft and Mach 7 ramjet missiles. Hydrogen's heat sink properties suited high-speed/high altitude missions (Mach 4, 30,500 m altitude, 4,500 kg payload) and aircraft concepts showed much greater range and lower mass than JP-4 designs, though still below the 10,200 km target. A hydrogen-fueled ramjet missile, however, far exceeded expectations, achieving 16,700 km at Mach 7, underscoring hydrogen's potential [**16**]. Unfortunately, these aircraft concepts ultimately lost out to intercontinental ballistic missiles, which offered more strategic advantages, and thus never advanced beyond the conceptual stage.

At the same time **NACA** was experimenting hydrogen powered aircraft with its Bee Project, the potential of hydrogen for high altitude aircraft had also sparked the interest of the US Air Force. Project Suntan (1956–1958) was a top-secret initiative to develop a hydrogen-fueled supersonic reconnaissance aircraft that could outperform the U-2. Despite the program's extraordinary secrecy—access was limited to just 25 individuals—it involved multiple contractors and was led by Kelly Johnson, the famed head of Lockheed's Skunk Works, assisted by Ben Rich, who would later design the F-117. The proposed aircraft, the Lockheed CL-400 (shown in Figure **I.11**), was designed to cruise at Mach 2.5 and 30,300 meters altitude with a radius of 4,070 kilometers. It carried nearly 10,000 kg of liquid hydrogen in triple-section vacuum-insulated tanks located within its

wide (3 m), 49-meter-long fuselage, with insulated fuel lines feeding its wingtip-mounted engines. Pratt & Whitney developed the hydrogen-powered 304-2 turbojet engine.

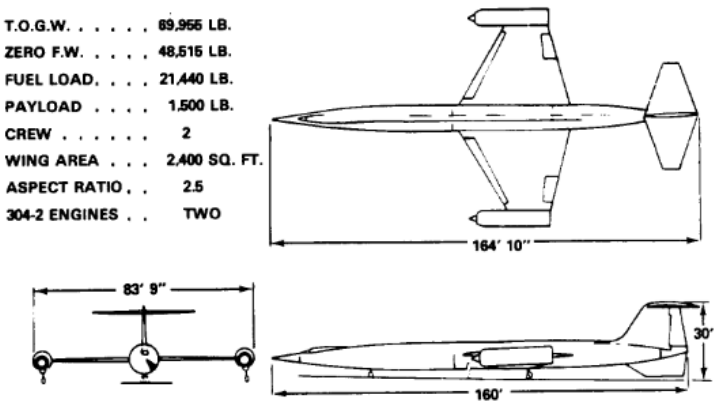

Figure I.11: Lockheed CL-400 reconnaissance aircraft prototype using liquid hydrogen (1955) [**16**]

A dedicated test facility at Fort Robertson, adjacent to the Skunk Works, enabled extensive hydrogen safety and tank experiments—some involving intentional rupture and ignition—to assess flammability and explosion risks. These tests demonstrated that hydrogen, while volatile, could be managed safely, often presenting fewer hazards than kerosene.

Despite significant technological advancements and discoveries, Project Suntan never progressed to a flight demonstration, primarily due to the limited range of the CL-400 and the lack of viable paths for improvement. Kelly Johnson, who initially led the effort, quickly concluded that the aircraft had no growth potential—the fuselage already contained the maximum possible amount of hydrogen, and the wings were unsuitable for additional storage. This assessment stood, despite differing views within his team, who believed further optimization might still be achievable. Nevertheless, much of the engineering work on the hydrogen propulsion system and cryogenic fuel infrastructure was later repurposed for U.S. space program, where it played a foundational role in advancing liquid hydrogen technology for rockets.

Hydrogen aircraft research came to a halt after the end of Project Suntan and remained dormant for nearly two decades, until the oil crisis of the 1970s reignited interest. The crisis highlighted the world's dependence on finite fossil fuels and oil-producing nations—an issue that remains relevant today. Because hydrogen can be produced locally through electrolysis, **NASA** launched several initiatives supervised by its Langley Research Center, in collaboration with Lockheed Martin, to explore the foundational technologies required for a liquid hydrogen–fueled commercial aircraft. Although no full-scale prototype was ever built as the oil crisis subsided a few year later, the research conducted during this period laid essential groundwork for future hydrogen aviation. Much of this work was led by C.E. Brewer [**20**][**21**][**22**][**23**], whose findings were later compiled in his seminal book Hydrogen Aircraft Technology [**24**], which remains a key reference in the field to this day. Brewer was tasked with evaluating the most suitable non–fossil fuel alternative for a wide range of aircraft types and missions. His analysis compared hydrogen-powered aircraft to those using liquid methane and synthetic fuels, covering both subsonic and supersonic flight regimes. The aircraft examined ranged from short-haul transports to

long-range and intercontinental designs, including military and hypersonic platforms. Beyond aircraft performance, Brewer also assessed the broader implications of adopting hydrogen—such as impacts on airport infrastructure, safety requirements, environmental effects, and economic viability. His long-range commercial hydrogen aircraft is presented in Figure I.12.

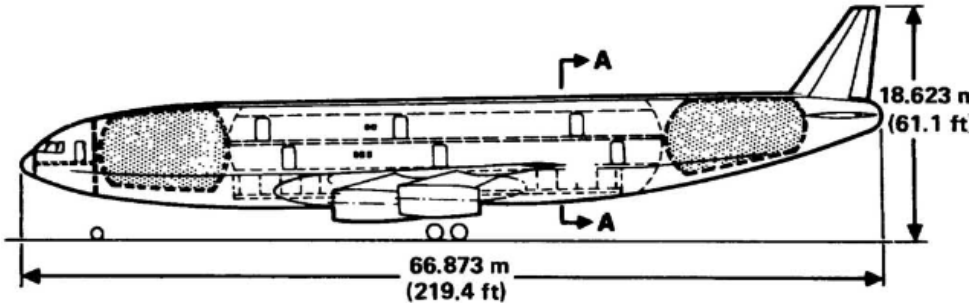

Figure I.12: Hydrogen-powered, double-deck commercial transport aircraft for a 400 passenger / 5500 nmi mission of G. D. Brewer[**24**]

His work included the detailed study and design of all critical hydrogen subsystems: cryogenic pumps, valves, fuel delivery systems, pressure relief devices and refueling systems. Special emphasis was placed on the cryogenic storage tank, which had already been recognized as one of the most critical and challenging components in hydrogen aircraft design. Various structural materials and insulation configurations were tested and compared to optimize both thermal performance and mechanical integrity. Brewer also focused extensively on hydrogen-adapted turbofan engines. By using hydrogen's heat sink capacity, these engines could cool components such as bleed air systems (see figure I.13, turbine blades, and compressor pre- and inter-cooling —resulting in efficiency gains estimated in the range of 5 to 10% compared to conventional jet engines.

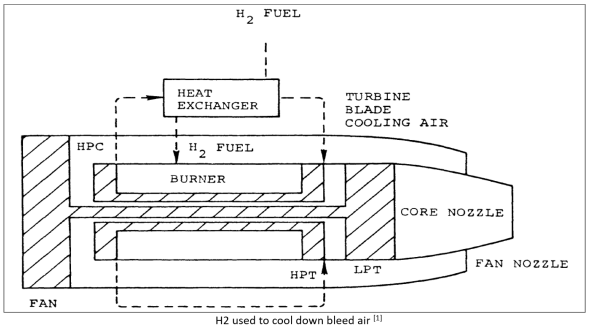

Figure I.13: Concept of aircraft engine with hydrogen-cooled bleed air [**24**]

Brewer concluded that hydrogen offers the greatest overall benefits among the alternatives considered. It produces no CO_2, CO, unburned hydrocarbons, sulfur oxides, or soot—and NO_x emissions can be significantly reduced. Hydrogen's high gravimetric energy density more than offsets its low volumetric density, resulting in superior aircraft performance across all flight segments—subsonic or supersonic.

As illustrated in Figure I.14, hydrogen-powered commercial aircraft consistently show

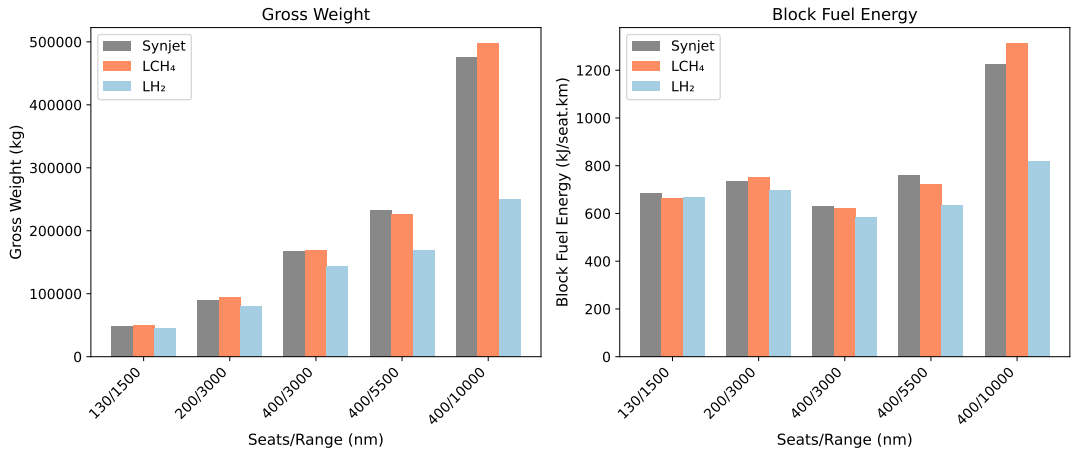

Figure I.14: Comparison of liquid hydrogen, liquid methane, and synthetic fuel aircraft on their gross weight and resource equivalent energy for different flight segments. Adapted from G. D. Brewer[**24**]

significantly lower gross weights, primarily due to reduced fuel mass. This translates to lower energy requirements for flight in terms of energy per seat.km, even when accounting for the energy cost of fuel production (resource equivalent energy). The advantage is even more pronounced in long-range aircraft, where fuel represents a larger portion of total weight. Brewer also made analysis with a life-cycle-analysis point of view, where he concluded that when considering also the energy needed to produce the fuel and liquify it, hydrogen aircraft was clearly above the other solution[**24**]. Given this and the finite nature of fossil fuels—which implies that their availability will inevitably diminish after reaching peak production, which he estimated would occur in the early 21st century—he strongly advocated for the continued development of hydrogen-powered aircraft, particularly given the long development times required for aircraft design and certification in the aerospace industry.

The ability to produce hydrogen almost anywhere—whether through electrolysis or by reforming fossil fuels other than oil (such as coal, of which the U.S. has abundant reserves)—renewed the U.S. Air Force's interest in hydrogen during the 1970s. This resurgence followed the oil crisis, which exposed the military's vulnerability to fluctuations in oil prices and supply. In response, the Air Force commissioned the RAND Corporation to study alternatives to petroleum for powering extremely large aircraft—those exceeding one million pounds (approximately 500 tonnes). Liquid hydrogen emerged as one of the leading candidates, alongside liquid methane, synthetic jet fuel (synjet), and nuclear propulsion systems [**25**].

The study concluded that, while hydrogen-powered aircraft were energy-efficient options, they also carried the highest costs—primarily due to the energy-intensive liquefaction process considered at the time, which accounted for about 40% of hydrogen's total cost. In the end, all proposed alternatives were more expensive than conventional petroleum-based fuels, and as long as oil remained sufficiently available and affordable, no significant effort was made to pursue these alternative propulsion systems further.

In 1982 however, Lockheed-Georgia decided to reexamines the results of this previous study this time incorporating the assumption that advanced technologies and new

design concepts would be developed and available by the year 2000 for integration into future aircraft. These advancements included the use of composite materials, improved aerodynamic features such as supercritical airfoils, double-slotted flaps, and leading-edge slats, as well as active control systems with gust load alleviation, a relaxed static margin (as low as -5%), more efficient high-bypass ratio engines, and fly-by-wire systems. The design optimization focused primarily on the wing geometry and engine power setting, and two aircraft configurations were designed for each fuel: one optimized for minimum ramp weight (which also corresponded to the lowest trip cost in their analysis), and another optimized for minimum fuel consumption. Their hydrogen aircraft fuel system concept builds upon the foundational work of Brewer [**22**], but introduces a novel tank configuration in the form of a multi-bubble tank layout, as illustrated in Figure **I.15**.

The study's results identified hydrogen-fueled aircraft as the most favorable option among the alternatives considered—hydrogen, synjet, and nuclear propulsion—in terms of trip cost, contrasting with the findings of the earlier study by Mikolowsky et al. [**25**] (note that conventional jet fuel was not included in this comparison). Additionally, hydrogen was found to be less sensitive to fluctuations in oil prices than synjet. As a result, the authors recognized hydrogen as the most promising fuel for future aircraft intended to carry heavy payloads over long-distance missions.

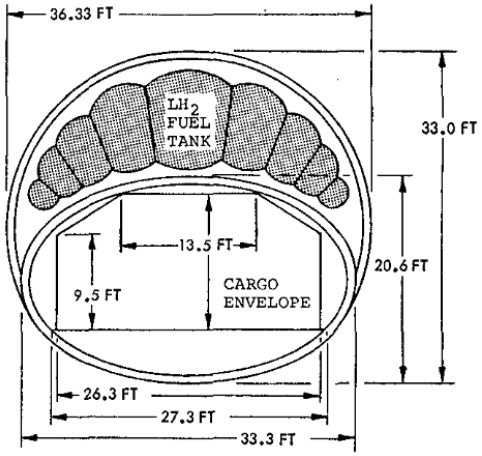

Figure I.15: Fuselage cross section of Muehlbauer hydrogen cargo aircraft [**26**]

Between those two last studies, **NASA**'s Langley Research Center also conducted its own evaluation of coal-derived alternative fuels for aviation—specifically liquid hydrogen, liquid methane, and synthetic jet fuel (synjet)—in collaboration with Lockheed under a contract study [**27**]. In their assessment, the most significant technical challenge for hydrogen-fueled aircraft was the containment and distribution system. Because hydrogen requires substantially more volume than conventional fuel and thermal insulation, it could no longer be stored in the wings. The study concluded that incorporating cryogenic hydrogen tanks within the fuselage—located both ahead of and behind the passenger cabin—offered the best overall aircraft performance. Although external tanks were easier to maintain and provided greater separation from passengers, they introduced significant drag penalties. In contrast, the internal tank configuration not only improved aerodynamic efficiency but also offered additional benefits, such as protection from engine burst

hazards and safer, more direct access for ground servicing operations.

The study also examined ground operations, including how refueling could be carried out. One solution involved an underground liquid hydrogen distribution network, with refueling trucks connecting directly to aircraft or with a refueling boom attached to a fueling control tower—concepts illustrated in Figure I.16 and I.17. The researchers concluded that the processes of liquefaction, storage, distribution, and aircraft refueling at airports were technically feasible.

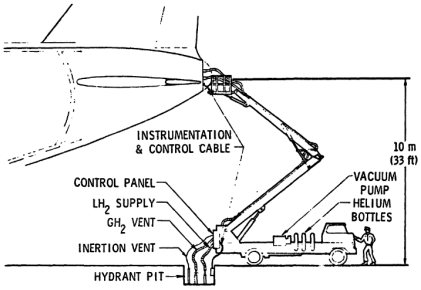

Figure I.16: H2 refueling truck [**27**]

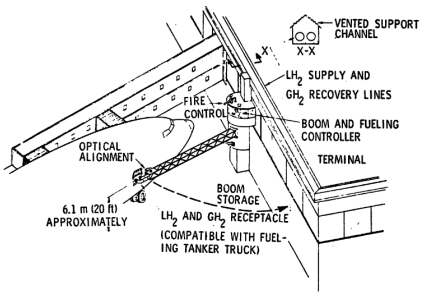

Figure I.17: H2 refueling boom [**27**]

Performance-wise, hydrogen-powered aircraft were again found to be more energy-efficient than their kerosene-fueled counterpart on medium to long-range missions. Energy advantages became evident at ranges above 4,000 km - or 8,000 km when accounting for the energy used in fuel production (Figure I.18). Across all scenarios, hydrogen consistently emerged as the most environmentally favorable option in terms of emissions.

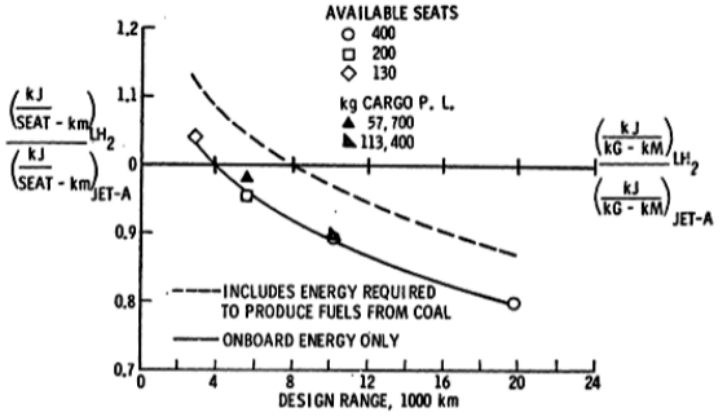

Figure I.18: Relative energy consumption of hydrogen and jet-A transport aircraft[**27**]

While much of the early research on hydrogen-powered aircraft was conducted in the United States, the USSR also pursued its own experimental efforts in the 1980s, led by the Kuibyshev Scientific Production Association ("Trud") and the Central Institute of Aviation Motors (CIAM). These initiatives were driven by similar concerns—namely, the anticipated decline in oil availability following peak production within the 21st century. In this context, liquid hydrogen was viewed as a promising long-term solution, with liquefied natural gas (LNG) considered a more immediate alternative to Jet A fuel [**28**].

To assess the feasibility of hydrogen-powered aviation, a Tupolev Tu-154 commercial

airliner was modified to include an 18 m^3 liquid hydrogen tank installed behind the passenger cabin. One of the aircraft's NK-8-2U engines was replaced with a modified NK-88 engine, capable of operating on kerosene, liquid hydrogen, or LNG [**29**]. The resulting experimental aircraft, designated Tu-155 (Figure I.19) completed its first flight in April 1988, during which the NK-88 engine successfully operated using both hydrogen and methane. However, certification requirements were not a primary consideration during its development.

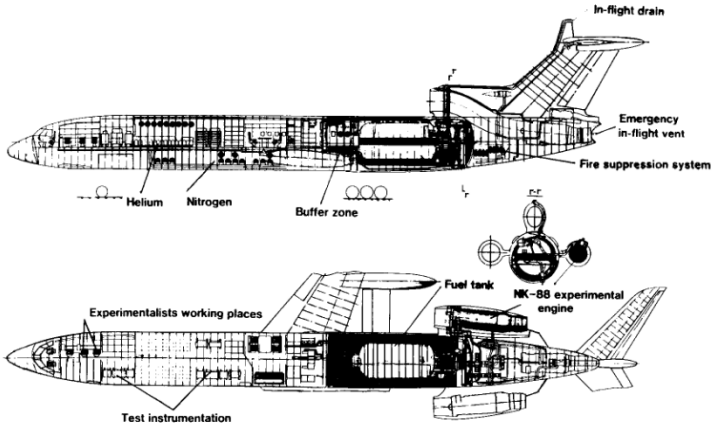

Figure I.19: The hydrogen-fueled Tu-155 aircraft with one LH2-powered NK-88 engine[**29**]

Following the early studies on hydrogen-powered aircraft—initially driven by concerns over future oil supply—academic and industry research gradually shifted its focus toward environmental sustainability.

Hydrogen-fueled aviation had already been recognized as a highly promising solution due to its potential for drastically reducing emissions of CO_2, but some studies started looking into into the reduction of Nox emissions. As part of the **Euro Quebec Hydro Hydrogen Project (EQHHPP)** project—which examined the feasibility of transporting Canadian hydropower to Europe by converting it into hydrogen via electrolysis—researchers studied for example the NOx emissions associated with hydrogen combustion systems. Hydrogen burns significantly faster and at a higher flame temperature than conventional fuels (see Figure I.21), which can lead to elevated NOx emissions and increase the risk of flashback within the engine.

However, the results demonstrated that innovative injector designs, such as premixed perforated plates, could reduce NO_x emissions by up to 95% compared to state-of-the-art kerosene engines from the late 1990s, when operated under lean-burn conditions. Although these designs exhibited some combustion stability issues at off-design points, alternative configurations offered a favorable balance between NO_x reduction and stability margin [**30**].

Subsequent studies [**31**] further validated the potential of low-NO_x hydrogen turbines by demonstrating that extremely lean combustion mixtures could effectively lower peak flame temperatures, thereby significantly reducing NO_x emissions (see Figure **I.20**).

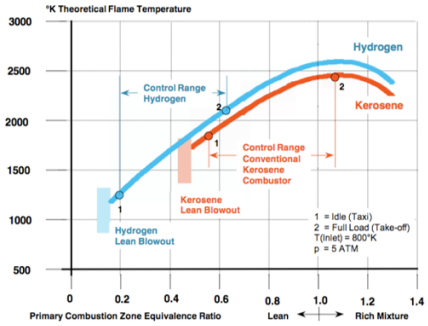

Figure I.20: Temperature characteristics of hydrogen combustion chambers [**32**]

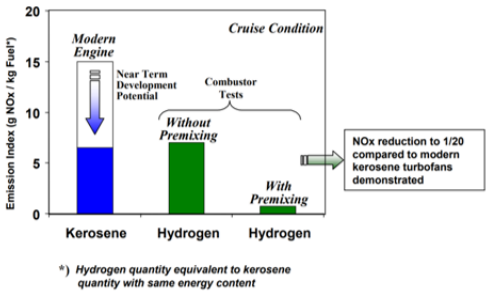

Figure I.21: Potential NOx Emissions reduction in hydrogen engine [**31**]

Beyond the narrower focus on reducing NO_x emissions from hydrogen-powered aircraft, one of the earliest and most comprehensive European initiatives addressing the broader environmental impact of aviation was the Cryoplane project, launched in the early 2000s [**33**]. This 26-month effort was coordinated by Airbus and brought together 35 partners—including industry stakeholders, research centers, and universities—from across Europe.

The primary objective of the project was to evaluate the feasibility of using liquid hydrogen as a fuel for commercial aviation and, more importantly, to lay the groundwork for the broader efforts needed to enable its development and eventual adoption in the sector. This involved assessing the performance and environmental advantages of hydrogen-powered aircraft, as well as identifying the major technical, economic, and regulatory challenges that must be overcome.

The study covered all categories of commercial aircraft by developing conceptual designs tailored to each operational flight segment. Several different aircraft configurations were considered, including unconventional configurations like the twin boom or the blended wing body (see figure **I.22**). It also addressed critical issues such as safety and the implications for airport infrastructure.

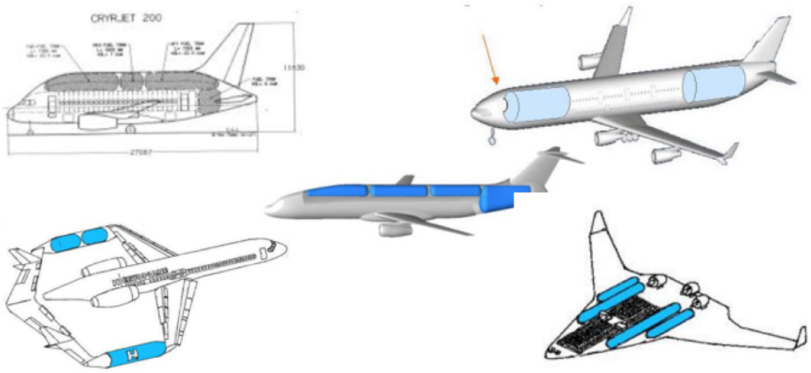

Figure I.22: Aircraft configurations studied in the cryoplane project [**33**]

Unlike earlier studies, the Cryoplane project concluded that hydrogen-powered aircraft would require more energy—ranging from 9% to 14% more, depending on the aircraft category. While hydrogen has a higher gravimetric energy density than kerosene, it requires

significantly more storage volume and heavy tanks. As illustrated in Figure I.23, this results in an increased empty weight—approximately 20–25% higher for most aircraft, and up to 48% for very large, long-range aircraft. The latter case is particularly affected by airport constraints, such as the 80 m box size limit, which forced a three-deck configuration with substantially higher mass and energy consumption.

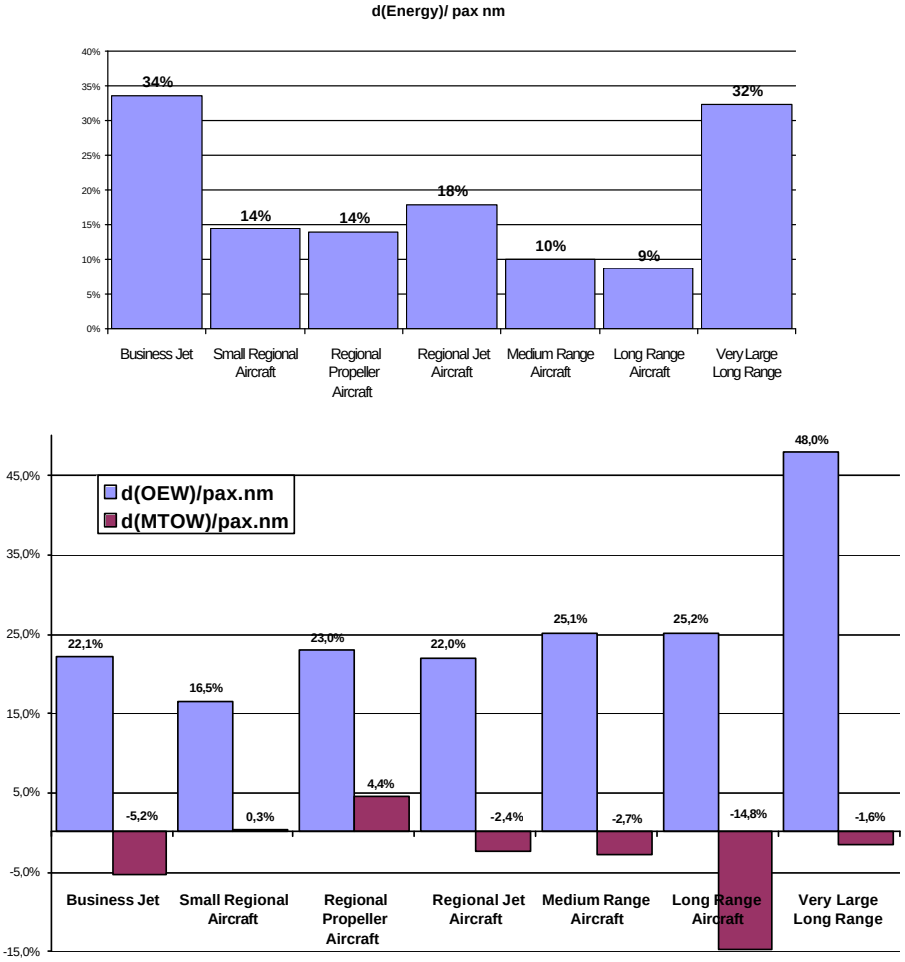

Figure I.23: Energy consumption (top) and mass variation (bottom) of hydrogen-powered aircraft compared to kerosene-fueled aircraft, as projected in the Cryoplane project [**33**]

In terms of energy use, and excluding the very large aircraft case, longer-range hydrogen aircraft still showed a smaller relative increase in energy consumption compared to smaller aircraft, consistent with earlier predictions. This system-level analysis led to several key conclusions:

- Unconventional configurations do not offer a significant advantage over conventional layouts, except potentially for the blended wing body in the case of very long-range aircraft—though this configuration was not investigated in detail.

- Hydrogen-fueled jet engines could match or exceed the efficiency of conventional engines, particularly if the cooling potential of hydrogen is fully exploited. How-

ever, several critical components—such as heat exchangers and fuel injection systems—while likely technically feasible, would still require further research.

- No major safety concerns were identified that would prevent the certification of hydrogen aircraft. These aircraft can be made as safe as their conventional counterparts.

- Hydrogen, when produced from renewable sources, offers substantial environmental benefits: it emits no CO_2, CO, soot, or unburned hydrocarbons. NO_x emissions can be significantly reduced due to hydrogen's combustion properties, such as its wide flammability range. While hydrogen-powered aircraft may produce more contrails, their lower optical thickness could result in a reduced climate impact. Additionally, studies have shown that lowering cruise altitude can significantly mitigate the environmental impact of contrails of hydrogen aircraft, with only a modest and environmentally justifiable increase in fuel consumption.

Ultimately, the Cryoplane project concluded that hydrogen-powered aircraft were both technically feasible and environmentally advantageous. It proposed medium- and long-term scenarios for a phased transition from conventional Jet A fuel to hydrogen in aviation. These scenarios envisioned the introduction of hydrogen aircraft as early as 2015, with all new aircraft potentially powered by hydrogen between 2025 and 2035, depending on the trajectory adopted. In all cases, strong political commitment and supportive policies would be essential to overcome the higher costs of the technology—especially to accelerate the transition toward 100% hydrogen-powered aviation. However, none of the proposed timelines materialized. This was likely due to the lack of willingness among stakeholders to absorb the higher costs of hydrogen aircraft, along with the significant investments required to deploy the necessary ground infrastructure for hydrogen production, storage, and airport distribution.

Around the same time, NASA reached similar conclusions through its Quiet Green Transport program, which aimed to develop commercial aircraft concepts with drastically reduced noise and emissions. The first concept (Concept A) featured a strut-braced wing and over-wing hydrogen turbofan engines running on liquid hydrogen [**34**], while the second (Concept B) explored a fuel-cell-powered blended wing body [**35**]. Both concepts demonstrated major reductions in noise and emissions, but their deployment was hindered by the high cost of hydrogen and the absence of a supporting hydrogen economy—particularly for Concept A, which did not face major technical barriers but required breakthrough technologies to become economically viable.

If the conditions were not met at that time for the introduction of hydrogen aviation, the research on the subject still continued. In 2005, Sefain [**36**] explored unconventional configurations such as the twin-boom concept, highlighting its structural efficiency but also noting aerodynamic drawbacks and a wide center-of-gravity travel range. He also conducted an in-depth analysis of hydrogen safety and certification issues, concluding that hydrogen aircraft could be as safe than kerosene-powered ones —maybe even safer in the event of a crash. New risks, such as hydrogen leakage, cryogenic hazards (e.g., freezing), and material embrittlement, were identified but considered manageable. For

ground operations, Sefain pointed out key changes such as handling boil-off during refueling, enforcing new safety rules to prevent hydrogen accumulation in confined areas, and replacing maintenance and refueling equipement—though these were not expected to significantly impact turnaround times. Similar conclusions were reached by Svensson, who examined the environmental potential of using liquid hydrogen in civil subsonic aviation [**37**].

Maniaci [**38**] explored the design of a hydrogen-powered counterpart to the Boeing 747, named the LH2-400 (Figure **I.2**), featuring a large liquid hydrogen tank mounted above an elliptical fuselage. His reserach showed that hydrogen and kerosene aircraft could achieve similar overall energy efficiency. However, Maniaci noted that hydrogen aircraft were more efficient in the early flight phases—take-off, climb, and initial cruise—thanks to their lighter fuel weight. As the flight progressed, this advantage faded since the aircraft still had to carry the heavy and bulky empty hydrogen tanks, unlike the 747. This behavior underscores the higher sensitivity of hydrogen aircraft to off-design missions, particularly at shorter ranges, where the additional tank mass and drag are not offset by the fuel efficiency advantage. Additionally, Maniaci highlighted a substantial increase in compressibility drag—mainly attributed to the bulky hydrogen tanks—which contributed to a lower drag divergence Mach number (0.75 for the LH2-400 vs. 0.78 for the B-747). He concluded that hydrogen aircraft might benefit from reduced cruise speeds, which could enhance aerodynamic efficiency and potentially lead to better fuel economy than conventional kerosene-fueled designs.

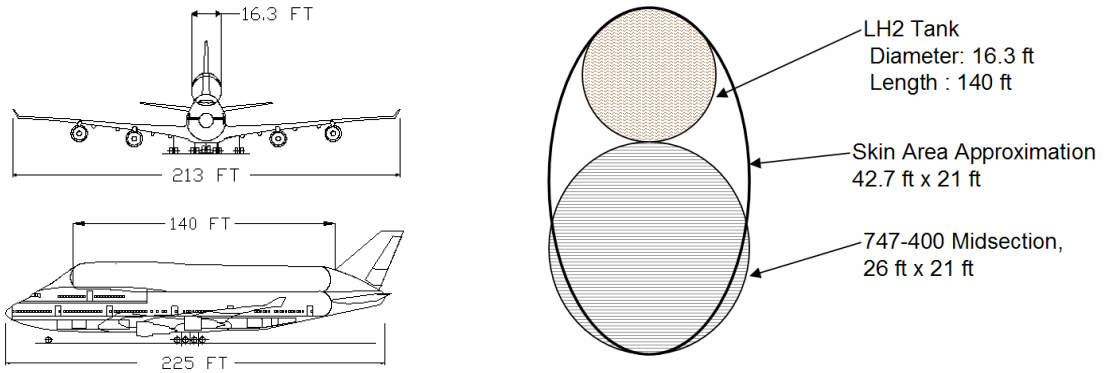

Figure I.24: LH2-400 long-range aircraft concept of Maniaci [**38**]

A few years later, Verstraete made a significant contribution to the field by developing one of the first integrated conceptual design tools specifically tailored for hydrogen-fueled aircraft[**32**]. His methodology extended beyond traditional aircraft design disciplines—such as aerodynamics, structural analysis, performance, and geometry sizing—to include hydrogen-specific considerations. Notably, he developed a thermodynamic model for cryogenic hydrogen tanks [**39**], building on the foundational work of Brewer [**24**]. This model was incorporated into his design tool to address the complex trade-offs between thermal insulation and structural integrity. Verstraete emphasized that the tank design is a critical factor in determining the overall feasibility and performance of hydrogen air-

craft, as it must balance lightweight construction with high insulation efficiency and long service life.
In addition to the tank model, Verstraete also developed a conceptual design framework for hydrogen gas turbines, which operates in tandem with the airframe tool to enable a holistic system-level analysis. Using this integrated approach, he conducted parametric studies on large, long-range hydrogen aircraft. His results indicated that such aircraft could achieve a 25% reduction in takeoff gross weight—primarily due to a 70% decrease in fuel mass—leading to lower lift requirements, smaller wing sizes, and ultimately an estimated 11% reduction in overall energy consumption [**40**].
However, for very large long-range aircraft, the benefits were notably diminished. These designs were severely constrained by the volumetric storage requirements of hydrogen and airport infrastructure limitations—issues previously highlighted in the Cryoplane project. As a result, the achievable weight and energy savings were more limited in this category. From an economic standpoint, Verstraete concluded that hydrogen aircraft could remain competitive if hydrogen fuel prices were four to six times higher (on an energy basis) than conventional kerosene for large long-range aircraft, or three to five times higher for very large aircraft. Furthermore, he proposed that flying at lower altitudes could substantially reduce the climate impact of contrail formation, and that operating at slightly lower cruise speeds might improve energy efficiency. The latter is due to the increased wetted area of hydrogen aircraft resulting from their larger fuselages, which accommodate the bulkier fuel tanks.

In recent years, the concept of utilizing hydrogen to decarbonize aviation has regained significant traction, driven by escalating concerns about climate change following the Paris Agreement in 2015 [**41**]. This renewed interest has spurred extensive research and collaboration among academia, government, and industry stakeholders. Notable initiatives include the Clean Sky 2 program, launched by the European Union in 2020 [**42**], and the FlyZero project, funded by the UK government [**43**]. Both projects aimed to evaluate the potential of hydrogen in achieving a sustainable aviation sector and involved collaborative efforts among industrial partners, universities, and research centers.

The findings from these initiatives suggest that hydrogen could play a pivotal role in the future clean technology mix for aviation, provided that research in this area is significantly accelerated. The studies primarily focused on short to medium-range aircraft, proposing various concepts that utilize hydrogen gas turbines or fuel cell electric propulsion systems for regional flights. While long-range aircraft present greater challenges for hydrogen adaptation, the FlyZero project noted that fewer airports would need hydrogen infrastructure to support a substantial portion of global air traffic if hydrogen technology were first implemented in long-range aviation. Clean Sky 2 estimated that hydrogen-powered aircraft could account for 40% of air traffic by 2050, although they may consume more energy and incur higher operational costs compared to conventional aircraft. This could result in a 20-40% increase in cost per passenger, though still potentially more economical than synthetic fuels, except for long-range flights. However, the FlyZero project demonstrated that even mid-size long-range hydrogen aircraft could be less costly than those

powered by **SAF**.
Both studies highlight a critical challenge: the industrial-scale supply of hydrogen, especially during the expected widespread adoption of the technology after 2040. Overcoming this challenge could enable hydrogen aircraft to meet a substantial portion of air traffic demand, potentially covering 100% of short-range routes and about 90% of long-haul flights, while remaining competitive with sustainable aviation fuels (SAF). Smith [**44**], in his comparative study of liquid hydrogen, LNG, and Jet A for powering future aircraft, found that hydrogen could address approximately 84% of air traffic demand. Similarly, Mukhopadhaya [**45**], who designed a short-range hydrogen turboprop and a medium-range hydrogen turbofan, estimated that these aircraft could cover around 60-70% and 90-100% of their respective flight segments in **Revenue Passenger Kilometer (RPK)**, representing about 35-40% of total air traffic in 2035. Like the previous projects, these studies also showed that hydrogen aircraft face certain penalties compared to conventional aircraft, including higher empty weight due to longer fuselages and heavy, voluminous tanks. This results in less efficient aircraft with reduced range or requires trading passenger capacity for range. However, these penalties could be mitigated if technology advances.
To achieve this vision, several technological barriers need to be addressed. Key areas requiring further investigation include:

- Fuel cell power density, with a target of around 2 kW/kg for short-range applications [**42**].
- Fuel distribution systems capable of handling cryogenic fluids, including pumps, valves, and piping.
- Thermal management systems.
- Low NOx gas turbines : if several studies have shown their feasibility, they are still far from certification and commercial use.
- Development of cryogenic hydrogen-compatible and fast-refueling equipment and procedures.
- Research on material behavior in cryogenic conditions and the development of hydrogen-compatible materials.
- Advancements in hydrogen storage technology: The most critical technology as it will dictate aircraft architecture and performance.

From a technical standpoint, hydrogen storage is probably the critical technology that will shape the future of hydrogen-powered aviation. The impact of the tank on overall aircraft performance is closely tied to its gravimetric efficiency, defined as:

$$\eta_{grav} = \frac{m_{H2}}{m_{H2} + m_{tank}} \tag{I.1}$$

The impact of hydrogen storage gravimetric efficiency (or index) on aircraft performance is illustrated in Figure **I.25**, as presented in the review by Adler and Martins [**46**]. The

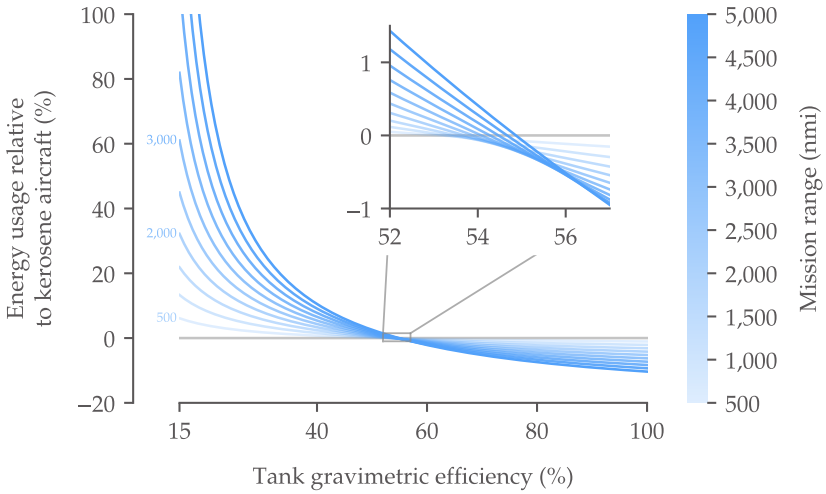

Figure I.25: Impact of hydrogen tank gravimetric efficiency on aircraft energy consumption depending on mission range [**46**]

figure demonstrates that hydrogen aircraft have a lower energy efficiency compared to kerosene aircraft when the gravimetric efficiency, η_{grav}, is below approximately 55%. This efficiency disparity grows exponentially with the aircraft range. This confirms that for medium- to long-haul aircraft, storing hydrogen in its liquid form is optimal due to its superior energy density and the absence of the need for a heavy tank structure to maintain high pressure, as required for compressed gaseous hydrogen (around 700 bar), which is then more adapted for short-range mission. This results in better gravimetric efficiencies, which are particularly crucial for longer-range aircraft.

Beyond the impact of hydrogen storage mass, the integration of voluminous tanks on an aircraft also presents significant challenges. Recent studies have consequently focused on evaluating the design and integration of hydrogen tanks and their impact on aircraft performance. For instance, Silberhorn et al. [**47**] developed an integrated multidisciplinary design tool for hydrogen aircraft, incorporating a medium-fidelity hydrogen tank model. They studied the impact of tank design and performance at the aircraft level across three different aircraft concepts, varying the tank placement: behind the cabin, on top of the fuselage, and in pods under the wing. Their findings highlighted the trade-off between a highly insulated tank, which reduces hydrogen loss due to boil-off, and a less insulated tank, which, while losing more hydrogen to boil-off, is lighter.

Winnefeld et al. [**48**] designed a hydrogen tank model to assess the storage mass for different tank shapes. They noted that, in terms of mass, a hydrogen tank completely filled with liquid hydrogen remains lighter than the fuel block of a conventional kerosene aircraft, although the required volume is significantly larger. They emphasized the importance of considering the mass of vented hydrogen due to boil-off and suggested that the optimum insulation is highly dependent on the mission and aircraft category.

Huete et al. [**49**], while investigating the impact of the tank within a more complete air-

craft model, confirmed that the optimal tank configuration and its associated gravimetric index could vary significantly between different missions and aircraft architectures. The gravimetric index is particularly affected by tank geometry, insulation, and internal pressure. In a subsequent study, Huete et al. [**50**] highlighted that the performance of larger and longer-range aircraft is more dependent on the gravimetric index compared to shorter-range aircraft. They suggested that achieving a gravimetric index of 0.7 could meet 98% of existing large-capacity aircraft mission demands.

Onorato et al. [**51**] developed an aircraft design and analysis framework to understand how and why the optimal tank configuration changes depending on the aircraft segment and mission. They attempted to identify optimal configurations in terms of tank structure, fuselage diameter, tank layout, shape, venting pressure, and pressure control. Their results suggested that an integral tank, where the tank is part of the fuselage, is always beneficial. They also found that splitting hydrogen storage into forward and aft tanks is advantageous for stability, and that increased fuselage diameter is detrimental.

Jagtap et al. [**52**], in a study assessing the sensitivity of the performance of large subsonic tube-wing LH2 aircraft to developments in four technology areas (aerodynamics, structures, cryo-tank gravimetric index, and overall efficiency), proposed a more optimist critical value of 0.52 for η_{grav} that could allow aircraft range up to 14000 km. They suggested that this value could be reduced to 0.35 by 2035 with technological improvements. However, they noted that progress in cryogenic storage technology is not the sole or even the most important area for improving hydrogen aircraft performance.

To mitigate some of the constraints associated with hydrogen aircraft, such as storage volume, and to enhance other aircraft characteristics like aerodynamics, recent studies have explored the use of hydrogen in more exotic configurations. For instance, Cipolla et al. [**53**] and Palaia et al. [**54**] investigated the retrofit of the European project PARSIFAL, which featured a box-wing aircraft with an elliptical fuselage, into a hydrogen aircraft. Similarly, Van Woensel [**55**] proposed a hydrogen-retrofitted Flying-V concept. Additionally, Palladino et al. [**56**], Soleymani et al. [**57**], and Nicolay [**58**] focused on hydrogen fuel cell electric aircraft, which appear to be a viable solution for short-range aircraft or general aviation.

Concurrently, significant industrial efforts have been directed towards hydrogen technologies in recent years. Several start-ups are currently developing hydrogen aircraft prototypes, and major players like Airbus have entered the field. Airbus is pursuing the ZEROe project, which studies three hydrogen aircraft concept (see figure **I.46**) and aims to introduce a hydrogen regional jet to the market by 2040.
All of those previous studies on hydrogen aircraft concluded that an hydrogen aircraft should be feasible but that technological, economic, and societal challenges will have to be overcome to make it a reality. If the specific economic and societal challenges are out of scope in this thesis, the technological challenges are still relevant. While numerous aircraft configurations have been proposed and evaluated for hydrogen-powered



Figure I.26: Three hydrogen fueled aircraft concepts presented by Airbus in its Zero-e program

flight, one of the most often referenced designs that could mitigate hydrogen integration complexity is the **BWB** thanks to its important internal volume. The subsequent section presents a comprehensive state-of-the-art review of the **BWB** configuration, examining its aerodynamic, structural, and operational benefits and its remaining design challenges.

I.3 Blended Wing Body: a revolutionary yet challenging concept promising to improve aircraft energy efficiency

The concept of the blended wing-body aircraft is rooted in a fundamental rethinking of conventional aircraft design. In traditional configurations, the fuselage primarily serves as a passenger compartment but incurs an aerodynamic penalty. The empennage, while essential for stability and control, adds both mass and drag. Only the wings generate lift, necessitating robust structural design to support the entire aircraft. The **BWB** paradigm introduces a transformative solution: the fuselage itself is designed to generate lift, while non-lift-generating components, such as the empennage, are entirely removed.

Although the modern conceptualization of the blended wing-body architecture emerged in the late 1980s, its foundational principles trace back to the earliest days of aviation. Indeed, some of the first aircraft designs, many of which were inspired from bird or plant, were inherently tailless configurations, such as Alphonse Pénaud's "aéroplane" (1876) and Clément Ader's Éole (1890), as well as the Etrich Glider (1890) [**59**] (see Figure **I.27**).

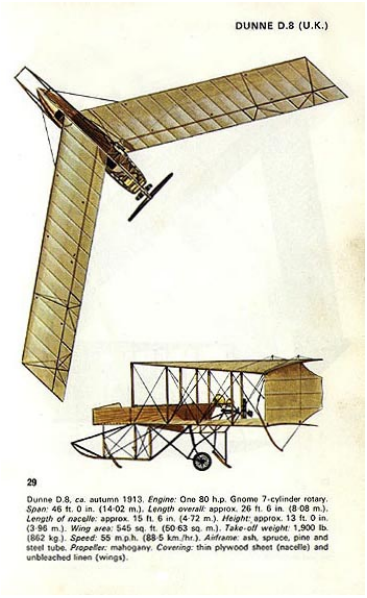

Figure I.28: John Dunne's D-8 tailless aircraft concept [**61**]

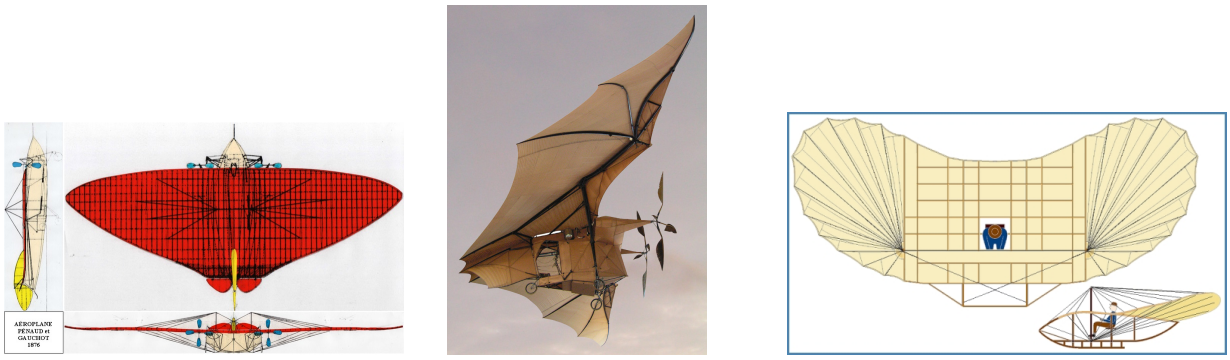

Figure I.27: Early aircraft concept of Penault "aéroplane" (left) [**60**], Ader's Eole (center) and Etrich's Glider (right)

The practical viability of empennage-free aircraft was however first demonstrated in the 1910s through John Dunne's series of tailless designs, including six aircraft and glider prototypes. This effort reached its most advanced form with the D-8 (Figure **I.28**)—the first fully functional tailless aircraft, explicitly engineered for inherent aerodynamic stability thanks to the sweep of the wings moving the aerodynamic center backwards [**59**].
In the subsequent decades, Captain Hill advanced the field with the Pterodactyl series, the first tailless aircraft capable of executing rolls and loops, and featuring an innovative variable-sweep flight control system that eliminated the need for trim adjustments [**59**]. Concurrently, Alexander Lippisch explored the flying-wing concept through a delta-wing configuration, driven by the goal of maximizing internal volume [**59**]. His work resulted in over 13 flying-wing designs, including the Delta I (Figure **I.29**) [**62**].

The Horten brothers (Reimar and Walter) made another landmark contribution, designing and constructing over 20 flying-wing aircraft, progressing from gliders to propeller-driven and, ultimately, turbojet-powered models [**59**]. Their work was dis-

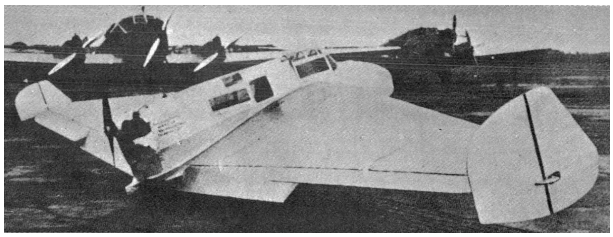

Figure I.29: The Delta 1 aircraft of Alexander Lippisch [**62**]

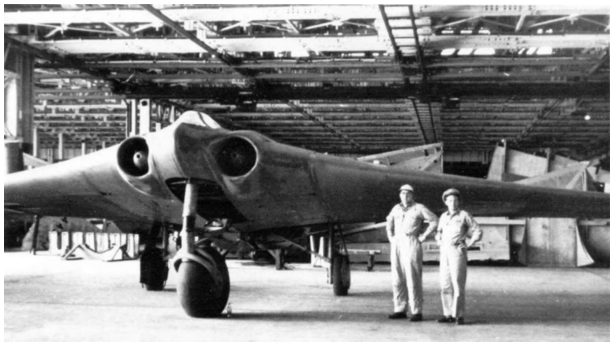

Figure I.30: The Horten Ho 229 V3 being captured by U.S Force in its manufacturing plant (Source: Wikicommons)

tinguished by innovative aerodynamic shape and control systems. Among their most notable achievements was the Ho 229, the world's first jet-powered flying wing, developed for the Luftwaffe during World War II. This aircraft was uniquely positioned to meet the "3×1000" requirement—delivering 1,000 kg of ordnance over 1,000 km at 1,000 km/h—a performance benchmark no other contemporary design could approach [**63**]. The program's development was cut short, however, when U.S. forces seized the third prototype at the war's conclusion (Figure **I.30**), which was later transferred to Northrop Corporation for technical evaluation.

On the other side of the Atlantic, inspired by the Horten brothers' pre-war glider concepts, Jack Northrop had indeed founded the Northrop Corporation in 1927 to investigate flying-wing designs. This initiative led to the 1928 semi-flying-wing aircraft (Figure **I.31**)—a hybrid design featuring a twin-boom tail for stability—and ultimately produced the N-1M in 1940, the first true flying-wing aircraft, proving the concept's feasibility.
Building on these advancements, Northrop constructed the N-9M, a one-third-scale **BWB** bomber mockup for the U.S. Air Force (Figure **I.33**). This was followed by the full-scale XB-35 (first flown in 1946, with later variants designated YB-35) and YB-49—all based on the same airframe, with the XB-35 powered by piston engines while the YB-49 made the transition to jet propulsion. Despite facing control, stability, and excessive fuel consumption challenges, these aircraft served as critical technological precursors to the Northrop Grumman B-2 Spirit, which remains one of the most advanced stealth bombers in service today and the only operational flying-wing design. Notably, the B-2 retains the same wingspan as the YB-49. The B-2 is now set to be succeeded by the B-21 Raider [**64**], which continues the flying-wing tradition.

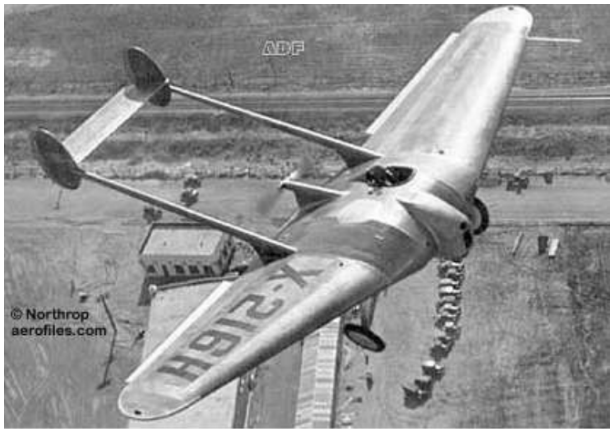

Figure I.31: Semi-flying wing aircraft developed by Northrop (Source : Smithsonian **NASA** Museum)

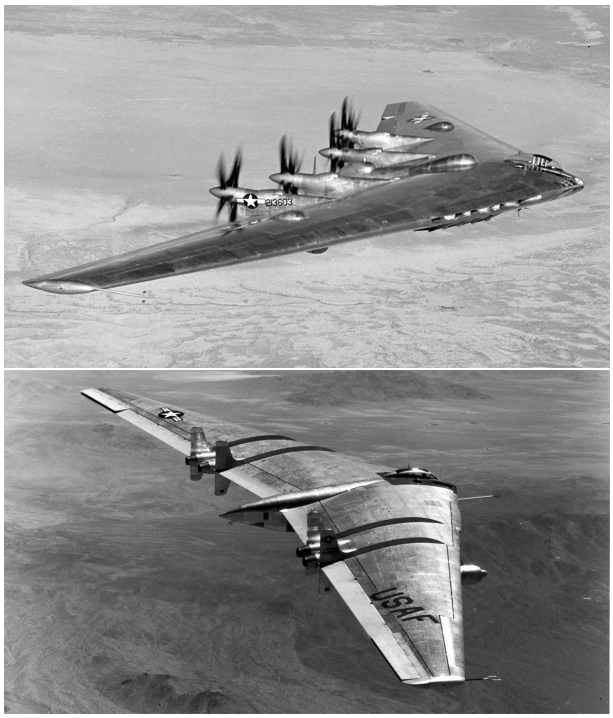

Figure I.32: Northrop Xb-35 (top) and YB-49 (bottom) aircraft (Source: U.S. Air Force photo, Public Domain)



Figure I.33: Northrop-Grumman B2 Spirit bomber (Source : US Air Force Website)

Like many advancements in aeronautics, early flying-wing research was primarily driven by military objectives, as demonstrated by the historical examples above. After a period of significant progress in this field through the 1950s —effectively proving the concept's technical feasibility- interest in flying-wing and lifting-fuselage designs diminished. One notable exception remained space reentry vehicles, where advancements in lifting-body aerodynamics and control systems persisted [**59**]. These efforts ultimately enabled the design of the Space Shuttle, further validating the underlying principles.

The modern blended wing-body concept—characterized by an expanded central fuselage to accommodate passengers or cargo, unlike traditional flying wings—was first introduced in the 1990s by Robert Liebeck at McDonnell Douglas (now Boeing). This initiative was sparked by Dennis Bushnell's 1988 provocative question to the aerospace community: "Is there a renaissance for the long-haul transport?" The challenge aimed to inspire radical new configurations for future long-range commercial aircraft. In response, a rapid feasibility study was launched at McDonnell Douglas, targeting a breakthrough in aerodynamic efficiency. At the time, the maximum lift-to-drag ratio of conventional aircraft had remained largely unchanged for three decades [**65**]. The study yielded the initial **BWB** concept (Figure **I.34**), which demonstrated a substantial improvement in lift-to-drag ratio, translating to significant fuel savings. However, as the design was refined, traditional constraints—such as passenger evacuation requirements and the need for cylindrical pressure vessels to maintain cabin pressurization—gradually pushed the configuration toward more conventional layouts, thereby reducing its performance advantages [**65**].

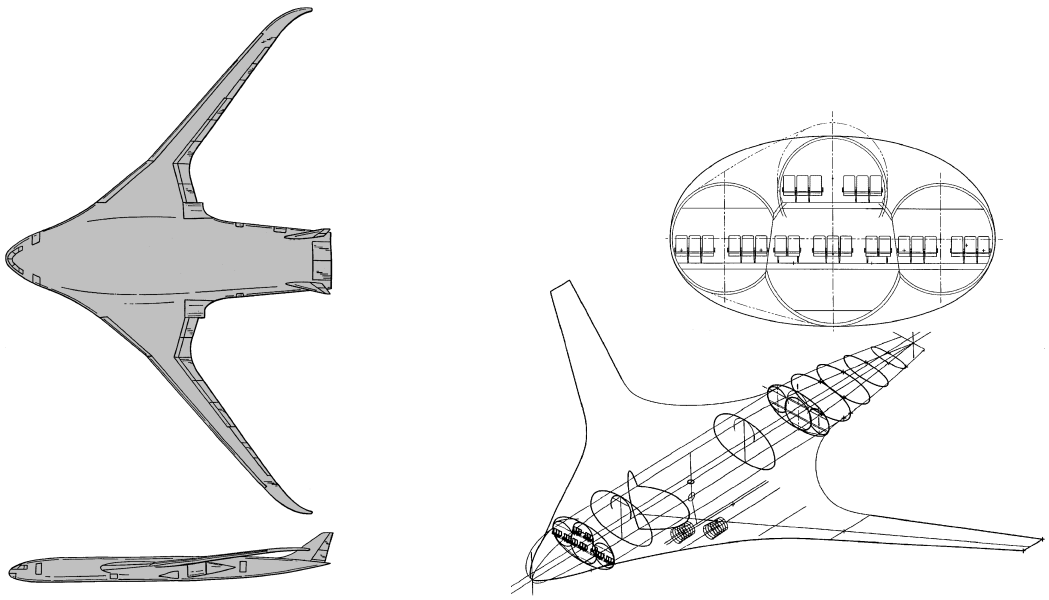

Figure I.34: Early **BWB** concept envisonned at McDonnell Douglas in 1988 [**66**]

A deliberate decision was made to abandon the traditional constraint of relying on hoop tension for cabin pressurization. As illustrated in Figure **I.35**, Liebeck's progression toward the blended wing body concept began with the fundamental objective of minimizing the wetted area required to enclose an 800-passenger cabin. Building on this volumetric foundation, the design was subsequently shaped to generate the necessary lift through the integration of wings. The final stage of the concept's evolution addressed the challenges of controllability and propulsion with the addition of engine and vertical surfaces, which also serve as winglets.

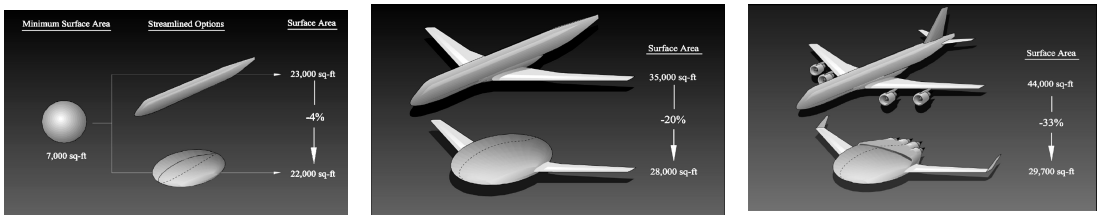

Figure I.35: Surface area comparison between conventional and **BWB** configurations through successive design stages [**66**]

Through further refinements —smoothly blending all surfaces, integrating the cockpit—and subsequent studies, the modern blended wing-body configuration emerged. Visible in figure **I.36**, the result was a fully integrated fuselage-wing structure, where the central body merges seamlessly with the wings, serving simultaneously as a lifting surface, engine inlet, and pitch control device. Unlike conventional tube-and-wing designs, the entire airframe—including the fuselage—generates lift, with a lift distribution closely approximating the ideal elliptical profile to minimize induced drag. Additionally, the elimination of the tail reduces total external surface area, lowering friction drag.
Liebeck's second-generation **BWB** concept, illustrated in Figure **I.36** and still considered a reference today, is designed to carry 800 passengers over 7,000 nautical miles, deliver-

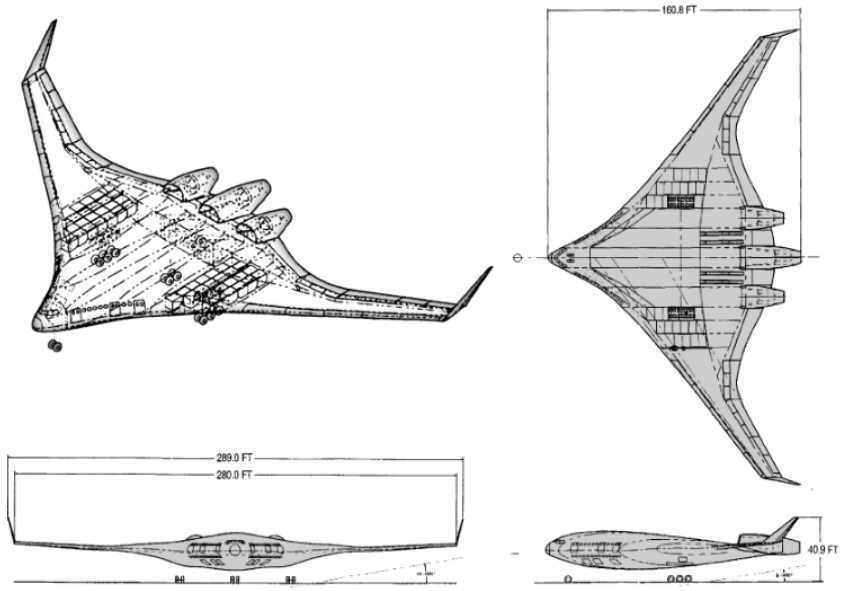

Figure I.36: Liebeck 800 passengers, double deck second generation **BWB** [**65**]

ing a 27% reduction in fuel burn per seat-mile compared to conventional aircraft. This improvement is driven by an increased lift-to-drag ratio (from 19 to 23) and a 15% lower takeoff gross weight (TOGW) [**65**][**66**]. The weight reduction is achieved through three key factors:

- Elimination of the empennage
- Elimination of one engine (3 instead of 4)
- Better alignment of inertial loads with lift distribution (Figure **I.37**), which reduces peak wing bending moments and shear forces to roughly half those of traditional tube-and-wing designs. This, in turn, lowers the structural reinforcement needed to handle these loads, contributing to overall weight savings.

This research led to the development of a flight demonstrator, the BW-17 (17-foot wingspan), built at Stanford University. The demonstrator confirmed the low-speed behavior of the **BWB** design and demonstrated strong handling qualities [**65**].

Following the initial study, Boeing launched a second investigation to design a 450-passenger **BWB** aircraft, a capacity chosen to facilitate direct comparison with contemporary airliners [**66**]. Given the multifunctional role of the centerbody in **BWB** configurations, the interdependence between design disciplines became a critical factor. This prompted the development of WingOpt, an integrated multidisciplinary design framework aimed at minimizing takeoff gross weight (TOGW) through optimization. The study also explored the feasibility of creating an entire aircraft family based on a core design (Figure **I.38**) and addressed key operational constraints, including:

- Airport compatibility (with a maximum 80-meter wingspan)

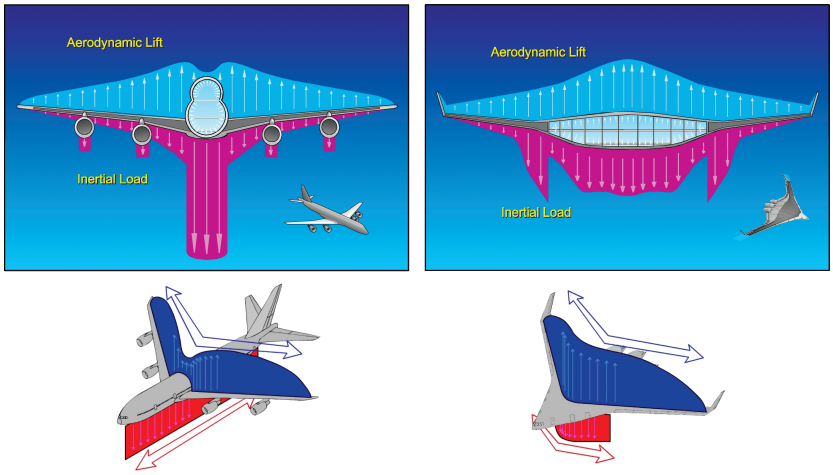

Figure I.37: Comparison of inertial and lift distribution between a conventional configuration and the **BWB** [**66**]

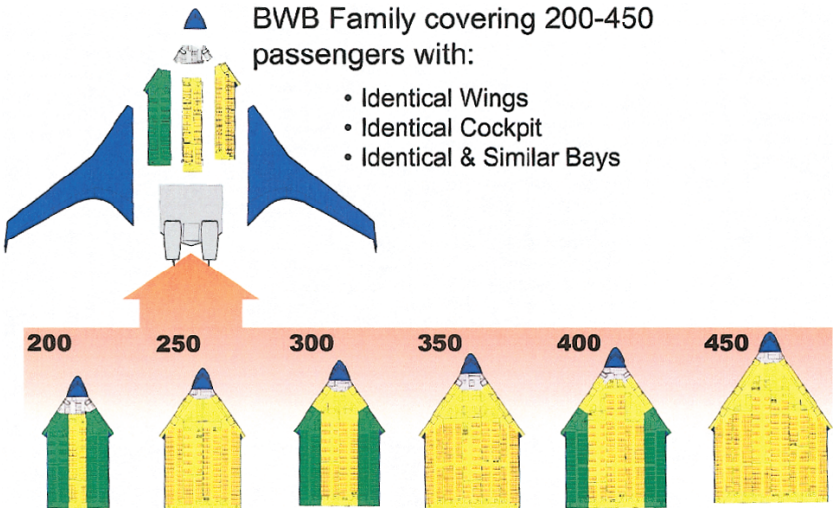

Figure I.38: Liebeck's proposed **BWB** aircraft family with shared structural components [**66**]

- Passenger evacuation, evaluating multiple cabin layouts and concluding that evacuation would not pose a significant challenge

Additionally, the spanwise lift distribution was carefully tailored to achieve a positive static margin—unlike the earlier concepts, which had a negative static margin—without resorting to wingtip download (a historical practice that increases induced drag by reducing effective aerodynamic span). The result was a design surpassing the efficiency of a comparable A380-700, with a 32% reduction in fuel burn.

Liebeck's pioneering work on the **BWB** concept reignited global interest, inspiring a wave of research projects and collaborative initiatives. At Boeing, the X-48 experimental aircraft (Figure **I.39**), developed in partnership with Cranfield University, was built to define the low-speed flight envelope and evaluate handling qualities of the **BWB**.



Figure I.39: NASA Dryden engineer Gary Cosentino prepares the X-48B for flight. Source: NASA website, Credit: Tony Landis

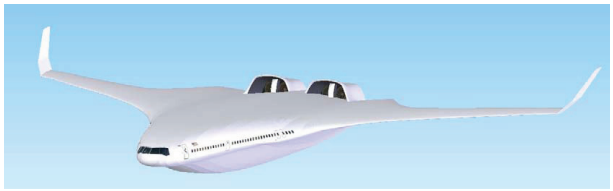

Figure I.40: H3.2 conceptual aircraft design of NASA for its N+3 program [**68**]

With a wingspan of over 20 feet, the prototype completed 122 successful flights and underwent wind tunnel testing [**67**]. Meanwhile, NASA selected a hybrid wing-body design (Figure **I.40**) in 2010 as a candidate to meet its N+3 performance goals—targets for aircraft three generations beyond current technology [**68**]. Compared to a Boeing 777-200LR, the **BWB** design achieved substantial improvements, including halved fuel burn, an 81% cut in NOx emissions, and a 46 EPNdB reduction in noise, though the D8 "double bubble" configuration also matched or slightly surpassed these gains.

In Europe, the European Commission funded a decade-long series of **BWB**-focused projects, engaging dozens of industrial, academic, and research partners. The MOB project (2000–2003) developed the Computational Design Engine, a multidisciplinary preliminary design tool tailored for **BWB** configurations [**69**, **70**]. The VELA project (2002–2005) designed a high-capacity **BWB** (750 passengers, 7,200 nmi range), exploring external wing positioning and under-wing engine placement. The final VELA 3 concept demonstrated improved stability and control, with 4–8% aerodynamic gains and a 10% reduction in MTOW [**71**].
The NACRE project (2005–2010) expanded on VELA's design, focusing on propulsion integration, landing gear kinematics, passenger evacuation, and new technologies (e.g., laminar flow wings) [**72**]. The ACFA 2020 project (2008–2012) targeted a smaller, 450-passenger **BWB**, aiming for reduced structural loads and advanced active control algorithms to enhance ride comfort.

Parallel to these efforts, Cambridge and MIT contributed to the Silent Aircraft Initiative, proposing a low-noise, 250-passenger **BWB** called the SAX-40 with a 25 dB noise



Figure I.41: Conceptual **BWB** configurations developed in the 2000's: NACRE (top), **Active Control for Flexible Aircraft (ACFA)** (middle), SAX-40 (bottom) [**71**]



Figure I.42: Airbus **MAVERIC** prototype aircraft (Source : AIRBUS)

reduction compared to a Boeing 777-200 and a 25% cut in block fuel.

Additionally, Airbus and Boeing collaborated with Russia's TsAGI to compare three **BWB** configurations (Integrated Wing Body, Lifting Body, and Pure Flying Wing) based on the VELA design. The Integrated Wing Body emerged as the highest performer, achieving a lift-to-drag ratio of 25 at Mach 0.85 [**73**]. Airbus also developed on its own the **Model Aircraft for Validation and Experimentation of Robust Innovative Controls (MAVERIC)** demonstrator in the late 2010's (see figure **I.42**), an experimental unmanned **BWB** with a 3.2m wingspann built in order to assess the controllability of **BWB** configuration with a potential for 20% reduction in fuel consumption [**74**].

Beyond institutional or industrial initiatives, academic research on blended wing-body

configurations has flourished, with numerous studies focusing on specific technical disciplines. In aerodynamics, notable contributions to define the optimal design of s include the work of :

- Qin, Le Moigne, and others colleagues who explored spanwise lift distribution and airfoil shaping to minimize induced drag. Their work [**75**, **76**, **77**] demonstrated how blended body designs could achieve near-elliptical lift distributions, reducing vortex drag and improving fuel efficiency.

- Peigin and Epstein [**78**], who employed a genetic algorithm combined with reduced-order modeling to conduct a multipoint drag optimization of the **BWB**

- Lyu et al. [**79**], who ran high fidelity aerodynamic optimization to minimize **BWB** drag

- Kuntawala et al. [**80**, **81**], who developed an optimization method to also minimize the wave and induced drag at transonic speed

- Meheut et al. [**82**] who optimized the **BWB** shape with take-off rotation constraint

- Reist, Zingg, and their teams [**83**, **84**, **85**, **86**], who used high-fidelity aerodynamic optimization using CFD (Computational Fluid Dynamics) on **BWB** to determine their optimal shape for different missions.

For structural analysis, key research has been conducted by:

- Mukhopadhyay et al. [**87**, **88**, **89**] who was the first to suggest structural sizing methodology adapted to **BWB** for conceptual design. Their work emphasized the challenges of maintaining cabin pressure without traditional cylindrical fuselages

- Bradley [**90**] who used finite element analysis to develop a weight estimation equation for the **BWB**

- Laughlin [**91**] introduced semi-analytical methods for rapid structural evaluation, enabling early-stage design iterations.

- Vos et al. [**92**] and Schmidt [**93**] who worked on the wide oval cabin concept and developed semi-analytical methods for estimating the weight of an oval fuselage configuration.

In the field of control and stability for blended wing-body aircraft, pivotal research has been conducted by :

- Voskuijl [**94**] who analyzed controllability challenges in **BWB** aircraft, particularly the lack of a traditional tail, and proposed novel control surface configurations to ensure stability.

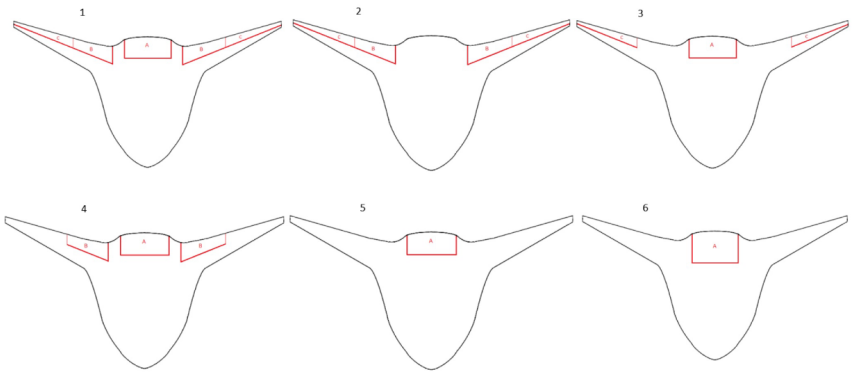

Figure I.43: The 6 control surfaces configurations proposed by Sgueglia [**99**]

- Meheut et al. [**95**] and Denieul [**96**], who focused on flight control laws and pilot workload, demonstrating how fly-by-wire systems could compensate for the unconventional aerodynamics of **BWB** designs. Denieul in particular proposes three types of control surface design that can be arranged in six configurations visible in figure **I.43**.

- Vicroy [**97**], who conducted low-speed wind tunnel test of a **BWB** prototype to evaluate static and dynamic stability

- Sargeant, Hileman and their teams [**98**] who developed a methodology to support aircraft designers in quantifying the required leading-edge carving for ensuring static stability in blended-wing-body configurations

- Kozek et al. [**71**] who applied multi-input/multi-output flight control techniques for rigid body and aeroelastic control to a **BWB** aircraft

Beyond discipline-specific research, several studies have developed comprehensive multidisciplinary analysis and optimization (MDAO) frameworks specifically tailored for the sizing and optimization of **BWB** aircraft. Notable examples include:

- Ko's MDO framework [**100**, **101**] which was applied to design an 800-passenger, 7,000 nmi-range **BWB** featuring distributed propulsion. This configuration achieved modest improvements over conventional **BWB** designs, with a 4% reduction in **Take-Off Gross Weight (TOGW)** and a 2% decrease in fuel consumption

- Martinez-Val et al. [**102**] development of a comprehensive analytical sizing methodology specifically for C-type and U-type flying wing configurations. When benchmarked against a 300-seat conventional aircraft, the C-type flying wing achieved a 17% reduction in **Maximum Take Off Weight (MTOW)**, while the U-type flying wing—equipped with laminar flow control—realized an even greater 24% **MTOW** reduction, leveraging the inherently low wing loading of **BWB** designs. However, the U-type configuration requires vectored thrust control to ensure longitudinal stability. These structural improvements translate to fuel efficiency gains of 8% for the C-type and an exceptional 32% for the U-type, marking a substantial advancement over traditional aircraft designs.

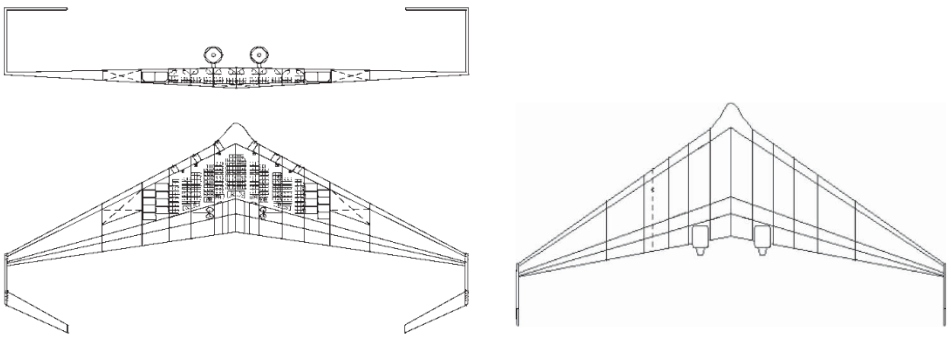

Figure I.44: C-type (left) and U-type flying wing concept of Martinez et al. [**102**]

- Bradley [**90**] adaptation of NASA's aircraft sizing tool, **Flight Optimization System (FLOPS)**, to design blended wing-body configurations for 200- to 450-passenger aircraft.

- The TU Delft **BWB** sizing methodology, developed by Brown and Vos [**103**], which was applied to 150, 250-seat and 400-seat **BWB** configurations. Results revealed lift-to-drag ratio evolution of 0, 2 and 3, respectively, compared to equivalent **T&W** aircraft, alongside a maximum fuel consumption reduction of 30% for the 250-passenger variant.

- CICAV [**104**, **105**, **106**, **107**]: An ONERA-developed **BWB** design framework based on OpenMDAO, capable of sizing both long- and short-range **BWB** configurations.

- **Future Aircraft Sizing Tool (FAST)** [**99**]: Introduced by Sguelia at ONERA and ISAE-SUPAERO, this tool was designed to size **BWB** aircraft with distributed electric propulsion. The FAST framework was later repurposed and expanded into FAST-OAD, although this evolution removed its **BWB**-specific capabilities.

- **GENUS Multi-variate Design Synthesis Optimization (GMDSO)**: developed by Okonkwo at Cranfield [**108**], was notably employed to conduct sensitivity analyses of Mach number, wing sweep, and camber on **BWB** aerodynamic and structural performance.

Most research and projects on the blended wing-body configuration highlight its potential to reduce fuel consumption—and thus emissions—by 10% to 50%, depending on mission profiles, technological maturity, and underlying assumptions. While these benefits are highly attractive to the aviation industry, the industrial, safety, and economic challenges tied to such a radical design have so far prevented manufacturers from commercializing **BWB** aircraft. However, emerging imperatives—such as the push for zero-emission flight, for which hydrogen powered aircraft seems one of the most promising solution— could redefine the feasibility and urgency of **BWB** adoption, as discussed in the following section.

I.4 Hydrogen-Powered Blended Wing-Body Aircraft: An Emerging Synergy of Technologies that could enable low-emission flight

As outlined in the first section of this study (I.1), the aviation industry faces growing pressure to achieve low-emission flight. While improvements in current technology can reduce aircraft emissions, these advancements alone will not suffice to reach net-zero goals. Decarbonizing aviation will ultimately require a shift in energy sources. In this context, hydrogen-powered aviation emerges as a promising solution, as it produces no carbon emissions during flight and could significantly reduce other in-flight pollutants.
However, as discussed in Section I.2, hydrogen-fueled aircraft pose substantial design challenges, particularly due to the complexities of handling and storing liquid hydrogen. The high storage volume required for hydrogen adds to these difficulties.

This is where the Blended Wing Body configuration could play a pivotal role in advancing hydrogen-powered aircraft—and ultimately, zero-emission flight. As previously noted, **BWB** aircraft consume less fuel, which helps alleviate the challenges associated with fuel storage volume. Moreover, compared to conventional tube-and-wing designs, the **BWB** configuration offers greater internal volume per passenger, including underutilized space. This additional space could accommodate hydrogen tanks without significantly increasing the aircraft's size or compromising its aerodynamic performance. Finally, several studies have shown that the comparative advantages of **BWB** over **T&W** designs become more pronounced as aircraft size increases. Since hydrogen fuel adaptation tends to increase overall aircraft size, this further strengthens the case for **BWB** configurations.
For these reasons, hydrogen-fueled **BWB** aircraft represent a highly compelling and emerging field of research.

Prior to this study however, published research on the topic was extremely limited. The only identified works focusing on hydrogen-powered Blended Wing Body design included:

- The Quiet Green Transport study of Guynn et al. at NASA [**35**], which aimed to achieve significant reduction in noise and emission. One of the concept of this study was a fuel cell-powered Blended Wing Body aircraft with distributed propulsion. The aircraft was sized using NASA computer code **FLOPS** which was calibrated specifically for a 225-passenger **BWB** configuration, alongside NASA's Numerical Propulsion System Simulation (NPSS). A specialized version of NPSS was developed to accommodate fuel cell and distributed propulsion systems. The modeling of liquid hydrogen-related systems was based on Brewer's earlier research [**24**]. However, the study revealed that meeting the design requirements was not feasible with the technology available at the time. The primary limitations were the low power-to-weight ratios of fuel cells and electric propulsion systems, which resulted in a propulsion system 10 to 20 times heavier than conventional turbofans, as well as an empty weight 60% higher than the target. By assuming aggressive technological advancements—such as a 30% reduction in airframe mass, a 60% increase in elec-

tric motor specific power, or an 85% improvement in fuel cell power density—over the following 30 years, the team successfully designed a feasible hydrogen-powered **BWB** concept. This design achieved zero in-flight emissions and a noise reduction of 8 to 22 dB EPNL at FAA certification points.

- Heinze, Seeckt et al. [**109**, **110**] developed a hydrogen-powered Blended Wing Body concept (see Figure **I.45**) as part of the German "Grüner Frachter" (Greener Freighter) project. The study involved sizing a long-range **BWB** cargo aircraft and comparing it to a conventional kerosene-powered design. The aircraft was sized using the **Preliminary Aircraft Design and Optimization (PrADO)** tool, developed by the Institute of Aircraft Design and Lightweight Structures (IFL) at TU Braunschweig [**111**]. **PrADO**, which primarily relies on physical modeling, was extended for this study to incorporate hydrogen tank and hydrogen turboprop engine simulations [**109**]. However, hydrogen boil-off was not modeled in this analysis. The results demonstrated a 6.5% reduction in **MTOW**, driven by a 66.5% decrease in fuel mass, though the empty weight increased by 25%. Notably, the **BWB**'s greater usable internal volume for hydrogen storage was identified as particularly promising. However, when compared to a hydrogen-powered tube-and-wing aircraft, the **BWB** exhibited similar overall performance. While its superior aerodynamic efficiency was an advantage, this benefit was offset by the increased weight associated with multiple smaller hydrogen tanks (50 tanks were integrated in the design). Consequently, the authors recommended further research into optimizing hydrogen tank arrangements within the **BWB** configuration.

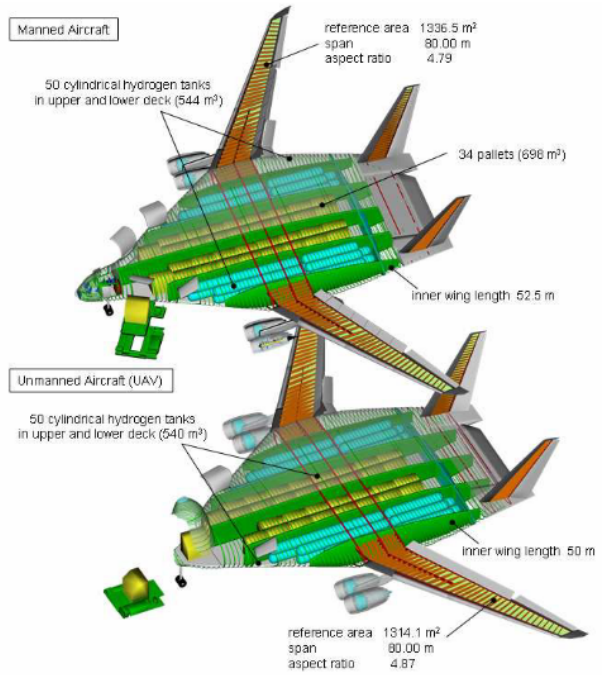

Figure I.45: Concept of a hydrogen powered cargo **BWB** developped for the german greener freighter project[**110**]

- Within the European project ENABLEH2, the Blended Wing Body configuration

was identified as the most synergistic design for hydrogen integration in long-range aircraft, selected among seven evaluated concepts [**112**]. The **BWB** demonstrated superior fuel efficiency, lower noise emissions, and greater revenue potential compared to other solutions. However, concerns were raised regarding its ability to form a family of aircraft variants, as well as challenges in emergency evacuation and maintainability. It is worth noting that the methodology used to assess these aircraft concepts was not disclosed, which affects the transparency of the evaluation process.

At the beginning of this thesis, these studies represented the near-totality of academic research on hydrogen-powered **BWB** aircraft. Since then, however, the topic has gained significant momentum, attracting growing interest from both industry (e.g., Airbus's ZEROe project, which includes a **BWB** concept—see Figure I.46) and academia. This surge in attention is reflected in the increasing number of publications on the subject over the past three years. Karpuk et al. [**113**] adapted a multidisciplinary aircraft design tool, originally developed for conventional **T&W** aircraft, to size a hydrogen-powered **BWB**. Their approach integrated **FLOPS** [**90**] for weight estimation, Brewer's and Verstraete's cryogenic tank models [**24**, **32**] for tanks weight and thermodynamic analysis, and a low-fidelity vortex lattice method for aerodynamic evaluation.



Figure I.46: Three concept of the Airbus Zero-e project announced in 2020

This study represents an attempt to parametrize a **BWB** configuration and was the first to propose a hydrogen tank sizing procedure tailored to **BWB** geometries. The proposed method involves placing the largest possible tank within the fuselage boundaries, positioned along the cabin side in the transition section. If the required volume is not met, additional tanks are placed adjacent to the first until the necessary capacity is achieved (see Figure **I.47**). While this approach does not necessarily yield the most optimized tank arrangement (and excludes placement behind the cabin), it enables the authors to determine hydrogen tank weight and center of gravity. Di Summa [**114**] later adapted this procedure for its own hydrogen-powered **BWB** design, expanding it to include tanks behind the cabin while also accounting for emergency exit constraints. Using a similar modeling framework to Karpuk et al., Di Summa explored three different tank arrangements (see Figure **I.48**).
Karpuk's original design demonstrated the potential to reduce carbon emissions by 88% compared to a Boeing 777-300ER, or by 81% compared to a kerosene-powered **BWB**, assuming the use of green hydrogen. However, Di Summa's sensitivity analysis revealed

that tank arrangements incorporating both side and rear placements improved energy efficiency by 1 to 3%, depending on the aircraft segment and emergency exit constraints. This refinement could further reduce emissions in hydrogen-powered **BWB** configurations.

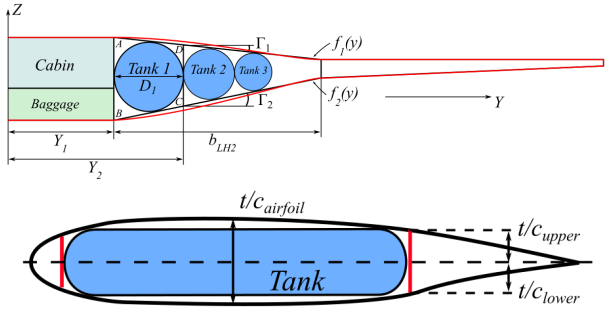

Figure I.47: Illustration of the hydrogen tank sizing methodology in a **BWB** of Karpuk et al.[**113**]

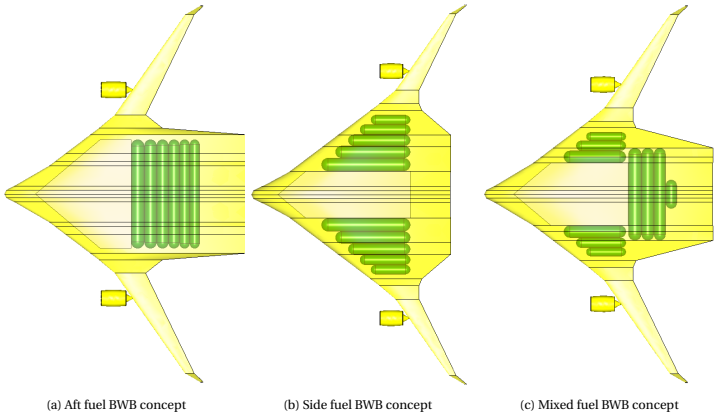

Figure I.48: Three tank arrangement in the hydrogen **BWB** tested by Di Summa [**114**]

Adler and Martins [**115**] conducted a comparative analysis of two Blended Wing Body configurations—one hydrogen-powered and one kerosene-powered—after optimizing their aerodynamic shapes. These configurations were benchmarked against a conventional **T&W** aircraft. Aerodynamic analysis was performed using OpenAeroStruct [**116**], while weight estimates for the **BWB** relied on Bradley's equations [**90**], except for the hydrogen tanks. In their study, hydrogen tanks were modeled as conformal (shaped to fit the transition region between the cabin and outer wing) and characterized solely by their gravimetric index of 0.6. Similarly, Jagtap et al. [**jagtap**] designed a long-range hydrogen **BWB**, but their methodology differed in several key aspects. They modeled hydrogen tanks using a higher gravimetric index of 0.78 and assumed cylindrical tank shapes. Their approach employed lower-fidelity methods, including simplified weight estimation equations (not explicitly detailed), the Breguet range equation for performance calculations, and no consideration of hydrogen thermodynamics or tank arrangement details. Results from these studies revealed contrasting trends:

- Adler and Martins reported a 3.1% increase in energy consumption for the hydrogen

BWB compared to its kerosene counterpart, while the TAW configuration experienced a 5.1% increase when switching to hydrogen.

- In contrast, Jagtap et al. observed a 7–10% decrease in energy consumption for their hydrogen **BWB** relative to a Jet A-fueled **BWB**.

While neither result presents a fundamental barrier to hydrogen **BWB** viability—and both remain below the energy consumption of comparable Jet A **T&W** configurations—the discrepancy may partially come from the differing gravimetric indices assumed in each study. Adler and Martins showed indeed that energy consumption is highly sensitive to the gravimetric index (Figure I.49). Their findings suggest, however, that the **BWB** configuration is less affected by lower gravimetric indices (i.e., less efficient tanks), thanks to its ability to accommodate more fuel in conformal tanks without increasing its overall size. This advantage remains to be validated for non-conformal tank configurations.

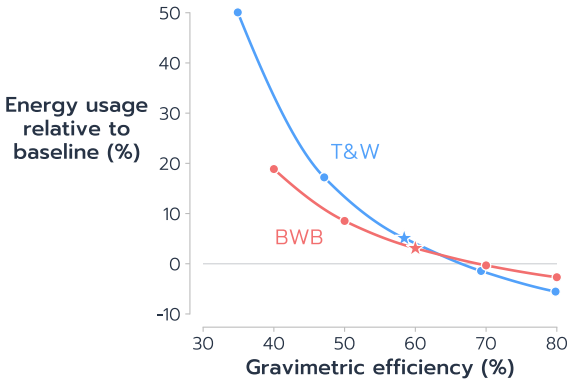

Figure I.49: Sensitivity analysis of the energy usage of hydrogen **BWB** and **T&W** aircraft to the gravimetric index [**115**]

Patel et al. [**117**] actively contribute to the **Integrated Zero Emission Aviation (IZEA)** project, which investigates the integration of multiple decarbonization technologies. Their research focuses on designing a short-range (2,000 nmi, 112-passenger) hydrogen-powered **BWB** aircraft, featuring boundary layer ingestion, electric distributed propulsion—powered by a hydrogen turbogenerator and fuel cell—and a superconducting power system. The study introduces a novel parametrization of the **BWB** geometry, building upon **FLOPS** for baseline aircraft sizing. Patel et al. are also developing customized models for critical components, including the fuel cell system, hydrogen storage tanks, superconducting power distribution, and hydrogen-powered turboelectric generators. The latter incorporates a heat exchanger to reheat liquid hydrogen and cool the superconducting systems. Additionally, multi-fidelity aerodynamic analyses were conducted to develop surrogate models and optimize the aircraft's geometry. While the project remains ongoing, with some models yet to be fully integrated into the design tool, preliminary results indicate a 34% reduction in energy consumption compared to an Embraer E190-E2 (assuming 2050-level technology advancements). This highlights the significant potential of integrating multiple advanced technologies in next-generation

aircraft.

However, these results are surpassed by the study of Chung et al.[**118**], which also examines a hybrid fuel cell/gas turbine **BWB** aircraft with superconducting motors. Chung's work employs **FLOPS** for weight estimation and a hydrogen tank model similar to previous studies, though it considers only one tank arrangement (positioned along the cabin side). Their findings report a 61% and 52% reduction in energy consumption for 352- and 162-passenger hydrogen **BWB** configurations, respectively, when compared to a Boeing 777-300ER and Boeing 737-800. Additionally, their designs achieve 22.7% and 28.7% energy savings relative to hydrogen-powered TAW aircraft in the same segments, despite an increase in **Overall Weight Empty (OWE)**. The notable discrepancy between Patel et al.'s and Chung et al.'s results is challenging to explain, as the first one does not fully detail all modeling assumptions. Nevertheless, Chung's research further demonstrates the promising advantages of hydrogen-powered **BWB** configurations, even without extensive optimization of the aircraft layout.

This review of recent studies on hydrogen-powered Blended Wing Body aircraft, including numerous cutting-edge publications, confirms the growing academic and industrial interest in this innovative concept. While not exhaustive—given the rapid expansion of research in this field—it provides a comprehensive overview of the current state of the art in hydrogen **BWB** design.

I.5 Research strategy

I.5.1 Literature Review synthesis and Research Objectives

The previous section's literature analysis leads to several critical observations :

- Environmental Imperative: The aviation industry faces urgent pressure to dramatically reduce its environmental footprint. This demands disruptive innovations—not only to slash energy consumption but, more importantly, to transition to new energy carriers.
- Hydrogen as a Climate Solution: Hydrogen-powered aircraft present a compelling response to aviation's climate challenge, emitting zero carbon in flight and offering the potential for substantial reductions in other pollutants.
- Blended Wing Body's Efficiency and Hydrogen Synergy: **BWB** configurations promise significant energy efficiency gains and possess inherent design features that make them particularly well-suited for hydrogen propulsion integration.
- Feasibility of Hydrogen and **BWB** Aircraft: Historical precedents confirm that there are no absolute technical barriers to hydrogen-powered flight or **BWB** configurations—hydrogen aircraft have flown, and flying wings operate today. While scaling these concepts into certifiable, large commercial transports poses technical

challenges, the primary constraints likely stem from economic viability, industrial risk, and the absence of supporting energy infrastructure—though these fall outside the scope of this study.

While no fundamental technical barriers have been identified, the literature on hydrogen-powered **BWB** aircraft—particularly at the outset of this study—remains limited and inconsistent in assessing their actual performance. Discrepancies persist across studies in terms of efficiency, optimal configurations, and overall performance. These inconsistencies likely arise from varied assumptions and arbitrary design choices (e.g., gravimetric indices, hydrogen tank placement) and/or too low-fidelity disciplinary models used in some part of the design process. In addition, most studies focus on single-point designs tailored to specific missions, rendering their methodologies too specialized and lacking the generality needed for broader applicability.

In consequence, the primary objective of this thesis was to develop and refine a modular and generic multidisciplinary design methodology for hydrogen-powered blended wing-body aircraft adapted for conceptual design, ensuring its adaptability to any mission profile. This approach aimed to identify during the early design stage the most promising configurations and design choices while reducing the uncertainties associated with the concept's performance potential.

I.5.2 Disruptive Aircraft Design: A New Conceptual Paradigm Enabled by the FAST-OAD Sizing Tool

The aircraft design cycle is traditionally structured into three key phases:

- Conceptual Design: This marks the initial phase, where engineers use low- to medium-fidelity models to identify the most suitable aircraft concept and configuration that aligns with the **Top Level Aircraft Requirements (TLARs)**, such as passenger capacity, range, and speed. This involves: Sketching the general geometry of potential concepts, estimating mass distribution, defining engine count and power requirements, and assessing performance metrics (e.g., fuel consumption, operational costs, payload-range capabilities) to select the optimal design.
- Preliminary design : the chosen concept undergoes further refinement through higher-fidelity analyses, enhancing the accuracy of performance predictions and defining all the required subsystems
- Detailed design: Once the program is confirmed, the aircraft is fully engineered down to the smallest components, including manufacturing plans and assembly details.

In the context of this thesis, which focuses on innovative aircraft concepts, the primary objective is to develop a methodology for the conceptual design phase. Historically,

aircraft conceptual design relied on semi-empirical equations applied through manual iterative loops. This approach was feasible due to extensive historical databases and limited computational power, which constrained optimization methods. However, for novel aircraft concepts—such as those explored here—this traditional method is no longer viable. These new designs deviate significantly from historical examples, rendering old empirical equations unreliable or nonexistent, particularly for components like hydrogen tanks.

To address this challenge, physics-based models must be developed. Yet, aircraft design remains a highly complex process due to its multidisciplinary nature, where disciplines like aerodynamics, structures, and controls are deeply interdependent. A classic example is the aero-structural coupling: aerodynamic loads on a wing depend on its shape, but those loads also deform the wing's structure, altering its shape and, consequently, the aerodynamic loads. Such inter-dependencies can be visualized using an **eXtended Design Structure Matrix (XDSM) [119]**, as shown in Figure **I.51**. In this format:

- Blue boxes denote individual analyses (e.g., a single function for rectangular boxes or a group of functions for octagonal boxes).
- The execution sequence follows a top-left to bottom-right flow, following the black line.
- Input variables for each analysis are listed vertically, while outputs are positioned horizontally.
- Thick gray lines indicate the data dependencies between functions.

At the conceptual design stage, discipline models must balance accuracy with computational efficiency, as the design process is inherently iterative and often involves numerous cycles. To manage these coupled multidisciplinary challenges, the **MDAO** paradigm has emerged. **MDAO** enables the automated, iterative solution of coupled analyses while simultaneously facilitating optimization.

Significant progress in **MDAO**-based aircraft design methods was already made at ONERA and ISAE-SUPAERO before this thesis, leading to the development of **Future Aircraft Sizing Tool for Overall Aircraft Design (FAST-OAD) [120]**. The core capability of FAST-OAD is preliminary aircraft sizing, using the **TLARs** and a few key geometric parameters. It then size and position the dimensions. The tool sizes and positions all key components like wing, fuselage, and tailplane while incorporating longitudinal stability considerations.
The open-source version of FAST-OAD includes computational models optimized for conventional single-aisle jetliners, like the A320, for which the tool was originally developed and validated. These models draw from classical aircraft design literature [**121**, **122**], as well as Airbus expertise compiled in the ISAE-SUPAERO handbook [**123**]. However, FAST-OAD is inherently modular, allowing any disciplinary model or submodel to be

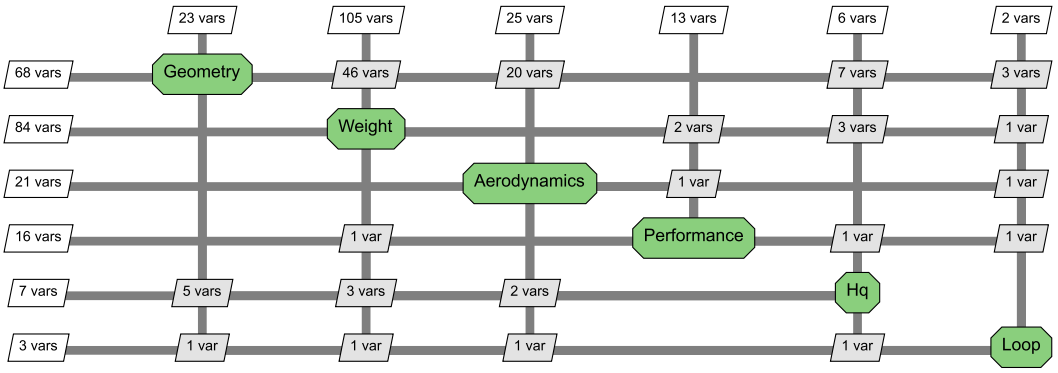

Figure I.50: FAST-OAD multidisciplinary Analysis process [**120**]

replaced or extended. For this reason, all developments conducted in this study were integrated into the FAST-OAD framework. This approach leverages the existing platform structure and reuses disciplinary models that remain applicable to new aircraft concepts. The standard models used in this thesis are summarized in Table **I.1**.
In its current version, **FAST-OAD** employs a **Multi-Disciplinary Analysis (MDA)** loop centered on the aircraft's block fuel mass. To ease this iterative process, **FAST-OAD** is implemented in Python using the OpenMDAO framework, developed by NASA [**126**], which is specifically tailored for such multidisciplinary optimization problems The process begins by estimating the fuel mass required for the mission based on an initial guess of the **MTOW**. The tool then sizes the aircraft structure using this fuel mass estimate and the **TLARs**. With the structural mass determined, FAST-OAD recalculates the updated **MTOW** and recomputes the fuel mass through a time-step integration of the mission profile. This iterative process continues until convergence is achieved, ensuring that both the fuel mass and aircraft mass align with a feasible aircraft design. The MDA workflow is illustrated in Figure **I.50**.

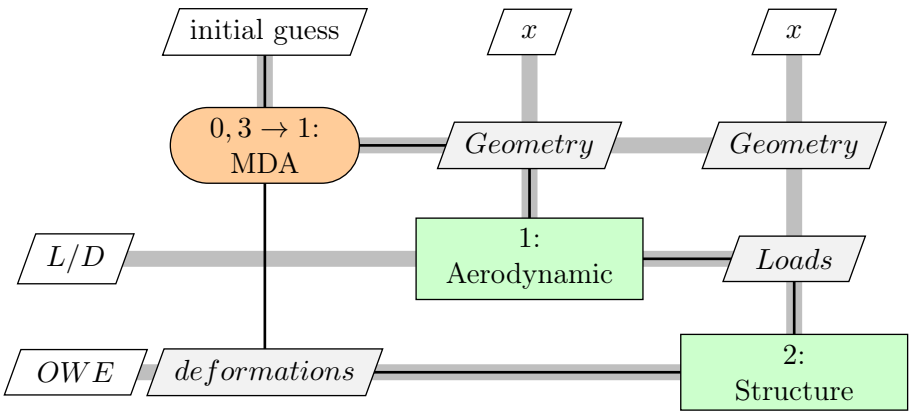

Figure I.51: Illustration of the aerodynamic-structure discipline coupling in aircraft design within an **XDSM** graph

Table I.1: Discipline-Specific Modeling Approaches in FAST-OAD

Discipline	Description
Aerodynamics	• **Low-fidelity model** based on analytical and semi-empirical equations, validated against CFD and experimental data by Moens [**124**], enabling rapid computation • The wing is divided into **3 sections (T&W) to 5 sections (BWB)**, each defined by key inputs: sweep angle, relative thickness, maximum lift coefficient, Korn factor (for wave drag calculations), and a laminar flow index X_{tra} • Primary output: **high-speed and low-speed drag polars** for the configuration • Capable of modeling **both T&W and BWB configurations**
Weight	• Mass breakdown follows the French standard 2001/B. • Parametric empirical correlations are used for each structural component and on-board systems, as provided in the ISAE-SUPAERO handbook.
Propulsion	• A "rubber engine" turbofan model, defined by inputs such as thrust at sea level or BPR, built by Roux [**125**]. • Engine sizing is not included in the iterative process.
Performance	• Three mission phases simulated: climb, cruise, and descent. • A time-step integration approach is implemented. • The full mission analysis can be replaced by a Breguet-Leduc range equation.
Geometry	• The fuselage geometry is determined with respect to cabin layout. • Theoretical and statistical equations are applied following the ISAE-SUPAERO handbook [**123**]. • A parametric geometry of lifting surfaces is used.
Handling Qualities	• Handling qualities are part of the iterative sizing loop. • Wing position is varied to allow the static margin to be between 5% and 10%. • Horizontal and vertical tails are sized with respect to balance and lateral controllability of the aircraft.

I.5.3 Methodology and Development Choices

To develop a modular and generic multidisciplinary design methodology for hydrogen-powered Blended Wing-Body aircraft within FAST-OAD, the first logical step was to extend FAST-OAD's capabilities to support the design of hydrogen-powered aircraft. A review of the literature highlights that the most significant design challenge for hydrogen aircraft lies in fuel storage: the voluminous and complex cryogenic tanks required for **SMR** or long-range mission necessitate fundamental changes in aircraft architecture.

As such, the initial phase of this thesis focused on developing a hydrogen cylindrical tank sizing procedure capable of estimating tank mass, center of gravity, and hydrogen boil-off. While the simplest approach for mass estimation is to assume a fixed gravimetric index, a review of existing research revealed significant discrepancies in published values—particularly for this key parameter (see Figure II.1). Furthermore, studies have shown that the gravimetric index is highly sensitive to both the aircraft mission and tank architecture [**49**]. This variability underscores the need for a detailed tank sizing methodology within a generic design framework, enabling self-assessment of the gravimetric index and mission-specific optimization.
This requirement is particularly critical for boil-off estimation, which necessitates a robust thermodynamic model of the tank. However, as highlighted by Adler and Martins [**46**] in their literature review, most existing hydrogen thermodynamic models lack sufficient fidelity, as they assume the tank behaves as a homogeneous volume.
To enhance the fidelity of models used in aircraft design, the initial phase of this study focused on developing a medium-fidelity thermodynamic model for cryogenic tanks, inspired by those designed for spacecraft applications. This model employs a time-integration approach, similar to the mission module procedure, to estimate the heat flow entering the tank and the evolution of its internal thermodynamic state. These estimates are essential for quantifying hydrogen loss during venting phases, which occur when the tank pressure reaches its design limit. To enable comprehensive hydrogen tank design and seamless integration into an aircraft sizing program such as FAST-OAD, a parametric structural sizing procedure—inspired by certified methods for pressurized fuselage tank design—was also developed in parallel to determine tank mass.

In the second phase, once **FAST-OAD** was capable of designing hydrogen-powered tube-and-wing aircraft, the focus shifted to extending its capabilities to include Blended Wing Body configurations. This was achieved by coupling the FAST-OAD framework with the **MDAO** process developed during the CICAV project at ONERA [**104**, **105**, **106**, **107**]. With this integration complete, FAST-OAD could now size **BWB** aircraft, but the hydrogen tank sizing procedure required adaptation for this new configuration. However, determining the optimal placement of hydrogen tanks in a **BWB** presents a significant challenge. In previous studies, authors often made arbitrary decisions regarding tank positioning or sizing. For example, Karpuk's sizing procedure [**113**] assumed a sequential placement strategy—fitting the largest possible tank first, followed by additional tanks if needed—while explicitly excluding tank placement behind the cabin. Di Summa et al.

[**114**], who later adapted this procedure, introduced greater modularity but ultimately evaluated only a limited number of configurations, selected somewhat arbitrarily. This highlights the need for a more systematic and flexible approach to hydrogen tank integration in **BWB** designs.
Thus, the next phase of this work focused on enhancing the **BWB** parametrization—originally developed in the CICAV project—to incorporate hydrogen tank number, size, and placement. This expansion enabled a broad range of possible tank arrangements, facilitating the modeling of a diverse set of hydrogen **BWB** configurations. Ultimately, this approach allowed for comprehensive exploration of the design space and the establishment of an optimization framework to identify the most promising configurations and assess their performance.

CHAPTER II

Development of a medium fidelity hydrogen tank thermodynamic model to estimate hydrogen boil-off

Résumé

L'analyse de la littérature présentée dans le chapitre précédent a révélé que, bien que les avions à hydrogène soient techniquement réalisables — comme le démontrent plusieurs prototypes déjà testés en vol —, leur développement rencontre encore des défis techniques majeurs. L'adoption de l'hydrogène comme carburant aéronautique nécessite en effet une refonte complète de la chaîne de propulsion et du stockage d'énergie à bord.

Parmi les changements les plus significatifs, on trouve l'intégration de réservoirs d'hydrogène. En raison de la faible densité énergétique volumétrique de l'hydrogène, ces réservoirs doivent être de grande taille pour contenir suffisamment de carburant pour un vol. Pour les missions dépassant les courts courriers, l'hydrogène doit être liquéfié pour atteindre un volume de stockage viable. Cependant, cela implique le développement et la gestion de réservoirs cryogéniques à bord, nécessitant des systèmes d'isolation thermique sophistiqués et potentiellement lourds. Les réservoirs d'hydrogène liquide qui en résultent sont non seulement encombrants, mais ajoutent aussi une masse significative, influençant profondément les performances et l'architecture globale de l'aéronef.

Il devient donc impératif d'intégrer la conception des réservoirs dès la phase pré-

conceptuelle du développement de l'aéronef. Cette intégration précoce permet d'évaluer les stratégies optimales d'intégration des réservoirs et d'en mesurer l'impact sur les performances globales de l'appareil. Une approche simple consiste à modéliser les réservoirs d'hydrogène à partir de leur efficacité gravimétrique, permettant d'estimer facilement la masse d'un réservoir en fonction de la masse d'hydrogène à stocker. Cependant, il existe une grande disparité dans les indices gravimétriques rapportés dans la littérature, reflétant des hypothèses et des choix technologiques variés — souvent non explicités — qui peuvent diverger de manière significative d'une étude à l'autre.

S'appuyer sur un indice gravimétrique arbitraire étant donc impossible, une méthodologie innovante de dimensionnement des réservoirs d'hydrogène est développée et intégrée directement dans l'outil de conception d'aéronefs FAST-OAD dans ce chapitre. Cette méthodologie permet d'inclure explicitement diverses hypothèses et choix technologiques comme variables de conception, offrant ainsi une évaluation rigoureuse de leur validité et de leur impact sur la conception globale de l'aéronef.

Ce chapitre commence par une revue de la littérature plus ciblée sur les modèles existants pour modéliser un réservoir cryogénique dans le cadre de la conception d'avions. Cette revue est structurée en deux axes principaux : les modèles d'estimation des flux thermiques entrant dans les réservoirs d'hydrogène, et les modèles d'auto-pressurisation permettant de prédire l'évaporation de l'hydrogène due à ces apports de chaleur.

Une méthode originale est ensuite développée pour estimer les flux de chaleur pénétrant dans les phases gazeuse et liquide de l'hydrogène. Celle-ci repose sur une analogie électrique par résistances thermiques, où chaque phénomène de transfert thermique impliqué dans un réservoir cryogénique est modélisé comme une résistance thermique. Ces résistances sont ensuite combinées en série ou en parallèle pour déterminer la résistance thermique totale du réservoir, et ainsi calculer le flux de chaleur entrant.
L'une des innovations importantes de ce travail réside dans la division du réservoir en plusieurs sections, chacune étant associée à un flux thermique spécifique en fonction des conditions environnementales internes et externes. Cette segmentation permet de prendre en compte de manière plus précise certains phénomènes physiques de transfert de chaleur.
Dans un deuxième temps, un modèle d'auto-pressurisation a été introduit, s'appuyant sur une division du réservoir en trois volumes de contrôle : la phase liquide, l'ullage (phase gazeuse) et leur interface. Ce modèle, inspiré de ceux utilisés dans l'industrie spatiale, s'éloigne des approches homogènes traditionnelles et permet de dériver un système d'équations temporelles décrivant l'évolution de l'état thermodynamique du réservoir. Il permet notamment d'estimer avec précision l'augmentation de pression interne, en accordant une attention particulière à la dynamique de pression au cours d'une mission aérienne.
Cette augmentation de pression, induite par les apports de chaleur, sert de base à la modélisation de la phase de purge, qui détermine la quantité d'hydrogène gazeux à évacuer pour maintenir la pression en dessous de la limite maximale et préserver l'intégrité structurelle du réservoir.

Enfin, ce modèle thermodynamique est intégré à l'outil de conception d'aéronefs FAST-OAD, permettant la conception d'avions à hydrogène en prenant en compte les pertes potentielles liées à l'évaporation. Cette intégration contribue ainsi à une approche plus réaliste et optimisée du dimensionnement des systèmes de stockage cryogénique.

Contents of this Chapter

II.1 Introduction 63
II.2 State-of-the-Art of Thermodynamic Models of H2 Tanks in Aircraft 65
II.2.1 Common Thermodynamic Framework for Tank Heat Inflow 66
II.2.2 Review of Internal Thermodynamic State Evolution Models for Hydrogen Storage 68
II.3 Enhanced Model for Estimating H2 Boil-Off in Aircraft Cryogenic Tanks . 72
II.3.1 Estimation of Heat Leak into a Hydrogen Tank Using an Enhanced Thermal Resistance Model 72
II.3.1.1 Definition of heat flows involved in aircraft cryogenic tanks 72
II.3.1.2 Formulation of a System of Equations to Determine Convective Heat Exchange in Gaseous and Liquid Hydrogen Phases 76
II.3.2 Derivation of a temporal equation system describing the evolution of the tank's internal state 79
II.3.2.1 Fundamental Assumptions and Representation of the Tank Model 80
II.3.2.2 Energy Conservation Analysis for the Bulk-Liquid Hydrogen Volume 81
II.3.2.3 Energy Conservation Analysis for the Ullage Volume . . . 84
II.3.2.4 Energy Conservation Analysis for the Interface 85
II.3.2.5 Governing System of Ordinary Differential Equations for Tank Thermodynamic State: Formulation and Comparative Analysis with Prior Studies 86
II.3.3 Development of a methodology to estimate hydrogen loss during venting 87
II.3.4 Hydrogen tank model implementation into FAST-OAD 88
II.4 Conclusion and perspectives 90

II.1 Introduction

The literature review presented in the previous chapter underscored that while hydrogen-powered aircraft are technically feasible—with several prototypes already having flown—they continue to pose significant technical challenges. The adoption of hydrogen as an aviation fuel necessitates the development of an entirely new energy and propulsion chain. Among the most transformative changes is the integration of hydrogen storage tanks on board the aircraft. Due to hydrogen's low volumetric energy density, large tanks are required to store the necessary fuel for an aircraft mission. For missions extending beyond regional ranges, hydrogen must be liquefied to attain a viable storage volume. However, this approach introduces significant additional challenges, particularly the management of cryogenic temperatures, which necessitates the implementation of sophisticated—and potentially heavy—thermal insulation systems. The resulting liquid hydrogen tanks are not only voluminous but also add significant mass, profoundly influencing both aircraft performance and overall architectural design.

Given these constraints, it becomes imperative to incorporate tank design considerations as early as the pre-conceptual phase of aircraft development. This early integration allows for the evaluation of optimal tank integration strategies and the assessment of their impact on overall aircraft performance. A straightforward approach to achieving this is to model hydrogen tanks using their gravimetric efficiency (Equation I.1). By assuming a gravimetric index, it is possible to estimate the mass of hydrogen tanks based on the block fuel requirement, thereby enabling the consideration of tank mass and volume during the initial design stages. As demonstrated by Adler and Martins in Figure I.25, aircraft energy consumption is highly sensitive to this parameter, particularly for medium- to long-range missions. However, Figure II.1 reveals a wide disparity in reported gravimetric indices across the literature. This variability stems from differing hypotheses and technological assumptions in each study—assumptions that are often not explicitly detailed and can diverge significantly.

Consequently, relying on an arbitrary gravimetric index was deemed both methodologically insufficient and overly restrictive, introducing unacceptable risks to the accuracy and reliability of the design process. Instead, a novel hydrogen tank sizing methodology was developed and integrated directly into the aircraft sizing tool, **FAST-OAD**. This methodology allows for the explicit inclusion of various hypotheses and technological assumptions as design variables, enabling a rigorous assessment of their validity and impact on the overall design.

The methodology for sizing hydrogen tanks consists of two primary components: First, a thermodynamic model of the cryogenic hydrogen tank is developed to quantify hydrogen losses resulting from boil-off over the course of the mission. Second, a structural sizing approach is employed to determine the tank's mass. This chapter is dedicated to the thermodynamic modeling of the cryogenic hydrogen tank, as implemented within the **FAST-OAD** framework. The structural sizing of the tank will be addressed in the

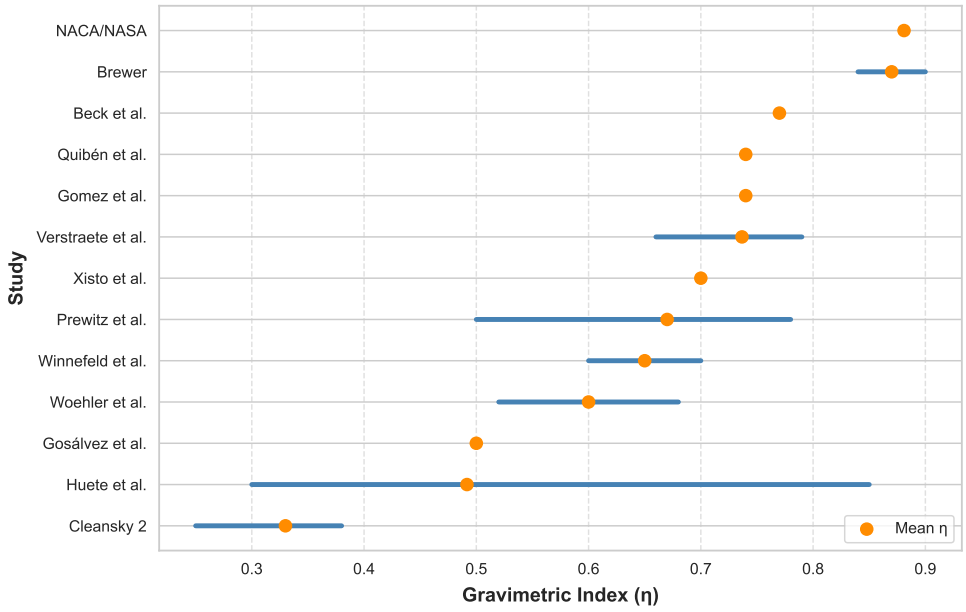

Figure II.1: Comparison of Gravimetric Index Values in LH2-Powered Aircraft studies (adapted from [**127**])

subsequent chapter.

Maintaining hydrogen in a liquid state at 20 K throughout a mission requires a detailed thermodynamic analysis. During flight, the tank is subject to dynamic temperature and pressure variations. Heat ingress into the tank will induce hydrogen boil-off, leading to increased internal pressure. To mitigate this, the tank undergoes periodic cycles of self-pressurization and venting, where hydrogen is released to maintain pressure below the maximum design threshold.

This chapter begins with a critical review of existing methods in the literature for modeling thermal and fluid dynamic phenomena in cryogenic tanks. The literature review is structured into two main categories:

- Models for estimating heat inflow into hydrogen tanks.
- Self-pressurization models for predicting hydrogen boil-off resulting from this heat inflow.

The second part of the chapter presents the implemented tank thermodynamic model. The estimation of heat flux entering the gaseous and liquid phases of hydrogen is conducted using an electrical resistance analogy model, which is slightly enhanced from the available models in literature. In this approach, each heat transfer phenomenon contributing to the tank's internal thermal load is represented as a thermal resistance, allowing for individual computation and analysis.

The self-pressurization model developed in this work and presented next introduces a novel standard for aircraft design. Unlike the traditional homogeneous models frequently

found in the literature, this model employs a three-control-volume system, separately modeling the bulk liquid, the ullage (gas phase), and the interface between them. Inspired by models used in the space industry, this approach enables the derivation of a system of temporal equations describing the evolution of the tank's thermodynamic state during an aircraft mission, with particular emphasis on the internal pressure dynamics.

The increase in internal pressure, driven by heat inflow into the tank, serves as the foundation for modeling the venting phase, discussed in the subsequent section. This phase estimates the amount of ullage that must be vented to maintain the tank pressure below its maximum design limit.

Finally, the chapter concludes with an explanation of how this thermodynamic model of a cryogenic hydrogen tank was integrated into the **FAST-OAD** aircraft design tool. This integration enables the design of hydrogen-powered aircraft while accounting for potential hydrogen losses due to boil-off, ensuring both safety and efficiency in the aircraft's fuel system.

A substantial portion of the thermodynamic modeling framework for cryogenic hydrogen tanks, as presented in this chapter, was initially developed and published in:

- R. Parello, S. Defoort, E. Benard, and Y. Gourinat. *Design and Integration of a Liquid Hydrogen Tank on an Aircraft.* en. In: AIAA SCITECH 2024 Forum. Orlando, FL: American Institute of Aeronautics and Astronautics, Jan. 2024. doi: 10.2514/6.2024-2638.

The earlier work established the core principles for estimating hydrogen boil-off, heat transfer dynamics, and thermal management within cryogenic storage systems. This chapter builds upon this article by detailing the model's equation and incorporation into **FAST-OAD**.

II.2 State-of-the-Art of Thermodynamic Models for Hydrogen Tanks in Aircraft Design

The majority of thermodynamic models for cryogenic hydrogen tanks in aircraft design originate from the foundational work of Brewer [**24**], which was subsequently refined by Verstraete [**32**]. These contributions established the standard methodology for modeling such specialized tanks and estimating hydrogen losses due to boil-off.
The approach involves simulating the temporal evolution of the tank's thermodynamic state using time-step integration :

- Under the assumption of steady-state conditions—which generally prevail during cruise—it is possible to first calculate the heat ingress through the tank's insulation at any given point in the mission.

- This heat flow is then incorporated into a time-dependent model of the tank's thermodynamic state, enabling the determination of the pressure rise rate.

- When the pressure reaches the structural limit of the tank, a venting phase is initiated.

While all models of cryogenic hydrogen tanks used in aircraft conceptual design adhere to this general approach, they may differ in the methods employed for each of the three key steps—especially in how physical phenomena are modeled and refined.

II.2.1 Common Thermodynamic Framework for Tank Heat Inflow

To estimate the heat flow entering the tank, Verstraete's model employs an electrical resistance analogy, treating the various physical phenomena associated with heat transfer as resistances connected in series. The total thermal resistance is then derived from these individual components following the methodology outlined by Carslaw and Jaeger [**128**]. The model accounts for three distinct thermal resistances, each corresponding to a specific heat transfer mechanism:

- **The external heat transfer resistance** R_{ext} : This resistance encompasses both convective and radiative heat transfer at the tank's outer surface—specifically, the aircraft skin exposed to the atmosphere. These two resistances are arranged in parallel, yielding:

$$R_{ext} = \frac{1}{A_{tank}} \frac{1}{h_{ext,rad} + h_{ext,conv}} \tag{II.1}$$

  Where A_{tank} represents the external surface area of the tank, and $h_{ext,rad}$ and $h_{ext,conv}$ denote the external radiative and convective heat transfer coefficients, respectively. These coefficients are defined as follows:

$$h_{ext,conv} = \frac{Nuk_{air}}{L} \tag{II.2}$$

$$h_{ext,rad} = \sigma\epsilon(T_{skin}^2 + T_{atmos}^2)(T_{skin} + T_{atmos}) \tag{II.3}$$

  Where L is the characteristic length for the heat transfer phenomenon, k_{air} the thermal conductivity of air and N_u the Nusselt number, T_{skin} and T_{atmos} are the temperature of the skin and atmosphere, respectively, σ is the Stefan-Boltzmann constant and ϵ the emittance of the skin.

- **The internal thermal resistance of the insulation** R_{ins} : The insulation may consist of either foam or **Multi-Layer Insulation (MLI)**, the latter comprising two walls separated by multiple radiation shields within a vacuum environment.

In case of foam :

$$R_{ins} = \frac{1}{2\pi r_i l_{tank}} \frac{ln\left(\frac{r_o}{r_i}\right)}{k_{foam}} \tag{II.4}$$

Where r_i and r_o denote the tank's inner and outer radii, respectively, l_{tank} represents its length, and k_{foam} refers to the thermal conductivity of the insulating foam. Given the temperature dependence of k_{foam}, Verstraete discretizes the insulation into 40 sub-layers of uniform thickness. The resistance of each sub-layer is calculated individually, and the total resistance is determined iteratively until the heat flux through each layer converges.

In the case of **MLI**, the thermal conductivity of the foam, k_{foam} is substituted by k_{MLI}, defines as follows -where t represents the thickness and q a heat flux :

$$k_{MLI} = \frac{q}{\frac{T_H - T_C}{t}} \tag{II.5}$$

- **The convection heat transfer resistance inside the tank between the wall and the liquid or gaseous hydrogen** R_{int} :

$$R_{int} = \frac{1}{2\pi r_i L} \frac{A_{LH2} + A_{GH2}}{h_{LH2} A_{LH2} + h_{GH2} A_{GH2}} \tag{II.6}$$

Where A_{LH2} and A_{GH2} correspond respectively to the wetted and dry area inside the tank, while h_{LH2} and h_{GH2} represent the convective heat transfer coefficients for liquid and gaseous hydrogen, respectively (defined analogously to Eq. II.2). r_i is the internal radius of the tank.

The total thermal resistance of the tank wall and insulation is then determined, enabling the calculation of the total heat transfer into the fuel, Q—with an additional 30% safety margin applied by Verstraete to account for the thermal transfer through the tank supports, connection and piping:

$$R_{tot} = R_{int} + R_{ins} + R_{ext} \tag{II.7}$$

$$Q_{tot} = 1.3 \frac{T_{amb} - T_{H2}}{R_{tot}} \tag{II.8}$$

The preceding equations constitute the foundational framework of the thermodynamic model for cryogenic tanks, as originally developed by Verstraete. This framework has been widely adopted in studies focused on liquid hydrogen aircraft. For example, Sekaran et al. [**129**] assessed the feasibility of integrating a liquid hydrogen storage tank into a turbo-electric distributed propulsion system, while Gomez and Smith [**130**] explored the adaptation of the MRT7-3 "Meridian" (Smith, 2007)—a conventional midrange civil transport designed at Cranfield University in 2008—into a hydrogen-powered aircraft. While most authors retain the core structure of Verstraete's model, some introduce modifications to specific correlations or incorporate additional phenomena. Notably, Van Woensel [**55**],

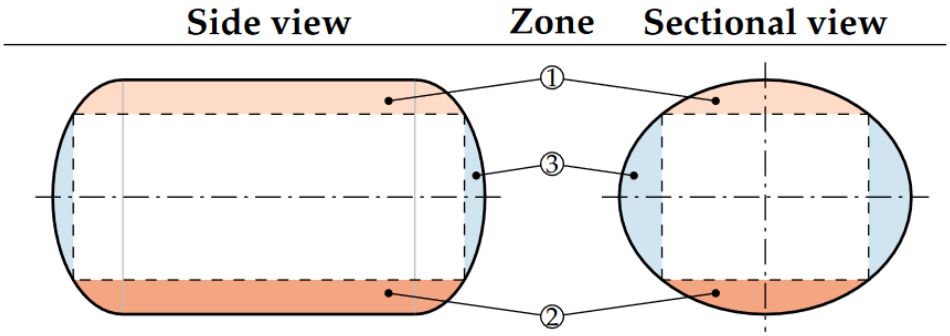

Figure 9. Geometric breakdown of the tank geometry.

Figure II.2: Tank zone breakdown breakdown by Winnefeld [**48**]

inspired by the work of Shi et al. [**131**], extends the model to account for the influence of solar radiation on the tank skin (Eq. II.9), the thermal boundary layer and an alternative formulation for skin radiation (Eq. II.20).

$$\dot{Q}_{solar} = q_{solar} A_{ext,solar} \alpha \tag{II.9}$$

$$h_{ext,rad} = (T_{skin}^4 - T_{sky}^4)\epsilon\sigma \tag{II.10}$$

Where T_{sky} is the atmospheric temperature adjusted for humidity.
Winnefeld et al. also employ a similar thermodynamic model but modify the Nusselt number correlation for free heat convection between the tank wall and liquid hydrogen, introducing a dependency on the wall angle. Their approach divides the tank into three distinct zones—two horizontal and one vertical (as illustrated in Figure II.2)—each governed by a different correlation. Silberhorn et al. [**47**], in their work to integrate a hydrogen tank model into an aircraft multidisciplinary design framework, adopt the same correlations. While some models, such as TankSIM [**132**], utilize correlations for convection that directly account for the wall angle, such detailed approaches have not been applied in the conceptual design phase of aircraft.

II.2.2 Review of Internal Thermodynamic State Evolution Models for Hydrogen Storage

The second component of all models designed to size cryogenic hydrogen tanks focuses on the internal thermodynamics of the tank. The objective is to characterize the state of the fuel inside, which is intrinsically linked to the previously computed heat flux (noting that this heat flux, Q, is itself dependent on the internal thermodynamic state, as hydrogen temperature and pressure influence Q—see Eq. II.8).
A foundational method for this analysis was initially developed during the Cryoplane project [**33**] and later refined by Verstraete, though its conceptual origins trace back to spacecraft and launcher applications in the work of Lin et al. [**133**]. This approach has since been widely adopted in studies concerning hydrogen-powered aircraft. This approach

is referred to as the **homogeneous model**, as it treats the tank as a single, uniform control volume, thereby enabling the direct application of the first law of thermodynamics on the entire tank (Eq. II.11):

$$\frac{dE}{dt} = \dot{Q} + W + \dot{m}_{in}h_{in} - \dot{m}_{out}h_{out} - p\frac{dV}{dt} \tag{II.11}$$

The heat flux is derived from the initial phase of the methodology, while the mass flow is characterized by a zero inflow (typical for aircraft applications) and an outflow equal to the engine's fuel consumption rate. These parameters collectively enable the determination of pressure dynamics within the tank over the course of the mission in equation II.12. When the internal pressure attains the maximum allowable threshold, venting is initiated, causing an immediate pressure reduction.

$$\frac{dp}{dt} = \frac{1}{\rho\left(\frac{\partial u}{\partial p}\right)_\rho}\left(\dot{Q} - \dot{m}_{out}h_{lg} - \left(x\frac{\rho_g}{\rho_l - \rho_g}\right)\right) \tag{II.12}$$

This model, however, relies on the assumption of a homogeneous tank, implying that the temperatures of both gaseous and liquid hydrogen remain uniform and equal to the boiling point of hydrogen. While the Cryoplane study [**33**] and Verstraete [**32**] recognize that, in practice, thermal stratification may occur—potentially increasing the pressure rise rate by a factor of 100 in a fully stratified tank if all the heat enters the gaseous phase—they argue that in-flight vibrations and fluid motion would significantly mitigate this effect. Brewer et al. [**134**] demonstrated that, across all tank architectures considered in their study, the temperature gradient between the bottom and top of the tank remains below 0.22 K. As a conservative compromise, Verstraete—following the approach of Lin et al. [**133**]—adopts a pressure rise rate twice that of the homogeneous model to account for safety margins. Thanks to its relative simplicity, this model is used in numerous other existing aircraft studies [**48**, **49**, **51**, **55**, **129**, **135**]

In contrast to the homogeneous model, **Computational Fluid Dynamic (CFD)** models offer the highest fidelity and accuracy for simulating cryogenic tanks. However, their computational and implementation demands render them impractical for pre-conceptual design phases. Similarly, other highly detailed programs developed for space applications—such as NASA's Generalized Fluid System Simulation Program—suffer from excessive complexity and prohibitively long computation times for conceptual design. For instance, modeling a single mission with this program requires several hours [**136**, **137**].

Among the most detailed yet analytically tractable models—therefore suitable for conceptual design—are those derived from the work of Ring [**138**]. These models offer a more refined and physically representative description of the phenomena occurring within the tank. In this framework, the tank can be divided into multiple distinct control volumes: the **ullage** (gaseous phase), the **liquid phase**, the tank wall, and an **interface**—a virtual control volume at the liquid-gas boundary, possessing negligible mass but a defined temperature equal to the saturation temperature (pressure-dependent). Some

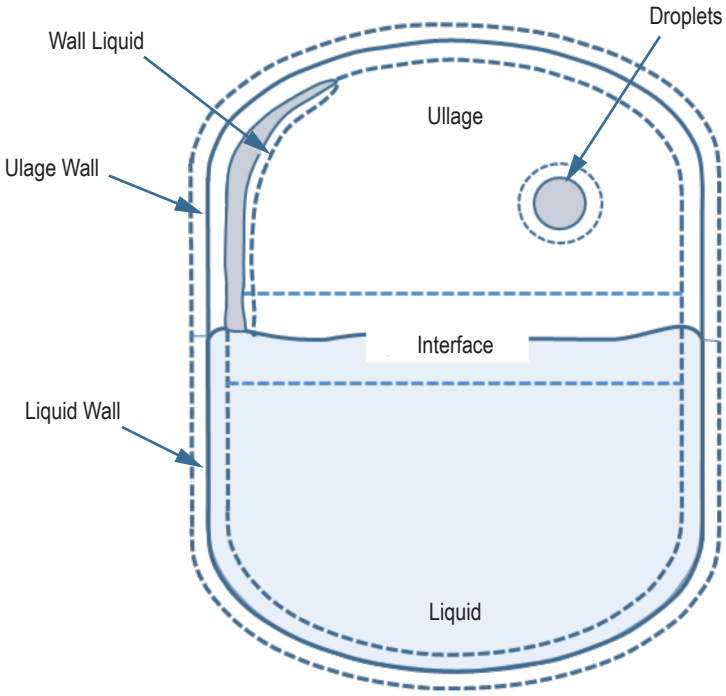

Figure II.3: Schematic representation of the seven control volumes in a hydrogen tank as modeled by NASA's TankSIM [**132**]

studies, such as those by Estey [**139**] introduce simplifications, such as consolidating or neglecting the tank wall control volumes.

This framework was further refined and expanded in NASA's TankSIM model [**132**], originally developed for high-accuracy simulation of spacecraft cryogenic tanks. TankSIM enhances the approach by dividing the tank into seven interacting control volumes, each exchanging mass and/or heat to model boil-off dynamics. These volumes, illustrated in Figure II.3, are as follows:

- **Wet tank wall**: wall exposed to liquid hydrogen.
- **Dry tank wall**: wall exposed to gaseous hydrogen.
- **Ullage**: Gaseous hydrogen
- **Liquid hydrogen**
- **Interface**: an infinitesimally thin control volume (no mass) with a finite temperature.
- **Liquid film**: adhering to the dry wall.
- **Liquid droplets**: suspended in the gaseous hydrogen

The state of each control volume is characterized by its temperature, mass, pressure, and volume (where applicable). In this model, dihydrogen gas is treated as an ideal gas,

while the interface temperature is fixed at the saturation temperature. These control volumes interact through heat and/or mass exchange. The conservation of energy (Eq. II.13) is applied individually to each volume. To simplify the system, Ramos omits the liquid film on the dry wall, suspended droplets, and wall heat capacity, reducing the model to three control volumes. This simplification results in a medium-fidelity model, yielding results comparable in accuracy to TankSIM, except at high fill levels, where the predicted pressure rise tends to be overly conservative. Since her focus is on designing cryogenic tanks for long-duration space missions, Ramos does not account for fuel consumption. In contrast, Silberhorn et al. [**47**] adopt a further simplified version of this framework, employing a two-control-volume model that distinguishes only between gaseous and liquid hydrogen.

$$\dot{Q}_{net} + \dot{W} + \sum_{in} \dot{m}h - \sum_{out} \dot{m}h = \frac{dE_{cv}}{dt} \tag{II.13}$$

In conclusion, a simplified version of the thermodynamic model—initially developed by Ring [**138**] and later refined by NASA [**132**] for simulating cryogenic tanks in space missions—appears well-suited for aircraft conceptual design. This model strikes a balance by offering higher fidelity than the homogeneous model proposed by Verstraete [**32**], while remaining computationally efficient enough to support the iterative demands of conceptual design, where boil-off estimates must be generated in seconds.
While Ramos [**140**] and Silberhorn et al. [**47**] have adopted similar approaches, their applications either neglect fuel consumption (as in space mission contexts) or rely on highly simplified two-control-volume models. This study therefore aims to develop a new medium-fidelity version of such a thermodynamic model, tailored specifically for aircraft design applications and which will be integrated in the aircraft design software **FAST-OAD**. To limit complexity, this study focuses exclusively on cylindrical tanks with hemispherical or elliptical bulkheads (with a 1:2 aspect ratio). The thermodynamic properties of all chemical species are computed using the CoolProp Python library [**141**].

II.3 Development of an Enhanced Literature-Based Model for Estimating Hydrogen Boil-Off in Aircraft-Integrated Cryogenic Tanks

II.3.1 Estimation of Heat Leak into a Hydrogen Tank Using an Enhanced Thermal Resistance Model

II.3.1.1 Definition of heat flows involved in aircraft cryogenic tanks

As previously discussed, the self-pressurization analysis of a cryogenic hydrogen tank can be conducted for conceptual design purposes under the steady-state assumption. This assumption is justified because the major transient phases—such as take-off, climb, and descent—occur over a relatively short duration compared to the total flight time of an aircraft. Furthermore, since the final self-pressurization model will be used to estimate boil-off through time integration, it is feasible to select a sufficiently large time step to mitigate the effects of transient phases.
Under this framework, the self-pressurization analysis can be decomposed into two distinct steps:

- Estimation of the heat ingress into the tank
- Evolution of the tank's thermodynamic state in response to this heat transfer.

The first phase, detailed in this section, employs a thermal circuit model, which draws an analogy with electrical resistance networks to quantify the incoming heat flow. Heat flows associated with different physical phenomena are individually calculated and subsequently combined—either in parallel when occurring on the same surface or in series when occurring sequentially. This approach aligns with the methodology developed by Verstraete [**32**], as discussed in Section II.2.1, which is widely adopted in the literature.
An effort was made to refine the expression of the heat flow coefficients by incorporating additional physical phenomena and by differentiating them based on the specific areas to which they apply (tank external area A_{ext}), tank internal are A_{int} or an intermediate area A_{inter}. This refinement allows for the distinction of incoming heat flow across different sections of the tank surface, a critical consideration further discussed in Section II.3.1.2.

Three heat flow mechanisms between the skin and the external environment, as depicted in Figure II.4, must be accounted for to evaluate the heat inflow [**32**, **131**]. These mechanisms are described in detail below:

- The convective heat flow, which can be forced convection if the tank is integrated as the tank skin is also the aircraft skin or natural convection otherwise:

$$\dot{Q}_{ext,conv} = (T_{recovery} - T_{skin}) A_{ext} h_{ext,conv} \tag{II.14}$$

  Where $h_{ext,conv}$ is the heat transfer coefficient for convection and $T_{recovery}$ the temperature inside the boundary layer:

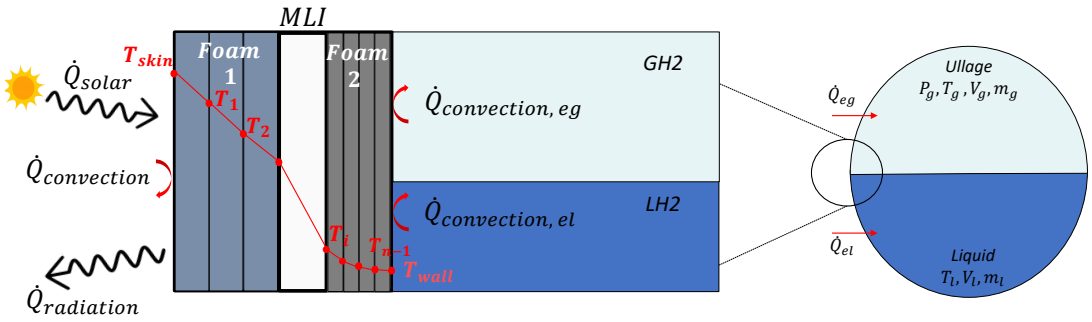

Figure II.4: Heat flows involved in a cryogenic hydrogen tank

$$T_{recovery} = T_{\infty}(1 + 0.5Pr^{0.5}(\gamma - 1)M^2) \tag{II.15}$$

$$h_{ext,conv} = \frac{Nuk_{air}}{L} \tag{II.16}$$

With γ being the heat capacity ratio, Pr the Prandlt number and M the mach number. The Nusselt number Nu quantifies the relative importance of convective heat transfer compared to conductive heat transfer within a fluid. The determination of Nu relies on empirical correlations, which are primarily expressed in terms of the Rayleigh number Ra and the Prandtl number Pr, or alternatively, the Grashof number $Gr = \frac{Ra}{Pr}$. To enhanced the model found in literature, different expressions for forced **[142]** or natural convection **[143]**, are implemented :

$$Nu_{forced} = 0.03625Pr^{0.43}Re^{0.8} \tag{II.17}$$

$$Nu_{natural} = 0.555Ra^{0.25} + 0.447 \tag{II.18}$$

$$Ra = \frac{g\beta\Delta TL^3Pr}{\nu} \tag{II.19}$$

- The radiative heat flow towards the exterior environment:

$$\dot{Q}_{rad} = (T_{sky}^4 - T_{skin}^4)A_{ext}\epsilon\sigma \tag{II.20}$$

Where T_{sky} is defined as a function of the dew point temperature T_{dp} **[131]**:

$$T_{sky} = T_{amb}(0.711 + 0.0056T_{dp} + 0.0073T_{dp}^2 + 0.0013)^{0.25} \tag{II.21}$$

- The heat flow associated to solar irradiation:

$$\dot{Q}_{solar} = q_{solar}A_{ext}\alpha \tag{II.22}$$

With $q_{solar} = 1420\ W/m^2$ (maximum solar heat flux above atmosphere)

After passing through the external skin, heat must cross the insulation. As shown in Figure II.4, the insulation is divided into multiple layers, with each layer associated with a node where the temperature is determined. This approach allows each layer to consist of different materials, such as combinations of foams or foam with **MLI**. Even when using a single insulation material, employing multiple nodes can be beneficial. This enables the adjustment of the material's thermal properties based on local temperature variations.
Figure II.5 illustrates that the thermal conductivity of polyurethane foam—a material commonly used for insulating cryogenic tanks—varies significantly with temperature. Specifically, its thermal conductivity increases by nearly a factor of 7 between 25 K and 300 K, a typical temperature range in cryogenic applications. Thus, accounting for temperature-dependent material properties is crucial for ensuring model accuracy.

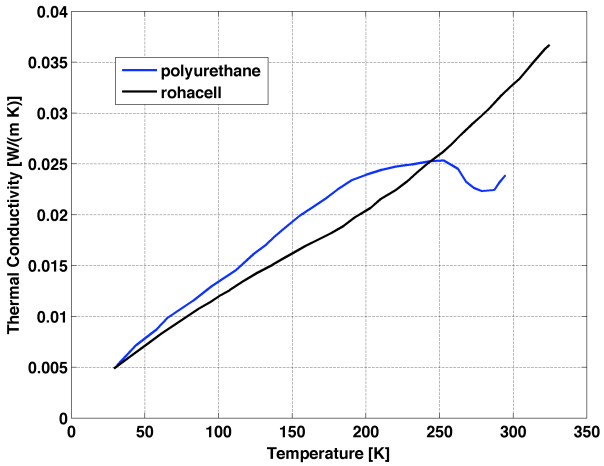

Figure II.5: Evolution of the thermal conductivity of polyurethane and rohacell foam with temperature [**32**]

Different expression are used to define the heat between two nodes in the insulation depending on the insulation technology. Different expressions are employed to define the heat transfer between adjacent nodes within the insulation, depending on the specific insulation technology. For an insulation system comprising n layers and $n+1$ nodes, where $T_0 = T_{skin}$ and $T_{n+1} = T_{wall}$, the incoming heat transfer for each node $i \in [\![1, n+1]\!]$ is determined by:

- **Foam insulation**: the heat transfer is a conductive heat flow depending on the local foam thermal conductivity $h_{cond,i}$:

$$\dot{Q}_{ins,i} = (T_{i-1} - T_i) A_{inter} h_{cond,i}(T_i) \tag{II.23}$$

- **MLI**: two empirical expressions can be used [**144**]:

  - The "Lockheed model", originally developed for **MLI** composed of perforated aluminized shields, nitrogen gas, and glass tissue spacer material, accounts for the total heat transfer as the sum of three distinct contributions: solid conduction through the spacer material, radiative heat transfer between shields,

and conduction through the residual gas:

$$\begin{aligned}\dot{Q}_{ins,i} =& A_{inter}\left(\frac{7.30\times10^{-8}\cdot(N^*)^{2.63}\cdot T_m\cdot(T_H-T_C)}{N_s}\right.\\ &+\frac{7.07\times10^{-10}\cdot\epsilon\cdot(T_H^{4.67}-T_C^{4.67})}{N_s}\\ &\left.+\frac{1.46\times10^{4}\cdot P\cdot(T_H^{0.52}-T_C^{0.52})}{N_s}\right)\end{aligned} \tag{II.24}$$

where T_H and T_C are the hot and cold temperatures on each side of the **MLI**, N_s is the number of shield layers, N^* is the shield layer density (per cm), ϵ is the shield emissivity, and P is the internal pressure inside the **MLI** (in torr).

- The "modified Lockheed model" retains the same foundational expression as the original but is adjusted for the specific insulation configuration used on the **Multipurpose Hydrogen test Bed (MHTB)** at NASA [**144**]. This modification accounts for the use of Dacron spacers (instead of Tissuglas) and larger perforations in the shields :

$$\begin{aligned}\dot{Q}_{ins,i} =& A_{inter}\left(\frac{2.4\times10^{-4}\cdot(0.017+7\times10^{-6}\cdot(800-T_m)+0.0228\cdot\ln(T_m))\cdot N_{\text{star}}^{2.63}\cdot(T_H-T_C)}{N_s}\right.\\ &+\frac{4.944\times10^{-10}\cdot\epsilon\cdot(T_H^{4.67}-T_C^{4.67})}{N_s}\\ &\left.+\frac{1.46\times10^{4}\cdot P\cdot(T_H^{0.52}-T_C^{0.52})}{N_s}\right)\end{aligned} \tag{II.25}$$

Once the heat has penetrated the insulation, it encounters the internal wall of the tank, which is treated as an additional insulation layer—albeit with significantly higher conductivity, as it is typically not an insulating material. The heat flow through this layer is defined using Equation II.23. The final stage of the heat inflow process involves heat exchange between the tank wall and the liquid or gaseous hydrogen contained within. This exchange is assumed to be primarily governed by convection, consistent with assumptions made in previous studies [**32**, **140**].

$$\dot{Q}_{int,conv} = A_{int}(T_{H2} - T_{wall})h_{conv,int} \tag{II.26}$$

$$h_{conv,int} = \frac{Nuk_{H2}}{L} \tag{II.27}$$

Where [**24**, **32**]:

- For natural convection between the wall and gaseous hydrogen:

$$Nu_{LH2} = 0.0605Ra^{\frac{1}{3}} \tag{II.28}$$

- For natural convection between the wall and liquid hydrogen:

$$Nu_{GH2} = 17 \tag{II.29}$$

II.3.1.2 Formulation of a System of Equations to Determine Convective Heat Exchange in Gaseous and Liquid Hydrogen Phases

To determine the heat flow entering the hydrogen, it is essential to calculate the internal convective heat transfer, which is a function of the wall temperature T_{wall} (as given in Equation II.26). Under the assumption that the tank remains in thermodynamic equilibrium—a valid approximation during cruise and sufficiently accurate for conceptual design—T_{wall} can be derived by solving the following system of $n+1$ equations:

$$\begin{cases} \dot{Q}_{ext,conv} + \dot{Q}_{rad} + \dot{Q}_{solar} - \dot{Q}_{ins,1} = 0 \\ \dot{Q}_{ins,1} - \dot{Q}_{ins,2} = 0 \\ ... \\ \dot{Q}_{ins,i} - \dot{Q}_{ins,i+1} = 0 \\ ... \\ \dot{Q}_{ins,n-1} - \dot{Q}_{ins,n} = 0 \\ \dot{Q}_{int,conv} - \dot{Q}_{ins,n} = 0 \end{cases} \tag{II.30}$$

This system consists of $n+1$ equations, where each equation involves only the temperatures of the two adjacent nodes as unknowns. Consequently, there are $n+1$ unknowns, corresponding to the temperatures at each of the $n+1$ nodes. The system thus admits a unique solution, representing the temperature gradient across the insulation. In practice, this system of equations is solved numerically using the fsolve function from the SciPy library in Python.
The resolution of this model enables the determination of two critical temperatures:

- The temperature of the exterior surface (or skin) of the tank, T_{skin}-which, in the case of an integral tank configuration, also corresponds to the aircraft skin—and,
- More importantly, the temperature of the interior surface of the tank, T_{wall}.

With T_{wall} and Equation II.26, it becomes possible to estimate the convective heat flux entering the liquid and gaseous hydrogen.
The system of equations (Equation II.30) requires the determination of the areas through which heat transfer occurs. However, the heat flow to consider may vary depending on the tank section. For example, the heat flow entering the liquid and gaseous hydrogen phases differs due to distinct internal convection phenomena.
To compute the total energy entering the hydrogen—whether in its gaseous or liquid phase—the system of equations (Equation II.30) must therefore be solved individually for each distinct section of the tank surface. The heat flow associated with each section is then

summed to obtain the total energy transfer. This section-specific approach is grounded in the unique external and internal environments that each tank section experiences :

- Internal Environment: The section may be in contact with either liquid or gaseous hydrogen
- External Environment: The section may be exposed to
  - The aircraft's fuselage interior (e.g., for tank bulkheads or in non-integral tank configurations), or
  - The atmosphere (in integral tank configurations). In the latter case, a section may also be exposed to solar radiation or remain shaded.

Overall, up to six distinct regions can be defined based on their internal and external environments.

- Sections in contact with Gaseous Hydrogen (GH_2):
  - Exposed to the **exterior environment** and **solar radiation**.
  - Exposed to the **exterior environment** but **not** exposed to solar radiation.
  - In contact with the **aircraft interior**.
- Sections in contact with Liquid Hydrogen (LH_2):
  - Exposed to the **exterior environment** and **solar radiation**.
  - Exposed to the **exterior environment** but **not** exposed to solar radiation.
  - In contact with the **aircraft interior**.

To determine the heat flow entering the tank, it is essential to calculate the surface areas of all the distinct sections described above. This primarily involves computing the wetted area A_{wet} and dry area A_{dry} of a cylindrical tank, which depend on the tank's geometric parameters: radius (r_{tank}) and diameter (d_{tank}); the length of the tank (l_{tank}); the liquid height in the tank (h_l); and the bulkhead dome height (h_d)—typically equal to $\frac{r_{tank}}{2}$ for a 1:2 elliptical tank.
For the wet area **[145]**:

$$A_{wet} = A_{wet,barrel} + A_{wet,bulkhead} \tag{II.31}$$

Where:

$$A_{wet,barrel} = 2l_{tank}r_{tank}\arccos\left(\frac{r_{tank}-h_l}{r_{tank}}\right) \tag{II.32}$$

$$A_{wet,bulkhead/hemispheric} = 2\pi r_{tank}h_l \tag{II.33}$$

$$A_{wet,bulkhead/elliptic} = 2\pi r^2 \cdot \frac{1}{2}\left[(FL-0.5)\sqrt{1+12(FL-0.5)^2}+1 + \frac{\ln\left(\frac{4e(FL-0.5)+\sqrt{1+12(FL-0.5)^2}}{2-\sqrt{3}}\right)}{4e}\right] \tag{II.34}$$

$$\text{with } FL = \frac{h_l}{d_{\text{tank}}}, \quad e = \begin{cases}\sqrt{1-\frac{4h_d^2}{d_{\text{tank}}^2}} & \text{if } d_{\text{tank}} > h_d,\\ \sqrt{1-\frac{4d_{\text{tank}}^2}{h_d^2}} & \text{if } h_d > d_{\text{tank}}.\end{cases} \tag{II.35}$$

For the dry area:

$$A_{dry} = A_{dry,barrel} + A_{dry,bulkhead} \tag{II.36}$$

Where:

$$A_{dry,barrel} = 2\pi r_{tank}l_{tank} - A_{wet,barrel} \tag{II.37}$$

$$A_{dry,bulkhead/hemispheric} = 4\pi r_{tank}^2 - A_{wet,bulkhead/hemispheric} \tag{II.38}$$

$$A_{dry,bulkhead/elliptic} = 2\pi r^2 \cdot \frac{1}{2}\left[(DL-0.5)\sqrt{1+12(DL-0.5)^2}+1 + \frac{\ln\left(\frac{4e(DL-0.5)+\sqrt{1+12(DL-0.5)^2}}{2-\sqrt{3}}\right)}{4e}\right] \tag{II.39}$$

$$\text{with } DL = \frac{d_{tank}-h_l}{d_{\text{tank}}}, \quad e = \begin{cases}\sqrt{1-\frac{4h_d^2}{d_{\text{tank}}^2}} & \text{if } d_{\text{tank}} > h_d,\\ \sqrt{1-\frac{4d_{\text{tank}}^2}{h_d^2}} & \text{if } h_d > d_{\text{tank}}.\end{cases} \tag{II.40}$$

The wetted and dry areas described above are computed three times to account for variations in the effective tank radius, depending on whether the insulation thickness is considered. This distinction is critical, as a non-negligible insulation thickness can significantly alter the calculated surface areas.

- **External area** (A_{ext}): This area includes the insulation thickness and is used to evaluate all phenomena occurring at the tank's outer skin surface.
- **Internal area** (A_{int}): This area excludes the insulation thickness and is used to compute the internal convection within the tank.
- **Intermediate area** (A_{inter}): This area is calculated at the midpoint of the insulation layers and is specifically used for analyzing heat flow through the insulation.

In addition to the external and internal surface areas, integral tank configurations—where the tank skin is also the aircraft skin—require the determination of the sun-irradiated area. As previously described, the calculation is performed separately for the irradiated sections in contact with gaseous hydrogen ($GH2$) and liquid hydrogen ($LH2$) on the internal side, adopting a worst-case scenario approach (where the maximum possible area is exposed) to remain conservative. For the section in contact with liquid hydrogen, which is always located at the bottom of the tank, the maximum irradiated area corresponds to half of the barrel section —a scenario that occurs when the sun is horizontal relative to the aircraft :

$$A_{\text{solar,LH2}} = \frac{A_{\text{tank barrel,LH2}}}{2} \tag{II.41}$$

For the section irradiated on the external side and corresponding to the gaseous phase, two scenarios are considered:

- If the tank is more than half filled ($h_l \geq r$), the worst-case scenario occurs when the sun is directly above the aircraft, irradiating the entire dry barrel are
- If the tank is more than half empty ($h_l \leq r$), the worst-case scenario again assumes the sun is directly above the aircraft, irradiating only the top half of the barrel section

$$A_{\text{solar,GH2}} = \begin{cases} A_{\text{tank barrel,GH2}} & \text{if } h_l \geq r, \\ 0.5 \cdot A_{\text{tank barrel, total}} & \text{otherwise.} \end{cases} \tag{II.42}$$

Once all these areas are computed for the 2 (non-integral tank) or 6 (integral tank) distinct sections, it becomes possible to solve Equation II.30. This allows for the determination of the temperature gradient and, most importantly, the wall temperature of each section (assuming negligible heat transfer between sections). Subsequently, Equation II.26 is used to calculate the actual energy flow entering either the liquid phase or the ullage for each section. Finally, these flows are summed to determine the total heat entering the liquid phase $\dot{Q}_{conv,LH2}$ and the ullage $\dot{Q}_{conv,GH2}$

II.3.2 Derivation of a temporal equation system describing the evolution of the tank's internal state

After solving the system (Equation II.30) for all the defined sections of the tank, it becomes possible to quantify the heat transfer to both the liquid and gaseous hydrogen inside the tank. This energy input inevitably leads to a rise in the internal tank temperature, resulting in the evaporation of liquid hydrogen into gaseous hydrogen. Since the tank is a closed system, this evaporation causes a corresponding increase in pressure. The objective of this section is to develop a thermodynamic model of the hydrogen tank capable of predicting the evolution of the ullage pressure. This model will enable the determination of when venting must occur to maintain safe operating conditions.
Unlike most previous studies in aircraft design—where authors typically adopted a homogeneous model (see Section II.2.2), assuming that all incoming heat contributed directly

to hydrogen evaporation and that the gas-liquid mixture remained at saturation temperature—this study introduces a more detailed and nuanced model.

II.3.2.1 Fundamental Assumptions and Representation of the Tank Model

The foundation of this model is the NASA liquid hydrogen tank model, originally developed for their TankSIM program [**132**]. Ramos also used this model as a basis in [**140**] but implemented several simplifications to reduce complexity. Her adapted model consists of three distinct control volumes:

- **Bulk liquid** hydrogen
- **Gaseous** hydrogen (ullage)
- **Interface** between the two phases, modeled as an infinitely thin layer with a defined temperature but negligible mass

In this simplified model, the liquid hydrogen film on the tank walls and droplets suspended in the ullage region are neglected. A representation of the model can be seen in figure II.6

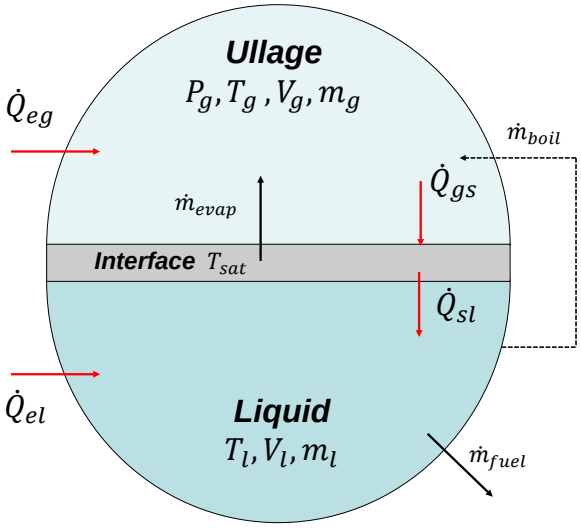

Figure II.6: Self-pressurizing hydrogen tank model

The state of each control volume is characterized by nine variables: the temperatures of the gas, liquid, and interface (T_g, T_l, $T_{\text{interface}}$), the masses of the gas and liquid (m_g, m_l), the ullage pressure (P_g), and the volumes of the gas and liquid (V_g, V_l).
However, by assuming that dihydrogen gas behaves as an ideal gas and that the interface temperature remains at the saturation temperature, the system can be fully described using just four of these parameters. Specifically, the ideal gas law introduces a relationship between T_g, m_g, and V_g in Equation II.43. The saturation temperature, which corresponds to the interface temperature, is determined by the ullage pressure P_g. The combined volume of the gaseous and liquid phases (V_g and V_l) equals the total tank volume. During

the self-pressurization phase, the change in the total mass inside the tank corresponds to the fuel flow rate supplied to the engine, denoted as $\dot{m}_f$ (as described in Equation II.45).

$$P_g V_g = \frac{m R T_g}{M_{H_2}} \tag{II.43}$$

$$\begin{cases} V_g + V_l = V_{tank} \\ \dot{V}_g + \dot{V}_l = 0 \end{cases} \tag{II.44}$$

$$\dot{m}_g + \dot{m}_l = \dot{m}_f \tag{II.45}$$

The three control volumes under consideration are not thermally or mass-isolated; rather, they exhibit dynamic interactions through both heat and mass transfer. To model the temporal evolution of the thermodynamic state within these three interconnected control volumes, the principle of energy conservation—expressed in Eq. II.46—is applied individually to each volume, following the methodology outlined by Ring and later adapted by Ramos [**138**, **140**].

$$\dot{Q}_{net} + \dot{W} + \sum_{in} \dot{m}h - \sum_{out} \dot{m}h = \frac{dE_{cv}}{dt} \tag{II.46}$$

In this formulation:

- $\dot{Q}_{net}$ represents the net rate of heat transfer into the control volume,
- $\dot{W}$ denotes the net rate of work output from the control volume,
- $\sum_{in} \dot{m}h$ and $\sum_{out} \dot{m}h$ account for the energy flux associated with the mass flow entering and leaving the control volume, respectively,
- $\frac{dE_{cv}}{dt}$ describes the rate of change of energy within the control volume.

This approach provides a rigorous framework for analyzing the dynamic behavior of the system.

II.3.2.2 Energy Conservation Analysis for the Bulk-Liquid Hydrogen Volume

The energy conservation principle is initially applied to the bulk-liquid control volume. The bulk liquid volume is subject to two incoming heat fluxes: $\dot{Q}_{int,conv/LH_2}$, determined by solving the thermal resistance system outlined in Section II.30, and $\dot{Q}_{sl}$, representing the heat flux originating from the liquid-gas interface. The formulation of $\dot{Q}_{sl}$ (Eq. II.48) follows the natural convection heat transfer framework described in Eqs. II.18 and II.26, incorporating empirical coefficients derived from Ring's work [**138**]. In this context, L_c denotes the characteristic length, defined as the ratio of the liquid volume V_l to the interface area $S_{interface}$.

$$\dot{Q}_{net} = \dot{Q}_{int,conv/LH2} + \dot{Q}_{sl} \tag{II.47}$$

$$\begin{aligned}\dot{Q}_{sl} &= \frac{k_{lh2}Nu}{L_c} S_{interface}(T_{sat} - T_l) \\ &= \frac{k_{lh2} \cdot 0.27Ra^{0.25}}{L_c} S_{interface}(T_{sat} - T_l)\end{aligned} \tag{II.48}$$

The interface surface area, $S_{interface}$, is calculated using Equation II.52, where:

- w_s represents the width of the surface,
- S_{barrel} denotes the interface surface area within the tank's barrel section,
- V_{tank} is the total volume of the tank, and
- h_{ds} corresponds to the height of the dome interface in the bulkhead region.

$$w_s = 4\sqrt{(0.5 \cdot d_{tank})^2 - (d_{tank} \cdot (FL - 0.5))^2} \tag{II.49}$$

$$S_{barrel} = w_s \cdot l_{\text{barrel}}, \tag{II.50}$$

$$h_{d_s} = h_{\text{bulkhead}} \cdot \sqrt{1 - \left(\frac{h_l - \frac{d}{2}}{\frac{d}{2}}\right)^2} \tag{II.51}$$

$$S_{\text{interface}} = \begin{cases} S_{barrel} + \pi \left(\frac{w_s}{2}\right)^2, & \text{if hemispherical bulkhead} \\ S_{barrel} + w_s \cdot h_{d_s} \cdot \pi, & \text{if elliptical bulkhead} \end{cases} \tag{II.52}$$

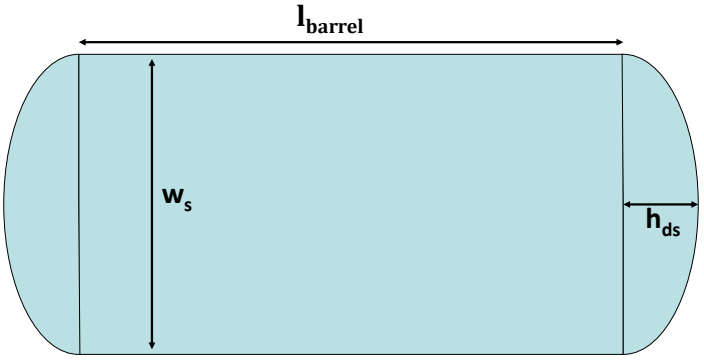

Figure II.7: Top-Down Representation of the Ullage-Liquid Hydrogen Interface Geometry at an Arbitrary Liquid Level

In this analysis, the work output rate associated with the bulk liquid is considered solely due to compression or expansion, as described in Eq.II.53. The rate of change in energy within the liquid phase is attributed to variations in internal energy, which arise from

changes in mass and temperature evolution, as detailed in Eq.II.57. In the absence of incoming mass flow into the liquid phase, four distinct outgoing mass flows are considered, each carrying an enthalpy h_l, as expressed in Eq. II.55:

- $\dot{m}_v$: The mass flow rate leaving the bulk liquid to enter the liquid-gas interface, where it undergoes evaporation.
- $\dot{m}_{fuel}$: The mass flow rate consumed by the engine for propulsion purposes. This term was not considered in the work of Ramos [**140**], as her study focused on self-pressurization during dormancy phases.
- $\dot{m}_{pres}$: In cases where the tank pressure falls below the required threshold, liquid hydrogen is extracted from the tank, vaporized in an external system, and reinjected into the ullage to maintain the minimum operational pressure.
- $\dot{m}_{boil}$: If the liquid temperature exceeds its saturation temperature, all incoming heat transfer to the bulk liquid is assumed to be entirely consumed by hydrogen boiling.

$$\dot{W} = P_l \dot{V}_l \tag{II.53}$$

$$\sum_{in} \dot{m}h = 0 \tag{II.54}$$

$$\sum_{out} \dot{m}h = \dot{m}_v h_l + \dot{m}_{pres} h_l + \dot{m}_{fuel} h_l + \dot{m}_{boil} h_l \tag{II.55}$$

$$\dot{m}_{boil} = \begin{cases} \dfrac{\dot{Q}_{int,conv/LH2}}{c_{p,l}(T_{sat} - T_l) + h_{vap} + (c_{p,g})\,(T_g - T_{sat})} & \text{if } T_l \geq T_{sat}(P_g), \\ 0 & \text{if } T_l < T_{sat}(P_g). \end{cases} \tag{II.56}$$

$$\frac{dE_{cv}}{dt} = \frac{dU}{dt} = \frac{d(m_l u_l)}{dt} = \dot{m}_l u_l + m_l c_{p,l} \dot{T}_l \tag{II.57}$$

By substituting Equations II.47 to II.57 into the energy conservation equation, the rate of change of the liquid temperature is derived, as presented in Equation II.58 :

$$\begin{aligned} \dot{m}_l u_l + m_l c_{p,l} \dot{T}_l &= \dot{Q}_{int,conv/LH2} + \dot{Q}_{sl} - P_g \dot{V}_g - \dot{m}_v h_l - \dot{m}_{pres} h_l - \dot{m}_{fuel} h_l - \dot{m}_{boil} h_l \\ \dot{T}_l &= \frac{\dot{Q}_{int,conv/LH2} + \dot{Q}_{sl} - P_g \dot{V}_g - \dot{m}_v h_l - \dot{m}_{pres} h_l - \dot{m}_{fuel} h_l - \dot{m}_{boil} h_l - \dot{m}_l u_l}{m_l c_{p,l}} \end{aligned} \tag{II.58}$$

Finally, the rate of change of the liquid volume, as expressed in Equation II.59, depends on both the evolution of the liquid mass—scaled by the liquid density—and the thermal expansion of the liquid hydrogen, which depend on the isobaric expansion coefficient of liquid hydrogen and the temperature rate of change. While often overlooked in previous studies, the temperature-dependent density variations of liquid hydrogen make thermal

expansion a non-negligible effect as ilustrated in Figure II.8. Earlier work conducted in this thesis, which excluded this term, led to an apparent "disappearance" of roughly 1% of the total fuel mass over the mission, underscoring the necessity of incorporating thermal expansion for precise modeling.

$$\dot{V}_l = \frac{\dot{m}_l}{\rho_l} + V_l \beta_l \dot{T}_l = -\frac{\dot{m}_v + \dot{m}_{fuel} + \dot{m}_{pres} + \dot{m}_{boil}}{\rho_l} + V_l \beta_l \dot{T}_l \tag{II.59}$$

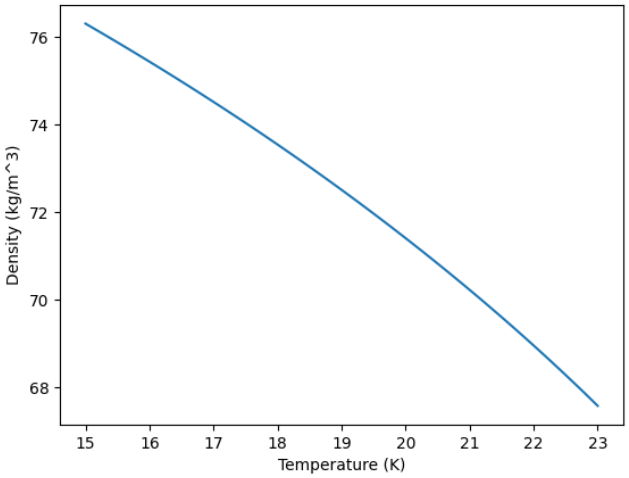

Figure II.8: Variation in Liquid Hydrogen Density as a Function of Temperature at 2 Bar

II.3.2.3 Energy Conservation Analysis for the Ullage Volume

In this section, the energy conservation principle is applied to the ullage, or gaseous hydrogen, control volume. The ullage is subject to two incoming heat fluxes: $\dot{Q}_{int,conv/GH_2}$, determined by solving the thermal resistance system outlined in Section II.30, and $\dot{Q}_{gs}$, representing the heat flux transferred from the ullage to the liquid-gas interface. The formulation of $\dot{Q}_{gs}$ (Eq. II.61) mirrors the heat transfer framework described in Equations II.18, differing only in the thermal conductivity term. This term is specifically evaluated for gaseous hydrogen at the mean temperature $T_m = \frac{T_g + T_{sat}}{2}$, which accounts for the thermal stratification between the ullage and the interface, as documented in the literature [**146**].

$$\dot{Q}_{net} = \dot{Q}_{int,conv/GH2} - \dot{Q}_{gs} \tag{II.60}$$

$$\begin{aligned} \dot{Q}_{gs} &= \frac{k_{gh2}(T_m) Nu}{L_c} S_{interface}(T_g - T_{sat}) \\ &= \frac{k_{gh2}(T_m) \cdot 0.27 Ra^{0.25}}{L_c} S_{interface}(T_{sat} - T_l) \end{aligned} \tag{II.61}$$

For the ullage, the work output rate is also considered solely due to compression or

expansion, as described in Eq.II.53, while the rate of change in energy is attributed to variations in internal energy, following Eq.II.57. Unlike the liquid phase, the ullage does not account for outgoing mass flow in this model, as the venting process is treated separately (see Section II.3.3). Additionally, hydrogen gas condensation is neglected, despite its potential significance—particularly after venting—due to the added complexity and uncertainty it introduces. Neglecting condensation provides a conservative estimate, as it implies that more hydrogen remains in gaseous form or is expelled during venting. In the absence of outgoing mass flow, two incoming mass flows are considered, each carrying an enthalpy h_g, as expressed in Eq. II.71:

- $\dot{m}_v$: The mass flow rate entering the ullage from the interface due to evaporation.
- $\dot{m}_{pres}$: The mass flow rate required to maintain the tank pressure above the minimum pressure differential.
- $\dot{m}_{boil}$: The mass flow of hydrogen boiling if the liquid is superheated.

$$\dot{W} = -P_g \dot{V}_g \tag{II.62}$$

$$\sum_{in} \dot{m}h = \dot{m}_v h_v + \dot{m}_{pres} h_g + \dot{m}_{boil} h_g \tag{II.63}$$

$$\sum_{out} \dot{m}h = 0 \tag{II.64}$$

$$\frac{dE_{cv}}{dt} = \frac{dU}{dt} = \frac{d(m_g u_g)}{dt} = \dot{m}_g u_g + m_g c_{v,g} \dot{T}_g \tag{II.65}$$

By substituting Equations II.70 to II.69 into the energy conservation equation, the rate of change of the ullage temperature is derived, as presented in Equation II.66 :

$$\begin{aligned} \dot{m}_g u_g + m_g c_{v,g} \dot{T}_g &= \dot{Q}_{int,conv/GH2} - \dot{Q}_{gs} - P_g \dot{V}_g + \dot{m}_v h_v + \dot{m}_{pres} h_g + \dot{m}_{boil} h_g \\ \dot{T}_g &= \frac{\dot{Q}_{int,conv/GH2} - \dot{Q}_{gs} - P_g \dot{V}_g + \dot{m}_v h_v + \dot{m}_{pres} h_g + \dot{m}_{boil} h_g - \dot{m}_g u_g}{m_g c_{v,g}} \end{aligned} \tag{II.66}$$

Moreover, as the total volume of the tank is constant (see equation II.44), the evolution of the ullage volume is :

$$\begin{aligned} \dot{V}_g &= -\dot{V}_l \\ &= \frac{\dot{m}_v + \dot{m}_{fuel} + \dot{m}_{pres} + \dot{m}_{boil}}{\rho_l} - V_l \beta_l \dot{T}_l \end{aligned} \tag{II.67}$$

II.3.2.4 Energy Conservation Analysis for the Interface

Finally, the same methodology is applied to the interface, which is defined as a conceptual control volume maintained at the saturation temperature but with negligible mass.

Consequently, the energy evolution of the interface is zero and there is no output work. Regarding heat fluxes, the interface receives one incoming flux from the ullage phase, $\dot{Q}_{gs}$, and releases one outgoing flux to the liquid phase $\dot{Q}_{sl}$. However, since condensation is neglected, the outgoing heat flux is constrained to be less than or equal to the incoming flux, such that $\dot{Q}_{sl} \leq \dot{Q}_{gs}$. Violating this constraint would imply energy creation at the interface, which would occur if condensation were considered, given its exothermic nature.

$$\dot{W} = 0 \tag{II.68}$$

$$\frac{dE_{cv}}{dt} = 0 \tag{II.69}$$

$$\dot{Q}_{net} = \dot{Q}_{gs} - \dot{Q}_{sl} \tag{II.70}$$

Regarding mass flows, the only contribution is the evaporating hydrogen mass flow, $\dot{m}_v$, which transitions from the liquid phase into the ullage. This mass flow enters the interface with an enthalpy of h_l and exits with an enthalpy of h_g, with the enthalpy difference detailed in Equation II.73.

$$\sum_{in} \dot{m}h = \dot{m}_v h_l \tag{II.71}$$

$$\sum_{out} \dot{m}h = \dot{m}_v h_g \tag{II.72}$$

$$h_g - h_l = c_{p,l}(T_{sat} - T_l) + h_{vaporisation} + (c_{v,g} + R_u)(T_g - T_{sat}) \tag{II.73}$$

By substituting Equations II.68 to II.73 into the energy conservation equation, $\dot{m}_v$ is derived from which $\dot{m}_g$ can be deduced as presented in Equation II.74 :

$$\begin{aligned} \dot{m}_g &= \dot{m}_v + \dot{m}_{pres} + \dot{m}_{boil} \\ \dot{m}_g &= \frac{\dot{Q}_{gs} - \dot{Q}_{sl}}{c_{p,l}(T_{sat} - T_l) + h_{vaporisation} + (c_{v,g} + R_u)(T_g - T_{sat})} + \dot{m}_{pres} + \dot{m}_{boil} \end{aligned} \tag{II.74}$$

II.3.2.5 Governing System of Ordinary Differential Equations for Tank Thermodynamic State: Formulation and Comparative Analysis with Prior Studies

The coupling of Equations II.58, II.66, II.67, and II.74 yields the system of **Ordinary Differential Equation (ODE)** governing the tank's thermodynamic state, as presented

in Equation II.75 :

$$\begin{cases} \dot{m}_g = \frac{\dot{Q}_{gs}-\dot{Q}_{sl}}{c_{p,l}(T_{sat}-T_l)+h_{vaporisation}+(c_{v,g}+R_u)(T_g-T_{sat})} + \dot{m}_{pres} + \dot{m}_{boil} \\ \dot{T}_g = \frac{\dot{Q}_{int,conv/GH2}-\dot{Q}_{gs}-P_g\dot{V}_g+\dot{m}_v h_v+\dot{m}_{pres}h_g+\dot{m}_{boil}h_g-\dot{m}_g u_g}{m_g c_{v,g}} \\ \dot{V}_g = \frac{\dot{m}_v+\dot{m}_{fuel}+\dot{m}_{pres}+\dot{m}_{boil}}{\rho_l} - V_l\beta_l\dot{T}_l \\ \dot{T}_l = \frac{\dot{Q}_{int,conv/LH2}+\dot{Q}_{sl}-P_g\dot{V}_g-\dot{m}_v h_l-\dot{m}_{pres}h_l-\dot{m}_{fuel}h_l-\dot{m}_{boil}h_l-\dot{m}_l u_l}{m_l c_{p,l}} \end{cases} \quad \text{(II.75)}$$

This model presents several key distinctions from the formulation proposed by Ramos in [**140**]:

- **Interface Heat Transfer Dynamics**: Ramos assumes the formation of a heated liquid hydrogen layer at the interface, which eventually inhibits heat transfer between the interface and the bulk liquid. However, in the context of an aircraft—where vibrations and sloshing are inevitable—this assumption is not retained. Instead, heat transfer between the interface and the bulk liquid is explicitly modeled, with the constraint that the heat flux from the ullage to the interface must exceed or equal the heat flux from the interface to the bulk liquid ($\dot{Q}_{gs} \geq \dot{Q}_{sl}$).

- **Engine Fuel Flow**: The model incorporates a mass flow term ($\dot{m}_{fuel}$), accounting for the liquid hydrogen being pumped to the engine for propulsion, which was not considered in Ramos' work.

- **Pressure Management through Vaporization**: The model includes a pressurization term $\dot{m}_{pres}$, representing the intentional vaporization of liquid hydrogen to maintain or increase tank pressure. This vaporization occurs in a separate system to avoid altering the temperature of the liquid fuel. The required mass flow rate is calculated using the ideal gas law to determine the amount of gas needed to achieve the minimum pressure threshold..

- **Temperature Constraint for liquid boiling**: During model resolution, the liquid temperature is constrained to remain at or below the saturation temperature. If the liquid temperature reaches saturation, all incoming heat flow into the liquid is assumed to be consumed by hydrogen boiling at the wall, as represented by the $\dot{m}_{boil}$ term.

II.3.3 Development of a methodology to estimate hydrogen loss during venting

The thermodynamic model presented in the two previous sections enables the estimation of the evolution of temperature, mass, and pressure of the hydrogen inside the tank during an aircraft mission. However, the tank structure is designed to withstand a specific maximum pressure differential between the interior of the tank and its external environment.

When the pressure rise due to hydrogen boil-off inside the tank reaches this maximum design pressure differential, a venting phase must be initiated. During this phase, a pressure relief valve opens to release gaseous hydrogen, thereby reducing the internal pressure.
The venting phase is modeled as an instantaneous gas ejection, occurring within a single time-step in the time-integration model. As such, interactions and mass exchange with the liquid hydrogen are neglected during this phase. The amount of gas released is precisely the quantity needed to reduce the pressure to the minimum allowable pressure inside the tank. This minimum pressure must always remain above the external pressure to prevent any air intake into the tank, which could result in air freezing in the cryogenic environment and potential damages to the cryogenic fuel distribution system. In previous work conducted in this thesis [**147**], the temperature of the ullage after venting was assumed to be equal to the saturation temperature. However, investigations revealed that in certain tank configurations, this assumption could lead to an increase in ullage mass during venting, which is physically impossible. This phenomenon occurs because the temperature after venting does not necessarily drop to the saturation temperature.

$$\sum_{out} \dot{m}h = \frac{dE_{cv}}{dt}$$

$$\dot{m}_g h_g = \dot{m}_g u_g + m_g c_{v,g} \dot{T}_g \tag{II.76}$$

The ideal gas law can also be derived :

$$\dot{P}_g V_g = \frac{R}{M_{H2}} (\dot{m}_g T_g + \dot{T}_g m_g) \tag{II.77}$$

By combining the two previous equations, the derivative of the ullage mass becomes II.78:

$$\dot{m}_g = \dot{P}_g V_g \frac{R}{M_{H2}} \frac{c_{v,g}}{c_{v,g} T_g + h_g - u_g} \tag{II.78}$$

As the variation of pressure during venting, equation II.78 can be solved in one or several step to determine the new ullage mass (100 steps implemented in the model as to have a venting time step much shorter than the thermodynamic model time step). The ideal gas law gives then the ullage temperature after venting.

II.3.4 Hydrogen tank model implementation into FAST-OAD

The tank thermal model developed in this chapter was integrated into the aircraft design tool, FAST-OAD, to enhance the **MDA** process for sizing hydrogen-powered aircraft. The existing **MDA** framework in **FAST-OAD** already performs time integration within the mission module, where flight physics equations are solved along the aircraft's mission trajectory. This integration enables the determination of instantaneous fuel consumption, which directly influences the evolution of the aircraft's fuel mass over time.

Given that the hydrogen tank thermodynamic model depends on both fuel consumption

and aircraft operational conditions—such as altitude and velocity (to assess heat inflow and pressure differentials)—an optimal solution would involve coupling the mission module with the tank thermodynamic model. However, such an integration would necessitate a complete redesign of the mission module, potentially compromising its compatibility with conventional kerosene-based aircraft configurations.
Additionally, the mission module incorporates an inner convergence loop to estimate the block fuel mass required for the mission. During early iterations, when the fuel mass has not yet converged, the mission module can still simulate the entire mission trajectory. Direct integration of the thermodynamic model would introduce challenges, particularly in scenarios where the block fuel is insufficient (e.g., when the tank is empty), as the physical model would fail to operate under such conditions.

To address these challenges, the estimation of hydrogen boil-off using the thermodynamic model was implemented in a separate post-processing module. This module leverages the converged block fuel data and the instantaneous engine fuel flow, along with the precise mission trajectory—all of which are computed by the mission module. This approach ensures compatibility with the existing framework while enabling accurate thermodynamic analysis of the hydrogen tank system.

Several variables within the thermodynamic model are exposed as **design variables**, enabling users to customize key parameters for the hydrogen tank system. These design variables include:

- **Insulation properties:**
  - Thickness,
  - Number of layers,
  - Number of nodes,
  - Material properties (defined either by a constant thermal conductivity or a temperature-dependent conductivity, particularly for foam materials).
- **Initial filling conditions:**
  - Liquid temperature,
  - Gas temperature and pressure.
- **Operational constraints:**
  - Maximum and minimum pressure differentials,
  - Tank surface emittance and absorptance,
  - Bulkhead shape (hemispherical or semi-elliptical)
  - Time-step for numerical integration.

The tank's actual dimensions are the only major variables not directly controlled by the user. Instead, users specify the number of tanks and the fuel distribution among them. This distribution is used to determine the tank dimensions, and the fuselage is stretched by the required length to accommodate the cryogenic tanks, with an additional one-meter allowance for the fuel distribution system. Notably, tanks are not placed in the tail section to maintain their cylindrical shape.
The volume of each tank is calculated with careful attention:

- The total mass of hydrogen,$m_{f/sizingBF}$, required for storage is initially determined by the fuel consumed by the engine, $m_{f/engine}$, which includes both the main mission and reserve fuel. This mass is further increased to account for boil-off losses:

$$m_{f/sizingBF} = m_{f/engine} + m_{f/boil-off} \tag{II.79}$$

- The mass $m_{f/sizingBF}$ must be converted into a volume of hydrogen for storage. However, the density of liquid hydrogen is highly temperature-dependent, and this temperature can also vary. To address this variability, a worst-case scenario is adopted: Before departure, when the tank is filled, the highest possible temperature of the liquid hydrogen—and thus the maximum volume it would occupy—is the saturation temperature, $T_{sat,LH2}$. This saturation temperature increases with pressure. The maximum pressure before departure is determined as the ground pressure, P_{ground} plus the maximum allowable pressure differential, ΔP_{max} :

$$V_{f,sizingBF} = m_{f/sizingBF} \cdot \rho_{H2}(T_{sat,H2}(P_{ground} + \Delta P_{max})) \tag{II.80}$$

- Finally, a margin mg_{tank} (typically around 3%), is added to the tank volume to account for both the systems immersed in the tank and to ensure that a fraction of gas is always present inside the tank:

$$V_{tanks} = \frac{V_{f,sizingBF}}{1 - mg_{tank}} \tag{II.81}$$

When multiple tanks are used, the fuel mass assigned to each tank—used to compute its volume—is determined by dividing the total hydrogen mass, $m_{f/sizingBF}$, by the fuel storage fraction allocated to each tank.

II.4 Conclusion and perspectives

In this chapter, a comprehensive review of existing methods for modeling thermal and fluid dynamic phenomena in cryogenic tanks was presented, categorizing the literature into two key areas: heat inflow estimation models and self-pressurization models for predicting hydrogen boil-off. Building on this foundation, a novel thermodynamic model was introduced, leveraging an enhanced electrical resistance analogy to estimate heat flux into the hydrogen tank's gaseous and liquid phases. By representing each heat transfer phenomenon as a thermal resistance, this approach enables precise, modular analysis of

the tank's thermal behavior. A significant advancement in this work is the division of the tank into multiple sections, each with its heat flux computed individually based on internal and external environmental conditions. This segmentation enhances the model's accuracy by accounting for localized thermal variations.

Additionally, the development of a three-control-volume self-pressurization model further advances the state of the art by independently modeling the bulk liquid, ullage, and their interface—departing from traditional homogeneous models. Inspired by space industry practices, this model provides a robust framework for deriving temporal equations that capture the evolution of the tank's thermodynamic state, particularly its internal pressure, during an aircraft mission. The resulting pressure dynamics form the basis for the subsequent venting phase modeling, which ensures the tank operates safely below its maximum pressure limit by estimating the necessary ullage venting.

Finally, the integration of this thermodynamic model into the FAST-OAD aircraft design tool marks a critical step forward in enabling the design of hydrogen-powered aircraft. By explicitly accounting for boil-off losses, this model facilitates a comprehensive evaluation of cryogenic fuel storage challenges, enabling critical trade-offs between enhanced insulation to minimize losses and weight reduction to improve overall aircraft efficiency. Additionally, it provides a framework for comparing different tank technologies at the aircraft level, supporting informed design decisions.

While the model introduced in this chapter incorporates innovative enhancements tailored for aircraft design, there remain opportunities for further refinement. Notably, certain physical phenomena were not included, such as liquid hydrogen boiling (when liquid temperature exceeds saturation temperature), wall boiling (a localized effect occurring when wall temperature surpasses local saturation conditions), and hydrogen gas condensation at interfaces or within suspended droplets. These phenomena were intentionally omitted—as in most previous studies for aircraft design—for several key reasons. First, they are relevant only under specific conditions. That means secondly that they exhibit threshold-dependent activation, which complicates the resolution of the system of equations (Equation II.30). Additionally, the complexity of accurately modeling these transient and localized phenomena presents significant challenges. Their modeling often relies indeed on empirical correlations or coefficients that are highly material-dependent [**148**, **146**]. Given the high complexity and cost associated with liquid hydrogen production, experimental data and validated empirical models remain scarce and largely confined to specialized industries or research laboratories, particularly those linked to the space or defense sectors. Historically, the lack of broader industrial interest in this field has further limited the public dissemination of such data. As a result, experimental validation of the proposed model was also significantly hindered by the limited availability of publicly accessible data on cryogenic tanks. Consequently, the validity of the model was evaluated based on its coherence with existing studies and the logical consistency of its results. This approach, while not ideal, provides a robust foundation for future validation efforts as more data becomes available.

It must be mentioned that, following the work presented in this chapter—much of which is documented in this publication [**147**]—subsequent studies have emerged, further exploring these critical topics. These developments underscore the growing interest and evolving understanding of cryogenic hydrogen storage systems in aeronautical applications.

In particular, the recent work of Adler and Martins [**149**] addresses several of the improvement points mentioned earlier. Adler developed a self-pressurization model based on the work of Ramos [**140**], which itself builds upon the model of Ring [**138**] and was later adapted by Estey et al. [**139**]. Consequently, this model shares many similarities with the one developed in this study, particularly in the logic behind deriving the system of ordinary differential equations that describe the evolution of the tank's internal state. Adler introduces however two significant enhancements: the explicit modeling of bulk boiling and gas condensation, which improves the model's fidelity, and the use of sigmoid activation functions to model the activation of these phenomena. This approach smooths the transitions of bulk boiling and condensation within the equation system, helping to overcome challenges that gradient-based optimizers might encounter. Additionally, through collaboration with Universal Hydrogen, Adler was able to validate his model against experimental data from an 890L prototype liquid hydrogen tank tested on the ground, leading to adjustments in some heat transfer coefficients to better match experimental results. Although Adler's model employs a simplified heat leak model compared to the one used in this study, it does not account for liquid hydrogen thermal expansion, and is not yet integrated into a global aircraft design sizing tool. The methodology he developed could certainly be used to improve the present work discussed in this chapter.

Another aspect of hydrogen tank sizing methodology, explored in Adler's work and numerous other studies (as discussed in Section II.2.2), but not yet addressed in this study, is the estimation of the tank's structural mass. Unlike conventional kerosene tanks—which contribute negligible weight as they are integrated into the wing structure—cryogenic hydrogen tanks introduce significant mass, thereby directly influencing the overall performance of the aircraft. Designing hydrogen-powered aircraft therefore requires a careful estimation of the tank's structural mass, as well as an analysis of the trade-offs between structural mass and hydrogen boil-off. This critical topic will be the focus of the next chapter of this thesis.

CHAPTER III

Development of a hydrogen tank structural sizing methodology compliant with CS-25 regulations for tank mass estimation

Résumé

Ce chapitre aborde le deuxième défi majeur de la conception des avions à hydrogène: le dimensionnement structurel et l'estimation de la masse des réservoirs cryogéniques. Alors que le chapitre précédent présentait un modèle thermodynamique pour évaluer les pertes par évaporation de l'hydrogène, ce chapitre se concentre sur l'estimation de la masse structurelle des réservoirs, un paramètre critique en raison de son impact significatif sur les performances globales de l'aéronef, du fait de leur poids dans une architecture propulsée à l'hydrogène.
Une revue des études existantes sur le dimensionnement des réservoirs d'hydrogène pour l'aéronautique est d'abord menée. Elle révèle que la plupart des travaux se concentrent sur des réservoirs cryogéniques non intégrés, dimensionnés principalement pour résister aux charges de pression, sans toujours prendre en compte les charges transmises par le fuselage ou les risques de flambage à quelques rares exceptions. Bien que certaines études aient abordé les réservoirs intégrés et ces charges transmises, elles utilisent pour cela des modèles haute fidélité, trop coûteux en calcul pour une phase de conception

préliminaire. À ce jour, les études comparant systématiquement les configurations de réservoirs intégrés et non intégrés restent rares. Elles peinent notamment à intégrer les contraintes mécaniques transmises par le fuselage suivant les règles de certification en vigueur pour les structures pressurisées en vol, tout en restant compatibles avec les exigences de la phase de conception préliminaire des avions.

Pour combler cette lacune, ce chapitre propose une méthodologie innovante dédiée au dimensionnement de réservoirs cylindriques cryogéniques (avec fonds hémisphériques ou semi-elliptiques), intégrant l'ensemble des contraintes identifiées. Cette approche repose, dans un premier temps, sur la détermination des charges — pression, effort tranchant, flexion et torsion — à l'aide d'un modèle simplifié de poutres mécaniques représentant la structure de l'avion. Ce modèle permet de calculer directement les charges appliquées aux réservoirs intégrés dans une configuration **T&W**, tandis que les réservoirs non intégrés sont modélisés via des facteurs de transmission définis par l'utilisateur, afin de prendre en compte la part des charges transmises par le fuselage.

La deuxième étape détaillée dans ce chapitre porte sur le dimensionnement proprement dit des composants du réservoir, à savoir sa paroi et sa structure de rigidification, composée de lisses (renforts longitudinaux) et de cadres (renforts circulaires). Ce dimensionnement s'appuie sur les exigences réglementaires de la CS-25, initialement conçues pour la conception des fuselages — eux aussi des structures pressurisées de forme circulaire. Conformément à ces règles :

- L'épaisseur de la paroi est calculée pour résister seule aux charges opérationnelles, sans contribution de la structure de rigidification.
- Le nombre de cadres et de lisses est déterminé par la contrainte de non-flambement de la paroi, jusqu'aux charges limites.
- Les sections des cadres et des lisses sont dimensionnées de sorte que la superstructure rigidifiante (renforts augmentés d'une portion de la paroi) reste dans le domaine élastique jusqu'aux charges limites, et qu'elle ne rompe pas sous les charges ultimes, en supposant que le reste de la paroi — potentiellement flambée — ne participe plus à la reprise des efforts.

Enfin, la dernière partie du chapitre présente le calcul de la masse totale du réservoir, basé sur les dimensions des composants préalablement déterminées. Elle expose également l'intégration de cette méthodologie dans FAST-OAD, permettant son utilisation dans un processus global de dimensionnement et d'optimisation des aéronefs.

Contents of this Chapter

III.1 Introduction 96
III.2 Hydrogen Tank structural sizing in literature 97
III.3 Development of a methodology to size a hydrogen tank and its stiffening structure respecting the CS-25 guidelines 102
III.3.1 Load Analysis for Hydrogen Tanks in Tube-and-Wing Aircraft Configurations 103
III.3.2 Development of a Methodology for Pre-sizing Structural Elements of Pressurized and potentially Integral Hydrogen Tanks in Aircraft . 105
III.3.2.1 Step 1 : Determination of the tank's wall thickness 105
III.3.2.2 Step 2: Optimization of Stringers and Frames Configuration to Prevent Buckling 107
III.3.2.3 Step 3: Sizing of Stringer and Frame Cross-Sections 107
III.4 Integration of the H2 Tank Weight Estimation Module into FAST-OAD . . 109
III.5 Conclusion and perspectives 110

III.1 Introduction

The previous chapter presented a thermodynamic model of a cryogenic hydrogen tank, which, when integrated into the aircraft sizing software FAST-OAD, enables the prediction of heat leak into the tank and the resulting hydrogen losses due to boil-off. While this model is essential for designing hydrogen-powered aircraft, the conceptual design phase must also include an estimation of the structural mass of the hydrogen tank.

Given that liquid hydrogen requires large storage volumes, it cannot be housed within the wing structure like conventional kerosene tanks. Instead, it must be stored in pressurized tanks, whose size and pressure constraints result in non-negligible weight. This structural mass must be accounted for early in the aircraft design process to ensure accurate performance assessments and trade-off evaluations.
This chapter aims to develop a hydrogen tank sizing methodology tailored for aircraft applications, drawing inspiration from the fuselage structural sizing methodologies that are strictly governed by certification regulations. The chapter will begin with a comprehensive review of previous studies on this topic to:

- Identify existing approaches and their applicability in conceptual aircraft design
- Assess how they can be integrated into a global multidisciplinary analysis and sizing methodology, and
- Determine potential areas for improvement.

The second part of this chapter focuses on the novel methodology developed in this study for estimating the mass of cylindrical cryogenic hydrogen tanks with hemispherical or semi-elliptical bulkhead in aircraft applications. The first section outlines the process used to determine the loads that such tanks must withstand, including pressure loads, shear flows, and bending or torsional moments. For integral tanks—those structurally integrated into the fuselage in a **T&W** configuration—these loads can be directly computed using a simplified beam model. Non-integral tanks are modeled through a user-defined transmission factor, which represents the proportion of the total fuselage load transmitted to the tank.

Once the loads are established, the subsequent section presents the sizing procedure for the tank, ensuring compliance with CS-25 regulations for pressurized airborne cylinders. This approach is analogous to the methodology employed for fuselage sizing. This begins with the formulation of an optimization problem to determine the tank wall thickness, which must remain elastic under operational loads—except for shear flow, where the limit load criterion applies.

Additionally, the tank wall must resist buckling up to the limit load, establishing a sizing criterion that dictates the number of stiffeners required. This is achieved by defining the maximum allowable pitch between circular frames and longitudinal stringers, as elaborated in the following section. The final part of the process described in this

chapter addresses the sizing of stiffener cross-sections according to CS-25 certification requirements. These regulations mandate that the super-stiffening structure must independently withstand limit loads while remaining in the elastic deformation region and ultimate loads without failure.

To conclude, this chapter describes the methodology for determining the tank wall thickness, the number and cross-section of stiffeners, and how the total tank mass is computed from these parameters. It also explains the integration of this methodology into the aircraft sizing tool **FAST-OAD**.

A substantial part of the methodology developed in this chapter for sizing the structural components of hydrogen tanks was originally presented in :

- R. Parello, Y. Gourinat, E. Benard, and S. Defoort. *Structural sizing of a hydrogen tank for a commercial aircraft.* In: Journal of Physics: Conference Series 2716 (1) (Mar. 2024), p. 012040. issn: 1742-6588, 1742-6596. doi: 10.1088/1742-6596/2716/1/012040.

.

III.2 Hydrogen Tank structural sizing in literature

Beyond the thermodynamic model, the **structural sizing** of hydrogen tanks represents another critical aspect of their design. Two primary tank configurations are considered:

- **Integrated Tanks**: In this configuration, the tank is fully incorporated into the aircraft's fuselage structure. Consequently, it must be designed to withstand not only the internal pressurization and mechanical loads associated with liquid hydrogen storage but also the structural loads of the fuselage itself.

- **Non-Integrated Tanks**: These are self-contained tanks with independent structural support, installed and secured within the fuselage. They can be considered as embedded, independent subsystems inside the aircraft. While they do not directly bear the fuselage's primary loads, some of these loads may still be transmitted through the tank's mounting system.

Brewer [**24**] considers the integral concept to be best in terms of mass and for inspection. He finds for example that for a maximum allowable stress in the structure of 40 000 psi, the fuel weight fraction in the integral tank was 0.927, compared to 0.855 for non-integral tank. Non-integral tanks can also represent a big safety hazard in the event of a leak in the fuselage, where the accumulation of hydrogen could lead to an explosion if not vented. Those reasons were the basis for Verstraete to also select an integral tank concept [**39**]. To achieve a precise design of such a tank, a finite element analysis is typically required, as demonstrated by Brewer for his aft-conical tank design. However, this approach requires

both precise knowledge of the structural loads imposed by the aircraft and computationally intensive analysis—a significant challenge during conceptual design, where the tank's final position is not yet defined and numerous design iterations are performed. Brewer addressed this issue for his forward fuselage tank by extrapolating load data from the aft tank analysis.
In the Cryoplane study [**33**], due to time constraints and the adoption of a minimal-change strategy, the tank was sized solely for pressure loads, without extending the analysis to include structural interactions. Similarly, Verstreate followed this simplified approach, sizing the tank based only on pressure considerations. For this purpose, he employed Barron's method [**150**], which determines the tank skin thickness as a function of the design venting pressure and material properties for a cylindrical tank with elliptical heads.
For the barrel section :

$$t_{wall/barrel} = \frac{\Delta P_{max} d_{tank}}{2\sigma_a e_w + 0.8 P_{max}} \tag{III.1}$$

For the tank bulkhead:

$$\begin{cases} t_{wall/bulkhead} = \frac{\Delta P_{max} d_{tank} K}{2\sigma_a e_w + 2P_{max}(K-0.1)} \\ K = \frac{1}{6}\left(2 + \frac{d}{d_1}\right) \end{cases} \tag{III.2}$$

Where:

- P_{max} is the **maximum venting pressure**,
- d_{tank} is the **tank diameter**,
- σ_a is the **allowable stress**,
- e_w is the **weld efficiency**,
- $\frac{d}{d_1}$ is the **ratio between the major and minor axes of the elliptical head**,
- $t_{wall/barrel}$ is the **tank wall thickness for the barrel section**,
- $t_{wall/bulkhead}$ is the **tank wall thickness for the bulkhead section**.

Winnefeld et al. [**48**] concentrated their research on non-integral, ellipsoid-shaped hydrogen tanks, establishing a methodology for sizing these configurations, as depicted in Figure III.1. This methodology relies on analytical equations to determine the tank's structural wall thickness, ensuring it can withstand internal pressure. The approach for cylindrical tanks is similar to the one used by Verstraete, while the one used for ellipsoidal shells involves iteratively solving for the wall thickness to meet a stress constraint defined by Grote and Feldhusen [**151**]. This iterative process ensures the tank's structural integrity under pressure loads. Their research revealed that ellipsoid tanks exhibit significantly lower gravimetric efficiency compared to other shapes, with the total tank mass potentially increasing by a factor of 3.5 as the height-to-width ratio changes from 1 to 1.5. Even minor variations ($\pm 5\%$) in this ratio can reduce gravimetric efficiency by up to 23%. Additionally, their analysis highlighted that the structural mass

constitutes 65% to 90% of the total tank mass, emphasizing the importance of selecting tank shapes that minimize structural weight relative to insulation weight. For a fixed hydrogen storage requirement, an optimal balance must be found between the tank's length and diameter, as larger diameters increase skin thickness requirements, while longer tanks demand more insulation.

Silberhorn et al. [**47**] further advanced this methodology by including conical-shaped tanks in their analysis, as illustrated in Figure III.2. Their approach for determining the tank wall thickness is based on the foundational work of Schwaigerer and Mühlenbeck [**152**]. Additionally, Silberhorn et al. validated their analytical model using finite element methods, achieving strong correlation between the analytical predictions and finite element results—particularly in the estimation of circumferential stress.

Adler and Martins, focusing specifically on pure cylindrical, non-integral tanks with hemispherical endcaps, employed a similar approach by sizing the inner tank wall thickness based on pressure load requirements. However, they extended their analysis to include vacuum-insulated tanks [**115**, **149**]. This involved designing an outer structural wall to maintain the vacuum within the double-walled insulation system. Since the atmospheric pressure on the tank's exterior exceeds the pressure in the vacuum region, the outer wall is subjected to compressive forces. Adler determined its thickness to withstand buckling loads, specifically calculating it as the minimum thickness required to remain within the elastic buckling region, based on the elastic buckling relationships outlined by Budynas [**153**]. This calculated thickness was then reduced by 20% to account for the additional stiffening provided by the tank's structural framework, although the stiffening structure itself was not explicitly sized in the analysis.

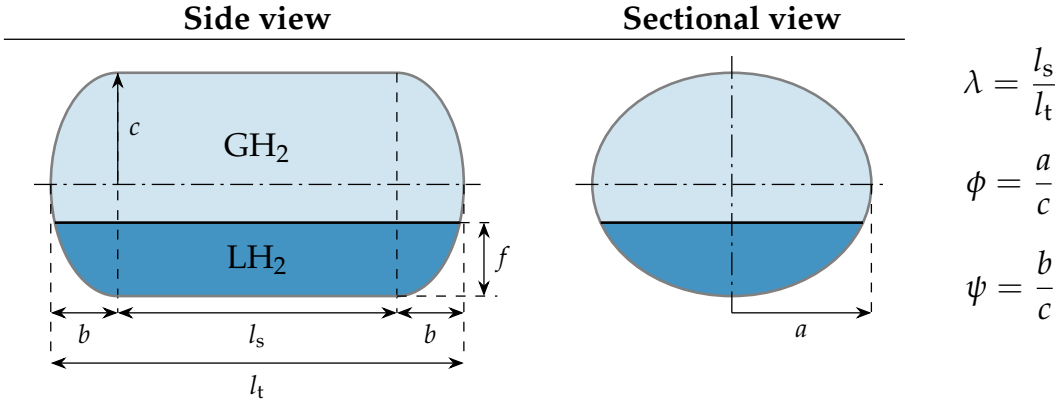

Figure 3. Nomenclature describing the geometric tank design.

Figure III.1: Ellipsoid tank representation used by Winnefeld [**48**]

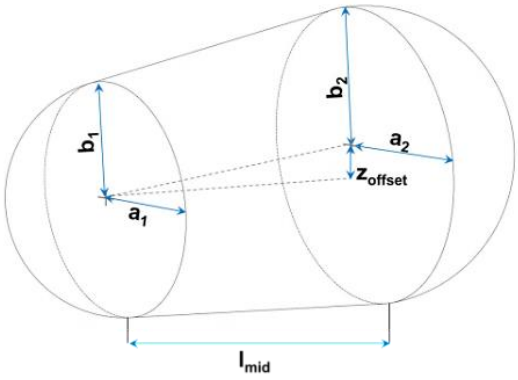

Figure III.2: Ellipsoid conical tank representation used by Silberhorn et al.[**47**]

Very few studies in the literature compare both integral and non-integral hydrogen tank concepts at the aircraft level, with notable exceptions such as Brewer [**24**] and Onorato et al. [**51**]. Onorato's approach builds upon Verstraete's model (Eq.III.1) for calculating tank skin thickness but further incorporates the weight of the tank's support structure, as illustrated in FigureIII.3. For non-integral tanks, the support weight is derived from Brewer's work [**24**], while for integral tanks, the mass of the stiffening structure is assumed to be equivalent to the mass of the stringers, frames, and respective skin thickness already accounted for in the fuselage structural sizing, effectively integrating the tank structure into the airframe. Consistent with Brewer's findings, Onorato concludes that integral tanks offer a significant mass advantage at the aircraft level. Specifically, an integral tank configuration can reduce the **MTOW** by approximately 3% for a short- to medium-range aircraft compared to a non-integral tank design. This underscores the potential benefits of integral tank integration in optimizing overall aircraft mass and efficiency.

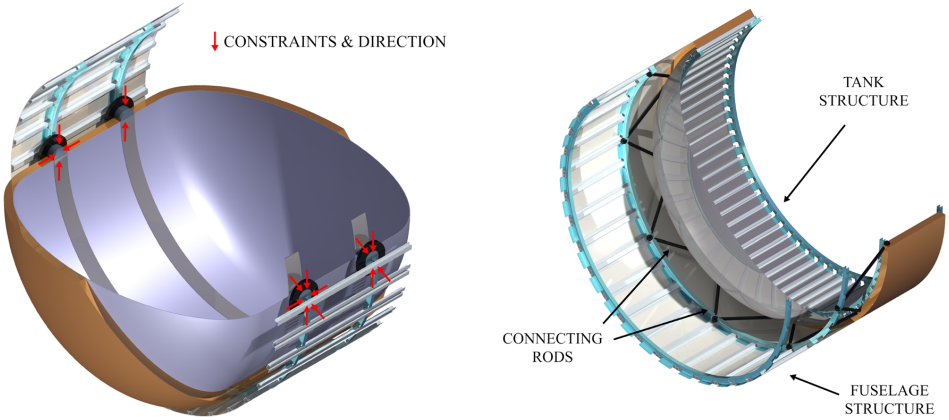

(a) Non-integral tank.

(b) Integral tank.

Figure III.3: Artist impression of tank attachments options considered by Onorato in [**51**]

One of the few attempts to conduct a high-fidelity analysis of an aircraft hydrogen tank is presented by Gomez and Smith [**130**]. Their hydrogen aircraft concept features two integral hydrogen tanks, both modeled using the CATIA CAD software: a conical tank located at the rear and an almost cylindrical tank positioned in front of the passenger

cabin. The front tank includes a side catwalk to provide cockpit access, as shown in Figure III.4. By employing finite element analysis and incorporating the catwalk, Gomez and Smith also modeled the stiffening structure and accounted for the bending and shear loads transmitted from the fuselage to the tank during maneuvers. This comprehensive approach enables a more accurate assessment of the tank's structural behavior and its integration within the aircraft. However, due to its high computational cost, such detailed finite element analysis is challenging to incorporate into the conceptual design phase, where rapid iteration and simplified models are typically preferred.

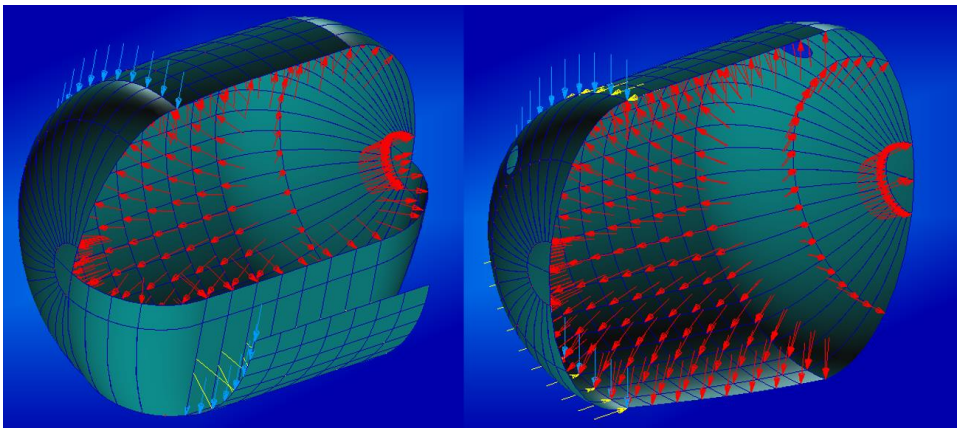

Figure III.4: Tanks CATIA model created by Gomez and Smith [**130**]

In summary, numerous studies have developed models for sizing cryogenic hydrogen tanks for aircraft applications. However, few have addressed both integral and non-integral tank configurations. Most research has focused on non-integral tanks, which are typically sized to withstand pressure loads alone, without accounting for loads transmitted by the fuselage or buckling effects. Adler's work is an exception, as it sizes the outer wall for buckling, but it does not include the sizing of the stiffening structure itself. Studies examining integral tanks have considered these phenomena, but only within high-fidelity models, which are computationally intensive and thus unsuitable for conceptual design.

The objective of this chapter is to develop a new hydrogen tank sizing methodology capable of estimating the mass of both cylindrical integral and non-integral tanks with hemispherical or elliptical bulkheads. This methodology will size both the tank wall and stiffening structure, accounting for pressure, bending, shear, and torsional loads transmitted by the fuselage. The approach is inspired by methods used for sizing pressurized fuselage structures in conventional tube-and-wing (TAW) aircraft, ensuring compliance with CS-25 certification standards for pressurized structures.

Due to time constraints and complexity, this study does not include the sizing of double-wall vacuum-insulated tanks or tank fixation systems for tube and wing or blended wing-body configurations. As a result, the exact estimation of load transmission between the fuselage and the tank for non-integral tanks remains unresolved.

III.3 Development of a methodology to size a hydrogen tank and its stiffening structure respecting the CS-25 guidelines

The primary objective of this method is to size a cryogenic hydrogen tank to estimate its mass while ensuring compliance with CS 25.305 (Strength and Deformation) and CS 25.307 (Proof of Structure) regulations [**154**], which apply to pressurized cylinders. This involves dimensioning the tank wall thickness and sizing the tank stiffening structure, consisting of stringers (longitudinal stiffeners) and frames (circular stiffeners), see Figure III.5.

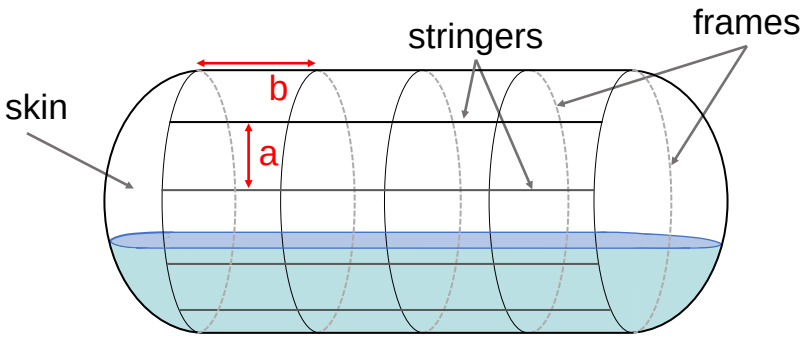

Figure III.5: Representation of a cylindrical hydrogen tank and its stiffening structure.

The sizing process adheres to the load terminologies defined by CS 25.301 (Loads) and CS 25.303 (Factor of Safety), which include:

- **Operational Load (OL)**: Loads encountered during normal operations.
- **Ultimate Load (UL)**: Defined as

$$UL = 2 \times OL \tag{III.3}$$

- **Limit Load (LL)**: Defined as

$$LL = \frac{UL}{1.5} \tag{III.4}$$

The methodology used to size cryogenic hydrogen tanks follows a structured approach analogous to fuselage sizing, as both are pressurized vessels onboard an aircraft. The sizing process—applicable to both fuselage and tank—consists of three sequential steps with the following logic:

- **Determination of Applied Loads**: Calculation of pressure loads, shear forces, and bending and torsion moments that the tank and its stiffening structure must withstand.

- **Sizing of the Tank Skin Thickness**: The skin is initially designed to withstand operational loads—including pressure, shear stress, and bending moments—while remaining elastic and free from buckling, without considering the stiffening structure.
- **Sizing of the Stiffening Structure**: The stiffening elements—stringers and frames—are sized to support all loads beyond operational levels, ensuring they prevent buckling at operational loads, remain elastic at limit loads (LL), and avoid failure at ultimate loads (UL). Above operational loads, the skin is assumed to have buckled and thus no longer contributes to load-bearing for the most part.

Unlike many previous models found in the literature, this methodology explicitly accounts for stiffening structure sizing and the various load cases specified by CS-25. Consequently, the resulting tank design may differ significantly from those derived from less comprehensive approaches.

III.3.1 Load Analysis for Hydrogen Tanks in Tube-and-Wing Aircraft Configurations

The initial step in sizing the tank involves determining the applied loads, which consist of three primary types:

- **Pressure load**: acts perpendicular to the tank skin and corresponds to the pressure differential between the tank's interior and its external environment—whether the atmosphere or the fuselage interior, particularly in the case of a non-integral tank. The pressure differential—the difference between the internal tank pressure and the external environment—is considered an input parameter. For non-integral tanks, it is assumed that the fuselage section containing the tank is not pressurized.
- **Bending and torsion moment load**: transmitted by the fuselage onto the tank.
- **Shear stress load**: Shear flow is also transmitted by the fuselage onto the tank.

If the pressure load is treated as a direct design variable, it becomes necessary to determine the bending and shear loads that the tank must withstand. At the current stage, this determination can only be performed for fully integral tanks within a conventional tube-and-wing (TAW) aircraft configuration. Cylindrical integral tanks are not envisaged for the blended-wing-body (BWB) configuration, and the portion of loads and moments transmitted to non-integral tanks depends strongly on the specific fixation mechanisms used to mount these tanks within the airframe—an aspect that lies beyond the scope of this study. For integral tanks, the full load is assumed to be transmitted through the tank structure, whereas for non-integral tanks, the load transfer is represented by a modulation factor defining the fraction of total loads transmitted to the fuselage. The sensitivity of both tank and overall aircraft mass to this modulation factor will be investigated in Chapter IV.

To evaluate the bending moment and shear load, the aircraft is modeled as a beam, as illustrated in Figure III.6, in accordance with the Kirchhoff beam theory. The weights of the various aircraft components and subsystems are distributed along the longitudinal axis x, ranging from 0 to $L_{fuselage}$, which corresponds to the total fuselage length. The fuselage, payload, and tank are each represented as distributed loads, with Figure III.6 providing an example for the fuselage weight. The aerodynamic lift is modeled as a concentrated force acting at 25% of the mean aerodynamic chord (MAC). Based on this representation, the distributions of bending moment along the x-axis and the corresponding shear stresses can be determined :

$$M_b(x) = \sum_i nm_i g(x - CG_i) + \sum_i \int_{X_{start}}^{min(x,X_{end})} \frac{nm_i g(x-y)}{l_i} dy \tag{III.5}$$

$$T_z(x) = \sum_i nm_i g + \sum_i \int_{X_{start}}^{min(x,X_{end})} \frac{nm_i g(x-y)}{l_i} dy \tag{III.6}$$

Here, n denotes the load factor, CG_i the x-coordinate of the center of gravity of element i, m_i its mass, and l_i its length, where applicable. For both load types, the first summation term represents the discrete (point) weights located upstream of position x, while the second term accounts for the distributed weights starting before x. Only the weights situated ahead of the considered position are included in the calculation. The bending and shear loads naturally depend on the load factor n. Although this load factor varies throughout the flight, a limit load factor is determined within **FAST-OAD** in accordance with the *CS-25* regulations.
For each load type (bending moment and shear flow), the maximum value reached over the x-span where the tanks are located is used for sizing purposes. Each tank must therefore be capable of withstanding the maximum bending moment and shear stress occurring within the fuselage section in which it is installed. Consequently, when multiple tanks are present, they may be sized according to different maximum load levels.

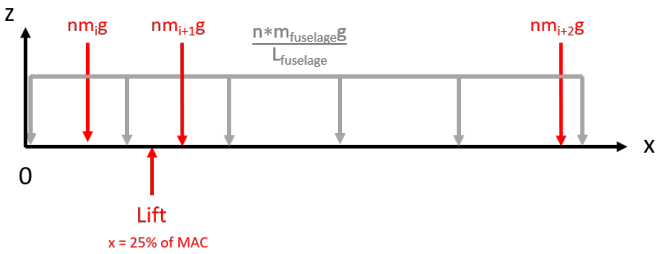

Figure III.6: Beam model of an aircraft

III.3.2 Development of a Methodology for Pre-sizing Structural Elements of Pressurized and potentially Integral Hydrogen Tanks in Aircraft

III.3.2.1 Step 1 : Determination of the tank's wall thickness

Once the bending moments and shear loads have been determined, the sizing of the tank skin can be carried out. This step requires the computation of the stress tensor within the skin.
As previously stated, the skin is sized to withstand the operational loads only, i.e., without accounting for the contribution of the stiffening structure. However, since the shear flow in the tank circulates exclusively within the skin, the skin must, in this specific case, be sized directly to the limit load. The shear flow originates from the shear stress, which depends on the angle θ (see Figure III.7), as well as on the torsional moment, and is expressed in equation III.7:

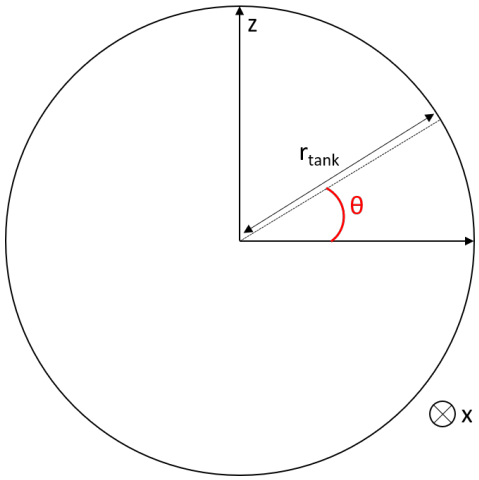

Figure III.7: Tank's section parametrization

$$\sigma_{xy}(\theta) = \sigma_{yx}(\theta) = \frac{T_{z,maxLL}cos(\theta)}{t_{skin}\pi r_{tank}} + \frac{M_{torsion,LL}}{2\pi t_{skin} r_{tank}^2} \tag{III.7}$$

where t_{skin} is the tank skin thickness, r_{tank} the tank radius, M_{torsion} the torsional moment, and $T_{y,\text{max}}$ the maximum shear stress along the tank, computed under the limit load condition.
In addition to the shear flow, both the bending moment and the internal pressure contribute to the overall stress state. The resulting stress tensor is expressed as **[155]**:

$$\Sigma(\theta) = \begin{pmatrix} \frac{\Delta P_{OL} r_{tank}}{t_{skin}} & \sigma_{xy}(\theta) & 0 \\ \sigma_{xy}(\theta) & \frac{\Delta P_{OL} r_{tank}}{2t_{skin}} - \frac{M_z sin(\theta)}{\pi t_{skin} r_{tank}^2} & 0 \\ 0 & 0 & 0 \end{pmatrix} \tag{III.8}$$

The stress tensor is a function of the angle θ. For sizing purposes, it is assumed that the critical points on the tank section correspond to one of three positions: $\theta = 0$, $\theta = \pi/2$, or $\theta = -\pi/2$. Only these three locations are considered in the subsequent optimization

process, in which the objective is to minimize the tank skin mass while ensuring that the Von Mises stress criterion is satisfied at all three points.

$$\begin{aligned} \underset{t_{skin}}{\text{minimize}} \quad & \textit{skin weight} \\ \text{subject to} \quad & \sigma_{VM}(0) \leq \sigma_e, \\ & \sigma_{VM}(\pi/2) \leq \sigma_e \\ & \sigma_{VM}(-\pi/2) \leq \sigma_e \end{aligned}$$

Here, σ_{VM} denotes the Von Mises stress, and σ_e is the elastic limit of the skin material. Since the Von Mises criterion can be overly conservative in certain cases and does not always accurately capture the behavior of composite materials, an alternative sizing criterion is introduced and can replace the Von Mises criteria in the optimization problem presented above. This new criterion is based on strain rather than stress. Although it was originally developed for the structural sizing of composite materials, it is increasingly applied to metallic and even ceramic materials. One of its key advantages is the integration of damage tolerance criteria, making it particularly well-suited for hydrogen tanks prone to embrittlement. Discussions with industry experts indicate that aircraft manufacturers frequently use this approach during preliminary sizing, and regulatory authorities are currently evaluating its validity for certification purposes. The criterion is expressed as follows, where $\epsilon_I, \epsilon_{II}, \epsilon_{III}$ denote the principal strains (i.e., the eigenvalues of the strain tensor):

$$-3 * 10^{-3} \leq \epsilon_{III} \leq \epsilon_{II} \leq \epsilon_I \leq 4.5 * 10^{-3} \tag{III.9}$$

For the hemispherical bulkhead, only the internal pressure load is considered. The bulkhead skin thickness, t_{bulkhead}, is sized to satisfy two criteria simultaneously: it must be sufficient to withstand the limit pressure load while remaining elastic, and it must also resist the ultimate pressure load without failure. This sizing requirement leads to the expression given in Equation III.10.

$$t_{bulkhead} = max(\frac{\Delta P_{LL} r_{tank}}{2\sigma_e}, \frac{\Delta P_{UL} r_{tank}}{2\sigma_b}) \tag{III.10}$$

If the bulkhead is semi-elliptical, the stress can be computed either in the circumferential (parallel) direction, σ_β, or in the meridional direction, σ_ϕ, using the expressions given in Equations III.11 and III.12. The determination of the bulkhead skin thickness is then performed by solving the minimization problem defined in Equation III.3.2.1. This is equivalent to finding the minimum skin thickness for which both the meridional and circumferential (parallel) stresses remain below the elastic limit under the limit pressure load, while simultaneously remaining below the ultimate stress under the ultimate pressure load.

$$\textit{Ellipsoidal meridian stress, } \sigma_\phi = \frac{\Delta P}{2bt_{skin}} \sqrt{r^2(b^2 - a^2) + a^4} \tag{III.11}$$

$$\textit{Ellipsoidal parallel stress, } \sigma_\beta = \frac{\Delta P}{2bt_{skin}} \frac{2r^2(b^2-a^2)+a^4}{\sqrt{r^2(b^2-a^2)+a^4}} \tag{III.12}$$

where

- a — semi-major axis,
- b — semi-minor axis,
- $r = R_2 \sin\phi$, with R_2 are the radius of curvature in the circumferential (parallel) direction and ϕ the angle along the meridional direction.

$$\begin{aligned} \underset{t_{bulkhead}}{\text{minimize}} \quad & \textit{bulkhead weight} \\ \text{subject to} \quad & \sigma_\phi(\Delta P_{LL}) \leq \sigma_e, \\ & \sigma_\phi(\Delta P_{UL}) \leq \sigma_b \\ & \sigma_\beta(\Delta P_{LL}) \leq \sigma_e, \\ & \sigma_\beta(\Delta P_{UL}) \leq \sigma_b \end{aligned}$$

III.3.2.2 Step 2: Optimization of Stringers and Frames Configuration to Prevent Buckling

After the preceding step, the skin thickness is fixed. It then becomes possible to determine the maximum allowable stress and shear that the skin can withstand before buckling, which also depends on the stiffening structure, specifically on the spacing of frames and stringers (cf. Figure III.5). Assuming that the skin must not buckle under the operational load and adopting the approximation $b = 4a$, this leads to the following expression [**155**]:

$$\frac{\sigma_{comp,maxOL}}{\sigma_{comp,buckling}} = \frac{\frac{M_{z,OL}}{t_{skin}\pi r_{tank}}}{3.3\frac{t_{skin}^2 E}{a^2(1-\nu^2)}} \leq 1 \tag{III.13}$$

$$\frac{\tau_{shear,max}}{\tau_{shear,buckling}} = \frac{\frac{T_{max,OL}}{t_{skin}\pi r_{tank}} + \frac{M_{torsion,OL}}{t_{skin}2\pi r_{tank}^2}}{4.9\frac{t_{skin}^2 E}{a^2(1-\nu^2)}} \leq 1 \tag{III.14}$$

Equations III.13 and III.14 provide the maximum allowable stringer spacing, a, which must be respected to prevent buckling under the operational load. The stringer pitch is then set to this value, while the frame pitch is taken as four times a, ensuring that the buckling model for each element of the stiffening structure remains conservative. This approach is supported by the asymptotic behavior of a rectangular-shaped shell under buckling, where the length-to-width ratio exceeds 3 [**155**]. Consequently, these criteria determine the total number of frames and stringers in the stiffening structure.

III.3.2.3 Step 3: Sizing of Stringer and Frame Cross-Sections

Above the operational load, the skin may buckle ; therefore, it is conservatively assumed that it no longer carries any load. However, not all of the skin buckles, particularly in

regions adjacent to the stiffener attachments. To account for this, a "superstiffening" structure is defined, consisting of the frames and stringers augmented by a portion of the tank skin, in accordance with Von Karman meta-stiffener concept, mentioned in the CS-25 [**154**]. For each stiffener, this corresponds to a skin area with a width equal to 15 times the skin thickness, centered on the stiffener attachment point (cf. Figure III.8). The superstiffening structure must be capable of withstanding the limit load while remaining within the elastic regime and must also remain below the ultimate stress under the ultimate load.

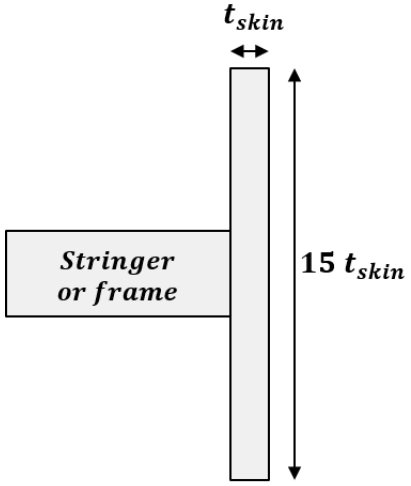

Figure III.8: Example of a super stiffener's section

These constraints allow for the sizing of the frame and stringer cross-sections. Since the frames primarily support the circumferential stress and the stringers the longitudinal stress, only the normal stress is considered for both types of stiffeners:

$$\sigma_{xx,super\ \ stringer}(\theta) = \frac{\Delta P \pi r_{tank}^2}{N_{stgr} A_{superstgr}} - \frac{M_z sin(\theta)}{I_z} \tag{III.15}$$

$$\sigma_{xx,super\ \ frame} = \frac{\Delta P L_{tank} r_{tank}}{N_{frm} A_{superfrm}} \tag{III.16}$$

Here, I_z represents the moment of inertia, N_{frm} and N_{stgr} are the number of frames and stringers, respectively, and A_{superfrm} and $A_{\text{superstgr}}$ correspond to the areas of a single super frame and super stringer. Each super stiffener area is equal to the area of the frame or stringer itself augmented by a portion of the skin, specifically $15\,t_{\text{skin}}^2$. Analogously to the skin sizing procedure, the stiffener cross-sectional area is determined through the following optimization loop:

$$
\begin{aligned}
\underset{A_{stringer}, A_{frame}}{\text{minimize}} \quad & \textit{tank weight} \\
\text{subject to} \quad & \sigma_{VM,LL}(\pi/2) \leq \sigma_e, \\
& \sigma_{VM,LL}(-\pi/2) \leq \sigma_e \\
& \sigma_{VM,UL}(\pi/2) \leq \sigma_{break} \\
& \sigma_{VM,UL}(-\pi/2) \leq \sigma_{break}
\end{aligned}
$$

III.4 Integration of the Hydrogen Tank Weight Estimation Module into FAST-OAD

Upon completion of the three previously outlined steps, the skin thickness of both the barrel and the bulkhead, as well as the number, type, and cross-sectional properties of the frames and stringers, are established. Consequently, it is now feasible to determine the structural weight of the tank in equation III.17

$$
\begin{aligned}
m_{tank} = & L_{\text{tank}}\, A_{\text{stringer}}\, \rho_{\text{stringer}}\, N_{\text{stringer}} \\
& + N_{\text{frame}}\, A_{\text{frame}}\, \rho_{\text{frame}}\, 2\pi r_{\text{tank}} \\
& + 2\pi r_{\text{tank}}\, L_{\text{tank}}\, t_{\text{wall}}\, \rho_{\text{wall}} \\
& + \begin{cases} \frac{4}{3}\pi r_{\text{tank}}\, t_{\text{bulkhead}} \rho_{\text{wall}} & \textit{if hemispheric bulkhead} \\ \frac{\pi\,(2r_{\text{tank}})^2}{8}\left[2 + \frac{1}{4\varepsilon}\ln\left(\frac{4\varepsilon\times 0.5+2}{2-\sqrt{3}}\right)\right] t_{\text{bulkhead}} \rho_{\text{wall}} & \textit{if semi-elliptical bulkhead, with } \epsilon = 0.866 \end{cases} \\
& + m_{insulation}
\end{aligned}
\tag{III.17}
$$

This methodology was subsequently integrated into the global aircraft sizing tool **FAST-OAD**. The module is embedded within the preexisting weight estimation discipline of the program, specifically within the mass breakdown and airframe mass module. Table III.1 summarizes the inputs required by the model, distinguishing between:

- User-defined variables, such as the tank's maximum pressure differential, sizing criteria, load transmission factor for non-integral tanks, and the materials used for insulation and structural components (which may differ for the tank wall, frames, and stringers);
- Coupled variables, which are computed in separate, preexisting **FAST-OAD** discipline modules. This includes the tank dimensions, which are determined in the geometry discipline to accommodate the required volume of hydrogen, as well as the mass and spatial position of all aircraft components necessary for the load estimation process.

It is important to note that, since the load determination process relies on the tank mass to compute shear flow and bending moments along the fuselage, this variable serves as

Table III.1: Hydrogen tank sizing process inputs

	Inputs	Unit	Origin
Tank Design	Tank length	m	Geometry module
	Tank diameter	m	Geometry module
	Bulkhead shape		User
	Max ΔPressure	Pa	User
	Sizing criteria		User
Tank Insulation	Thickness	mm	User
	Density	$kg.m^{-3}$	User
Tank material	Density	$kg.m^{-3}$	User
	Poisson ratio		User
	Young modulus	GPa	User
	Elastic limit stress	MPa	User
	Elastic break stress	MPa	User
Load computation	Fuselage mass	kg	Weight module
	Subsystem and Furniture mass	kg	Weight module
	Wing mass	kg	Weight module
	Engine mass	kg	Weight module
	Vertical tail mass	kg	Weight module
	Horizontal Tail mass	kg	Weight module
	Landing gear mass	kg	Weight module
	Payload mass	kg	Weight module
	Tank mass	kg	Tank Weight module
	Fuselage length	m	Geometry module
	Subsystem and Furniture CG	m	Geometry module
	Wing CG	m	Stability module
	Engine CG	m	Geometry module
	Vertical tail CG	m	Geometry module
	Horizontal Tail CG	m	Geometry module
	Landing gear CG	m	Geometry module
	Payload CG	m	Geometry module
	Bending transmission factor	%	User
	Shear transmission factor	%	User
	Torsion transmission factor	%	User

both an input and an output of the model. Consequently, the openMDAO driver of **FAST-OAD** must iteratively resolve this dependency.

III.5 Conclusion and perspectives

This chapter has addressed a fundamental challenge in the design of hydrogen-powered aircraft: the structural sizing and mass estimation of cryogenic hydrogen tanks. Building upon the thermodynamic model introduced in the previous chapter—which was integrated into FAST-OAD to predict heat leakage and hydrogen boil-off—the present study advances this framework by developing a methodology for estimating

the structural mass of hydrogen tanks, a critical parameter in the conceptual design phase.

A comprehensive review of existing studies on hydrogen tank sizing for aircraft applications was first conducted. This review highlighted that while numerous studies have proposed both low- and high-fidelity methods for estimating tank mass, most have focused on non-integral tanks, which are typically designed to withstand pressure loads alone, often neglecting loads transmitted by the fuselage or buckling effects (with the notable exception of Adler's work [**115**]). Although some studies have addressed integral tanks and considered these phenomena, they have done so using high-fidelity models, which are computationally demanding and impractical for conceptual design. Additionally, few studies have attempted to model and compare both configurations.

To address these gaps, a novel methodology was developed for sizing cylindrical cryogenic hydrogen tanks with hemispherical or semi-elliptical bulkheads. The methodology includes the determination of loads—such as pressure, shear, bending, and torsional moments—using simplified beam models for integral tanks in a **T&W** aircraft configuration, and user-defined transmission factors for non-integral tanks. Central to this methodology is its compliance with CS-25 regulations. It ensures, for instance, that the tank wall thickness is optimized to withstand operational loads, while the stiffener distribution is designed to prevent the tank wall buckling. The process also involves formulating an optimization problem for sizing stiffeners, ensuring they can independently endure limit loads within the elastic deformation range and ultimate loads without failure.

Finally, this chapter demonstrates how the total tank mass is derived from these parameters and details the integration of the methodology into FAST-OAD, facilitating its application within a broader aircraft sizing and optimization framework. By combining in FAST-OAD the developped methodology with the thermodynamic model of cryogenic tank detailed in the previous chapter, this work provides a comprehensive and practical tool for assessing the feasibility and performance of hydrogen-powered in **T&W** aircraft. The next chapter will therefore focus on parametric studies of those aircraft to highlight the aircraft performance sensibilities to hydrogen tank design variables.

While the methodology developed in this chapter provides a robust foundation for estimating the structural mass of cryogenic hydrogen tanks, numerous possibilities for further refinement remain. To enhance the model's accuracy and reliability, future work should prioritize the following improvements: First, a thorough validation of the model is essential to confirm that all relevant physical phenomena have been appropriately accounted for and that no critical aspects have been overlooked. Second, the representation of non-integral tanks remains incomplete without a detailed model of the tank fixation system. Although modeling such systems in the conceptual design phase is challenging due to their complexity and the precision required, incorporating this detail would enable a more accurate determination of the loads transmitted from the fuselage to the tank in non-integral configurations. This refinement would facilitate more precise comparisons between integral and non-integral tank designs. Additionally, the sizing and mass esti-

mation of auxiliary tank subsystems—such as support structures, insulation, and thermal management systems—could have a significant impact on overall aircraft performance. These elements should be considered in future iterations of the model to ensure a comprehensive assessment, but several studies on that topic, such as the one from Sarr et al. [**156**], have already promising results that could be exploited. Finally, the methodology for estimating loads applied to tanks should be extended to **BWB** configurations. However, this extension presents substantial challenges, as it requires both the development of a fixation system model for non-integral hydrogen tanks and a clear definition of what constitutes an integral cylindrical tank within a blended wing body architecture. Both tasks are inherently complex and demand careful consideration. Addressing these areas in future research will further enhance the fidelity and applicability of the model, ultimately contributing to the advancement of hydrogen-powered aircraft design and the broader goal of sustainable aviation.

CHAPTER IV

Design Exploration of a Tube and Wing Hydrogen Aircraft through Parametric Studies

Résumé

Le premier chapitre de cette thèse a présenté un modèle thermodynamique de réservoir cryogénique. Ce modèle est capable d'estimer les pertes d'hydrogène au cours d'une mission d'un avion qui sont causées par les fuites thermiques dans le réservoir et qui entraînent l'évaporation de l'hydrogène liquide. Le chapitre suivant s'est concentré sur l'élaboration d'une méthodologie de dimensionnement structurel des réservoirs d'hydrogène, permettant d'en estimer la masse. Ces modèles et méthodes ont été intégrés à l'outil de dimensionnement d'aéronefs **FAST-OAD**, dont le module géométrique a été adapté pour accueillir des réservoirs d'hydrogène en position arrière de fuselage. Grâce à ces améliorations, **FAST-OAD** est désormais capable de prendre en compte les aspects les plus critiques des aéronefs à hydrogène, étendant ainsi ses fonctionnalités à la conception d'aéronefs à hydrogène en architecture Tube and Wing.

Ce chapitre démontre ces capacités renforcées de **FAST-OAD** pour la conception d'aéronefs à hydrogène, en exploitant les modèles thermodynamiques et structuraux précédemment développés pour générer un grand nombre de designs d'avions à hydrogène. Cette capacité est utilisée dans une première partie dans une étude par plans d'expériences qui est menée pour évaluer l'influence des variables clés de conception des

réservoirs sur les performances de l'aéronef et l'efficacité des réservoirs. Les analyses paramétriques qui en découlent dans une seconde partie quantifient des compromis essentiels, tels que l'impact de l'épaisseur d'isolation, du différentiel de pression maximal, de la durée de dormance, du diamètre du fuselage et des réservoirs, ainsi que du choix entre des configurations de réservoirs intégrés ou non.

Les résultats montrent que l'optimisation des performances en vol passe au niveau des réservoirs cryogéniques par la réduction de leur masse structurelle. Pour limiter l'évaporation de l'hydrogène, il est plus efficace d'augmenter l'épaisseur de l'isolation que de concevoir des réservoirs capables de supporter un différentiel de pression élevé avec l'extérieur. Une mission sans purge peut ainsi être réalisée même avec un différentiel de pression maximal réduit, combiné à une isolation modérée (150–200 mm), évitant ainsi un alourdissement excessif du réservoir.

Cependant, les périodes de dormance entre deux vols posent toujours un défi majeur. Les technologies d'isolation actuelles ne permettent pas de maintenir une absence totale de purge au-delà d'une ou deux heures sans entraîner une pénalité significative sur l'efficacité énergétique. Une solution pragmatique consisterait donc à revoir les exigences de dormance, en limitant les contraintes de non-purge à une heure maximum. Les analyses paramétriques confirment par ailleurs que les réservoirs intégrés offrent un léger avantage en termes d'efficacité énergétique globale. En revanche, bien que les réservoirs de plus grand diamètre présentent de meilleurs indices gravimétriques, ils imposent un fuselage plus large, ce qui détériore l'efficacité énergétique globale de l'aéronef en raison d'une masse et d'une traînée accrues. Par conséquent, il est préférable d'opter pour des conceptions de réservoirs plus élancées afin de préserver les performances globales du système.

À l'issue de ces analyses, des paramètres optimaux de conception — tels qu'une isolation de 100 mm, un différentiel de pression de 1 bar et une configuration de réservoirs intégrés — sont identifiés et fixés pour simplifier l'espace de conception. Un aéronef à hydrogène est ensuite dimensionné avec ces paramètres et comparé à un aéronef conventionnel à kérosène. Les résultats montrent que, bien que la propulsion à hydrogène réduise la masse de carburant de 60% et la **MTOW** de 2,7%, l'augmentation de la masse à vide (14%) et la détérioration du rapport portance/traînée entraînent une hausse de 10% de la consommation énergétique totale de la mission, bien que la pénalité énergétique pour la mission principale soit limitée à 3,5%.

Ces résultats valident donc les capacités étendues de **FAST-OAD** pour la conception d'aéronefs à hydrogène en architecture Tube and Wing, mais mettent également en évidence la nécessité d'explorer des configurations innovantes pour réduire cette pénalité énergétique. Le chapitre suivant introduit ainsi une nouvelle méthodologie de dimensionnement pour les aéronefs à hydrogène en configuration Blended Wing Body, une architecture prometteuse pour atténuer, voire éliminer, cette perte d'efficacité.

Contents of this Chapter

IV.1 Introduction 116
IV.2 Case Study Setup for the Design of a SMR Hydrogen Aircraft 117
IV.3 Evaluating FAST-OAD Hydrogen Aircraft Design Capabilities 118
IV.4 Parametric Analysis to Assess Sensitivity in H2 Aircraft Design 122
IV.4.1 Influence of tank insulation and design pressure 122
IV.4.2 Influence of fuselage width for integral tanks configurations 124
IV.4.3 Integral and non-integral tank trade-off 126
IV.4.4 Influence of a zero venting constraint during dormancy phase . . . 128
IV.5 Performance Comparison: Optimal H2 vs. Jet-A Aircraft Design 129
IV.5.1 Optimal Hydrogen Aircraft Design Selection Based on Parametric Analysis 129
IV.5.2 Sizing and Analysis of the identified optimal hydrogen aircraft design 130
IV.6 Conclusion 134

IV.1 Introduction

The first chapter of this thesis introduced a thermodynamic model capable of estimating hydrogen losses during an aircraft mission, resulting from heat leakage into the cryogenic tank, which causes liquid hydrogen boil-off. The following chapter then focused on developing a methodology for sizing the structure of hydrogen tanks to estimate their mass. The methods and models developed were integrated into the aircraft sizing tool **FAST-OAD**, and its geometry module was adapted to accommodate hydrogen tanks at the rear of the fuselage. With these enhancements, **FAST-OAD** is now equipped to account for the most impactful aspects of hydrogen-powered aircraft, thereby extending its capabilities to design hydrogen aircraft with a Tube and Wing architecture.

This chapter aims to demonstrate the new capabilities of **FAST-OAD** by conducting parametric studies of hydrogen aircraft. These studies seek to reveal the sensitivities of hydrogen aircraft and their cryogenic tanks to various design variables, particularly those related to the hydrogen tank. Another objective is to identify appropriate values for these design variables, which will be utilized in the next chapter for the conceptual design of a hydrogen-powered Blended Wing Body aircraft. By fixing these hydrogen tank design variables in advance, the design space dimension can be reduced, avoiding an overly broad and complex optimization process.

The first section of this chapter focuses on defining the design test case used to conduct the aforementioned studies. This test case represents a typical **SMR** mission for a single-aisle aircraft, which is subsequently adapted into a hydrogen-powered configuration. The initial study involves a design of experiments targeting key tank design variables to assess their influence on both tank and aircraft performance.

The design of experiments findings then inform a series of parametric studies in the second part, where trade-offs between pairs of design variables—such as insulation thickness, maximum pressure differential, dormancy duration, fuselage and tank diameter, and the choice between integral and non-integral tank configurations—are quantified in terms of their impact on aircraft fuel efficiency, tank mass, and boil-off prevention. These analyses enable the informed selection of optimal tank design parameters, which are subsequently fixed for the remainder of the study. In the final section, a hydrogen-powered aircraft is sized using these optimized parameters, and its performance and characteristics are rigorously analyzed in comparison to a conventional jet-fuel aircraft.

A significant portion of the work presented in this chapter builds upon research previously published in :

- R. Parello, S. Defoort, E. Benard, and Y. Gourinat. *"Integrating Cryogenic Tanks Model in Hydrogen Aircarft Design for Parametric Performance Analysis"* (International Concil of the Aeronautical Science 2024. Florance, Italy: Sept. 2024).

This article, which focused on the design of experiment and the parametric analysis of

hydrogen tank design, laid the groundwork for the methodologies and findings discussed here. This chapter expands on those results, incorporating additional analyses and refinements to further explore the implications for hydrogen-powered aircraft design.

IV.2 Case Study Setup for the Design of a Small-to-Medium Range Hydrogen-Powered Aircraft

While the integration of the hydrogen tank model into **FAST-OAD** represents the primary modification enabling the design of hydrogen-powered aircraft, several additional adjustments were implemented compared to the standard version of the software. These include:

- **Fuel consumption**: Previous experiments [**18**, **29**] have demonstrated that conventional jet engines can be adapted to hydrogen fuel with minimal modifications, suggesting that hydrogen-fueled turbofan engines would likely exhibit performance characteristics similar to those of current engines. As a result, no specific changes were made to the propulsion module in **FAST-OAD**, except for a 15% reduction in **Specific Fuel Consumption (SFC)** compared to the baseline rubber engine [**125**] to reflect projected propulsion advancements by 2035. Concerning hydrogen aircraft, to account for the higher specific energy of hydrogen, the **SFC** is simply adjusted by dividing it by a factor of 2.79, which is the ratio of lower heating value between kerosene and hydrogen. This factor reflects the increased energy content of hydrogen compared to conventional jet fuels.

- **Aerodynamics**: The low-fidelity aerodynamic model in **FAST-OAD** was upgraded to a higher-fidelity analytical model, which has been validated using CFD (Computational Fluid Dynamics). In this updated model, the wing is represented through three distinct segments, each characterized by its sweep angle, relative thickness, maximum lift coefficient, Korn factor (used for wave drag calculations), and a laminar flow index X_{tra} [**124**].

- **Geometry** : As previously mentioned, the geometry module was modified to first determine the tank dimensions, specifically their length, based on the volume of hydrogen to be stored, the fuselage diameter, and the number of tanks. The tank length is then used to calculate both the new fuselage length and the tank center of gravity, which is assumed to be at the center of each tank. These parameters are subsequently integrated into the global aircraft stability analysis.

With these modifications in place, **FAST-OAD** now enables the design of hydrogen-powered aircraft and the evaluation of their performance and sensitivity to tank configuration. This analysis focuses on a narrow-body aircraft designed for 240 passengers and a 2,500 NM range, comparable to the Airbus A321neo. The design mission profile is illustrated in Figure IV.1, including the Mach speed evolution throughout the mission.

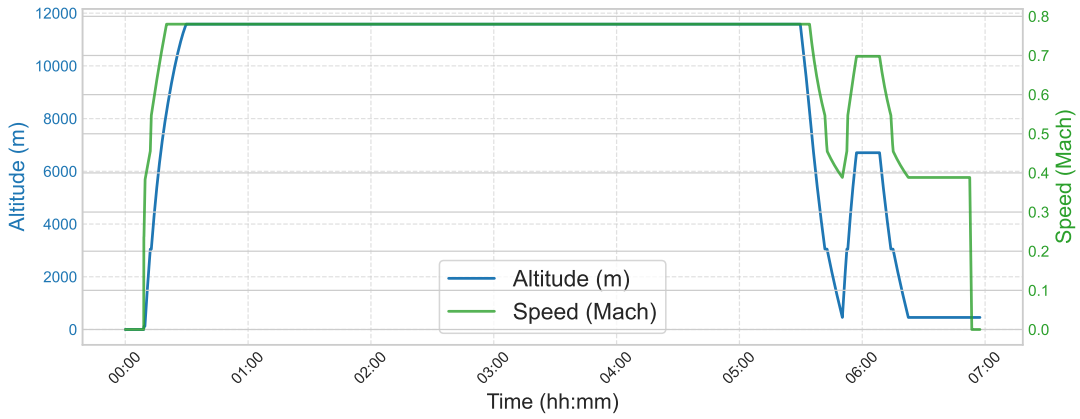

Figure IV.1: Design Mission Profile of a Medium-Range Hydrogen Aircraft

For this preliminary analysis, several key design choices were fixed:

- The aircraft is equipped with a single hydrogen tank
- The tank is integral and positioned aft of the cabin, with a 0.2 m margin between the cabin bulkhead and the tank.
- The insulation consists of polyurethane foam placed inside the tank, with thermal conductivity as defined in Figure II.5.
- The tank structure is made of aluminum 2024

The fixed tank design inputs are summarized in Table IV.1. The reasoning behind the material selection for insulation and tank structure is explained in the appendix A.2.

IV.3 Evaluating Hydrogen Aircraft Design Capabilities via a Design of Experiments on Tank Parameters

This chapter has two main objectives: first, to demonstrate the capabilities of the methodology developed within **FAST-OAD** for sizing hydrogen aircraft across a wide range of design parameters; second, to investigate the sensitivities of hydrogen aircraft and their tanks to key design variables. To achieve these goals, a **DoE** was conducted on critical tank-related variables. This analysis validated the new design tool's ability to size and assess the performance of a large number of aircraft configurations, while also providing a comprehensive overview and identifying key parametric studies, which are detailed in Section IV.4.
The DOE focused on seven continuous aircraft parameters, listed in Table IV.2, all of which directly impact the hydrogen tank:

- **Max ΔP and min ΔP** : the maximum and minimum pressure differentials between the tank interior and the external environment, which influence both the venting pressure requirements and the structural design of the tank.

Table IV.1: Tank model inputs

	Inputs	Value	Unit
Mission and Design	Passenger	239	
	Seat per row	6	
	Range	2500	NM
	Cruise altitude	33 000	ft
	Cruise speed	0.78	mach
	Dormancy time	30	min
	Thrust-to-weight ratio	0.35	
	Aspect ratio	9.9	
Tank initial State	Pressure	1.5e5	Pa
	Ullage temperature	25	K
	Max Fill level	97%	
Insulation	Thermal conductivity	0.026	$W.m^{-1}.K^{-1}$
(Polyurethane Foam)	Density	33	$kg.m^{-3}$
Tank material	Density	2825	$kg.m^{-3}$
(Aluminium 2026)	Poisson ratio	0.33	
	Young modulus	73.8	GPa
	Elastic limit stress	240	MPa
	Elastic break stress	420	MPa
	Thermal conductivity	230	$W.m^{-1}.K^{-1}$
	Tank skin infrared emittance	0.9	
	Tank sink solar absorptance	0.26	
Model time step		10	s

- **Initial Liquid Temperature**: The temperature of liquid hydrogen at the start of the mission
- **Insulation Thickness**: The thickness of the polyurethane foam insulating the tank
- **Fuselage Width**: Determines the tank diameter, as the tank is integral to the fuselage. However, it should be noted that cabin length remains unchanged in this study, even for wider fuselages that could potentially accommodate more seats per row.
- **Shear and Bending Transmission Ratios**: These ratios assess how much of the bending and shear loads from the fuselage are transmitted to the tank. A ratio of 1 means the tank must withstand the full fuselage load, while a ratio of 0.1 implies only 10% of the load is transferred, allowing for a lighter tank structure. The objective is to assess to sensibility of tank weight and aircraft performance to that parameter in order to evaluate the trade-off between integral and non-integral tanks.

A 300-point **DoE** was generated using the **Latin Hypercube Sampling (LHS)** method **[157]**, with parameter bounds specified in Table IV.2. For each DOE point, an aircraft was sized with **FAST-OAD** according to the methodology outlined in the previous chapters. Figure IV.2 illustrates six essential performance metrics for each design configuration:

Table IV.2: Tank inputs DOE

Inputs	lower	upper	Unit
max ΔP	0.8	4	bar
min ΔP	0.2	0.6	bar
Initial liquid temperature	15	21	K
Insulation thickness	0.02	0.2	m
Fuselage width	3.9	5.5	m
Shear load transmission ratio	0.1	1	-
Bending load transmission ratio	0.1	1	-

- The aircraft's Overall Empty Weight
- The Tank Weight
- The Block Fuel
- The amount of hydrogen lost due to boil-off
- The tank-adjusted gravimetric index (GI), defined in Equation IV.1, which integrates the impact of boil-off on the gravimetric efficiency. This index ensures that well-insulated tanks are accurately differentiated from those that appear lightweight solely due to poor insulation performance.
- The aircraft's Fuselage Length

$$\eta_{grav} = \frac{m_{H2} - m_{boil_off}}{m_{H2} + m_{tank}} \tag{IV.1}$$

Above all, Figure IV.2 demonstrates the robustness of the hydrogen-adapted version of FAST-OAD. The tool successfully sizes a wide range of hydrogen aircraft configurations with diverse design inputs, while maintaining efficient computational performance. Each design case requires only a few minutes of computation on a standard laptop—representing minimal overhead compared to the original FAST-OAD. Additionally, the multidisciplinary analysis (**MDA**) exhibits high stability, with virtually no iteration failures, provided that the design inputs remain physically coherent (e.g., feasible initial conditions). Aside from that general conclusion, Figure IV.2 reveals several important trends regarding the influence of tank design parameters on hydrogen aircraft performance:

- The adjusted gravimetric index spans a range of approximately 0.55 to 0.85 across all designs, underscoring the strong dependency of tank efficiency on design choices as evidenced in the literature review (see Fig. II.1). This variability justifies the inclusion of tank sizing as a critical step in the preliminary aircraft design phase. However, the weight of the hydrogen subsystems is not accounted for here, which partly explains some of the very high index values.
- The tank weight and efficiency appear most sensitive to the maximum design pressure differential (max ΔP), as evidenced by the clear grouping of data points along

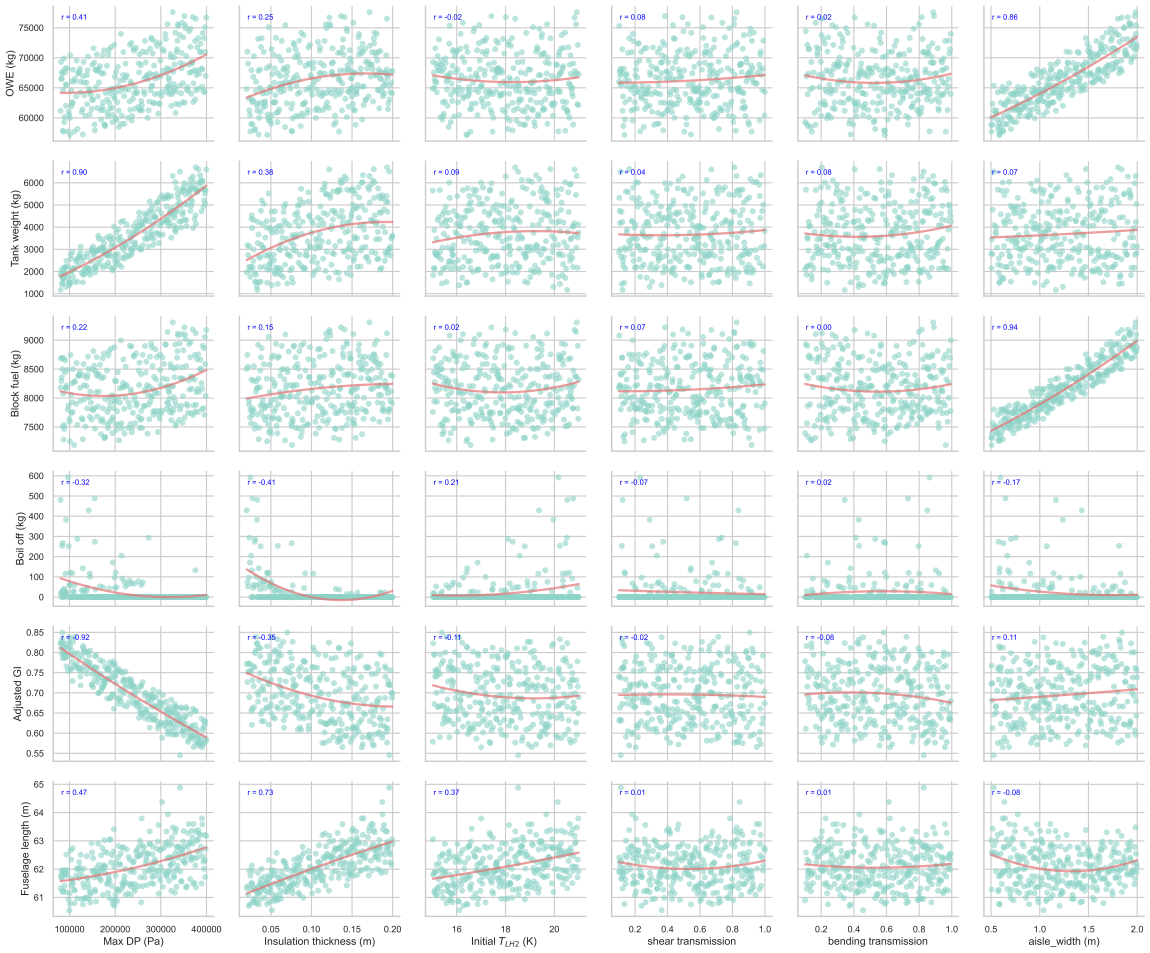

Figure IV.2: Design of Experiments: Impact of Tank Design Variables on a Tube-and-Wing Hydrogen Aircraft

distinct lines in the leftmost column. Increasing max ΔP not only raises tank weight and the **OWE** but also tends to lengthen the fuselage, likely due to the need for a larger tank to accommodate the increased block fuel mass. However, the amount of vented hydrogen does not show a direct, strong correlation with max ΔP. The data instead indicate a threshold behavior: beyond a certain max ΔP value, venting becomes rare, and most missions operate with zero hydrogen loss. At lower max ΔP values, hydrogen losses tend to be more pronounced, though this trend is not universally consistent, suggesting other variables like the insulation thickness have also a significant impact.

- The amount of vented hydrogen decreases indeed exponentially with insulation thickness. Thin insulation layers (e.g., 2 cm) can result in substantial hydrogen losses (up to 500 kg), but these losses diminish rapidly as thickness increases. However, even with thick insulation (20 cm), venting may still occur, particularly when combined with a low max ΔP.

- Among the parameters analyzed, fuselage width exerts the strongest influence on block fuel mass, with a 1.5 m increase in width resulting in a 20–25% rise in block

fuel—a relationship that follows a linear trend. Initially, fuselage length decreases as width (and thus tank radius) increases, since the tank volume scales with the square of the radius, allowing for a shorter tank in wider configurations. However, this trend reverses as the higher block fuel demand—driven by the increased fuselage width—requires a longer tank and fuselage to accommodate the additional fuel volume. While tank mass, efficiency, and vented hydrogen mass remain largely unaffected by changes in fuselage width, the aircraft empty weight increases significantly. This suggests that the rise in block fuel is not primarily driven by the hydrogen tank itself, but rather by other aircraft-level effects associated with a wider fuselage, such as structural or aerodynamic considerations.

- The initial liquid temperature shows a small influence on vented hydrogen, as colder liquid requires time to reach saturation temperature. It also has a slight impact on fuselage length, since the tank is sized based on the hydrogen liquid density at the initial temperature.

- The shear load transmission ratio shows no discernible effect on aircraft or tank performance, while the bending transmission ratio may have a marginal impact on tank weight and efficiency—though this effect is one to two orders of magnitude smaller than that of other parameters. The choice between intergal or non-integral tank seems to have so a marginal effect on aircraft fuel efficiency performance.

With most gravimetric indexes exceeding 0.5, the analysis conducted by Adler and Martins [**46**] (see Figure I.25) suggests that hydrogen aircraft are feasible and capable of achieving energy consumption levels comparable to kerosene-powered aircraft. Nevertheless, this DOE highlights that certain tank parameters—such as max ΔP, fuselage width, and insulation thickness—have a substantial impact on aircraft performance and characteristics. Given the varying magnitude of these effects, further in-depth parametric studies were conducted in the following section to quantify these dependencies more precisely.

IV.4 Parametric Analysis to Assess Sensitivity in H2 Aircraft Design

IV.4.1 Influence of tank insulation and design pressure

Two of the most critical design variables for cryogenic hydrogen tanks are insulation thickness and the maximum pressure differential that the tank structure must withstand. While increasing either parameter reduces hydrogen losses from boil-off and venting, it also adds to the tank's empty weight. To get some insight into this trade-off, a parametric study was conducted on these variables, maintaining the same assumptions as in Section IV.3. The tank is also still fully integral, meaning fuselage bending and shear loads are fully transmitted to the tank structure, and the fuselage width is fixed at 4 m, consistent with current medium-range aircraft like the A320 family.

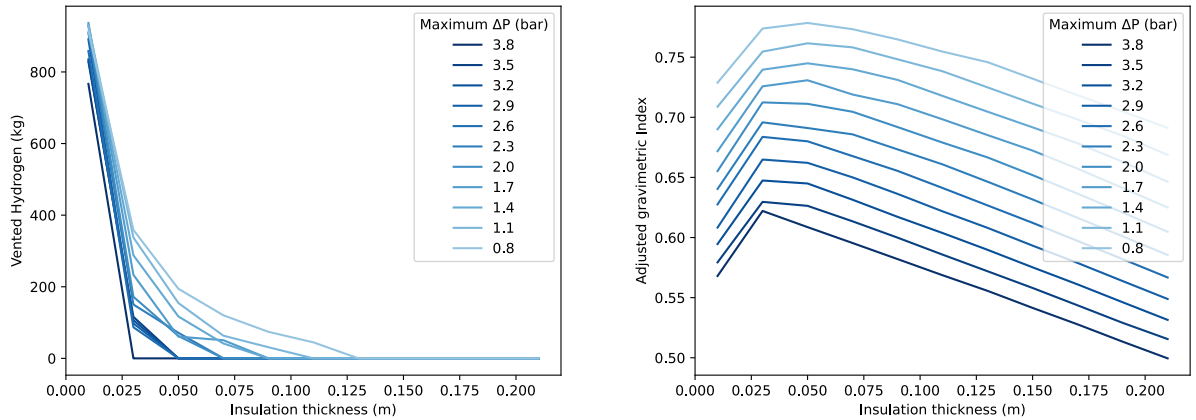

(a) Hydrogen boil-off loss

(b) Gravimetrix efficiency

Figure IV.3: Impact of maximal pressure differential and insulation thickness on tank efficiency [**158**]

Figure IV.3 illustrates the impact of this trade-off on tank performance. For thin insulation (e.g., 1 cm), hydrogen losses can be substantial, reaching around 1 ton of vented hydrogen per mission. However, these losses decrease exponentially with increasing insulation thickness, leading to improved adjusted gravimetric indexes. The optimal insulation thickness—maximizing the gravimetric index—lies between 6–7 cm, depending on the max ΔP, with optimal values ranging from 0.6 (high pressure) to 0.78 (low pressure differential). This 20% range remains consistent across all insulation thicknesses.

Figure IV.4 demonstrates that total tank mass increases almost linearly with max ΔP for a 7 cm insulation thickness, and this trend holds for all insulation levels. The results confirm earlier findings reported in [**159**], highlighting the significant contribution of the stiffening structure to the tank's total mass—particularly as the sizing pressure differential rises. At max ΔP values above 3 bars, the stiffening structure accounts for roughly half of the tank's mass.

Zero-venting designs are achievable with reasonable insulation thicknesses, such as 5 cm when max ΔP exceeds 2.5 bars (Figure IV.3). However, this threshold becomes more challenging to meet at lower max ΔP values, requiring 10–12 cm of insulation if ΔP is only 1 bar. If venting cannot be entirely eliminated, the sensitivity of hydrogen boil-off to insulation thickness is extremely high, meaning even small deviations from the optimal thickness can lead to significant hydrogen losses, representing a non-negligible fraction of block fuel. Precise identification of the optimal insulation thickness is therefore essential, and conservative safety margins should be applied. Additionally, a longer dormancy phase after landing could further increase hydrogen venting. If venting is prohibited during this phase, it may impose stringent constraints on insulation thickness, as discussed in Section IV.4.4.

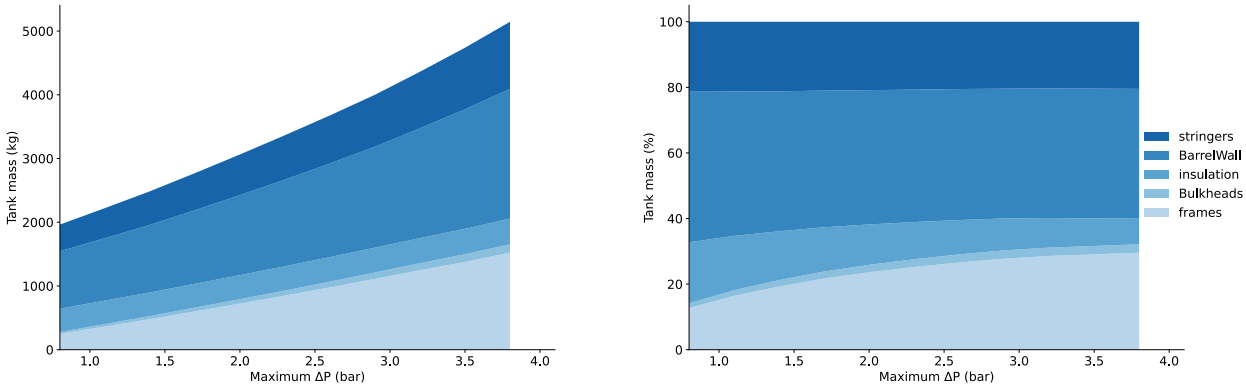

(a) Absolute mass (b) Mass breakdown

Figure IV.4: Impact of maximal pressure differential on tank mass (insulation thickness fixed to 7 cm)[**158**]

IV.4.2 Influence of fuselage width for integral tanks configurations

According to the Design of Experiments results presented in Figure IV.2, while tank characteristics—such as insulation thickness and design pressure—significantly influence tank performance, fuselage width emerges as the most impactful parameter on overall aircraft efficiency. To delve deeper into this phenomenon, a parametric study was conducted focusing on fuselage width. The study maintains the same design assumptions: the tank remains integral, meaning its diameter matches the fuselage width, and 7 cm of insulation is placed inside the tank.

Figure IV.5 illustrates how block fuel and tank mass evolve with respect to fuselage diameter for various values of the maximum design pressure differential. As anticipated, the left graph (Figure IV.5a) reveals that block fuel increases substantially with fuselage width—by approximately +10% per meter—regardless of the maximum design pressure differential.

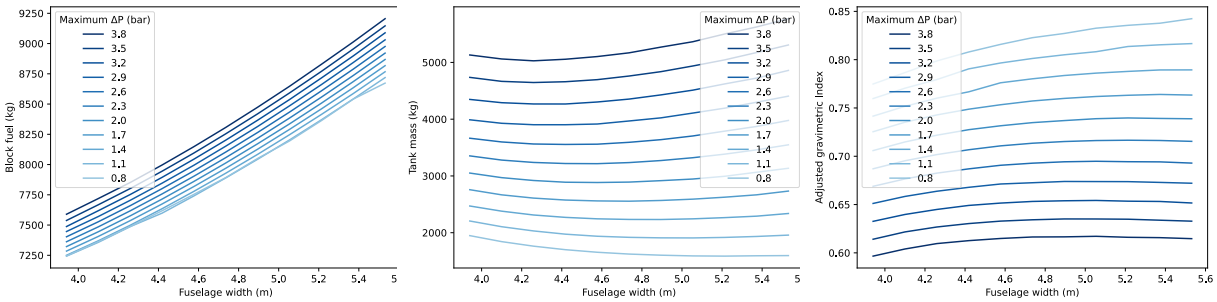

(a) Block fuel (b) Tank mass (c) Gravimetric index

Figure IV.5: Evolution of aircraft consumption, tank mass and tank gravimetric index with fuselage width [**158**]

The right graph in Figure IV.5b shows that fuselage diameter has only a modest effect on tank mass, particularly at low design pressures. This can be explained by two counteracting effect : increasing the tank radius raises wall and stiffening structure stresses—since stress is radius-dependent—, which tends to thicken the wall and to enlarge frame sections to compensate. However, a larger radius improves the volume-to-external-surface ratio, meaning less wall area is required. This reduces bending moment stresses, shortens the tank length, and potentially decreases the need for stringers and frames. The results of this trade-off suggest a clear advantage for wider tanks in terms of pure tank mass efficiency. Although the tank mass initially decreases slightly with increasing tank radius before rising again, the block fuel requirement grows substantially, requiring a larger tank. Despite this, the associated increase in tank weight remains minimal. This behavior is confirmed in Figure IV.5c, where the gravimetric index of the hydrogen tank improves with wider radii, an effect that is even more pronounced at lower design pressures.
If the tank mass remains nearly constant as fuselage width increases, the rise in aircraft fuel consumption must stem from other factors. A deeper analysis reveals two primary contributors: a heavier fuselage and a larger wetted surface, which increases drag. The impact of these factors is illustrated in Figure IV.6: increasing the fuselage diameter by 1.5 m (+ 38%) can raise the aircraft empty weight by 15–20%, depending on the maximum design pressure. Additionally, the lift-to-drag ratio decreases by approximately 4–5%, directly contributing to the increase in fuel consumption. However, these results likely overestimate the actual consumption increase. The fuselage length remains unchanged (the cabin layout is fixed as a single-aisle, 6-seat (3–3) configuration throughout the study), and the semi-empirical relations used to estimate fuselage mass were developed for single-aisle, aluminum fuselages. In contrast, modern wide-body fuselages increasingly use composite materials, which significantly reduce structural weight.

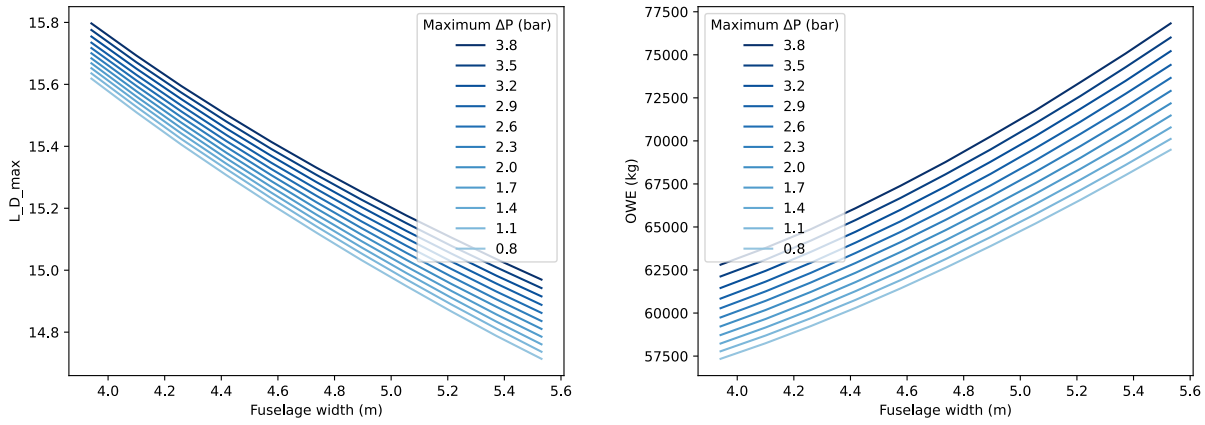

(a) L/D ratio (b) **OWE**

Figure IV.6: Impact of fuselage width on aircraft operational empty weight and lift-to-drag ratio[**158**]

To further confirm the significant impact of fuselage radius on aircraft efficiency, an addi-

tional analysis was conducted. Three twin-aisle aircraft configurations—with cabin layouts of 7 seats per row (2-3-2), 9 seats per row (3-3-3), and 10 seats per row (3-4-3)—were modeled and compared to a reference single-aisle aircraft. Unlike the previous study, the cabin length was optimized based on the number of seat rows required for each layout. Figure IV.7 illustrates how aircraft characteristics evolve for each cabin layout compared to the reference single-aisle configuration. As expected, block fuel increases significantly with wider fuselages, reaching a maximum rise of 18% for the 10-seat-per-row layout. This trend is primarily due to higher empty weight and reduced aerodynamic efficiency: although wider fuselages are 12% to 20% shorter, their wetted area expands by 7%, 15%, and 22% for the 7-, 9-, and 10-seat-per-row layouts, respectively. This results in greater mass (increasing by 3% to 14%) and higher friction drag that degrade the maximum lift-to-drag ratio up to 8%. The hydrogen tank's ability to maintain a nearly constant gravimetric index is then insufficient to counteract those performance penalties associated with a larger fuselage.

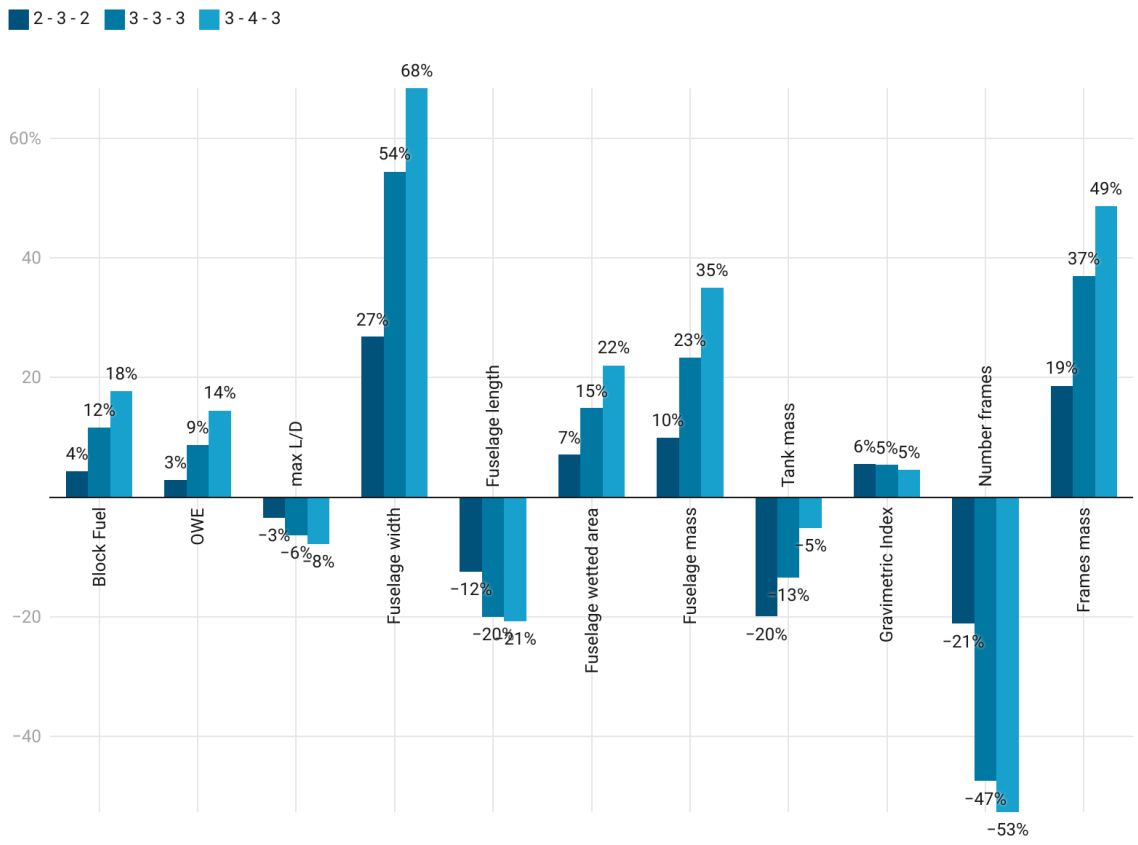

Figure IV.7: Evolution of hydrogen aircraft characteristics and performance of twin-aisle cabin configurations compared to a single-aisle

IV.4.3 Integral and non-integral tank trade-off

In previous analyses, all modeled tanks were integral designs, where the entire fuselage bending and shear loads are transmitted directly to the tank. However, some hydrogen aircraft designs feature non-integral tanks, which are housed inside the fuselage. This

configuration offers two key advantages: simpler insulation placement (as it can be applied to the tank's external surface) and easier integration into existing aircraft designs. Yet, this approach also introduces certain drawbacks, including:

- More complex access for tank inspection or repairs
- Additional weight from the fuselage structure surrounding the tank.
- Load transmission dependencies, where the transfer of fuselage bending and shear loads relies on the tank's attachment structure.
- A potential safety hazard from the risk of tank leaks, which could lead to hydrogen accumulation inside the fuselage, increasing the risk of explosion. While this risk also exists for integral tank designs, leaks are more likely to occur externally in such configurations, reducing the probability of internal hydrogen buildup.

Since the current version of FAST-OAD does not model this attachment structure, a parametric study was conducted to assess how these loads could influence tank design. For this analysis, the insulation thickness was fixed at 7 cm, and the maximum design pressure differential was set to 1 bar.

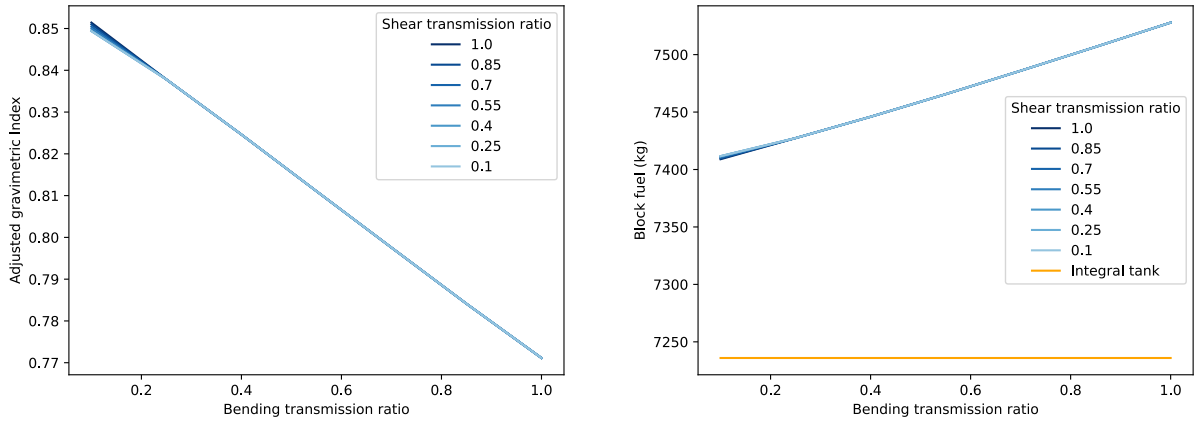

(a) Gravimetric efficiency

(b) Block fuel

Figure IV.8: Impact of fuselage loads transmission to the tank on aircraft performance [**158**]

Figure IV.8 illustrates how tank gravimetric efficiency and block fuel vary with the proportion of fuselage shear and bending loads transmitted to the tank. The impact of shear loads on tank design is negligible, showing only a minor effect at low bending load transmission ratios. In contrast, bending moments have a substantial influence on the tank. Figure IV.9a demonstrates that a tank fully subjected to fuselage bending moments can be up to 70% heavier than a lightly loaded tank. This increase is primarily due to the tank wall and stringer mass, whose contribution to the total tank mass nearly doubles as the load transmission ratio rises from 0.1 to 1 (see Figure IV.9b). Consequently, the gravimetric efficiency index drops by 0.08, leading to higher block fuel requirements.

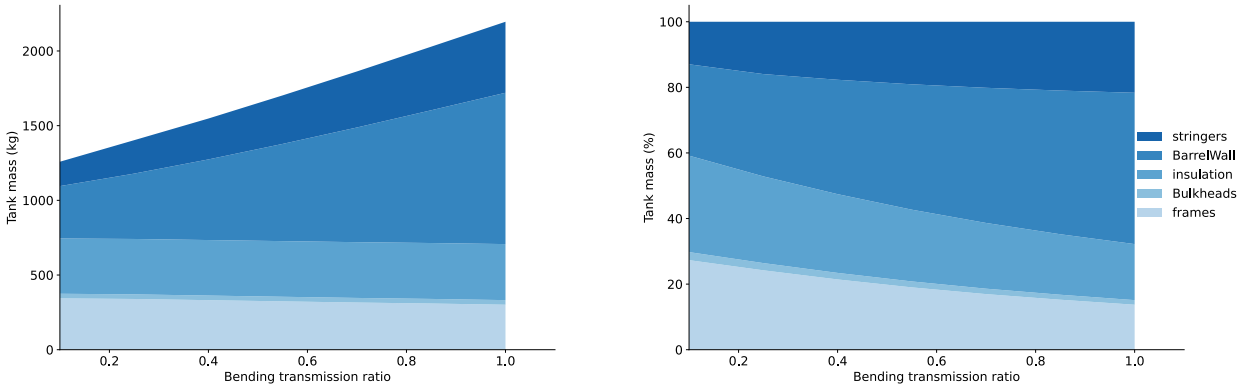

(a) Total mass

(b) Mass breakdown

Figure IV.9: Impact of fuselage loads transmission on hydrogen tank mass [**158**]

These findings indicate that a non-integral tank achieves greater mass efficiency when only a limited portion of the bending load is transferred to it. However, since this analysis does not account for the structural components required to secure the tank within the fuselage, further research is needed to quantify how the added weight of such a system might diminish this advantage. Regardless, hydrogen aircraft with non-integral tanks appear to exhibit 2% to 4% lower fuel efficiency compared to integral tank designs, even before factoring in the weight of the attachment structure. This discrepancy is primarily due to the additional weight penalty imposed by the surrounding fuselage structure. While this efficiency penalty is notable, it remains sufficiently modest that other operational considerations—such as maintenance accessibility, safety requirements, or integration constraints—could ultimately drive the decision between integral and non-integral tank designs.

IV.4.4 Influence of a zero venting constraint during dormancy phase

Under the current air transport model, aircraft often spend several hours at airports between flights, including overnight periods of up to 12 hours parked on the runway—a phase known as dormancy time. Airlines have raised concerns about the safety implications of hydrogen aircraft during dormancy, as regulations may prohibit all hydrogen venting on the ground to prevent fire or explosion risks. This necessitates a trade-off analysis to evaluate the feasibility of zero-venting hydrogen aircraft designs during dormancy.
Figure IV.10 presents the results of a sensitivity analysis where insulation thickness (4–40 cm) and dormancy time (0–12 hours) were varied. The maximum design pressure differential was fixed at 1 bar, as prior analyses indicated that improving insulation offers a better trade-off than adjusting pressure differentials.
The findings reveal that long dormancy phases significantly increase block fuel requirements. This is driven by two factors:

- Excessive hydrogen venting at low insulation thicknesses.

- Deteriorated aircraft performance due to the volume and weight of thicker insulation.

For example, the empty tank mass quadruples when insulation thickness increases from 5 cm to 40 cm—half of this increase is due to the insulation weight, and the other half to the longer tank required to maintain storage capacity as the fuselage radius is fixed. Even with 40 cm of insulation, the current model shows that zero-venting dormancy cannot exceed 7 hours. A more practical 20 cm insulation allows for only 2 hours of dormancy, but with a minor increase in block fuel (around 1.5%).
These results highlight that the zero-venting dormancy constraint is highly impactful on aircraft performance and should be minimized where possible. Alternative solutions—such as connecting the aircraft to a fuel distribution system to safely vent hydrogen—could be more economically viable. Otherwise, advanced insulation technologies (e.g., multi-layer or vacuum insulation) may be necessary, though they would likely significantly increase tank weight.

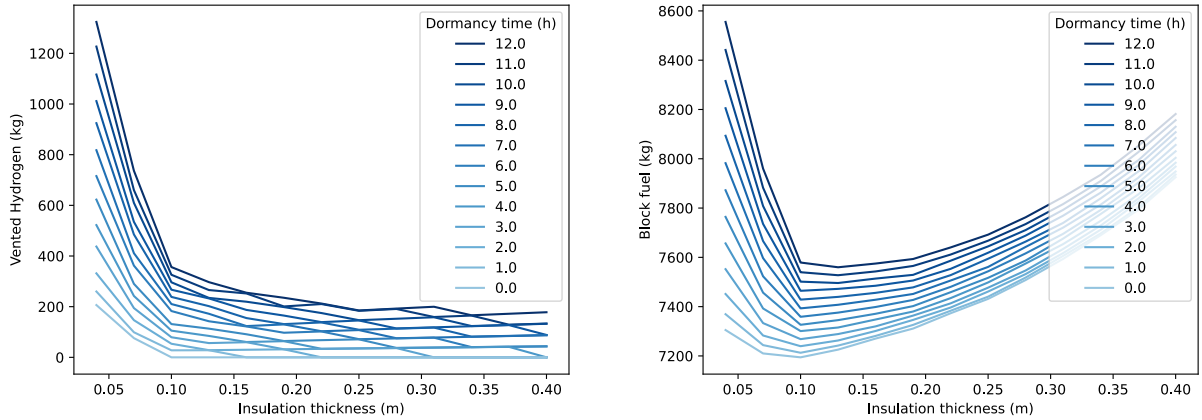

Figure IV.10: Impact of Insulation Thickness on Hydrogen Loss During Dormancy and related Block Fuel Performance [**158**]

IV.5 Performance Comparison: Optimal Hydrogen Aircraft Design vs. Jet Fuel Aircraft

IV.5.1 Optimal Hydrogen Aircraft Design Selection Based on Parametric Analysis

The parametric analysis presented in the previous section yields several significant conclusions regarding the optimization of hydrogen storage tanks for aircraft applications:

- **Tank mass-insulation performance trade off:** To enhance tank performance during the in-flight phase, the optimal balance between reducing structural mass and minimizing boil-off losses prioritizes minimizing the tank's structural weight. This is

achieved by maintaining a low pressure differential between the internal and external environments of the tank. The resulting higher hydrogen losses due to more frequent venting can be effectively mitigated with a relatively modest insulation thickness. Typically, 50–100 mm can be adequate to ensure zero-venting conditions for the entire duration of the flight.

- **Dormancy Constraints:** The dormancy period poses, however, a substantial challenge if venting is prohibited. Under current foam insulation technologies, achieving zero-venting conditions for more than a few hours appears impractical. Even short durations (e.g., one to two hours) without venting incur significant energy efficiency penalties.

- **Tank Design Efficiency:** From a purely efficiency-oriented perspective, integral tanks demonstrate superior performance compared to alternative configurations.

- **Fuselage Integration Trade-offs:** While wider tanks exhibit improved performance in energy efficiency, their integration requiring a wider fuselage adversely impacts overall aircraft energy efficiency. Thus, such configurations should be avoided to preserve system-level performance.

Based on the conclusions drawn, it was possible to determine the values of key design variables for the hydrogen tank configuration of an optimal hydrogen-powered aircraft tailored for **SMR** missions comparable to those of an A321neo—specifically, transporting 239 passengers over a range of 2,500 nautical miles. These parameters must be fixed for the subsequent phase of this study, during which the hydrogen tank design model will be integrated into a **BWB** aircraft sizing tool to optimize the design of a hydrogen-powered **BWB** aircraft. Retaining these variables as open design parameters at this stage would unnecessarily expand the design space, complicating the initial optimization process.

Consequently, in the rest of this study, the insulation thickness was set to 100 mm, utilizing polyurethane foam with five nodes modeled in the thermal resistance analysis, while the pressure differential, ΔP, was fixed at 1 bar (100,000 Pa). This configuration ensures a minimal tank structural mass while targeting a zero-venting mission profile. Avoiding hydrogen venting is critical, as it represents an energy loss, introduces potential boiling within the tank (a phenomenon not yet fully modeled and thus subject to higher uncertainty), and carries environmental implications. The 100 mm insulation thickness is designed to prevent venting during both the flight and a short dormancy period (e.g., one hour), during which the aircraft may quite often not to be connected to a fuel venting system at the airport.

IV.5.2 Sizing and Analysis of the identified optimal hydrogen aircraft design

To establish a reference baseline, an initial hydrogen-powered aircraft was sized using the previously identified optimal parameters. The design incorporated two integral hydrogen

tanks, selected both for their demonstrated efficiency and to ensure system redundancy. The mission profile remained consistent with that used in the parametric analysis (see Figure IV.1), and all other fixed parameters were retained as specified in Table III.1. For comparative purposes, a conventional jet-fuel-powered aircraft was also sized under identical **TLARs**.
The technical specifications of both aircraft are summarized in Table IV.3. Figure IV.11 illustrates the planform configurations of the two designs. Notably, the hydrogen-powered aircraft exhibits a significantly longer fuselage (65 meters, compared to 45 meters for the conventional design) to accommodate the two 7-meter-long hydrogen tanks and a 1-meter-long cryogenic box. Additionally, the relocation of the galleys, toilets, and rear exit—traditionally positioned in the aft fuselage but now situated forward of the tanks—further contributes to the increased fuselage length.

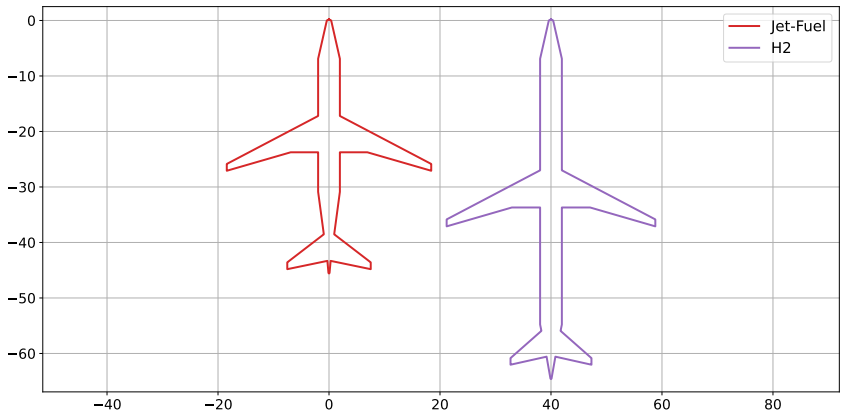

Figure IV.11: Planform comparison of Jet-A and hydrogen-powered **T&W** aircraft

The aerodynamic consequences of the elongated fuselage are evident in the aerodynamic polars of both aircraft, as depicted in Figure IV.12. The hydrogen-powered aircraft demonstrates a rightward shift in its polar curve, indicating increased drag and a corresponding reduction in aerodynamic efficiency. Specifically, the lift-to-drag ratio decreases by 0.8 points. A comparative analysis of the average drag breakdown—adjusted for the hydrogen aircraft's wing surface area to account for its higher cruise lift coefficient—confirms that the drag penalty primarily stems from the extended fuselage length. However, a portion of the drag increase is also attributable to higher induced drag, which can results from the reduced aspect ratio. And while the longer fuselage permits a reduction in empennage size and its associated drag, this benefit is insufficient to offset the overall drag penalty.

Figure IV.14 illustrates the evolution of key aircraft characteristics during the transition to hydrogen propulsion. As anticipated, the increased tank weight and elongated fuselage result in a significant rise in empty weight—approximately 14%—a penalty that the smaller wing and empennage do not fully offset. However, due to the low density of hydrogen, the fuel mass is reduced by about 60%, allowing the **MTOW** of the hydrogen-powered variant to remain slightly lower than that of its conventional counterpart. Consequently, if the thrust-to-weight ratio is maintained, the required thrust can also be reduced. Despite

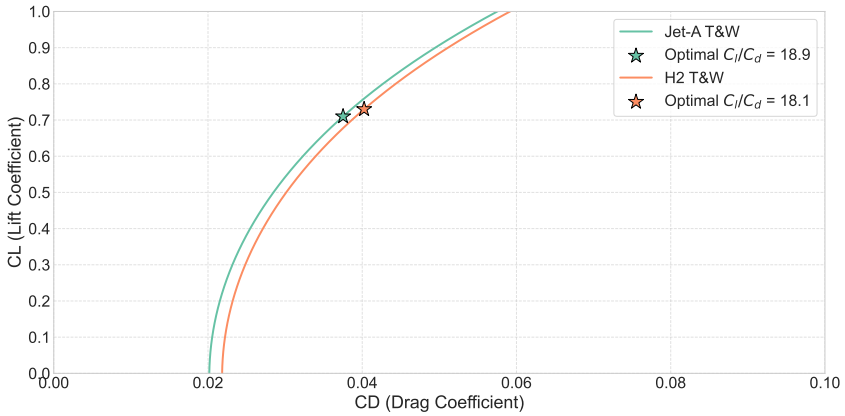

Figure IV.12: Aerodynamic Polar Curves of Jet-A and hydrogen-powered **T&W** aircraft

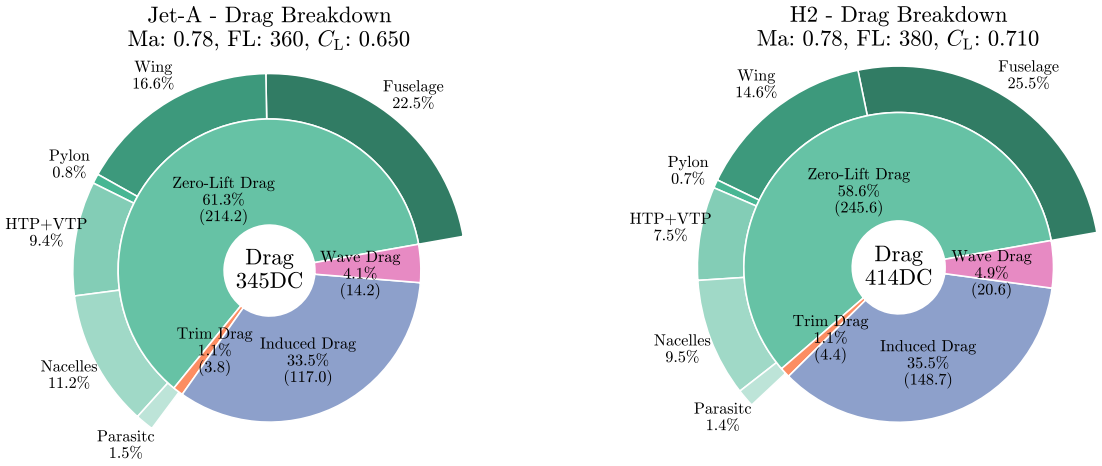

(a) Jet-A (b) H2

Figure IV.13: Drag Breakdown Comparison Between the Jet-A and the H2-Powered **T&W** aircraft at their average cruise lift-to-drag ratio. The drag of the H2 version was corrected by the ratio of surface area to compensate the different cruise CL

this, the combined effect of modest weight reduction and degraded lift-to-drag ratio leads to a total mission energy consumption increase of roughly 10%.

Figure IV.15 reveals that, in the initial phase of the mission, the difference in cumulative engine energy consumption (excluding boil-off and hydrogen-specific fuel margins) is minimal—on the order of 1%. The disparity widens progressively as the jet-fuel aircraft's total weight decreases more rapidly. Notably, the energy consumed for the primary mission route (excluding reserves) is only 3.5% higher (still excluding boil-off) than that of the conventional aircraft. This metric is particularly significant, as energy expended during reserve phases—rarely utilized in practice—carries less operational relevance.

Figures IV.16 and IV.17 offer detailed insights into the thermodynamic behavior of the hydrogen tank during flight. In Figure IV.16, the pressure variation within the tank demonstrates that the 100 mm insulation thickness effectively minimizes venting: the maximum pressure differential is reached only three times, resulting in a total vented hydrogen mass of 45 kg per tank—equivalent to just 1.4% of the total fuel. However, the first venting event occurs during climb, as the external pressure decreases

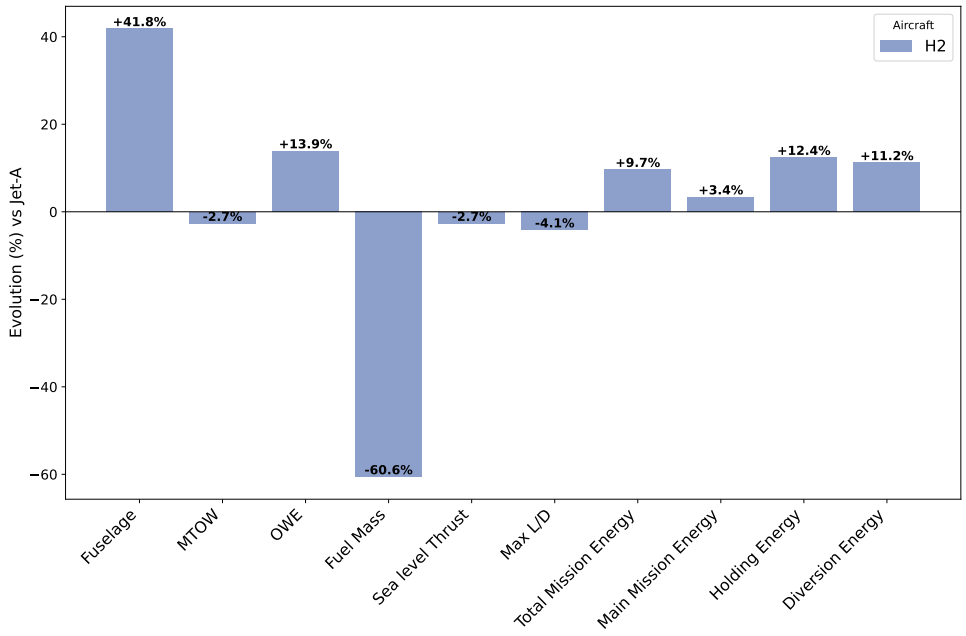

Figure IV.14: Evolution of key design performance of hydrogen aircraft compared to the jet-fuel aircraft

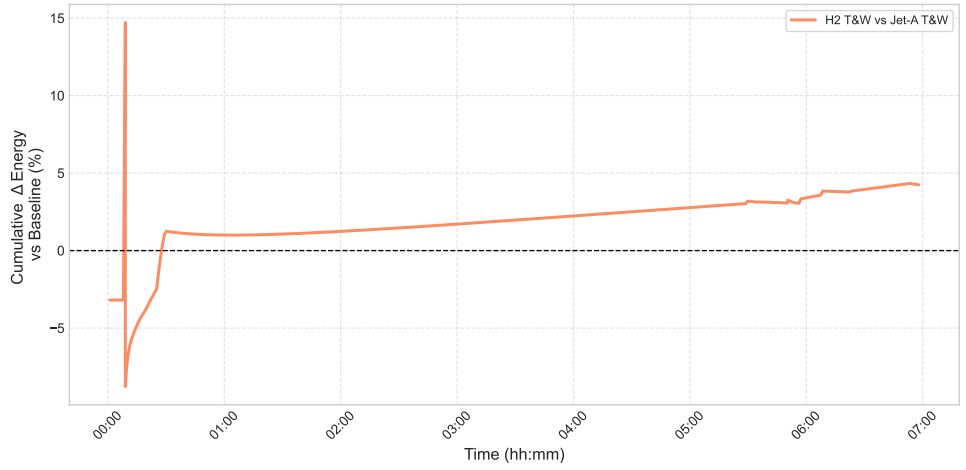

Figure IV.15: Cumulative Engine Energy Consumption: Hydrogen vs. Conventional Aircraft from Mission Start

more rapidly than the internal pressure. This suggests that an optimized initial filling pressure could potentially mitigate this early venting. A notable observation is also the pressure drop during takeoff and climb, attributed to the high fuel flow demand from the engines, which exceeds the natural boil-off rate. Although this drop does not immediately violate the minimum pressure differential threshold, the threshold is breached after the first venting event, necessitating several active pressurizations after approximately 20,000 seconds. However, it is worth emphasizing that implementing an adaptive ullage pressure management strategy—where the amount of hydrogen to be vented is dynamically optimized in real time based on the current and anticipated mission phases—could potentially eliminate the need for venting or active pressurization entirely. Such an approach would significantly enhance the overall energy efficiency of the hydrogen propulsion system.

Another significant phenomenon is the accelerated self-pressurization rate following the first venting, which is substantially higher than pre-venting levels. As illustrated in the top graph of Figure IV.17, this behavior arises because the liquid hydrogen becomes superheated (i.e., its temperature exceeds the saturation point) during this phase. Consequently, all incoming heat flow is immediately consumed by evaporation, whereas it previously contributed only to heating the liquid volume. This graph also highlights temperature disparities—between the ullage and the liquid (10–20 K difference), as well as between the dry and wetted internal tank walls (at least 80 K difference)—validating the necessity of modeling these control volumes separately, unlike in homogeneous models.

Additionally, the external temperature plays a critical role, as the heat flow into the tank fluctuates rapidly during the initial and final mission phases, when altitude changes induce swift variations in ambient temperature. These dynamics underscore the importance of accounting for time-dependent thermal boundary conditions in the tank's thermodynamic analysis.

IV.6 Conclusion

This chapter demonstrated the enhanced capabilities of the new version of **FAST-OAD** that integrates the thermodynamic and structural models developed in previous chapters by conducting comprehensive parametric studies of hydrogen-powered aircraft. Building on the thermodynamic model for estimating hydrogen boil-off losses and the structural sizing methodology for cryogenic tanks, the integrated tool—now adapted to accommodate rear-fuselage hydrogen tank placement—successfully enabled the design and analysis of a large number of hydrogen aircraft within a Tube and Wing architecture during a design of experiments. This design of experiments enables also the systematically evaluation of the influence of key tank design variables on aircraft performance and tank efficiency. The subsequent parametric studies quantified critical trade-offs, including the effects of insulation thickness, maximum pressure differential, dormancy duration, fuselage and tank diameter, and the choice between integral and non-integral tank configurations.

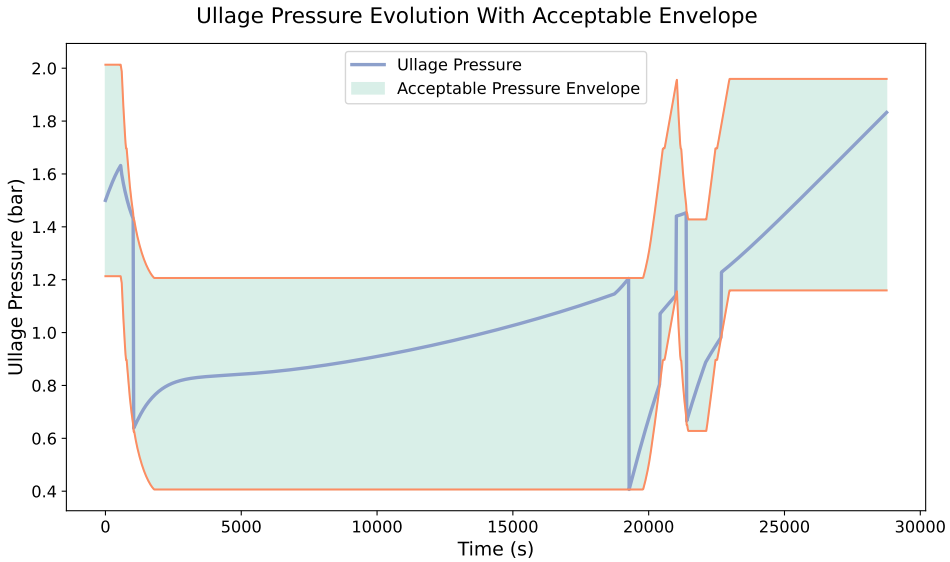

Figure IV.16: Ullage Pressure Evolution in a Hydrogen Tank During Mission

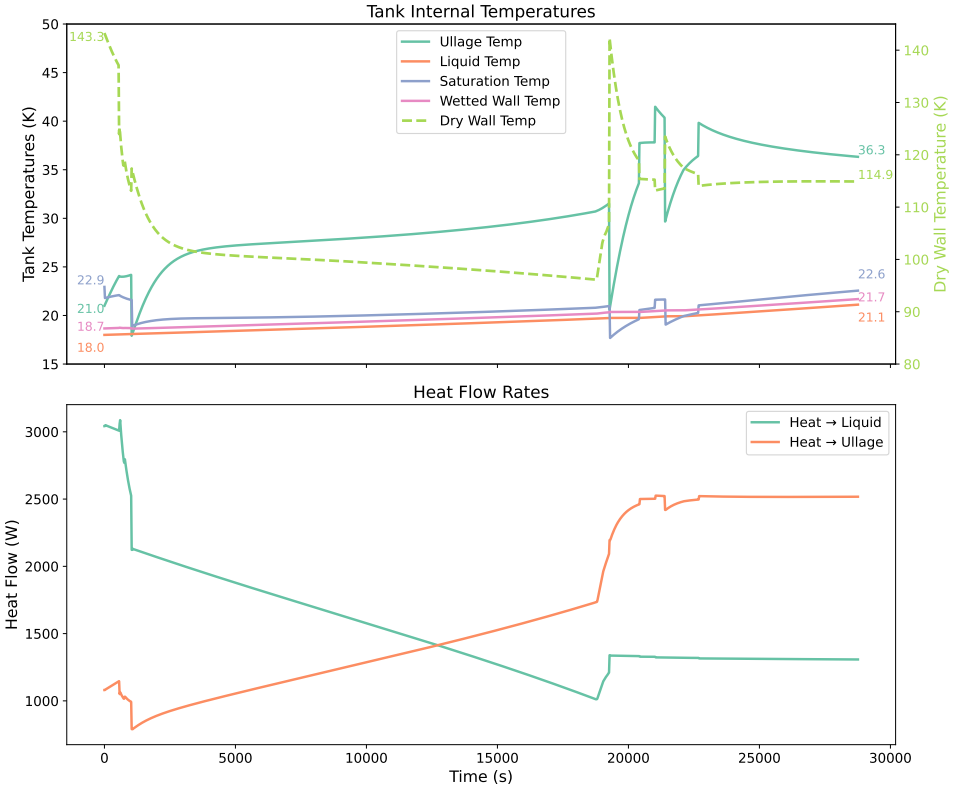

Figure IV.17: Temporal Variation of Tank Temperature and Heat Transfer During Flight Hydrogen Aircraft Mission

Table IV.3: Technical Specifications of Hydrogen and Jet-Fuel Aircraft

Category	Variable	Jet-A	H2
Aerodynamic	Optimal C_L	0.71	0.73
	Optimal C_D	0.038	0.040
	Max L/D	18.93	18.14
	MAC [m]	4.48	4.57
Geometry	Total length [m]	45	65
	Wing area [m^2]	137	143
	Wing aspect ratio	9.90	9.90
	Root Sweep angle (p0) [deg]	27.7	27.7
	Vertical Tail area [m^2]	30.4	28.8
	Vertical Tail span [m]	7.4	7.2
	Horizontal Tail area [m^2]	45.2	42.5
	Horizontal Tail span [m]	15.0	14.6
	Cabin height [m]		3.8
	Cabin length [m]	36.8	34.0
	Cabin width [m]		3.7
	Nacelle diameter [m]	2.4	2.4
	Nacelle length [m]	3.1	3.1
Weight	MTOW [kg]	95972	93411
	OWE [kg]	54653	62257
	ZFW [kg]	79653	87257
	Payload [kg]	25000	25000
	Fuselage mass [kg]	12357	14635
	(External) Wing mass [kg]	11079	12105
	Engine mass [kg]	8443	7994
	Landing gear mass [kg]	3199	3112
	Block Fuel mass [kg]	16712	6590
	Fuel main mission [kg]	13509	5022
	Fuel diversion mission [kg]	1286	514
	Fuel holding [kg]	919	372
	Furniture and system mass [kg]	9918	11232
Hydrogen Tank	Global adjusted gravimetrix index		0.71
	Global gravimetrix index		0.71
	Empty mass H2 tanks [kg]		2630
Propulsion	Thrust at sea level [N]	164704	160309
	Thurst to weight ratio	0.35	0.35

These analyses demonstrated that optimizing in-flight performance favors minimizing structural mass by maintaining a low pressure differential over increasing insulation thickness to prevent boil-off. Achieving zero-venting missions is feasible even with a low maximum pressure differential, provided that moderate insulation thickness (e.g., 150–200 mm) is applied without significantly increasing tank weight. However, dormancy periods remain a challenge, as current foam insulation technologies cannot sustain zero-venting beyond a few hours without incurring substantial efficiency penalties. This suggests that redefining dormancy requirements—limiting zero-venting constraints to no more than one hour—could be a pragmatic solution for hydrogen aircraft operations.
Beyond this trade-off, integral tanks were found to be slightly more efficient, while wider tanks, although advantageous in terms of tank weight and insulation, required larger fuselages that adversely impacted overall aircraft fuel efficiency. This highlights the importance of adopting slender tank designs to preserve system-level performance.

Following these analyses, optimal tank design parameters—including 100 mm insulation, a 1 bar pressure differential, and integral tank placement—were identified and fixed to simplify the design space for subsequent optimization. A hydrogen-powered aircraft was then sized using these parameters and compared to a conventional jet-fuel aircraft. The results indicated that while hydrogen propulsion reduces fuel mass by 60% and **MTOW** by 2.7%, the increased empty weight (14%) and degraded lift-to-drag ratio resulted in a 10% increase in total mission energy consumption, though the primary mission energy penalty was limited to 3.5%, the additional penalty stemming from the diversion flight requirement.
While these findings validate the enhanced capabilities of **FAST-OAD** for designing hydrogen tanks and tube and Wing aircraft, they also underscore the need for further innovation to reduce the drop in energy efficiency of hydrogen aircraft. Consequently, the next chapter introduces a new methodology for sizing hydrogen-powered Blended Wing Body aircraft, a promising configuration in that regard.

CHAPTER V

Extending FAST-OAD for Hydrogen Blended Wing Body Sizing: A Framework for Flexible Tank Configuration Design

Résumé

Ce chapitre présente l'extension du programme FAST-OAD, incluant une méthodologie permettant de dimensionner des ailes volantes à hydrogène par l'exploration et l'optimisation d'un vaste espace de conception relatif aux configurations possibles de réservoirs d'hydrogène (nombre, taille et positionnement).

La première partie présente l'adaptation de FAST-OAD aux géométries de type aile volante. Pour ce faire, les modèles de dimensionnement géométrique et structurel initialement intégrés dans FAST-OAD et limités aux configurations **T&W** sont remplacés par ceux développés précédemment dans le cadre du projet CICAV de l'ONERA, spécifiquement conçus pour les ailes volantes. Le premier module permet ainsi de dimensionner la cabine puis la cellule de l'aile volante à partir des **TLARs**, selon une paramétrisation détaillée. Le module structure en déduit ensuite la masse, en considérant une architecture dotée d'une paroi structurante capable de supporter à la fois la pression interne et les charges aérodynamiques, grâce à une structure rigidifiante. Parallèlement

à l'intégration de ces modèles dans FAST-OAD, un nouveau modèle est développé afin d'estimer la marge statique d'une aile volante, et donc sa stabilité longitudinale, au moyen d'une analyse aérodynamique de type *Vortex Lattice Method* réalisée avec le logiciel VSP AERO. Par ailleurs, afin d'anticiper le déplacement du centre de gravité induit par l'intégration des réservoirs d'hydrogène, de nouveaux modules sont implémentés pour optimiser la position des moteurs et du train d'atterrissage principal.

Une fois FAST-OAD capable de dimensionner une aile volante conventionnelle, le chapitre introduit un cadre spécifique pour le design d'une aile volante à hydrogène. Pour cela, une nouvelle paramétrisation a été développée, permettant de définir le nombre, la position et la géométrie de réservoirs cylindriques intégrés dans l'aile volante. Cette approche offre un large éventail de configurations possibles. Les réservoirs sont répartis en deux familles : ceux disposés longitudinalement de part et d'autre de la cabine, et ceux placés derrière celle-ci, parallèlement aux rangées de sièges selon l'axe transversal. Chaque famille est organisée en rangées, pouvant accueillir plusieurs réservoirs. Cette paramétrisation, implémentée dans FAST-OAD, permet ainsi de faire varier librement le nombre de rangées, le nombre de réservoirs par rangée (potentiellement différent d'une rangée à l'autre), ainsi que les dimensions et le positionnement de chaque réservoir individuel.

Si de nombreuses configurations peuvent être générées, il reste impossible de déterminer a priori lesquelles sont optimales, voire même physiquement réalisables. En effet, définir dès ce stade une stratégie de dimensionnement arbitraire conduirait probablement à des solutions faisables mais sous-optimales. De ce fait, la boucle de design classique est adaptée : en l'absence d'une unique solution pour la **MDA** satisfaisant les contraintes, on se tourne vers une démarche d'analyse et d'*optimisation* multidisciplinaires. Un ensemble de contraintes est alors introduit afin de garantir la faisabilité des configurations explorées. Ces contraintes concernent le volume minimal de stockage en hydrogène, la marge statique de l'avion (qui doit rester positive pour assurer la stabilité longitudinale), ainsi que les contraintes géométriques d'intégration, imposant que les réservoirs puissent effectivement s'insérer dans le volume de la cellule sans se chevaucher.

Le design d'une aile volante à hydrogène se formule ainsi comme un problème d'optimisation sous contraintes, présenté dans la dernière partie du chapitre. Ce problème, particulièrement complexe, implique un grand nombre de contraintes et de variables, dont certaines sont continues et d'autres catégorielles, définissant un problème à variables mixtes. Par ailleurs, elles sont organisées de façon hiérarchique, certaines variables conditionnant l'existence d'autres. La structure de l'implémentation MDAO réalisée pour sa résolution y est ensuite détaillée.

Contents of this Chapter

V.1 Introduction 142
V.2 Implementation of a FAST-OAD Extension for BWB Geometry Generation, Structural Sizing, and Stability Analysis Using the CICAV Framework 142
V.2.1 Description of the Geometry Module 143
V.2.2 Description of the Structure Module 144
V.2.3 Description of the Stability Module 146
V.2.4 Development of a New System Positioning Module 147
V.3 Development of a Hydrogen Tank Sizing and Positioning Framework for BWB 149
V.3.1 Development of a new Parametrization for Cylindrical Tank Integration into a BWB 149
V.3.1.1 Parametrization of Tank Number and Placement 150
V.3.1.2 Parametrization of Tank Geometry 152
V.3.1.3 Parametrization of Tank Spacing 153
V.3.2 Formulation of Design Space Constraints for Feasible and Optimal Hydrogen Blended Wing Body Configurations 155
V.3.2.1 Fuel Tank Volume Constraint 156
V.3.2.2 Geometric Constraints on Rear–Side Tank Intersections . 157
V.3.2.3 Tank Positioning Constraints Relative to Control Surfaces 158
V.3.2.4 Limitations on Tank Radius Imposed by Airframe Thickness 159
V.3.2.5 Static Margin Constraints for Aircraft Stability 160
V.4 Set-up of MDAO Framework in FAST-OAD for the Sizing of Hydrogen BWB 161
V.4.1 Specification of the Multidisciplinary Optimization Problem 161
V.4.2 Complete MDAO Framework for Hydrogen BWB Design 165
V.5 Conclusion 166

V.1 Introduction

When Sgueglia first developed the aircraft sizing tool **FAST** in 2019 [**99**], it was capable of designing both **T&W** and **BWB** configurations. Since then, the platform has evolved into the open-source software **FAST-OAD**, through continuous module development, a redesigned software architecture, and the integration of projects originating from both ONERA and ISAE-SUPAERO. During this evolution, however, the capability to model **BWB** configurations was unfortunately lost.
In parallel, ONERA has developed **CICAV**, another sizing platform implemented in Python and built on the OpenMDAO framework—similar to FAST-OAD—but specifically designed for the conceptual design of **BWB** configurations [**104**]. Despite their shared foundations, FAST-OAD has been prioritized as the primary development platform, especially for shared work between ISAE-SUPAERO and ONERA, due to the common open source core available to researchers and students. For this reason, the decision was made in this thesis to extend FAST-OAD's capabilities to include BWB sizing by integrating the relevant disciplinary modules from **CICAV**. The first section of this thesis focuses on this adaptation. To enable **FAST-OAD** to handle flying-wing configurations, its original geometric and structural sizing models were replaced with specialized models developed under the **CICAV** project, tailored specifically for BWB aircraft. Additionally, a new aerodynamic model was introduced to assess the static margin—a key parameter for longitudinal stability—using VSP AERO. New modules were also implemented to optimize the positioning of engines and the main landing gear, ensuring compatibility with the unique demands of BWB designs.

Building on this foundation, the chapter introduces next a comprehensive framework for hydrogen-powered flying-wing design. A novel parameterization method is established to define the number, position, and geometry of cylindrical hydrogen tanks within the flying wing, enabling a diverse range of configurations. To ensure the feasibility of the aircraft, a set of geometric and stability constraints is also incorporated.
Given the complexity of the resulting design space, the traditional Multidisciplinary Analysis approach used in FAST-OAD is evolved into a Multidisciplinary Design Analysis and Optimization framework. This transformation allows for a systematic exploration and refinement of potential solutions, ensuring that the final design meets all technical and operational requirements.

V.2 Implementation of a FAST-OAD Extension for BWB Geometry Generation, Structural Sizing, and Stability Analysis Using the CICAV Framework

While developing a **FAST-OAD** version specialized for **BWB** configurations, several existing modules could be reused without modification. For instance, the aerodynamic

module [**124**], already employed for the design of hydrogen **T&W** aircraft in Chapter IV, can also be applied to **BWB** configurations (see Table I.1). In this case, the wing is defined with five segments instead of three, and the fuselage is simply omitted. Similarly, the performance module, which performs a time-step integration of the mission to evaluate fuel consumption, can also be kept as is, as it only requires a drag polar, a mass breakdown, and an engine performance table as input, and is therefore not directly impacted by the configuration change.
The truly missing components are a geometry module, to define the aircraft shape from the TLARs, and a structural module capable of estimating the mass of the aircraft as defined by the geometry. In addition, a stability analysis module should be included, since the current **FAST-OAD** approach of adjusting the wing position to ensure a positive static margin is not applicable to **BWB** configurations.

V.2.1 Description of the Geometry Module

The geometry module of **CICAV**, slightly adapted to the requirements of this thesis (in particular to allow for the later integration of hydrogen tanks) generates the aircraft shape using the Top-Level Aircraft Requirements (TLARs) and sectional inputs for each wing segment. It supports two primary configurations: a short-to-medium range layout with a single-level cabin and a cargo hold alongside the passenger compartment, and a long-range layout featuring a wider cabin with the cargo hold beneath the central cabin section. Each half-wing of the **BWB** is defined by five lateral sections, labeled from Plan 0 (P0) to Plan 3 (P3), as shown in Figure V.1. The sequence of planes, from the central symmetry plane to the wingtip, is defined as :

- **p0**: Central symmetry plane of the aircraft.
- **p0.1**: First vertical frame designed to reinforce the structure and carry the pressure loads. In a **SMR** configuration, it also marks the limit of the cabin, whereas in a long-range configuration it corresponds to the limit of the hold located beneath the cabin.
- **p1**: End of the pressurized section, where the bulkhead is located. This point also marks the end of the hold in a **SMR** configuration, or the end of the cabin in a **Long-Range (LR)** aircraft. It is also the start of the transition zone.
- **p2**: Limit of the transition zone and beginning of the external wing.
- **p2.1**: Wing kink of the external wing.
- **p3**: Wing tip, where the winglets are attached.

For each section, a different airfoil can be selected. The geometry module also needs the sweep, the twist and the ratio of the chord dedicated to the control surface of each plan. From there the process is divided in three main steps:

- **Cabin sizing:** Based on the dimensions of the seats, galleys, toilets, and aisles, together with the cabin row layout, the compartment width is determined. Knowing the total number of passengers and assuming equal wing sweep at p0 and p0.1, the

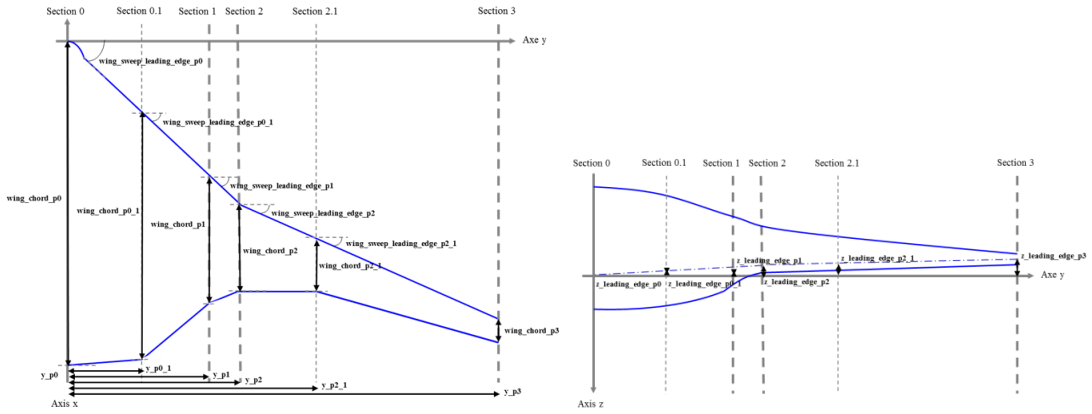

Figure V.1: **BWB** geometry parametrization of **CICAV** which divide the wing in five segment[**105**]

cabin length and width can then be derived. A similar procedure is applied to define the size of the hold—whether positioned alongside or beneath the cabin. The positions of the doors and the cockpit are also established at this stage, completing the definition of the pressurized section of the aircraft.

- **External wing sizing:** With the cabin and hold dimensions defined, the planform of the central part of the BWB can be deduced. From the airfoil thickness ratio t/c at p0 and the maximum cabin (and possibly hold) height h_{max-p0}, the chord at p0 is obtained as

$$c_{p0} = \frac{h_{max-p0}}{t/c}.$$

  The trailing edge is then set parallel to the y-axis between p0 and p1, which fixes the chord lengths at p0.1 and p1 (with the cabin and hold corner boxes truncated to fit within the airfoil envelope). The transition zone is subsequently defined (its width being an input) to connect to the external wing. For this outer wing, the airfoil, chord, and sweep are inputs, while the span is obtained by stretching the wing until the maximum allowable span is reached.

- **Engine Sizing** : Once the planform of the aircraft is known, the engines are positioned either over the central body or under the wings.

V.2.2 Description of the Structure Module

The Structure and Weight module is integrated into the **MDAO** process to determine the aircraft's mass breakdown, balance, and inertia. These quantities are obtained through a two-step procedure:

- **Primary Structure Sizing** : In the first step, the module constructs a **Finite Element (FE)** model of the aircraft's primary structure. For BWB configurations, this structure consists in the pressurized section—housing both the passenger cabin and the cargo hold—as well as the wing fuel tanks. The primary structure is bounded by the leading- and trailing-edge spars, visible in black in the figure V.2, which

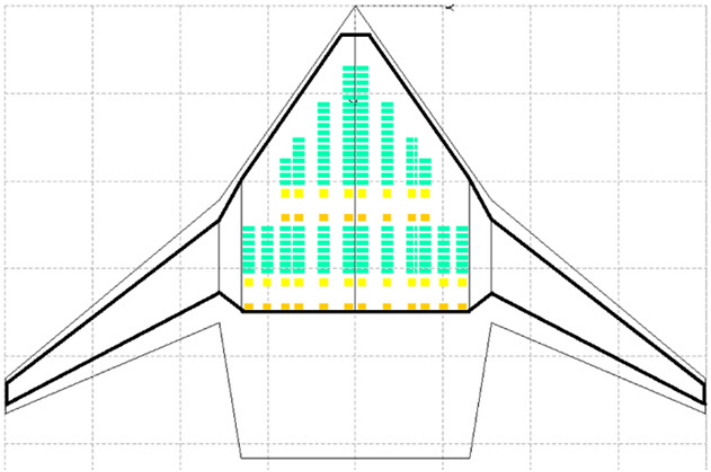

Figure V.2: Primary structure contours on a typical BWB configuration planform (top view) [**107**]

enclose both the pressurized section and the wing tanks. The adopted structural concept is a single-shell design, where the aircraft's outer skin—supported by a stiffening structure—bears both pressure and aerodynamic loads. This contrasts with alternative concepts proposed by Liebeck [**160**], such as the multi-bubble shell (where pressure loads are carried by interconnected cylindrical structures) and the double-shell design (featuring two walls separated by a sandwich structure).

In CICAV, the pressurized part is so represented as a thin composite shell reinforced with stringers on the upper and lower skins. These skins sustain both the internal pressurization loads and the external aerodynamic loads. Stringers are distributed in the longitudinal and spanwise directions, as can be seen in figure V.3 while the upper and lower skins are interconnected by structural rods acting as partition walls (some are are placed in the cabin and are use as compartment delimiting walls). The primary structure of the wing is modeled using conventional wing-box architecture with ribs. For conventional kerosene-powered aircraft, fuel is stored in these external wings.

The FE model is used to size the primary structure against two main load categories: pressurization loads, and the flight load cases defined in the CS-25 certification specifications [**154**] (e.g. maneuvers, gusts), applied under the most critical aircraft weights and flight configurations. From this sizing process, the mass breakdown, balance, and inertia of the primary structure are directly obtained.

- **Subsystems Integration** : In a second step, the module accounts for all other subsystems distributed throughout the BWB geometry, including power units, landing gear, systems, furnishings, and operator items. Their mass properties are estimated using expert rules and statistical correlations derived from existing aircraft. Finally, the contributions from the primary structure and all subsystems are aggregated to compute the overall aircraft mass breakdown, balance, and inertia at different mission points (e.g. take-off, cruise, landing, operational empty weight). The weight, balance, and inertia of the wing fuel tanks are also evaluated under several filling

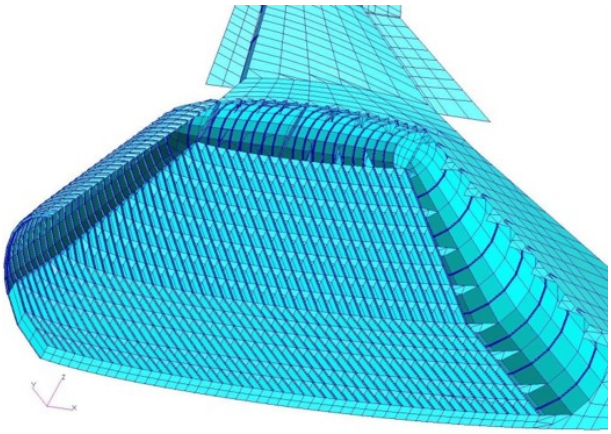

Figure V.3: 3D view of the bottom part of the primary structure of a BWB in CICAV with visible stiffeners

conditions.

V.2.3 Description of the Stability Module

This module aims to analyze the longitudinal stability of a **BWB** aircraft configuration. Unlike conventional aircraft, a BWB does not rely on a horizontal tail for pitch stability. Instead, it utilizes reflex airfoils, which produce downward lift at their trailing edges to dynamically balance the aircraft's lift distribution. Consequently, the approach implemented in FAST-OAD for **T&W** aircraft—primarily based on adjusting the wing position along its axis to optimize the aerodynamic center—is not applicable to BWB configurations. While the CICAV framework already included a stability assessment module for **BWB** configurations, a new, simplified module was developed for this study. The original module was too complex for the intended application and lacked the flexibility required to evaluate hydrogen-powered configurations with shifted centers of gravity.

To assess the longitudinal stability of a BWB, an aerodynamic analysis of the entire aircraft body is required. Pitch stability is typically characterized by the static margin, defined in Equation V.2. The static margin quantifies the distance between the aircraft's center of gravity and its neutral point, normalized by the **Mean Aerodynamic Chord (MAC)**. The neutral point, denoted as x_{np}, is also referred to as the aerodynamic center. It is defined as the location where the lift-induced pitching moment coefficient $c_{m,L}$ remains independent of the angle of attack α (and thus independent of c_L). Mathematically, this condition is expressed as: $\frac{dc_m}{dc_L}\Big|_{x_{np}}$. It can be computed with equation V.1

$$x_{np} = \frac{-\frac{dc_{m,L}}{d\alpha}}{\frac{dc_L}{d\alpha}} c_{MAC} \tag{V.1}$$

$$SM = \frac{x_{cg} - x_{np}}{c_{MAC}} \tag{V.2}$$

To evaluate the static margin, it is necessary to determine the mean aerodynamic chord

(MAC), as well as the derivatives of the lift coefficient and pitching moment coefficient with respect to the angle of attack.
To address this objective, the Handling Qualities Module automates the analysis by means of a batch-processing workflow, illustrated in Figure V.4. The process is initiated by the Geometry Module, which computes the geometric definition of the aircraft and writes it to a `.vspscript` file. This file is then used as input to OpenVSP [**161**], where a three-dimensional model of the BWB configuration is generated. The OpenVSP model is subsequently converted into a degenerate geometry representation of the aircraft, which serves as input for VSPAERO. The software performs an aerodynamic analysis using the **Vortex Lattice Method (VLM)**. The VSPAERO model is configured to evaluate aerodynamics in cruise conditions, incorporating compressibility effects through the second-order Karman-Tsien Mach correction. When running VSPAERO in steady stability mode through the batch process, the analysis outputs the required derivatives, enabling the estimation of the static margin - the center of gravity being computed within the structure module.

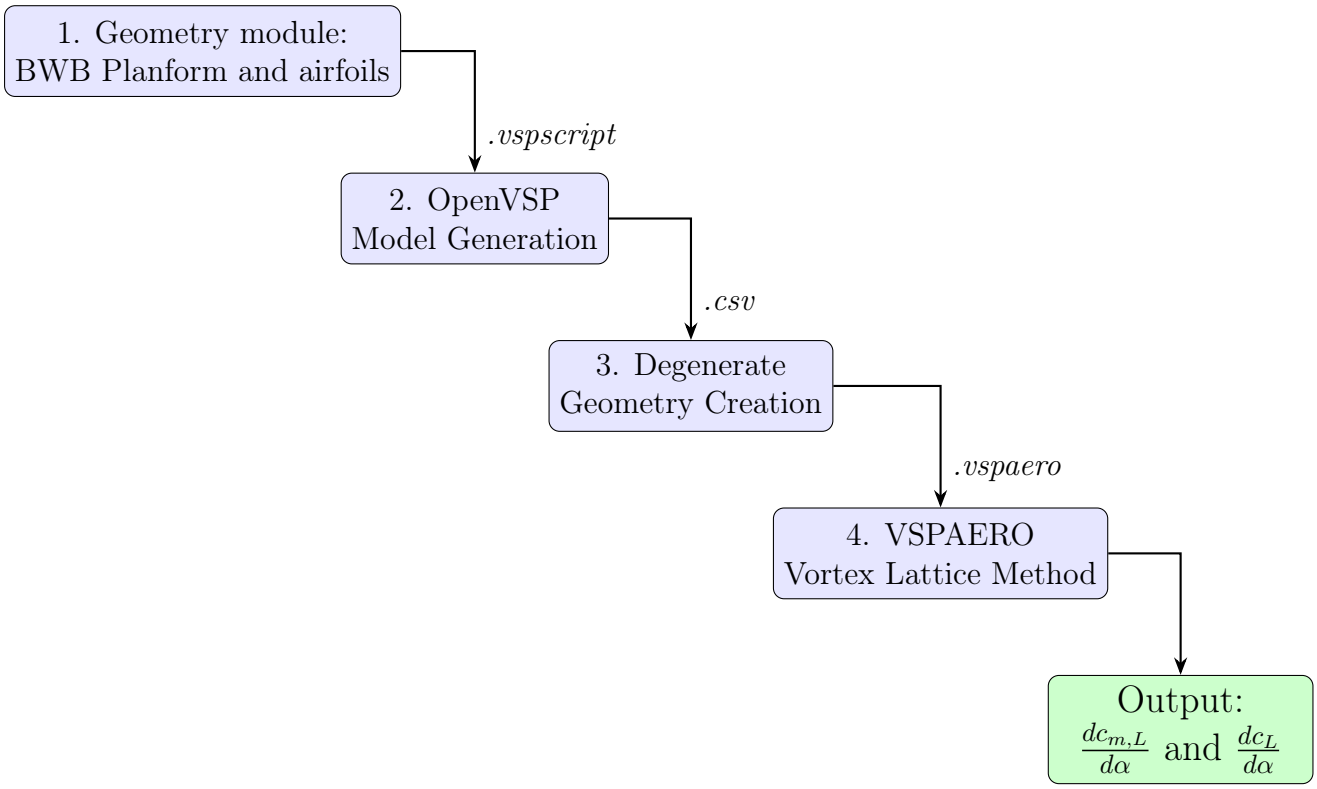

Figure V.4: Workflow for BWB stability analysis

V.2.4 Development of a New System Positioning Module

In the original CICAV design procedure, the position of certain subsystems—such as the landing gear, consisting of a nose gear and two main gears—was treated as a fixed input rather than determined during the sizing process. Similarly, the engines were systematically placed on the upper surface of the central section of the airframe, just ahead of the control surfaces.

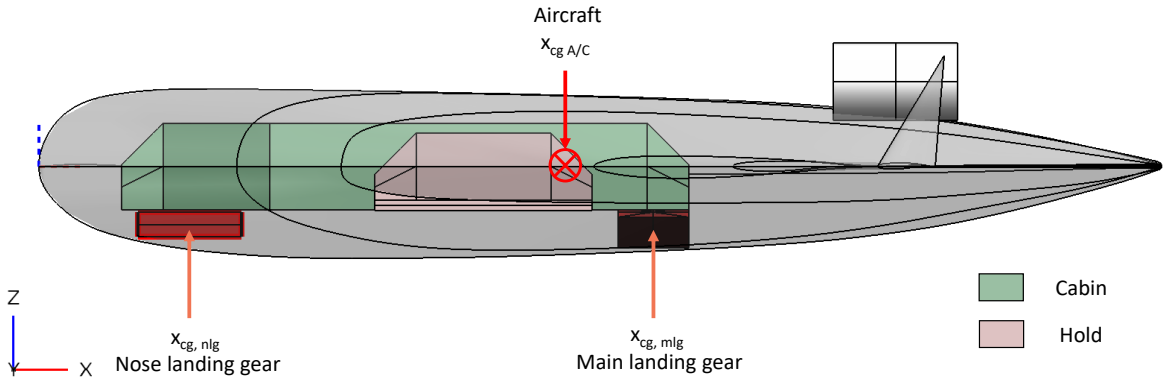

Figure V.5: Side view of the landing gear longitudinal position on a blended wing body

The integration of hydrogen tanks, however, can lead to substantial modifications in the **BWB** configuration. The additional mass of the tanks strongly influences the aircraft's center of gravity. With a fixed landing gear layout, some configurations may result in the center of gravity shifting aft of the main gear location, which would cause instability on the ground or during taxiing.

To overcome this issue, a new module was developed to adaptively position both the engines and the landing gear. For the engines, they remain mounted on the upper surface of the airframe, but are shifted forward so that the inlets are located just aft of the last rear tank row (see Figure V.7). In some configurations, side tanks may intersect the engine inlet plane, but since they are offset laterally, the risk associated with an uncontained engine failure was considered acceptably low, given the narrow angular range in which a potential blade release could be problematic.

For the landing gear, the adopted strategy is to dynamically adjust the longitudinal position of the main landing gear in order to achieve an appropriate load distribution between the main and nose landing gears when the aircraft is on the ground. More specifically, the position of the main landing gear x_{mlg} (see Figure V.5) is set such that the nose gear supports 8% of the total aircraft mass when the center of gravity $x_{cg,A/C}$ is at its most aft location (typically corresponding to the condition of full tanks with no payload).

This condition can be expressed mathematically as:

$$x_{mlg} = \frac{x_{cg,A/C}}{0.92} + x_{nlg} \tag{V.3}$$

V.3 Development of a Hydrogen Tank Sizing and Positioning Framework for Blended Wing-Body Aircraft

V.3.1 Development of a new Parametrization for Cylindrical Tank Integration into a BWB

The updated version of FAST-OAD described in the previous section is capable of performing preliminary sizing of Blended Wing Body aircraft, but thus far only under the assumption of conventional kerosene propulsion. Extending this capability to the conceptual design of hydrogen-powered **BWB**s requires the explicit modeling of hydrogen storage, since the same fundamental challenges associated with hydrogen fuel remain. In particular, hydrogen requires large, heavy, pressurized, and cryogenic tanks, whose impact on the overall aircraft architecture and performance is as significant for **BWB** as for **T&W**. This justifies the necessity of also including their representation at the early stages of hydrogen BWB design.

For conventional **T&W** aircraft, the options for tank integration are relatively limited. The number of tank is usually set to two, mainly for redundancy. Excluding unconventional configurations, tanks are generally located within the fuselage or mounted in pods beneath the wing. Once one of these options is selected, the tanks—and correspondingly the fuselage or pod—can be extended as needed to achieve the required storage volume, as discussed in Chapter II.

In contrast, tank integration within a **BWB** configuration is considerably less straightforward. The large volume available in the transition region between the cabin and the outer wing, or in the aft section behind the cabin, would in principle be well-suited for conformal tanks. However, the design of cryogenic and pressurized conformal tanks—assuming their feasibility and structural efficiency—remains a significant challenge and lies beyond the scope of this study.

When considering cylindrical tanks as an alternative—or as an intermediate step toward fully conformal tanks to improve volume efficiency—the optimal number of tanks and their placement are not immediately obvious. The influence of tank geometry and positioning on the overall aircraft architecture is indeed inherently more complex than in conventional tube-and-wing designs. Unlike the latter, the process cannot be reduced to simply stretching the fuselage by the required length. Most studies to date have instead relied on arbitrarily fixed tank configurations or on simplified sizing procedures (see Section I.4), neither of which has been demonstrated to yield optimal solutions.

To address these challenges, this study develops a new parametrization method for cylindrical tank positioning and geometry within a **BWB** configuration. This approach enables the systematic definition of a wide range of tank configurations—including variations in position, size, number, and placement—thereby facilitating comparative analysis and the identification of optimal arrangements. The proposed methodology provides a rigorous framework for evaluating tank integration strategies that were previously limited by simplified assumptions or arbitrary placements.

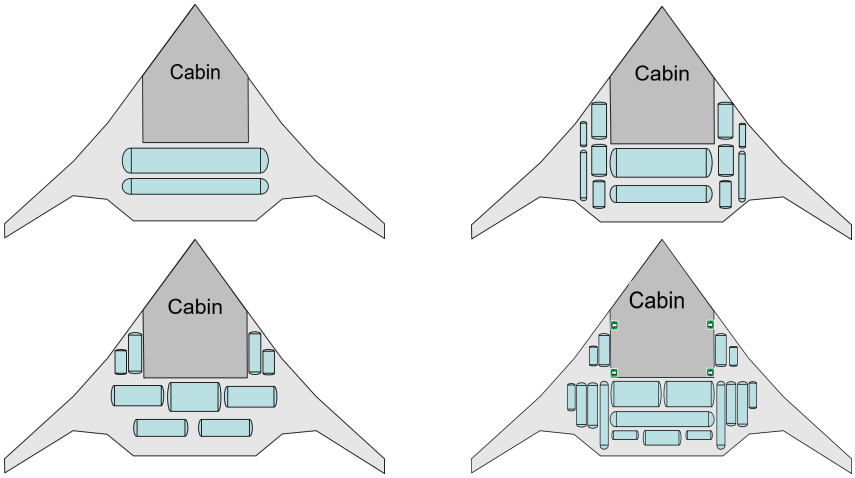

Figure V.6: Illustration of the range of possible tank configuration in a hydrogen BWB aircraft with four conceptual examples

V.3.1.1 Parametrization of Tank Number and Placement

As previously discussed, determining the optimal number and placement of hydrogen tanks in a **BWB** is not straightforward. In order to reduce the otherwise vast design space and make the problem more tractable, a set of simplifying assumptions has been introduced :

- Redundancy Requirement: A minimum of two tanks is mandated to ensure operational redundancy
- Symmetry Constraint: All tank configurations are required to be symmetric with respect to the aircraft's longitudinal axis.
- Orientation Options: Tanks may be oriented either
  - Parallel to the longitudinal axis (x-axis) within the cabin transition zone
  - Parallel to the lateral axis (y-axis) aft of the cabin in the rear fuselage section

Despite these constraints, a wide range of feasible tank configurations remains. Figure V.6 presents four representative arrangements that could be envisioned within a **BWB** architecture. At the preliminary design stage—when essential parameters such as the required fuel volume, tank system mass, and the resulting influence on the aircraft's center of gravity are still uncertain—it is not yet possible to identify a single optimal configuration. Moreover, the most suitable arrangement is expected to be mission-dependent, implying that different operational profiles may call for distinct tank integration strategies.

To mathematically define all those different configuration, a parametric framework is introduced. Within this formulation, tanks are organized into distinct rows. The maximum number of rows along the cabin transition zone is denoted by $\boldsymbol{Max_{side}}$, while the maximum number of row in the aft fuselage section is represented by $\boldsymbol{Max_{rear}}$. The number of tanks on the side rows or rear rows are specified by $\boldsymbol{N_{side}}$ and $\boldsymbol{N_{rear}}$ such that :

- N_{side} is a vector of dimension Max_{side} : $\boldsymbol{N_{side}} \in \mathbb{N}^{\boldsymbol{Max_{side}}}$
- $\boldsymbol{N_{rear}}$ is a vector of dimension Max_{rear} : $\boldsymbol{N_{rear}} \in \mathbb{N}^{\boldsymbol{Max_{rear}}}$

The number of tanks per row is subject to specific limitations:

- Side Rows: Each side row is constrained to a maximum of $\boldsymbol{Max_{tank/srow}}$ tanks per row, a limit uniformly applied across all side rows.

  While this parameter is typically set to 3 for baseline configurations, it remains adjustable to accommodate alternative design requirements.

- Rear Rows: The rear rows are limited to a maximum of $\boldsymbol{Max_{tank/rrow}} = 4$ tanks per row

Two conceptual example of hydrogen **BWB** configuration are presented in figure V.7a and V.7b. The first aircraft place a majority of the fuel in rear tanks, whereas the second has a more distributed repartition between rear and side rows. Those two tank arrangements are defined by :

- Figure V.7a :

$$\begin{cases} \text{Max}_{\text{side}} = 3 \\ \text{Max}_{\text{rear}} = 3 \\ N_{\text{side}} = (1, 1, 0) \\ N_{\text{rear}} = (3, 2, 0) \\ \text{Max}_{\text{tank/srow}} = 3 \\ \text{Max}_{\text{tank/rrow}} = 4 \end{cases}$$

- Figure V.7b :

$$\begin{cases} \text{Max}_{\text{side}} = 3 \\ \text{Max}_{\text{rear}} = 2 \\ N_{\text{side}} = (3, 1, 1) \\ N_{\text{rear}} = (1, 1) \\ \text{Max}_{\text{tank/srow}} = 3 \\ \text{Max}_{\text{tank/rrow}} = 4 \end{cases}$$

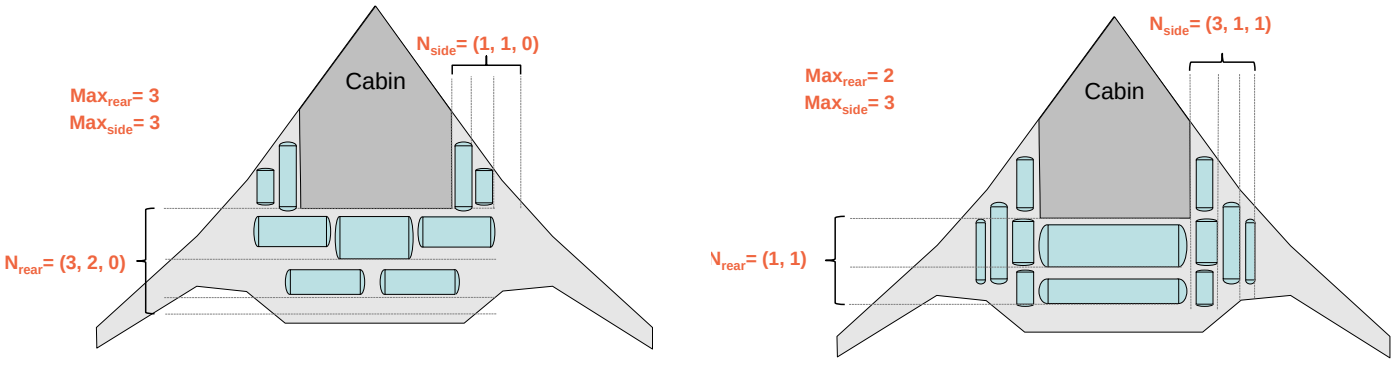

(a) Example 1

(b) Example 2

Figure V.7: Examples of tank number parametrization

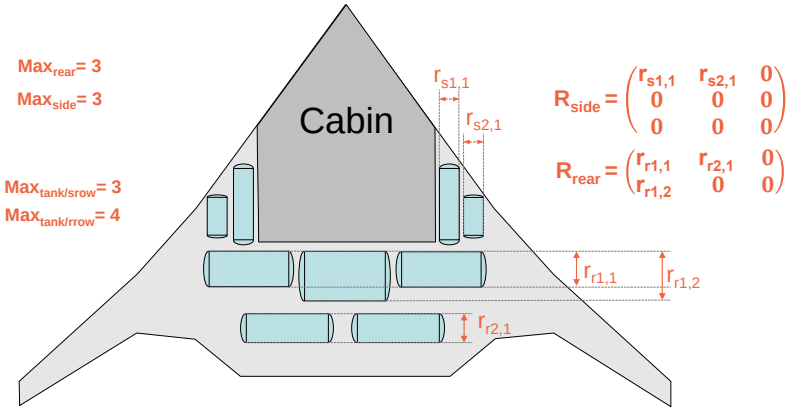

Figure V.8: Example of tank radius parametrization

V.3.1.2 Parametrization of Tank Geometry

Following the determination of the number of tanks, the geometry of each tank must be specified. The geometry is characterized by three main variables: the radius (r), the total length (l), and the bulkhead type. The total length includes the contribution of the bulkhead. For simplicity, the bulkhead is modeled as either hemispherical or elliptical, with the latter assuming a 1:2 aspect ratio between the major and minor axes (called semi-elliptical). Consequently, the dome height of the bulkhead corresponds either to the tank radius (hemispherical) or to half the radius (elliptical).
To facilitate the representation, the tank radius and length are represented using matrices. Each column corresponds to a tank, while each row represents a specific arrangement row of tanks. Two matrices are used for both the radius and length: one for the side rows and another for the rear rows. Due to the aircraft's symmetry, the side-row matrices define the geometry for both sides of the cabin. For the rear tanks, given the constraint of a maximum of four tanks per row and the requirement for symmetry, only two distinct geometries per row are possible.
An example of tank radius parametrization is illustrated in Figure V.8, with the corresponding definitions provided below:

- The side row radii are defined by $\boldsymbol{R}_{\text{side}} \in \mathbb{M}^{\text{Max}_{\text{tank/srow}} \times \text{Max}_{\text{side}}}$:

$$R_{\text{side}} = \begin{pmatrix} r_{s1,1} & r_{s2,1} & r_{s3,1} \\ r_{s1,2} & r_{s2,2} & r_{s3,2} \\ r_{s1,3} & r_{s2,3} & r_{s3,3} \end{pmatrix} = \begin{pmatrix} r_{s1,1} & r_{s2,1} & 0 \\ 0 & 0 & 0 \\ 0 & 0 & 0 \end{pmatrix}$$

- The rear row radii are defined by $\boldsymbol{R_{rear}} \in \mathbb{M}^{2 \times \text{Max}_{\text{rear}}}$:

$$R_{\text{rear}} = \begin{pmatrix} r_{r1,1} & r_{r2,1} & r_{r3,1} \\ r_{r1,2} & r_{r2,2} & r_{r3,2} \end{pmatrix} = \begin{pmatrix} r_{r1,1} & r_{r2,1} & 0 \\ 0 & 0 & 0 \end{pmatrix}$$

Another example for tank length parameterization is illustrated in Figure V.9, with the

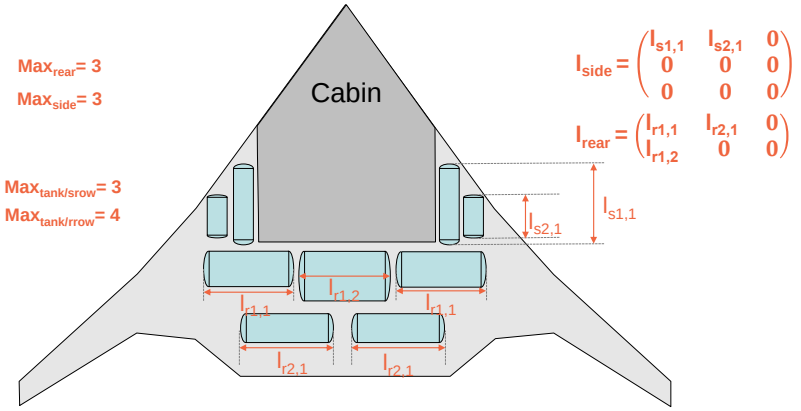

Figure V.9: Example of tank length parametrization

corresponding definitions provided below:

- The side row lenths are defined by $\boldsymbol{L}_{\text{side}} \in \mathbb{M}^{\text{Max}_{\text{tank/srow}} \times \text{Max}_{\text{side}}}$:

$$L_{\text{side}} = \begin{pmatrix} l_{s1,1} & l_{s2,1} & l_{s3,1} \\ l_{s1,2} & l_{s2,2} & l_{s3,2} \\ l_{s1,3} & l_{s2,3} & lr_{s3,3} \end{pmatrix} = \begin{pmatrix} l_{s1,1} & l_{s2,1} & 0 \\ 0 & 0 & 0 \\ 0 & 0 & 0 \end{pmatrix}$$

- The rear row lengths are defined by $\boldsymbol{L_{rear}} \in \mathbb{M}^{2 \times \text{Max}_{\text{rear}}}$:

$$L_{\text{rear}} = \begin{pmatrix} l_{r1,1} & l_{r2,1} & l_{r3,1} \\ l_{r1,2} & l_{r2,2} & l_{r3,2} \end{pmatrix} = \begin{pmatrix} l_{r1,1} & l_{r2,1} & 0 \\ 0 & 0 & 0 \end{pmatrix}$$

V.3.1.3 Parametrization of Tank Spacing

Once the number and geometry of the tanks are defined, the final step in configuring a **BWB** hydrogen storage system is to determine the spatial positioning of the tanks. While it is possible to specify tank positions using absolute Cartesian coordinates (x, y, z), this approach has the drawback of possibly generating unintended overlaps between tanks, particularly when their geometries are parametrically defined.
To mitigate this issue, a relative positioning strategy was adopted. Rather than fixing absolute coordinates, the tanks are positioned with respect to one another, the cabin structure, or the aircraft planform. This approach ensures spatial compatibility and avoids geometric conflicts within the tank arrangement.

The parametrization of tank positioning is again divided between side tanks and rear tanks. For each group, the spatial arrangement is characterized by the spacing between rows of tanks and the spacing between individual tanks within a row or relative to reference structures, such as the cabin or the aircraft's leading edge. This method ensures a systematic and conflict-free integration of the tanks within the BWB configuration. The

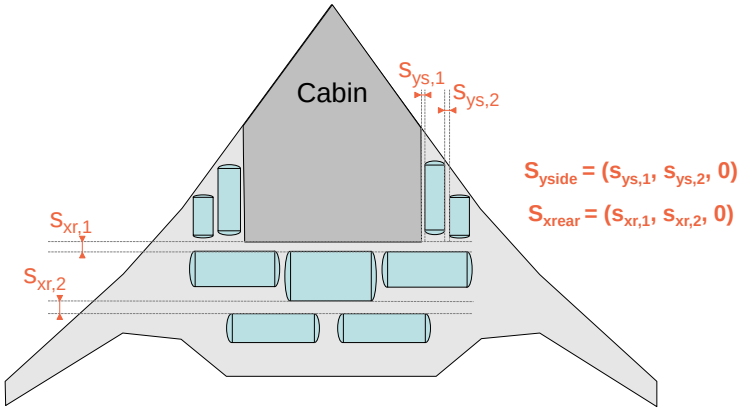

Figure V.10: Illustration of rear and side row spacing parameters $\boldsymbol{S_{xrear}}$ and $\boldsymbol{S_{yside}}$

only possible remaining conflict is between side and rear tanks, but that case will be dealt with in the next section V.3.2.
Figure V.10 presents the selected parameters for characterizing row spacing, detailed below :

- **Rear rows** : the initial spacing is defined as the x-axis distance between the cabin bulkhead and the forward limit of the first tank row. Subsequent spacings are determined by the x-axis distance between the aft-most limit of the tanks in a given row and the forward limit of the following row. Those distance are represented in the vector $\boldsymbol{S_{xrear}} \in \mathbb{R}^{Max_{rear}}$. In the case of the maximum three-rear-row configuration in figure V.10:

$$S_{xrear} = (s_{xr,1}, s_{xr,2}, s_{xr,3}) = (s_{xr,1}, s_{xr,2}, 0)$$

- **Side rows** : the initial spacing is defined as the y-axis distance between the cabin side bulkhead and the outer limit of the first tank row. Subsequent spacings are determined by the y-axis distance between the outermost limit of the tanks in a given row and the innermost limit of the adjacent, more centrally located row. These distances are compiled in the vector $\boldsymbol{S_{yside}} \in \mathbb{R}^{Max_{side}}$. In the case of the maximum three-side-row configuration in figure V.10:

$$S_{yside} = (s_{ys,1}, s_{ys,2}, s_{ys,3}) = (s_{ys,1}, s_{ys,2}, 0)$$

The parameters used to define the spacing between tanks within each row are presented in Figure V.11 and described as follows:

- **Rear rows** : The spacing is characterized by the variable $(S_{yrear}) \in \mathbb{R}^{Max_{rear} \times 2}$. The parametrization varies according to the number of tanks per row, as described below: :

  - *Zero or one tank*: No lateral spacing is required, as the tank is centered on the longitudinal axis. This is the case in figure V.11a.

- *Two tanks*: The tanks are positioned symmetrically about the x-axis. The spacing is defined as the y-distance between the x-axis and the innermost bulkhead top of each tank. An example is provided in Figure V.11b, specifically in the second rear row.
- *Three tanks*: This configuration combines the previous cases. A single tank is centered on the x-axis, flanked by two symmetrically placed tanks. The spacing is defined as the lateral distance between the outermost point of the center tank and the innermost point of each side tank. Due to symmetry, only one variable is necessary. This arrangement is depicted in Figure V.11b, specifically in the first rear row.
- *Four tanks*: This configuration extends the two-tank case by adding two additional tanks, one on each side. Two spacings are defined: the first is analogous to the two-tank case, and the second represents the lateral distance between the central and external tanks.

In the case of the maximum two-rear-row configuration in figure V.11b:

$$S_{yrear} = \begin{pmatrix} S_{yr1,1} & S_{yr2,1} & S_{yr3,1} \\ S_{yr1,2} & S_{yr2,2} & S_{yr3,2} \end{pmatrix} = \begin{pmatrix} S_{yr1,1} & S_{yr2,1} & 0 \\ 0 & 0 & 0 \end{pmatrix}$$

- **Side rows** : For the side rows, the spacing is defined for each row as follows: The initial spacing represents the x-distance between the leading edge and the foremost point of the first tank bulkhead. Subsequent spacings correspond to the x-distance between each consecutive tank within the row. The spacing is characterized by the design variable $(S_{xside}) \in \mathbb{R}^{Max_{\text{tank/side}} \times Max_{\text{side}}}$.

  In the case of the maximum three-side-row configuration in figure V.11a:

$$S_{xside} = \begin{pmatrix} S_{xs1,1} & S_{xs2,1} & S_{xs3,1} \\ S_{xs1,2} & S_{xs2,2} & S_{xs3,2} \\ S_{xs1,3} & S_{xs2,3} & S_{xs3,3} \end{pmatrix} = \begin{pmatrix} S_{xs1,1} & S_{xs2,1} & S_{xs3,1} \\ S_{xs1,2} & 0 & 0 \\ S_{xs1,3} & 0 & 0 \end{pmatrix}$$

V.3.2 Formulation of Design Space Constraints for Feasible and Optimal Hydrogen Blended Wing Body Configurations

The parametrization framework for hydrogen tank configuration, as outlined in the previous section, enables the design of a vast array of potential Blended Wing-Body architectures. However, during the preliminary design phase, selecting an optimal arrangement is inherently challenging for two primary reasons: first, the block fuel volume is initially unknown, and second, there exists a potentially infinite number of feasible configurations. While it is possible to implement a process to determine tank geometry and arrangement, such a method inherently imposes predefined design choices—for example, prioritizing rear or side tanks—thereby limiting the exploration of the design space and potentially

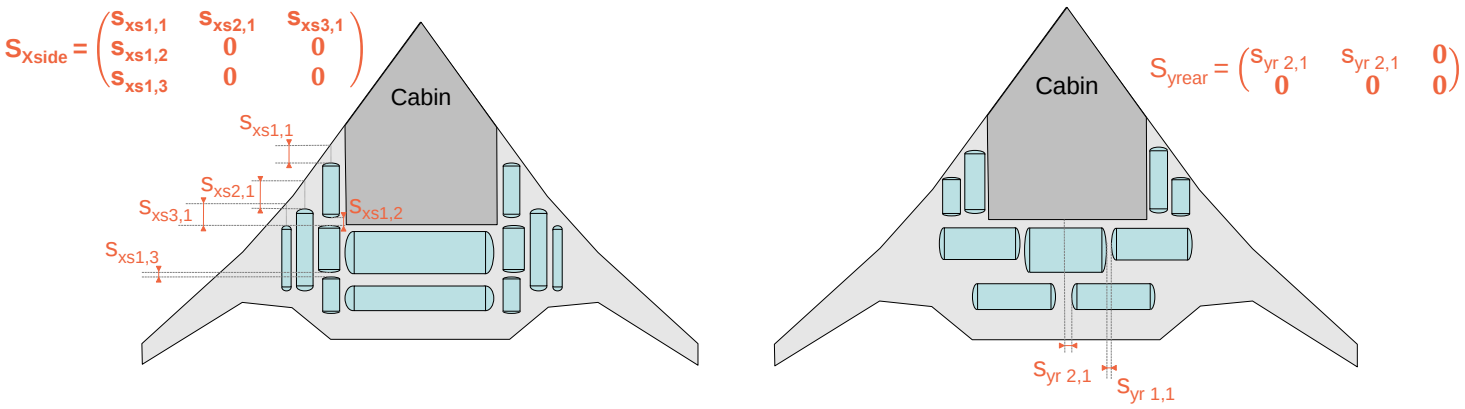

(a) $\boldsymbol{S_{xside}}$ (b) $\boldsymbol{S_{yrear}}$

Figure V.11: Illustration of the tank spacing parameters $\boldsymbol{S_{xside}}$ and $\boldsymbol{S_{yrear}}$

precluding the identification of an optimal configuration. As no knowledge is available about such optimal configurations, this would be detrimental to aircraft performance.

This challenges calls for a fundamental shift in the traditional aircraft design methodology. Conventionally, aircraft design is approached as a multidisciplinary *analysis*, where the objective is to converge toward a unique solution of a nonlinear system comprising various disciplines that describe the aircraft and its mission. In that case, the MDA inherently converges towards a geometrically feasible aircraft satisfying the top-level requirements. However, the complexity introduced by hydrogen tank integration necessitates a shift toward multidisciplinary design *optimization*. A standalone **MDA** approach may generate infeasible designs because it lacks the capability to automatically size and position tanks based on fuel storage requirements, mass balancing, and adjustments to the **BWB** shape to accommodate tank geometry. By contrast, **Multidisciplinary Optimization (MDO)** -when coupled with an appropriate set of constraints and a robust optimization algorithm- enables the identification of feasible designs, i.e the right hydrogen tank parameter of the previous optimization, and, ultimately, the determination of an optimal configuration. This approach ensures that the design process is both comprehensive and adaptive, capable of navigating the vast solution space to achieve performance and feasibility objectives. Unlike **MDA**, **MDO** indeed systematically explores the design space to identify feasible and optimal solutions for the parametrization described earlier.

For a **MDO** to reliably yield feasible aircraft configurations, it is essential to establish a comprehensive and robust set of constraints. These constraints serve to ensure that compliance with all specified requirements directly translates into the overall feasibility of the resulting aircraft design

V.3.2.1 Fuel Tank Volume Constraint

The iterative process of the **MDA**, executed at each optimization iteration, is centered on the fuel mass. By design, the MDA ensures that the fuel mass always satisfies the mission

requirements. However, a critical feasibility concern arises if the storage volume—defined as the combined available volume of the hydrogen tanks—is insufficient to accommodate the required fuel mass. Consequently, the primary constraint in the optimization—whose purpose is to determine the optimal tank dimensions—is to guarantee sufficient storage volume. This requirement is expressed as the sizing fuel volume $V_{f,sizingBF}$ (defined in Eq. II.80), augmented by a small margin mg_{tank} (typically around 3%). This margin accounts for the systems located inside the tank and ensures that a non-zero ullage volume is always maintained.

$$\sum_i V_{tank_i} \geq \frac{V_{f,sizingBF}}{1 - mg_{tank}} \tag{V.4}$$

V.3.2.2 Geometric Constraints on Rear–Side Tank Intersections

As previously discussed, the current parametrization of tank spacing—where tank positions are defined relatively to one another—ensures that no overlap occurs within individual rows or between adjacent rows. However, this parametrization does not inherently prevent intersections between tanks located in rear rows and those in side rows. Such overlaps are possible and are illustrated in Figure V.12. To address this issue, an additional constraint was introduced, focusing on the 2D representation of the aircraft configuration (with 3D intersection volumes neglected due to computational complexity). The constraint requires that the total overlapping area, denoted as $A_{overlap}$, must be zero. This area represents the sum of all overlapping areas between each side tank (identified by its row i and position j, with area $a_{i,j}$) and the outermost tank in each rear row (indexed by k with an area a_k). The intersecting area is denoted $a_{k,i,j}$ Mathematically, this constraint is expressed as:

$$\begin{aligned} A_{overlap} &= 0 \\ \Leftrightarrow \sum_{k}^{Max_{rear}} \sum_{i}^{Max_{side}} \sum_{j}^{Max_{\mathbf{tank/side}}} a_k \cap a_{i,j} &= 0 \\ \Leftrightarrow \sum_{k}^{Max_{rear}} \sum_{i}^{Max_{side}} \sum_{j}^{Max_{\mathbf{tank/side}}} a_{k,i,j} &= 0 \end{aligned} \tag{V.5}$$

The implementation of this constraint in the FAST-OAD software is achieved using the Shapely Python library, which is built on the GEOS computational geometry library [**162**]. Each tank is modeled as an instance of the Polygon class within the Shapely library. This approach enables the calculation of the intersection area between two polygons using the intersection method provided by the class.

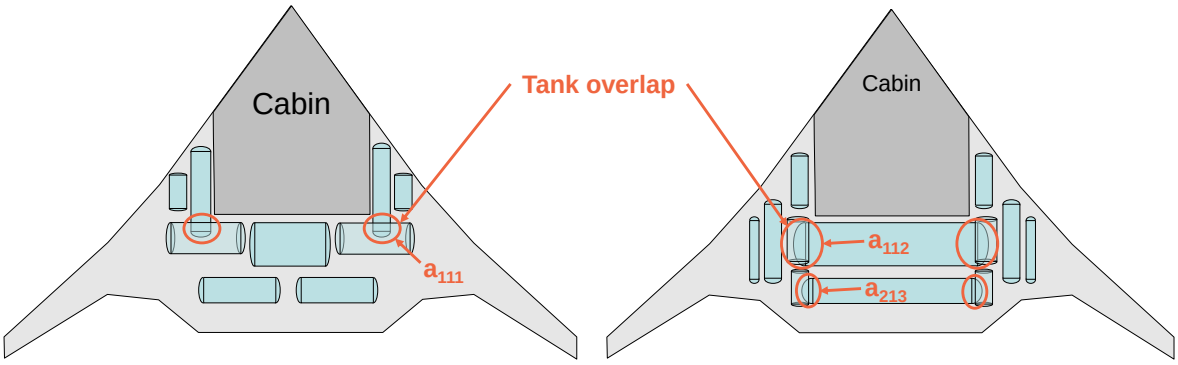

Figure V.12: Example of hydrogen **BWB** configuration with tank overlap

V.3.2.3 Tank Positioning Constraints Relative to Control Surfaces

Another set of constraints arises from the requirement that the tanks must fit within the BWB airframe. Two types of limitations can be defined: the tank diameter must be smaller than the available height in the BWB profile at its placement location, and the tank must not be placed in sections reserved for control surfaces.
Regarding the latter point, since control surfaces are located on the trailing edge, enforcing a constraint on a positive distance between certain tank points and the control surfaces ensures that no tank will interfere with them. Figures V.13 shows the different location where such a constraint must be defined :

- Rear row : Two distances d_{xri1} and d_{xri2}, are checked on each row i to prevent interference between the rear tank row and the control surfaces. These distances represent the longitudinal separation between the bulkhead dome top or the barrel's outermost section of the most outward tank in the ith rear row and the start of the control surface on the trailing edge.

- Side rows: For each side row i, the distance $d_{xs,i}$ between the aft top dome of the most aft tank in the row and the start of the control surface on the trailing edge is defined as a constraint.

Mathematically, the requirement for a positive distance is expressed as:

$$\forall i \in [\![1\ ;\ Max_{rear}]\!], \forall j \in \{1,2\} \quad d_{xr,ji} \geq 0 \tag{V.6}$$

$$\forall i \in [\![1\ ;\ Max_{side}]\!] \quad d_{xsi} \geq 0 \tag{V.7}$$

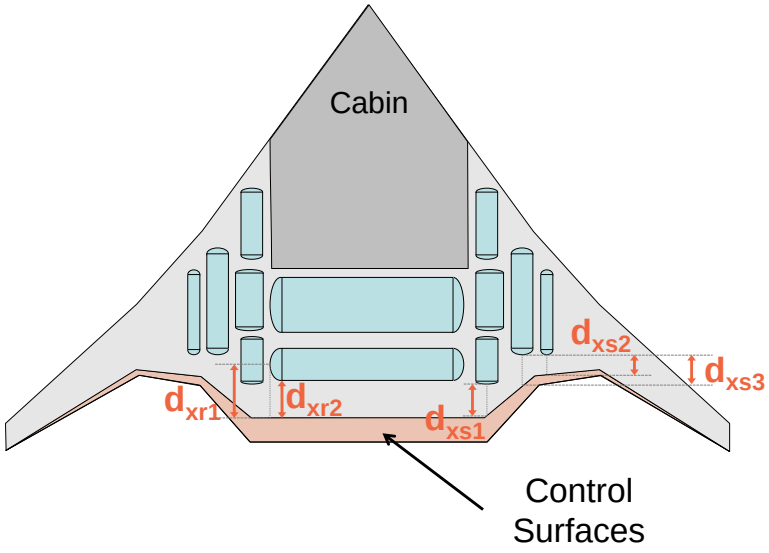

Figure V.13: Illustration of the minimal tank-surface control distance constraint

V.3.2.4 Limitations on Tank Radius Imposed by Airframe Thickness

The final set of geometric constraints relates to the available thickness in the BWB airframe to accommodate hydrogen tanks. Due to their distinct orientations, the constraints are defined differently for tanks located in the side rows versus those in the rear rows:

- Side tanks: Tanks placed in side rows are aligned with the longitudinal axis. Each side tank must be entirely contained within a local airfoil section, as illustrated in Figure V.14. The constraint is consistently defined in the central x–z plane. Because of the possible complexity of the airfoil shapes, the available thickness is measured both at the tank barrel front and rear side. For the jth tank positioned in the ith side row, the available front height is noted $h_{sfront,ij}$, while the rear available height is denoted $h_{srear,ij}$

- Rear tanks: For tanks arranged in the rear rows, the diameter must remain smaller than the available profile height at their respective locations, denoted $h_{r,i,j}$, where i refers to the row index and j to the tank index within that row. These tanks are oriented along the lateral (y) axis, with their centerlines collinear with it, ensuring horizontal placement. As shown in Figure V.15, the available height is defined as the vertical distance between the lowest point of the extrados and the highest point of the intrados along the tank barrel at its central x-location.

Those two sets of constraints can be mathematically expressed as :

$$\forall\, i = 1, \ldots, Max_{side}, \quad \forall\, j = 1, \ldots, Max_{\text{tank/side}} : \quad h_{sfront,ij} > 2r_{s,ij}. \tag{V.8}$$

$$\forall\, i = 1, \ldots, Max_{side}, \quad \forall\, j = 1, \ldots, Max_{\text{tank/side}} : \quad h_{srear,ij} > 2r_{s,ij}. \tag{V.9}$$

$$\forall\, i = 1, \ldots, Max_{rear}, \quad \forall\, j = 1, 2 : \quad h_{r,ij} > 2r_{r,ij}. \tag{V.10}$$

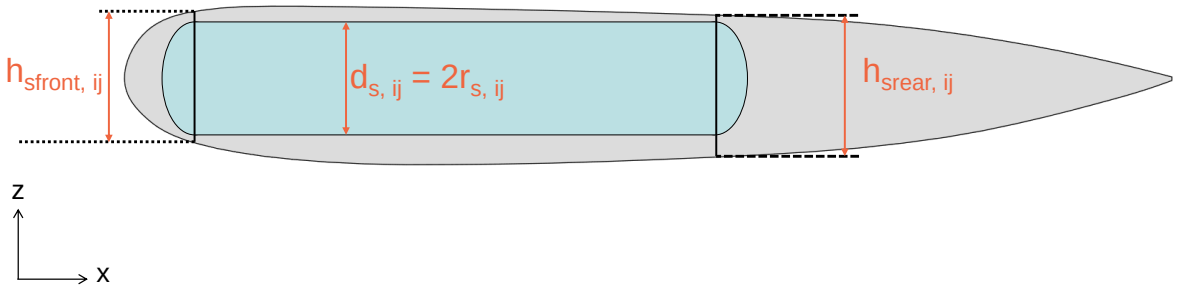

Figure V.14: Constraint formulation for the side tank radius within the BWB airframe

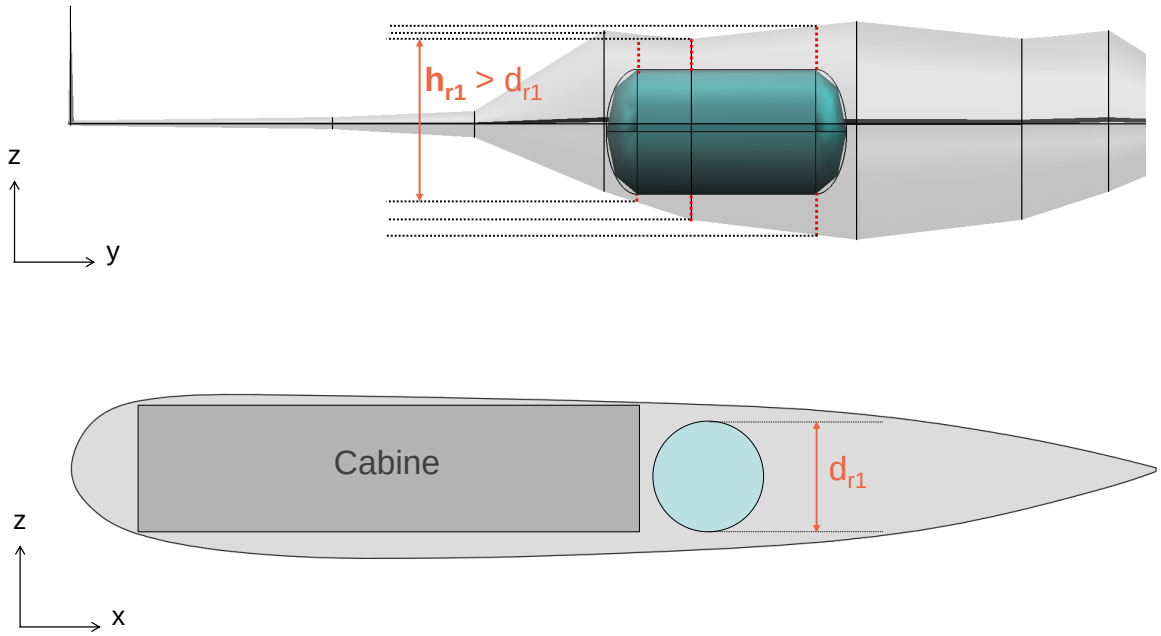

Figure V.15: Constraint formulation for the rear tank radius within the BWB airframe

Due to the symmetry hypothesis, constraints are defined only for one side of the BWB geometry in equations V.5, V.6, and V.10. Additionally, a constraint on the distance between the rear tank and the leading edge, which could be relevant in the case of very long rear tanks, was not defined. This omission is justified because scenarios where such a constraint would be violated are already addressed by the constraint on the rear radius.

V.3.2.5 Static Margin Constraints for Aircraft Stability

The final category of constraints necessary to ensure a feasible aircraft concerns the static margin. As defined in V.2, the static margin is the distance between the aircraft's neutral point and its center of gravity, normalized by the **MAC**. For longitudinal stability, the

static margin is typically required to be positive, see V.11, which ensures that the aircraft can be trimmed—that is, that the lift moment can be balanced at the center of gravity. While certain aircraft, particularly fighter jets, can operate with a negative static margin due to advanced fly-by-wire systems—which increase instability but enhance maneuverability—commercial aviation standards have consistently favored a positive static margin for safety.

$$SM = \frac{x_{cg} - x_{np}}{c_{MAC}} \geq 0 \tag{V.11}$$

V.4 Set-up of Multidisciplinary Analysis and Optimization Framework in FAST-OAD for the Sizing of Hydrogen Blended-Wing-Body Aircraft

V.4.1 Specification of the Multidisciplinary Optimization Problem

As presented earlier, the design of a hydrogen **BWB** has now been reformulated: instead of a purely multidisciplinary analysis, where the goal was to identify a single set of variable values satisfying the nonlinear equations governing the aircraft and its mission, the problem is extended to a multidisciplinary analysis and *optimization*. In this new formulation, multiple feasible solutions exist, all satisfying the nonlinear equations and the imposed constraints, among which local or global optima can be identified. The objective is therefore to solve an optimization problem consisting of a single global objective function subject to the constraints defined in equations V.4 through V.10. In the context of aircraft design, where efficiency is the primary concern, the block fuel was selected as the optimization objective. However, this choice is not restrictive, and the framework could equivalently be applied using an economic or environmental performance index. The optimization problem can be defined as such :

$$
\begin{aligned}
\min \quad & m_{blockfuel} \\
\text{w.r.t} \quad & N_{side}, N_{rear}, R_{side}, R_{rear}, L_{side}, L_{rear}, S_{yside}, S_{yrear}, S_{xside}, S_{xrear} \\
\text{s.t.} \quad & \sum_i V_{tank_i} \geq V_{totalBF} \\
& \sum_k^{Max_{rear}} \sum_i^{Max_{side}} \sum_j^{Max_{\mathbf{tank/side}}} a_k \cap a_{i,j} = 0 \\
& d_{xrij} \geq 0 \quad , i \in [\![1 \ ; \ Max_{rear}]\!], \quad j \in \{1, 2\} \\
& d_{xsi} \geq 0 \quad , i \in [\![1 \ ; \ Max_{side}]\!] \\
& h_{r,ij} > 2r_{r,ij} \quad , i = 1, \ldots, Max_{rear}, \quad j = 1, 2. \\
& h_{sfront,ij} > 2r_{s,ij} \quad , i = 1, \ldots, Max_{side}, \quad j = 1, \ldots, Max_{\text{tank/side}}. \\
& h_{srear,ij} > 2r_{s,ij} \quad , i = 1, \ldots, Max_{side}, \quad j = 1, \ldots, Max_{\text{tank/side}}. \\
& SM \geq 0
\end{aligned}
\tag{V.12}
$$

A key challenge arises from the fact that, in its current form, the optimization problem may not always admit a feasible solution. For a fixed aircraft geometry, it may indeed be impossible to identify a tank configuration that simultaneously fits within the airframe, provides sufficient storage capacity, and maintains a positive static margin. To maximize the likelihood of finding feasible configurations, several key geometric parameters defining the airframe must therefore also be treated as design variables so as to vary the outer shape of the airframe and pilot the available volume.

To address this issue at a preliminary stage, two additional geometric parameters were introduced into the set of optimization variables: Δy_{p1-p2}, which represents the spanwise extension of the transition zone between the pressurized cabin and the outer wing where the side tanks are located, and ϵ_{p0}, defined as (see Figure V.16):

$$\epsilon_{p0} = \frac{h_{p0} - h_{\text{cabin}}}{2} \tag{V.13}$$

The parameter ϵ_{p0} corresponds to the distance between the cabin roof and the upper surface of the airframe in the central section, and therefore directly controls the maximum airfoil thickness at station $p0$. Since the airfoil shape is fixed, the thickness-to-chord ratio remains constant; thus, varying ϵ_{p0} effectively modifies the central chord length. This variation propagates to stations $p0_1$ and $p1$, altering both airfoil thickness and chord. As a result, ϵ_{p0} can either tighten or relax the constraints related to tank radius, clearance from control surfaces, and static margin, thereby enabling feasible solutions to emerge. To accomodate airframe stiffening structure however, a lower bound of 200 mm is imposed on ϵ_{p0}. Although additional geometric design variables could be included in the optimization variable set to enable a more refined and exhaustive optimization, the choice was made to restrict the variable set to only those necessary to ensure feasibility. This limitation helps contain the complexity of the optimization problem while preserving its ability to identify viable configurations.

The resulting optimization problem is inherently complex due to the large number of design variables and constraints involved. As expressed in V.12, the number of variables

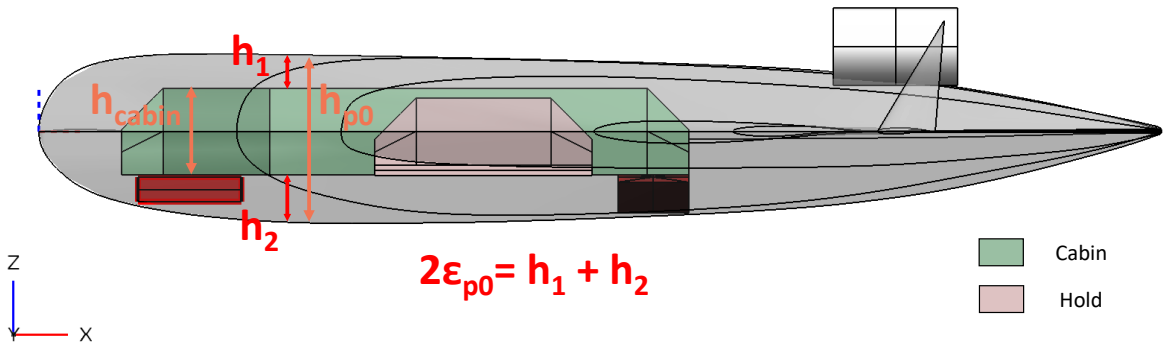

Figure V.16: Definition of a new design variable: ϵ_{p0}

is given by:

$$N_{vars} = Max_{side}(2 + 3Max_{tank/side}) + 8Max_{rear} + 2 \tag{V.14}$$

For instance, considering a configuration with three side rows and three rear rows, each side row containing three tanks, the problem already involves 59 design variables. In this same configuration, the number of constraints reaches 44, which represents a significant challenge for any optimization algorithm.
Several simplifications were introduced in order to mitigate this complexity:

- **Fixing tank spacing:** To reduce the number of design variables, the spacing between adjacent tanks and between successive tank rows was fixed at 100 mm. Consequently, all elements of the spacing variable matrices $S_{y,\text{side}}, S_{y,\text{rear}}, S_{x,\text{side}}, S_{x,\text{rear}}$ were set to a constant value of 0.1 m.

- **Constraints elimination**: Since the control surfaces are expected to be located primarily in the central section (between p0 and p1) or on the outer wing, constraint V.7 was considered less critical. Furthermore, preliminary experiments indicated that the side tank radius constraint V.9 is more restrictive, making V.7 largely redundant

- **Constraints concatenation**: To further reduce the number of constraints, aggregated constraints were introduced by concatenating those defined in Section V.3.2. The underlying idea is to sum, for each category of constraint, the violations that occur, such that:

$$D_{xr1} = \sum_{i}^{Max_{rear}} d^{-}_{xri1} \tag{V.15}$$

$$D_{xr2} = \sum_{i}^{Max_{rear}} d^{-}_{xri2} \tag{V.16}$$

$$D_{xs} = \sum_{i}^{Max_{side}} d^{-}_{xsi} \tag{V.17}$$

$$H_{sfront} = \sum_{i}^{Max_{side}} \sum_{j}^{Max_{\mathbf{tank/side}}} (h_{sfront,ij} - 2r_{s,ij})^{-} \tag{V.18}$$

$$H_{srear} = \sum_{i}^{Max_{side}} \sum_{j}^{Max_{\mathbf{tank/side}}} (h_{srear,ij} - 2r_{s,ij})^{-} \tag{V.19}$$

$$H_{rear} = \sum_{i}^{Max_{rear}} \sum_{j}^{2} (h_{r,ij} - 2r_{r,ij})^{-} \tag{V.20}$$

With those modification, a new optimisation problem can be defined :

$$\begin{aligned}
\min \quad & m_{blockfuel} \\
\text{w.r.t} \quad & N_{side}, N_{rear}, R_{side}, R_{rear}, L_{side}, L_{rear}, \Delta y_{p1-p2}, \epsilon_{p0} \\
\text{s.t.} \quad & \sum_{i} V_{tank_i} \geq V_{totalBF} \\
& \sum_{k}^{Max_{rear}} \sum_{i}^{Max_{side}} \sum_{j}^{Max_{\mathbf{tank/side}}} a_k \cap a_{i,j} = 0 \\
& D_{xr1} = 0 \\
& D_{xr2} = 0 \\
& H_{rear} = 0 \\
& H_{sfront} = 0 \\
& H_{srear} = 0 \\
& SM \geq 0
\end{aligned} \tag{V.21}$$

This new optimization problem now contains only 8 constraints, regardless of the number of tanks. The number of design variables is also significantly reduced, given by $N_{vars} = Max_{side}(1 + 2Max_{tank/side}) + 5Max_{rear} + 2$,which, for a configuration with three side rows and three rear rows, each side row containing three tanks, corresponds to 38 variables—down from 59. This reduction makes the problem considerably more manageable; however, two aspects make this problem particularly challenging:

- **Mixed Variables**: The vectors N_{rear} and N_{side} are composed of integer variables, while all other design variables are continuous. This characteristic significantly limits the choice of applicable optimization algorithms, as they must handle mixed variables and cannot rely solely on gradient-based methods.
- **Hierarchical variables**: Certain variables can be regarded as hierarchical because

their values affect the bounds of other variables or even the total number of design variables. In particular, the elements of N_{rear} and N_{side} specify the number of tanks. In the current implementation, a row cannot contain any tanks if the preceding row is empty. Furthermore, the total number of rows dictates how many tank radii and lengths need to be considered in the optimization.

V.4.2 Complete MDAO Framework for Hydrogen BWB Design

The developments presented in the previous section provide a framework for designing a hydrogen Blended Wing Body aircraft by mathematically formulating the specific problem of hydrogen tank sizing and placement. The last step consists of integrating this framework into the version of **FAST-OAD** that has already been enhanced with the extended CICAV modules, as described in section V.2.
The integration of the specifically developed hydrogen tank configuration model was carried out primarily within the geometry module. To maintain backward compatibility and avoid disrupting other ongoing projects, the tank geometry definition was implemented as a submodule that executes after the main geometry discipline. The main tasks of this new submodule are:

- Determining the internal volume of each tank, their storage capacity, and the fuel distribution between them.
- Defining the structural dimensions of each tank based on its geometry, the position of the insulation (internal or external), and its thickness.
- Calculating the center of gravity of each tank, assumed to coincide with its geometric center.
- Evaluating all geometric constraints described in sections V.3.2.1 through V.3.2.4, which include limitations on minimum storage volume, potential intersections between tanks, minimum clearances between tanks and control surfaces, and restrictions on tank radius relative to the airfoil thickness.

In addition to implementing this submodule, the hydrogen tank models developed in Chapters II and III were also integrated. A similar approach to that used for the geometry module was adopted for the tank structure evaluation: it is implemented as a submodule of the main structure discipline and runs after the CICAV structure solver. However, it was not feasible to develop a generic method for estimating the shear, bending, and torsional loads applied to each tank, as is done for conventional aircraft. Such an approach would require a detailed modeling of each tank's attachment system, which is both highly complex in the context of this open design framework and too time-consuming to implement.
As an alternative, the tanks were modeled as non-integral components, meaning their structure does not contribute to carrying the airframe loads. In addition, a minimum clearance of 200 mm was imposed between each tank and the aircraft outer skin to account for the stiffening structure. This margin directly affects the constraints defined

in V.8, V.9, and V.10. To account for the unavoidable residual loads transmitted through their contact points, a minimal stiffening structure was introduced. This consists of three stiffening frames of 400 *mmr* per tank, complemented by stringers of 250 *mmr*, distributed every 250 mm along the tank circumference. This design choice was inspired by results on tank stiffening structures used in conventional aircraft.

The thermodynamic modeling of the tanks follows also the conventional aircraft approach, being applied as a post-processing step after the main mission time-step integration performed within the performance discipline (see Figure V.17). The main difference lies in the potentially large number of tanks to be sized and modeled. To reduce computational time, aircraft symmetry is exploited wherever possible, so that only one of each pair of symmetric tanks needs to be sized and modeled.

The structure is organized as follows:

- **First-level MDA loop** (CICAV core): This loop corresponds to the traditional **MDA** already implemented in CICAV. The disciplines are executed in cascade: geometry (aircraft sizing), structures (mass and center of gravity), aerodynamics (polars at low and high speed), propulsion (engine deck, specific fuel consumption as a function of altitude and Mach), and performance (mission time-step integration). The performance analysis provides the block fuel, which acts as the main coupling variable.
- **Second-level MDA loop** (tank thermodynamics): The tank thermodynamic analysis is performed in a separate **MDA**, after the first one, with the model developped in Chapter II. This choice is motivated by two reasons: (i) the model relies on physical equations that are not valid in early design iterations when block fuel and fuel consumption values are unrealistic; (ii) the analysis is significantly more computationally expensive, especially with multiple tanks (10–15 seconds per tank), so convergence of the global process is accelerated when it is treated as a separate loop.
- **Optimization loop**: On top of the second **MDA**, the optimizer varies the design variables, i.e the tank arrangement, and feeds updates to the geometry, structures, and thermodynamic modules. Once the second **MDA** has converged, the stability module is called to compute the static margin of the aircraft, which is enforced as a constraint. Additional constraints are directly evaluated within the geometry module.

V.5 Conclusion

This chapter presents the extension of the FAST-OAD framework, incorporating a methodology for designing hydrogen-powered flying-wing aircraft through the exploration and optimization of a vast design space related to hydrogen tank configurations.

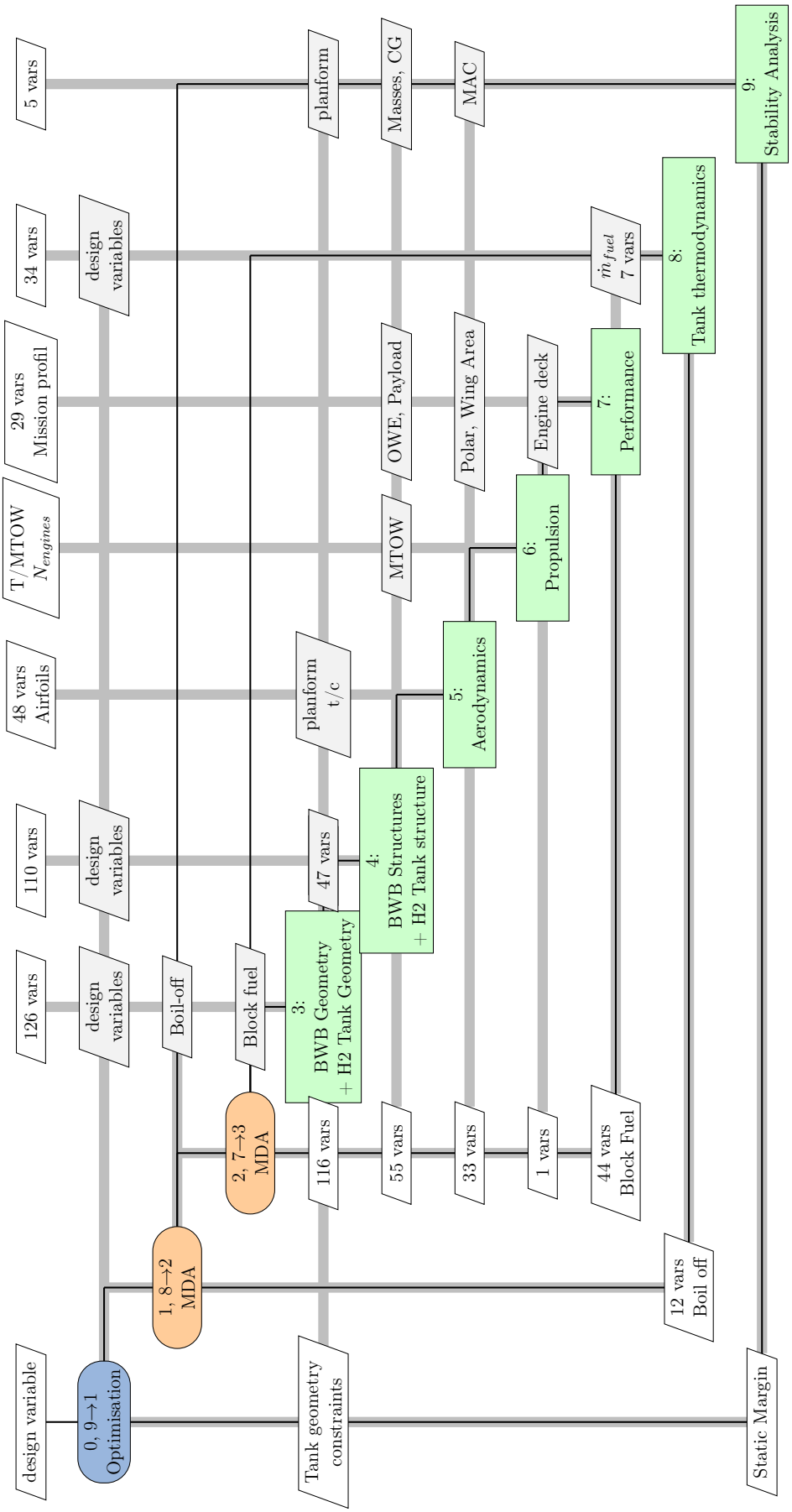

Figure V.17: XDSM of the **MDAO** use for hydrogen **BWB** design

First, FAST-OAD was adapted to flying-wing geometries by replacing its original geometric and structural sizing models with those developed under the ONERA CICAV project, specifically tailored for this type of configuration. The first module enables the sizing of the cabin and the flying-wing airframe based on **TLARs**, using a detailed parameterization. The structural module then derives the mass, considering an architecture with a load-bearing wall capable of withstanding both internal pressure and aerodynamic loads, reinforced by a stiffening structure. Alongside these integrations, a new model was developed to estimate the static margin—and thus the longitudinal stability—of the flying wing using a **VLM** aerodynamic analysis performed with VSP AERO. Additionally, to account for the shift in the center of gravity caused by hydrogen tank integration, new modules were implemented to optimize the positioning of the engines and the main landing gear.

Once FAST-OAD was capable of sizing a conventional flying wing, this chapter introduced a dedicated framework for hydrogen-powered flying-wing design. A new parameterization was developed to define the number, position, and geometry of cylindrical hydrogen tanks integrated into the flying wing, offering a wide range of possible configurations. The tanks are categorized into two families: those arranged longitudinally on either side of the cabin (side tanks) and those positioned behind it, aligned transversely with the seat rows (rear tanks). Each family is organized into rows, which can accommodate multiple tanks. This parameterization, implemented in FAST-OAD, allows for flexible variation in the number of rows, the number of tanks per row (which may differ between rows), and the dimensions and positioning of each individual tank.

While numerous configurations can be generated, determining which are optimal—or even physically feasible—remains challenging. Arbitrarily defining a sizing strategy at this stage would likely yield feasible but suboptimal solutions. Consequently, the classical design loop was adapted: in the absence of a unique solution for the Multidisciplinary Design Analysis, a multidisciplinary analysis and optimization approach was adopted. A set of constraints was introduced to ensure the feasibility of the explored configurations, including minimum hydrogen storage volume, positive static margin (to guarantee longitudinal stability), and geometric integration constraints to ensure tanks fit within the airframe. The design of a hydrogen-powered flying wing is thus formulated as a constrained optimization problem, detailed in the final section of this chapter. This problem is particularly complex, involving a large number of variables—some of which are mixed and hierarchically organized—as well as numerous constraints. The chapter concludes by outlining the structure of the **MDAO** implementation developed to solve this optimization challenge.

While this framework for sizing hydrogen-powered blended wing-body aircraft represents an innovative and complex advancement, it has yet to be validated in existing literature. Therefore, the final chapter of this work is dedicated to demonstrating the capabilities of this model and its practical implementation by designing a hydrogen-powered blended wing-body aircraft optimized for short- to medium-range missions.

CHAPTER VI

Demonstrating the Hydrogen Blended Wing Body Sizing Method in FAST-OAD: Design Exploration and Optimization of Short-to-Medium-Range Configurations

Résumé

Les premiers chapitres de ce travail ont introduit un modèle thermodynamique d'un réservoir d'hydrogène cryogénique, développé pour estimer les pertes par évaporation tout au long d'une mission aérienne, ainsi qu'une méthodologie de dimensionnement permettant de déterminer la masse correspondante du réservoir. Ces développements ont ensuite été intégrés dans le cadre **MDA** de **FAST-OAD**, permettant ainsi la conception d'aéronefs propulsés à l'hydrogène. Le cadre a été étendu et transformé dans le chapitre précédent en une méthode de conception **MDAO** pour prendre en charge les configurations de type aile volante. Cette nouvelle méthode offre la possibilité d'explorer un vaste espace de conception en termes d'architectures de réservoirs au sein d'une aile volante, dans le but d'identifier des solutions optimales par une approche **MDAO**.
Ce chapitre a pour objectif de mettre en évidence les capacités et le potentiel de la méthodologie de conception d'aile volante à hydrogène, à travers la conception préliminaire d'un

aéronef de ce type dimensionné pour des missions court et moyen-courriers. En révélant le fort potentiel d'amélioration de l'efficacité énergétique de l'aile volante à hydrogène par rapport aux configurations classiques de type Tube and Wing, cet exercice démontre l'intérêt de cette solution technologique ainsi que la pertinence et la performance de la méthode développée pour sa conception.
La première section de ce chapitre présente la spécification du cas d'étude de conception de l'aéronef, en commençant par la définition d'une mission de type moyen-courrier visant à transporter 150 passagers sur une distance de 3 000 milles marins (nmi). Elle inclut également la sélection et la justification des valeurs des paramètres de conception clés qui sont fixés pour cette étude. Enfin, trois aéronefs de référence sont présentés pour servir de base comparative :

- une aile volante alimentée au kérosène
- un avion conventionnel de type Tube and Wing à hydrogène,
- et un avion conventionnel de type Tube and Wing au kérosène.

La section suivante présente la construction et les spécificités de l'espace de conception de l'aile volante à hydrogène, qui se distingue par sa grande dimension (37 variables de conception) et sa complexité, en raison de la présence de variables mixtes et hiérarchiques. Cet espace est donc exploré au moyen d'un plan d'expérience à grande échelle (**DoE**), rendue possible grâce à la parallélisation de la boucle de conception **MDA** sur des serveurs de calcul haute performance. L'analyse du **DoE** met en évidence une hiérarchie parmi les contraintes de conception, avec la contrainte de marge statique minimale qui s'avère particulièrement restrictive et va influencer de manière significative la conception pour assurer la stabilité de l'aéronef. Dans le cadre de l'espace de conception défini et des paramètres fixés, deux autres contraintes — celles portant sur le diamètre avant des réservoirs latéraux et l'espacement entre l'extrémité des réservoirs arrière et les gouvernes — peuvent être écartées pour simplifier le processus d'optimisation, car elles ne sont jamais activées dans cet espace de conception. De plus, l'analyse des configurations géométriquement réalisables issues du plan d'expérience fournit des données statistiques permettant de caractériser les régions de faisabilité de l'espace de conception, ainsi que celles optimisant l'efficacité énergétique de l'avion. Ces résultats incluent également les principales métriques de performance associées aux avions dans ces régions.
Dans la dernière partie de ce chapitre, les connaissances tirées de l'exploration du **DoE** sont exploitées pour simplifier le problème d'optimisation. En se focalisant sur les architectures favorisant la faisabilité, le nombre de variables d'optimisation est réduit à 17, en limitant la configuration à un seul rang de réservoirs arrière et deux rangs latéraux, avec un maximum de deux réservoirs par rang latéral. Cette simplification permet de mener une boucle complète de conception en résolvant une optimisation globale de l'aile volante à hydrogène avec une efficacité computationnelle raisonnable. En pratique, l'optimisation est réalisée à l'aide de l'optimiseur bayésien nommé **Super Efficient Global Optimization Mixture Of Expert (SEGOMOE)**, développé à l'ONERA, dont le processus itératif est détaillé. Le design optimisé finalement obtenu est une aile volante équipée de

six réservoirs à hydrogène : deux réservoirs jumeaux à l'arrière et quatre autres répartis en deux rangs de chaque côté.
La comparaison avec une aile volante conventionnelle à kérosène révèle que la transition vers l'hydrogène nécessite un corps central plus volumineux pour accueillir les réservoirs cryogéniques, bien que l'optimisation ait permis de limiter au maximum cette augmentation. Cette contrainte est principalement due aux exigences de stabilité, qui imposent de placer la majorité des réservoirs vers l'avant pour équilibrer l'avion, empêchant ainsi d'exploiter le volume disponible à l'arrière. Ce plus grand corps central engendre une détérioration des performances aérodynamiques, ainsi qu'une augmentation substantielle de la masse structurelle, bien au-delà de l'impact lié au poids des réservoirs eux-mêmes. En conséquence, la consommation énergétique de la version à hydrogène s'avère accrue d'environ 40% par rapport à son homologue à kérosène.
Une analyse comparative plus pertinente opposant l'aile volante à hydrogène aux architectures conventionnelles de type Tube & Wing est ensuite réalisée, ces dernières constituant ses principaux concurrents. Bien que l'aile volante à hydrogène présente une masse à vide et une masse maximale au décollage supérieures à celles d'un Tube & Wing à hydrogène, son efficacité aérodynamique supérieure lui confère un avantage énergétique d'environ 3% en termes de consommation. En se limitant à la mission principale (sans inclure la mission de réserve, rarement effectuée et durant laquelle l'aile volante, en particulier à hydrogène, est moins efficace en raison d'un éloignement de son optimum aérodynamique et d'une masse plus élevée), l'économie énergétique atteint près de 7%. Ainsi, dans ce cadre, l'aile volante à hydrogène affiche une consommation légèrement inférieure à celle d'un avion Tube & Wing propulsé au kérosène.
Les résultats obtenus, bien qu'issus d'une optimisation partielle et ne couvrant pas l'intégralité des variables de conception pertinentes pour une aile volante à hydrogène, suggèrent un potentiel d'amélioration significatif. Une optimisation plus exhaustive, intégrant un espace de conception élargi, pourrait permettre à cette architecture de dépasser significativement les performances énergétiques des aéronefs actuels, contribuant ainsi à réduire l'impact environnemental du secteur aérien. Quoi qu'il en soit, ces résultats démontrent la robustesse, l'efficacité et la pertinence de la méthodologie de dimensionnement et d'optimisation développée pour les ailes volantes à hydrogène. Cette méthode, validée par les études menées, offre une base solide pour conduire des analyses plus poussées dans ce domaine.

Contents of this Chapter

VI.1 Introduction . . . 173
VI.2 Description of the case study . . . 173
VI.2.1 Mission selection . . . 173
VI.2.2 Specifications of Model Inputs and Configuration Assumptions . . . 174
VI.2.3 Design of reference aircraft . . . 176
VI.3 First exploration of the design space through a DOE analysis . . . 177
VI.3.1 Design Space Construction . . . 177
VI.3.2 Analysis of Constraint Characteristics Across the DOE . . . 179
VI.3.3 Analysis of Feasible Region Trends from the DOE . . . 183
VI.4 Optimisation of Small-to-Medium-Range Hydrogen-BWB . . . 189
VI.4.1 Establishing a Mixed-Variable Optimization Process . . . 189
VI.4.2 Assessment of Iterative Optimization Behavior . . . 192
VI.4.3 Evaluating the Performance and Key Design Features of an Optimized Hydrogen-Powered Blended Wing Body Aircraft for SMR missions . . . 195
VI.4.3.1 Presentation of the optimized hydrogen powered Blended Wing Body design . . . 195
VI.4.3.2 Evaluating Optimization Impact on Hydrogen **BWB** Performance and Attributes . . . 198
VI.4.3.3 Potential of Hydrogen **BWB** Compared with Hydrogen and Jet-Fuel **T&W** Aircraft . . . 205
VI.5 Conclusion . . . 211

VI.1 Introduction

The initial chapters of this work introduced a thermodynamic model of a cryogenic hydrogen tank, developed to estimate boil-off losses throughout an aircraft mission II, together with a sizing methodology to determine the corresponding tank mass III. These developments were subsequently integrated into the **MDA** framework of **FAST-OAD**, thus enabling the design of hydrogen-fueled aircraft. The framework was further extended and transformed into a **MDAO** design method to model blended wing body configurations, allowing for the exploration of a broad design space of tank architectures with the objective of identifying optimal solutions through the **MDAO** approach. The aim of the present chapter is to demonstrate the capabilities and potential of this enhanced design methodology, which will be illustrated through the conceptual design of a short-to-medium-range hydrogen blended wing body.
The first section of this chapter focuses on specifying the aircraft design case study. This includes defining the **SMR** design mission, selecting and justifying the values of key design parameters, and presenting the four reference aircraft used for comparison.
The following section details the construction of a design space for the hydrogen **BWB**. This design space is then explored through a large-scale design of experiments (**DoE**), enabled by the parallelization of the **MDA** design loop on high-performance computing servers at ONERA. The analysis of the **DoE** reveals a hierarchy among design constraints, with the minimum static margin constraint proving to be particularly restrictive and significantly influencing the design, while other constraints can be disregarded under the chosen parameters. Additionally, the **DoE** provides statistical insights that characterize aircraft architectures favoring feasibility or efficiency, along with their key performance metrics.
Finally, the knowledge gained from the **DoE** exploration is used to simplify the optimization problem, enabling the full optimization of the hydrogen **BWB** with reasonable computational efficiency using the Bayesian Optimizer **SEGOMOE**. The resulting optimized design is then presented, and its characteristics are detailed. This design is first compared to a conventional jet-fuel **BWB** aircraft to quantify the impact of transitioning to on-board hydrogen storage and accommodating hydrogen tanks. Subsequently, it is compared to both hydrogen- and jet-fuel-powered **T&W** configurations to determine which architecture offers the best energy efficiency—and for what reasons—and to assess whether the **BWB** architecture holds potential for facilitating the energy transition in aviation.

VI.2 Description of the case study

VI.2.1 Mission selection

The mission selected for this design exercise falls between the short- and medium-range segments. The target passenger capacity is relatively modest, at 150 passengers, while the design range is set to 3,000 nautical miles (5,550 km). These parameters were chosen to align with the previously designed SMILE concept at ONERA [**106**], which is a conven-

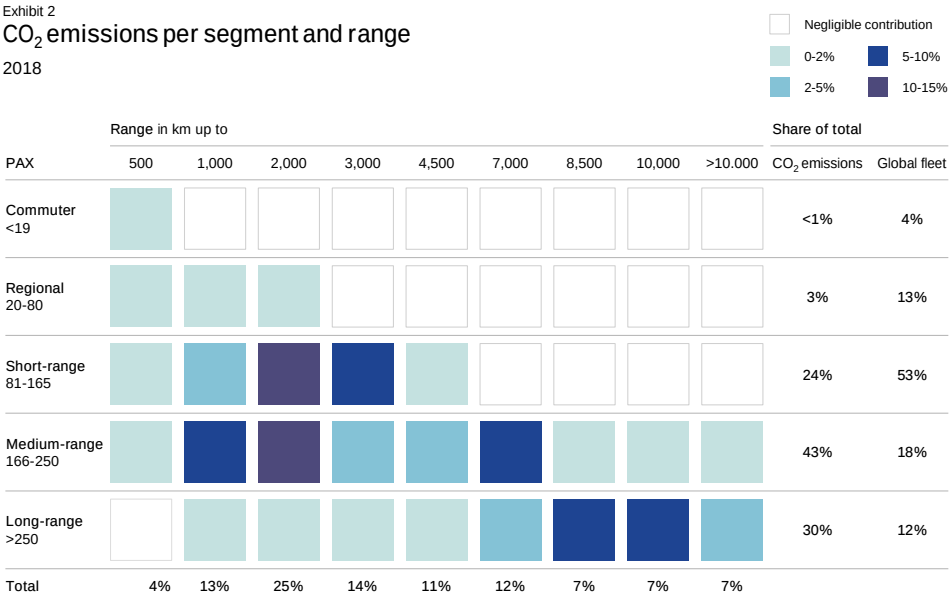

Figure VI.1: Aircraft Emissions and Fleet Composition by Segment and Operational Range [**163**]

tional blended wing body. The limited passenger capacity allows for the development of a **BWB** with a single deck and cargo holds positioned alongside the cabin. Nevertheless, the specified range is sufficient to cover approximately half of all aircraft emissions and 65% of all flights, as illustrated in Figure VI.1. Consequently, a low-emission aircraft with a 3,000 nautical mile range already demonstrates significant potential for reducing overall aviation emissions.

The mission profile, depicted in Figure VI.2, is structured into a main mission and a subsequent reserve mission. The main mission begins with a 15-minute taxi-out phase, followed by a climb from ground level to an altitude of 12,600 m (41300 ft). This is succeeded by a cruise segment of approximately six hours at Mach 0.78 and a descent to 450 m (1,500 ft). At this point, the reserve mission begins, consisting of a second climb to 4,000 m (13100 ft), a 200 nmi cruise to an alternate airport at Mach 0.6, a 30-minute holding phase at Mach 0.4, and a final descent, which concludes with a 7-minute taxi-in. Furthermore, to account for potential delays in gate availability, a one-hour dormancy period is incorporated into the hydrogen tank simulation. As concluded in Chapter IV, imposing a longer dormancy period would be overly impactful, at least with foam insulation technology.

VI.2.2 Specifications of Model Inputs and Configuration Assumptions

In addition to the mission definition, several modeling assumptions and input choices were made to define the base configuration. The most significant parameters are summarized in Table VI.1 and further detailed below.

- **Payload**: Each passenger is assumed to represent a mass of 90 kg, including both

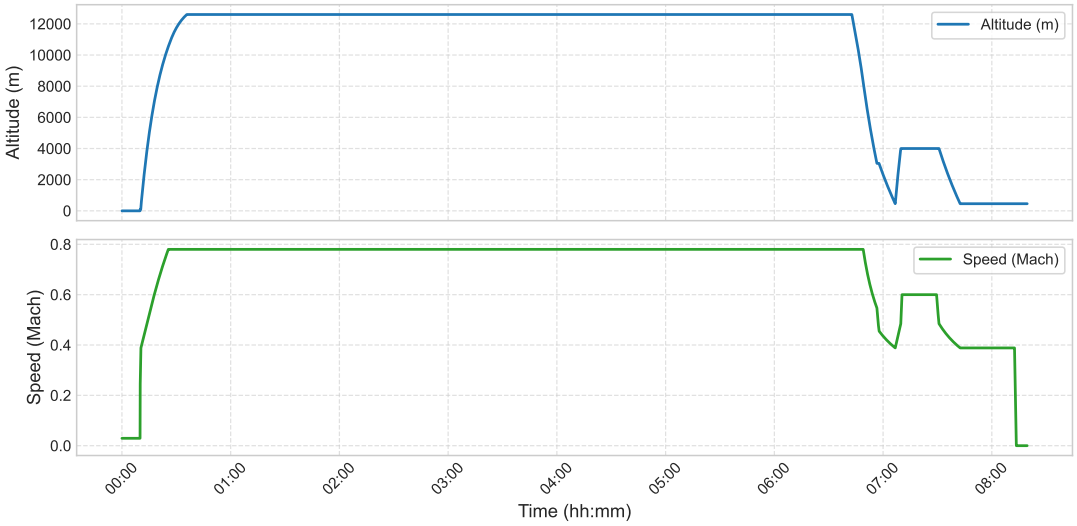

Figure VI.2: Design mission profile for the hydrogen **BWB**

the individual and associated luggage. This corresponds to a design payload, also equal to the maximum payload, of 13,500 kg for the passengers, to which 200 kg is added for the flight crew.

- **Geometry**: The aircraft geometry partially derives from the SMILE concept previously developed at ONERA [**106**]. The cabin layout is divided into two main bays, each featuring a single aisle flanked by three seats on either side, with the exception of the triangular forward section. Four galleys and four lavatories are positioned at the rear of the cabin, and the two bays are separated by an internal partition. The cockpit, located at the nose of the aircraft, extends over 2 m, while the baggage holds, also 2 m wide, are placed on either side of the cabin and separated by partitions. The sweep angles for the different sections are preserved from the SMILE optimised design and are provided in Table VI.1. Control surfaces are assumed to cover 15% of the chord in the central section and between 20–25% in the external wing. Additionally, the configuration incorporates 2.5 m-high winglets for yaw stability, although their structural sizing is not yet included in the design process.

- **Hydrogen tanks and subsystems**: To reduce the number of design variables in the present study, several tank design parameters were fixed based on the results of Chapter IV. The pressure differential between the tank interior and exterior is fixed at a maximum of 1.4 bar (minimum 0.2 bar). In combination with a 100 mm polyurethane foam insulation layer placed outside the tank structure, these parameters are intended to effectively limit boil-off during both flight and the one-hour dormancy period. The selected values represent a compromise between minimizing hydrogen losses and avoiding excessive structural or insulation mass. The initial filling pressure of the tank is set to 1.5 bar, with initial fluid temperatures of 18 K for liquid hydrogen and 20 K for gaseous hydrogen. The tank structure material is aluminum, as detailed in Table VI.1. For the thermodynamic tank model, five nodes are used to evaluate the heat inflow. Finally, a mass allowance of 300 kg for the

Table VI.1: **BWB** sizing case inputs

	Inputs	Value	Unit
Mission	Passenger	150	
	Range	3000	NM
	Cruise altitude	33 000	ft
	Cruise speed	0.78	mach
	Dormancy time	60	min
	Thrust-to-weight ratio	0.35	
Geometry	Seat per row	(2 x 3) x 2	
	Wingspan	36	m
	Distance $y_{p2} - y_{p2_1}$	3.25	m
	Sweep angle $p0 - p2$	51.7	deg
	Sweep angle $p2 - p2_1$	45.9	deg
	Sweep angle $p2_1 - p3$	40.2	deg
	Control surface allocation $p0 - p1$	15	%
	Control surface allocation $p2$	20	%
	Control surface allocation $p3$	25	%
	Cockpit length	2	m
	Holds width	2	m
Tank Design	Max ΔPressure	1.4e5	Pa
	Min ΔPressure	0.2e5	Pa
	Filling pressure	1.5e5	Pa
	Filling temperature LH2	18	K
	Filling temperature GH2	20	K
	Associated subsytem mass	300	kg
Tank Insulation (Polyurethane Foam)	Thermal conductivity	0.026	$W.m^{-1}.K^{-1}$
	Density	33	$kg.m^{-3}$
	Thickness	100	mm
Tank material (Aluminium 2026)	Density	2825	$kg.m^{-3}$
	Poisson ratio	0.33	
	Young modulus	73.8	GPa
	Elastic limit stress	240	MPa
	Elastic break stress	420	MPa
	Thermal conductivity	230	$W.m^{-1}.K^{-1}$
	Tank skin infrared emittance	0.9	
	Tank sink solar absorptance	0.26	

entire aircraft is included to account for all hydrogen-related subsystems, including refueling, pressurization, and venting according to initial findings from Sarr et al. [**156**].

VI.2.3 Design of reference aircraft

In addition to the hydrogen-powered **BWB** aircraft, three reference configurations were defined for comparative analysis:

- **Kerosene-fueled BWB**: Designed to assess the impact of hydrogen propulsion and tank integration on overall aircraft performance, with a focus on mass and energy consumption.
- **Hydrogen-fueled T&W**: Established to evaluate the benefits of the blended wing body configuration compared to a conventional tube-and-wing design when powered by hydrogen.
- **Kerosene-fueled T&W**: Considered to quantify differences in energy consumption and aircraft mass relative to a conventional aircraft representative of today's fleet.

All four aircraft configurations were sized using FAST-OAD based on the same design mission, employing the rubber engine model implemented in FAST-OAD [**125**]. A 15% reduction in **SFC** relative to the baseline rubber engine was applied to reflect anticipated propulsion advancements by 2035. For hydrogen-powered aircraft, the SFC was further adjusted by dividing it by a factor of 2.79, corresponding to the ratio of the lower heating values of kerosene to hydrogen. For the **T&W** hydrogen aircraft, the fuel is divided in two twin tanks for redundancy reasons, and the tanks are nonintegral to assure a fair comparison with the **BWB** counterpart. Even if they are using different settings due to the different geometry parameterization, the aerodynamic and structural model use the same modelling approach for both **T&W** and **BWB** configurations.

VI.3 First exploration of the design space through a Design of Experiment analysis

VI.3.1 Design Space Construction

As discussed in the previous Chapter V, the design process for the hydrogen **BWB** has evolved into a complex optimization problem. Prior to attempting to solve this problem, it was deemed beneficial to explore the design space through a **DoE** approach. This approach serves several objectives:

- **Gaining insight into the feasible design space**: While optimization may identify an optimal configuration, it does not provide information about the trends within the design space or the characteristics of the feasible regions. Conducting a **DoE** allows for the identification of sensitivities of constraints and objectives to design variables, estimation of the extent and number of feasible regions, and a comparison of their common features and differences. This process provides an understanding of the robustness of potential optimal configurations.
- **Constraining the design space**: By gaining insights into the design space, it may be possible to refine and restrict it, thereby aiding the optimization process. For instance, identifying constraints that are systematically more restrictive than others or pinpointing threshold values for design variables that lead to infeasible regions could serve to define new bounds for the variables—particularly in the case of integer variables.

- **Accelerating the optimization process**: In addition to restricting the design space and reducing the number of constraints, some optimization algorithms can benefit from a database of previously executed design iterations, including their input variables and associated constraints and objectives. Machine learning algorithms can leverage this database to accelerate the identification of optimal solutions or, at the very least, to initiate the search from an already feasible starting point.

For the reasons outlined above, a Design of Experiments (DOE) was implemented. To limit the number of design variables in the design space, the maximum number of rear and side rows was fixed at three, with a maximum of three tanks per row for the side and four tanks per row for the rear. Table VI.2 provides the bounds for each variable in detail. Special care was taken when defining these bounds to prevent infeasible tank geometries. In particular, a minimum tank length was set to be at least twice the maximum radius, consistent with the chosen semi-elliptical tank bulkhead shape, where the bulkhead length equals the tank's radius. The remaining bounds were selected as a compromise between maintaining a sufficiently large design space and restricting the domain to regions more likely to yield feasible designs.

As outlined in Chapter V, certain design variables exhibit a hierarchical dependency, whereby the value of one variable can determine the existence or admissible bounds of another. Within this framework, the dependent variable is termed a decreed variable, while the governing variable is referred to as the meta variable. Incorporating such a hierarchical structure enables a further reduction of the design space. Table VI.3 presents the organization of this hierarchy, which is built upon two fundamental principles:

- A row cannot contain tanks if the preceding row does not contain at least one tank. For instance, it is not feasible to have tanks in row 3 if row 2 contains none.
- The radius and length of a tank are defined only if the corresponding tank exists. For example, assigning radius and length values to a second tank in a row is meaningless if the row contains only one tank.

The construction of this intricate design space was carried out using the Python library **Surrogate Modeling Toolbox (SMT)**[**164**, **165**]. Unfortunately, the current version of this library does not support multi-level hierarchical structures, i.e., cases where a variable simultaneously acts as both a decreed and a meta variable. This limitation is particularly problematic in the hydrogen **BWB** problem, since for configurations with three rear or side rows, the number of tanks in the second and third rows should logically function as both decreed and meta variables. Specifically, the number of tanks in the second row depends on the presence of at least one tank in the first row, but it also governs the existence of tanks in the third row (which requires a non-zero second row) as well as the definition of tank radii and lengths for the second row. Similarly, the number of tanks in the third row depends on the existence of a second row, while at the same

time determining the radii and lengths to be defined within that row.

To address this issue, the design space was reduced by imposing the presence of at least one tank in every first row, thereby removing the decreed nature of the variable defining the number of tanks in the second row. As no complete solution was found for the dependency of the third-row radii and lengths, their definition was just declared conditional on the existence of at least a second row.

One of the main advantages of the Design of Experiments methodology is that each sampling point is independent of the others, which makes their evaluation inherently parallelizable. This characteristic can substantially reduce computational time, in contrast to iterative optimization methods where each iteration depends on the outcome of the previous one. As a result, employing a DOE to generate a hot start for the optimization process constitutes an efficient strategy.
In the present work, the hydrogen **BWB** sizing multidisciplinary analysis (MDA) loop—without the optimization overlay—was adapted to allow the parallel evaluation of multiple designs. The FAST-OAD framework was further modified to operate within a Linux environment, thereby ensuring compatibility with the high-performance computing infrastructure available at ONERA. This configuration facilitated the execution of a DOE comprising approximately 19,000 sampling points over 37 design variables, distributed across 80 parallel cores. Approximately 90% of these points were successfully evaluated, with the remainder predominantly failing to converge within the required timeframe. The complete computation was achieved in roughly three days. While this extensive DOE may exceed the requirements for later use as an initial training set for optimization, it provides a robust foundation for the statistical analysis presented in the following section.

VI.3.2 Analysis of Constraint Characteristics Across the DOE

The large number of converged designs enables detailed sensitivity analyses. Figure VI.3 illustrates the distribution of the concatenated constraints (defined in equations V.15 through V.20) across the DOE. It can be observed that some constraints are more restrictive than others. For instance, D_{xr1} and D_{xr2}—which correspond to the distances between the rear tank bulkhead dome or barrel extremity and the control surface, respectively—are generally less restrictive than the tank radius constraint. Among them, D_{xr2} is comparatively more limiting, with only 45.3% of designs satisfying this constraint, versus 59.1% for D_{xr1}. This is consistent with the typical positioning of the tank barrel extremity closer to the trailing edge. There are only 55 designs in which D_{xr2} is inactive while D_{xr1} remains active, all corresponding to very long and slender tanks. In contrast, there are only two cases where D_{xr1} is the sole active constraint while the other five constraints are satisfied, and in these instances the constraint violation is minimal (on the order of a few centimeters). Consequently, this constraint could potentially be removed to simplify the optimization.

Regarding the tank radius constraint, the side tank appears more challenging to accom-

Table VI.2: **DoE** design variable bounds

Design variables				**Lower bound**	**Upper bound**
	ϵ_{p0}			0.4	1
	Δy_{p1-p2}			2.5	5
Tank config.	Rear	row 1		1	4
		row 2		0	4
		row 3		0	4
	Side	row 1		1	3
		row 2		0	3
		row 3		0	2
Rear tank	Radius	row 1	$r_{r1,1}$	1	2
			$r_{r1,2}$	1	2
		row 2	$r_{r2,1}$	0.3	1.5
			$r_{r2,2}$	0.3	1.2
		row 3	$r_{r3,1}$	0.2	1
			$r_{r3,2}$	0.2	1
	Length	row 1	$l_{r1,1}$	3	10
			$l_{r1,2}$	3	8
		row 2	$l_{r2,1}$	2	10
			$l_{r2,2}$	2	6
		row 3	$l_{r3,1}$	2	7
			$l_{r3,2}$	2	5
Side tank	Radius	row 1	$r_{s1,1}$	0.3	1.5
			$r_{s1,2}$	0.3	1.5
			$r_{s1,3}$	0.3	1.5
		row 2	$r_{s2,1}$	0.3	1.1
			$r_{s2,2}$	0.3	1.1
			$r_{s2,3}$	0.3	1.1
		row 3	$r_{s3,1}$	0.2	0.8
			$r_{s3,2}$	0.2	0.8
			$r_{s3,3}$	0.2	0.8
	Length	row 1	$l_{s1,1}$	1.55	8
			$l_{s1,2}$	1.55	5
			$l_{s1,3}$	1.55	2
		row 2	$l_{s2,1}$	1.2	6
			$l_{s2,2}$	1.2	2
			$l_{s2,3}$	1.2	2
		row 3	$l_{s3,1}$	1	5
			$l_{s3,2}$	1	3
			$l_{s3,3}$	1	2

Table VI.3: **DoE** design variable hierarchical structure

Decreed variable			Meta variable		Explanation
			Name	**Value**	
Rear Tank	Row 1	$r_{r1,2}$	n_{r1}	{3, 4}	Applicable only for rows with 3 or 4 tanks
		$l_{r1,2}$	n_{r1}	{3, 4}	
	Row 2	$r_{r2,1}$	n_{r2}	{1, 2, 3, 4}	Applicable only if row has at least 1 tank
		$l_{r2,1}$	n_{r2}	{1, 2, 3, 4}	
		$r_{r2,2}$	n_{r2}	{3, 4}	Applicable only for rows with 3 or 4 tanks
		$l_{r2,2}$	n_{r2}	{3, 4}	
	Row 3	n_{r3}	n_{r2}	{1, 2, 3, 4}	A tank in row 3 requires a tank in row 2.
		$r_{r3,1}$	n_{r2}	{1, 2, 3, 4}	
		$l_{r3,1}$	n_{r2}	{1, 2, 3, 4}	Only applies if there is a tank in row 2; otherwise, row 3 has no tank
		$r_{r3,2}$	n_{r2}	{1, 2, 3, 4}	
		$l_{r3,2}$	n_{r2}	{1, 2, 3, 4}	
Side Tank	Row 1	$r_{s1,2}$	n_{s1}	{2, 3}	Applicable only for rows with 2 or 3 tanks
		$l_{s1,2}$	n_{s1}	{2, 3}	
		$r_{s1,3}$	n_{s1}	{3}	Applicable only for rows with 3 tanks
		$l_{s1,3}$	n_{s1}	{3}	
	Row 2	$r_{s2,1}$	n_{s2}	{1, 2, 3}	Applicable only if row has at least 1 tank
		$l_{s2,1}$	n_{s2}	{1, 2, 3}	
		$r_{s2,2}$	n_{s2}	{2, 3}	Applicable only for rows with 2 or 3 tanks
		$l_{s2,2}$	n_{s2}	{2, 3}	
		$r_{s2,3}$	n_{s2}	{3}	Applicable only for rows with 3 tanks
		$l_{s2,3}$	n_{s2}	{3}	
	Row 3	n_{s3}	n_{s2}	{1, 2, 3}	A tank in row 3 requires a tank in row 2.
		$r_{s3,1}$	n_{s2}	{1, 2, 3}	
		$l_{s3,1}$	n_{s2}	{1, 2, 3}	
		$r_{s3,2}$	n_{s2}	{1, 2, 3}	Only applies if there is a tank in row 2; otherwise, row 3 has no tank
		$l_{s3,2}$	n_{s2}	{1, 2, 3}	
		$r_{s3,3}$	n_{s2}	{1, 2, 3}	
		$l_{s3,3}$	n_{s2}	{1, 2, 3}	

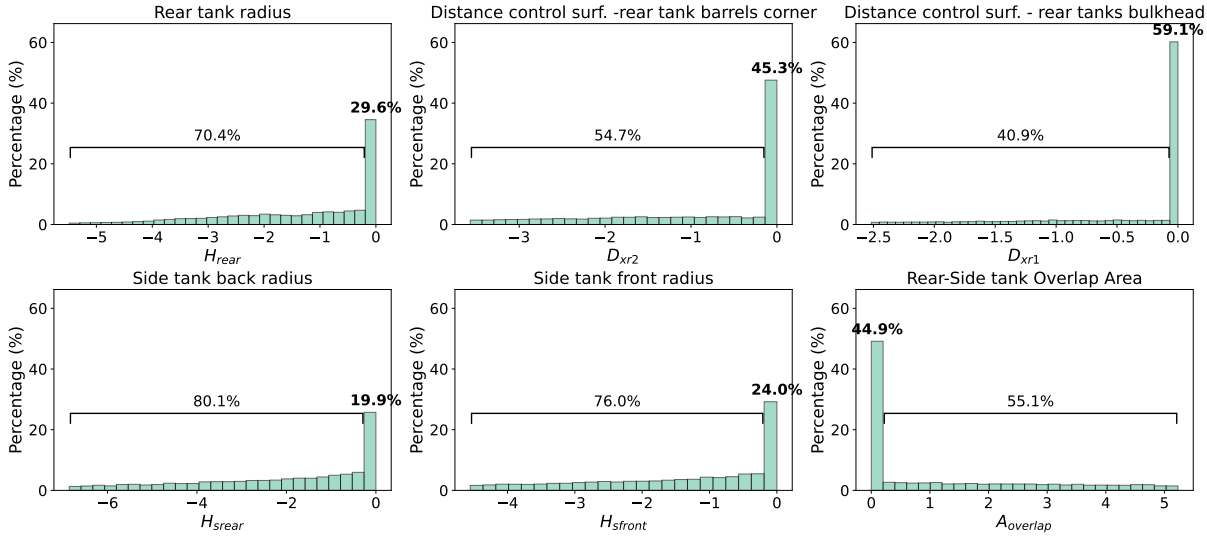

Figure VI.3: Distribution of aggregated constraints values across the **DoE**. Negative values for radius and distance constraints indicate violated constraints.

modate than the rear tank, which is expected due to the reduced available thickness near the cabin compared to the rear section. Furthermore, the constraint on the rear radius of the side tank is consistently stricter than that on the front radius. This behavior can be attributed to the minimum distance imposed between the side tank front and the fuselage, as well as the **BWB** airfoil geometry, which tends to be thicker near the leading edge. Consequently, this suggests that the front radius constraint may be redundant for the optimization within the current design space with the chosen variable bounds
The distributions of the two remaining constraints are shown in Figure VI.4. While the fuel volume constraint is readily satisfied within the current design space, stability represents a significant challenge, with only 0.3% of designs achieving a positive static margin. The average minimum static margin (case with full payload and fully filled tanks) is approximately -6%. Notably, among the 57 designs that satisfy the distance, radius, overlap, and fuel volume constraints (collectively referred to as geometrical constraints), none exhibit a positive static margin. In this particular subset, illustrated in Figure VI.5, the average static margin is around -5%, with the most stable design achieving only -2.2%.

These results indicate that the current, stringent stability constraint severely restricts the feasible design space. If the optimization fails to identify any feasible solutions—which is likely—then either the constraint will need to be relaxed to allow for negative static margins, or the design space must be expanded. Potential strategies to improve stability include shifting the engine forward (potentially under the wing) or increasing the flexibility of the design space by incorporating parameters such as wing sweep angle and wingspan as additional design variables. Figure VI.5 suggest that there might be two types of configuration that do satisfy the geometrical and fuel constraints as the density of feasible configuration (with respect to this constraint) shows a double peak. One type of configuration seems to have indeed a better minimum static margin, meaning that the center of gravity is more forwards, probably thanks to fuel tanks preferentially placed on the cabin side, while the other type probably have more tanks in the rear section. If

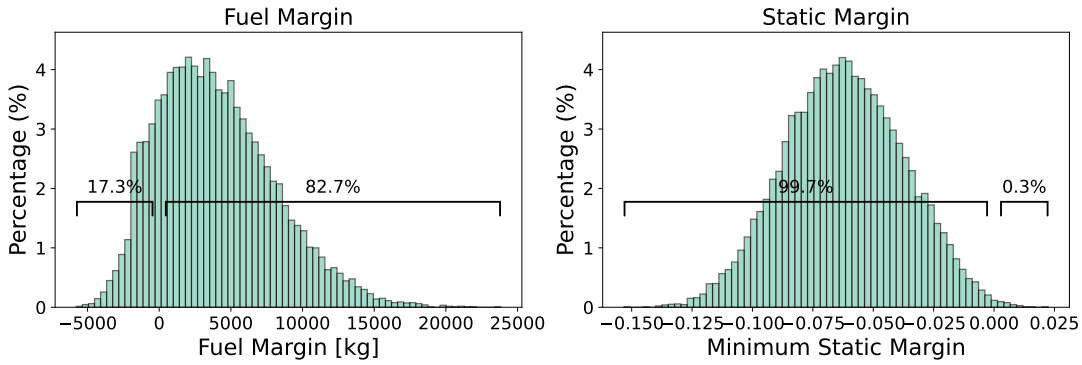

Figure VI.4: Distribution of fuel margin and static margin constraints values across the **DoE**

the second type have so a even lesser minimum static margin, they also seem to present better fuel efficiency as the 10 best fuel-efficient configurations are more present around that peak. To confirm that trend, more studies that characterize the feasible region are carried out in the next section.

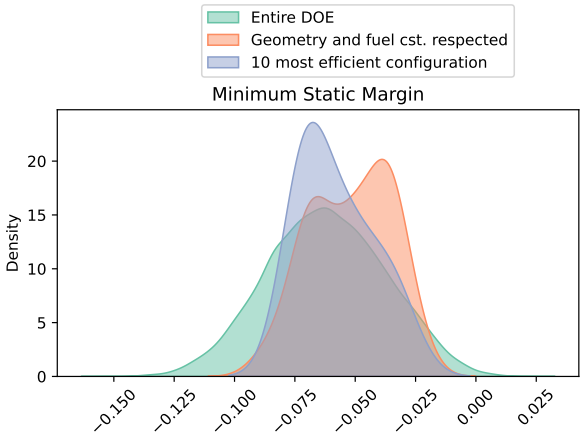

Figure VI.5: Minimum static margin distributions: full DOE vs feasible vs most efficient feasible designs

VI.3.3 Analysis of Feasible Region Trends from the DOE

To investigate configurations favoring feasibility, the analysis is restricted to the 57 designs—out of 18,000 DOE points—that satisfy all geometrical and fuel volume constraints (excluding static margin; see Section VI.3.2). Among these, the 20 most fuel-efficient configurations are shown in Figure VI.6, ordered from highest to lowest efficiency (top left to bottom right). Although these designs comply with the geometrical constraints, they exhibit significant unused internal volume, confirming that further optimization is required to obtain competitive configurations. Nonetheless, comparative analysis of this subset provides useful preliminary insights.

Traditional analytical methods—such as pair plots and parallel coordinate plots—used to



Figure VI.6: Twenty hydrogen **BWB** designs from the **DoE**, satisfying geometrical constraints and ranked by fuel efficiency (left to right, top to bottom)

identify trends and sensitivities in **DoE** studies are however not adapted in this study due to the presence of discrete variables. These methods proved indeed uninformative for analyzing the **DoE**, as all design points were concentrated at identical discrete values, obscuring meaningful insights. To address this challenge, Figure VI.7 introduces a customized histogram designed specifically for this problem. It illustrates the percentage distribution of the number of tanks in the first rear row within the subset of the **DoE** that satisfies all constraints except the minimum static margin requirement. This distribution is further refined into four distinct cases:

- **All geometrically feasible designs** : Distribution across the entire **DoE** subset.
- **30 most fuel-efficient designs**: Distribution of the 30 configurations with the highest fuel efficiency within the subset.
- **10 most fuel-efficient designs**: Distribution of the 10 configurations with the highest fuel efficiency within the subset.
- **10 highest min static margin designs**: Distribution of the 10 configurations with the highest minimum static margin (which should ideally be positive to satisfy all constraints but remains negative in all cases)

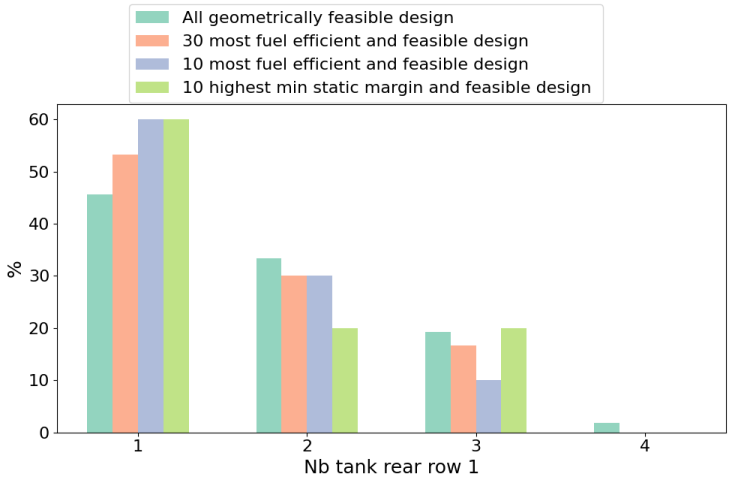

Figure VI.7: Tank count distribution on the first rear row : Comparison Between Geometrically Feasible **DoE** Subset, Energy-Optimized feasible Configurations, and Stability-Optimized feasible Configurations

Figure VI.7 shows for example that feasible configurations tend to favor a reduced number of tanks in the first rear row. This trend is equally relevant for maximizing the static margin and becomes slightly more pronounced in the subset of the most fuel-efficient designs. Since configurations with four tanks in this row are virtually absent, the corresponding upper bound could be lowered in the optimization. To be able to draw similar conclusions on all design variables, figure VI.8 illustrates the distribution of tank counts in each rear and side row within the feasible region. Several observations can then be drawn:

- In the second rear row, one or two tanks appear most favorable, although feasible and fuel-efficient designs with three or four tanks are also present. By contrast,

configurations without a tank on the second row are almost absent. For maximizing static margin, fewer tanks are generally preferable.

- The necessity of a third rear row is less clear. Approximately one-third of feasible configurations exclude this row, a proportion that is similarly reflected among the most fuel-efficient designs. When present, configurations with a single tank are more frequent, though arrangements with two, three, or four tanks are also represented. Interestingly, rows with one or three tanks appear advantageous, likely due to tank positioning in cases with an odd number of tanks. The centrally located tank in those configurations benefits from maximum thickness and chord length, relaxing the geometrical constraint, and a three-tank row allows for two smaller tanks to be placed symmetrically on either side.

- For the first side row, a single tank appears slightly more favorable; however, configurations with two or three tanks also occur in both the most fuel-efficient and highest static margin subsets, making it difficult to draw a definitive conclusion.

- Regarding the second and third side rows, the absence of tanks clearly facilitates feasibility. Nevertheless, in the second row, the most fuel-efficient subset includes relatively more configurations with one or two tanks compared to the baseline, suggesting the possibility of an optimum in this region.

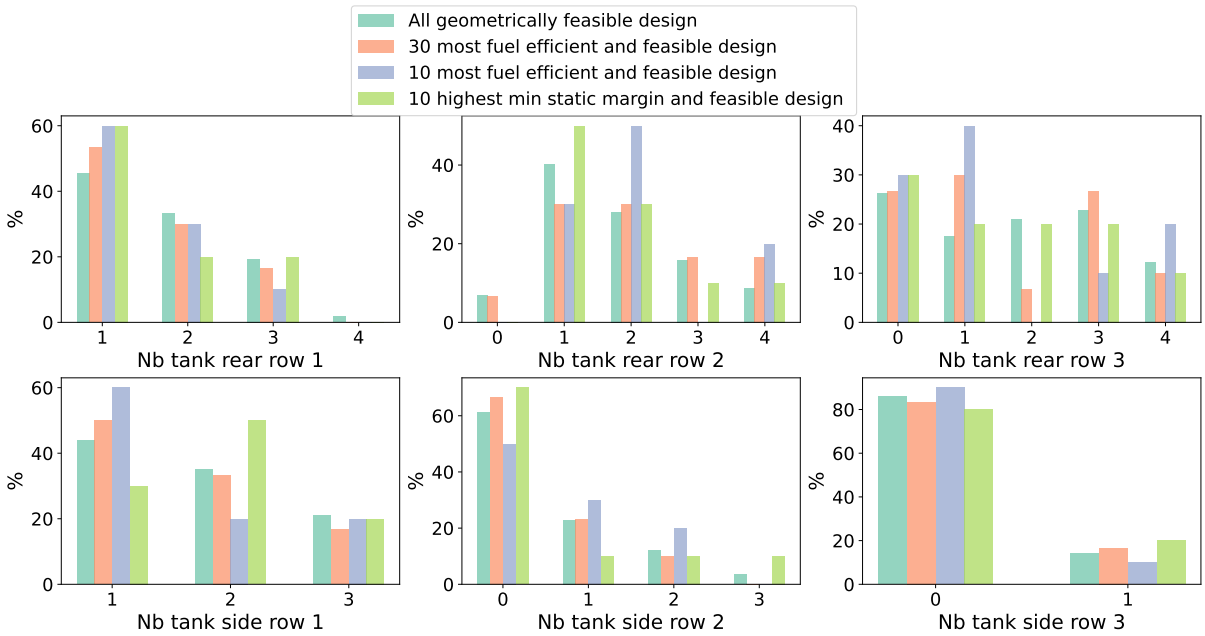

Figure VI.8: Tank count distribution in geometrically feasible DOE subset

It is also instructive to examine the geometric and performance characteristics within this partially feasible region. Figure VI.9 presents several relevant parameters, including the lateral width of the transition section between the central body and outer wing in the **BWB** (see Figure V.1), the fuel mass, wing area, aerodynamic efficiency, and central chord length at plan p0. The results highlight a clear divergence between geometrically

feasible and fuel-efficient designs on the one hand, and more stable configurations on the other:

- As anticipated, designs that satisfy the geometrical constraints while achieving the highest fuel efficiency tend to minimize the external dimensions of the aircraft. The ten best-performing configurations in this category exhibit transition zone widths of 3–4 m and central chord lengths clustered around 27 m—approximately 1 m and 2.5 m shorter, respectively, than the average feasible configuration. These reductions translate into wing surface areas 10–20% smaller than the average and yield a fuel mass concentrated around 7,000 kg.

- In contrast, configurations that maximize the minimum static margin (i.e., bring it closer to zero) favor elongated geometries, with average central chord lengths of 29 m and transition zone widths concentrated near the upper bound of 4.5–5 m. This results in wing surface areas larger than the global feasible average and limits the lift-to-drag ratio to values below the 18.5–19 range characteristic of the most fuel-efficient designs. Consequently, the average fuel mass in this subset is close to the global mean, representing a 5–10% increase compared to the best fuel-efficient designs.

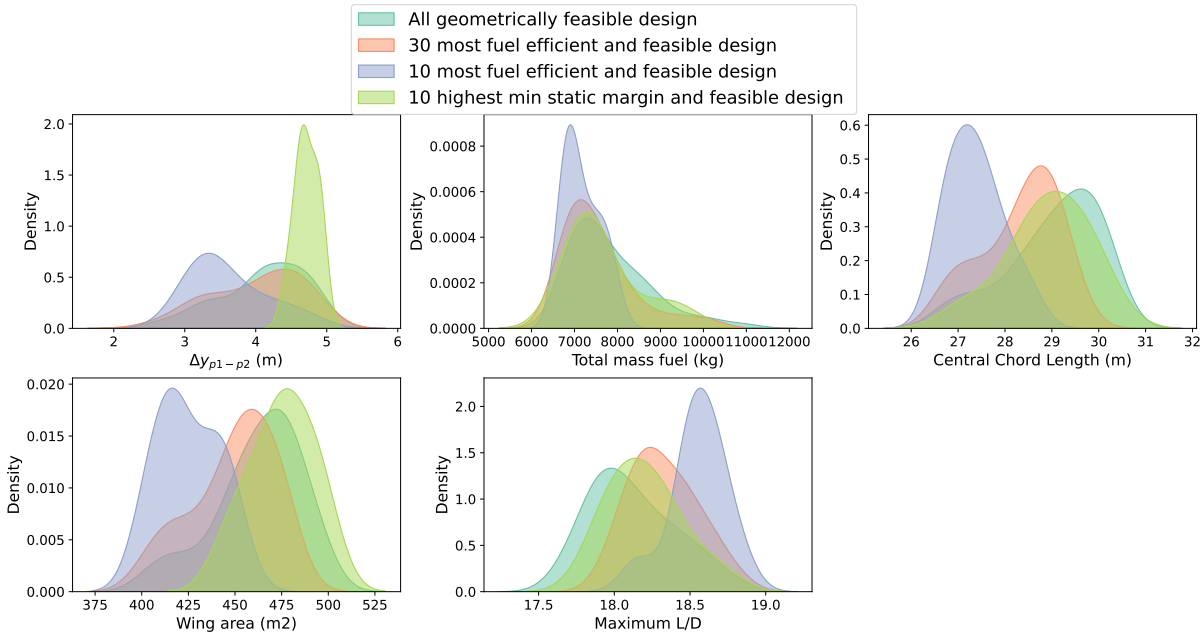

Figure VI.9: Distribution of aircraft characteristics in the geometrically feasible DOE subset

Further statistical analysis of tank dimensions—specifically length and radius—for both rear and side rows may be conducted, though interpreting trends in these variables presents greater complexity. Selected results are illustrated in Figure VI.10 (with comprehensive analyses provided in Appendix, Figures A.33 and A.34). Notably, several geometric variables exhibit bimodal distributions, indicating the presence of at least two distinct feasible configurations. For instance, the second tank in the first rear

row (defined only in configurations with three or four tanks per row, as the two-tank arrangement consists of identical twin tanks specified by the first tank, row 1; see Section V.3) demonstrates enhanced feasibility at lengths of approximately 4 m or 9 m and radii of 1.35 m or 1.8 m. In both cases, designs with the larger dimensions tend to yield higher efficiency, while intermediate values are less favorable.

A further observation underscores the persistent divergence between tank geometries optimized for fuel efficiency and those satisfying static margin requirements. To meet static margin constraints, tanks in the second side row must be shorter, whereas those in the first side row must be wider. This pattern can be attributed to the spatial arrangement of the tanks: those in the second side row are typically positioned aft of the aircraft's center of gravity, such that increased length would further degrade the static margin. Conversely, the first tank in the first side row is located furthest forward, making a wider diameter advantageous for maximizing forward fuel storage and thus improving static margin—despite the tendency of a larger diameter to induce a rearward shift due to the sweep angle.

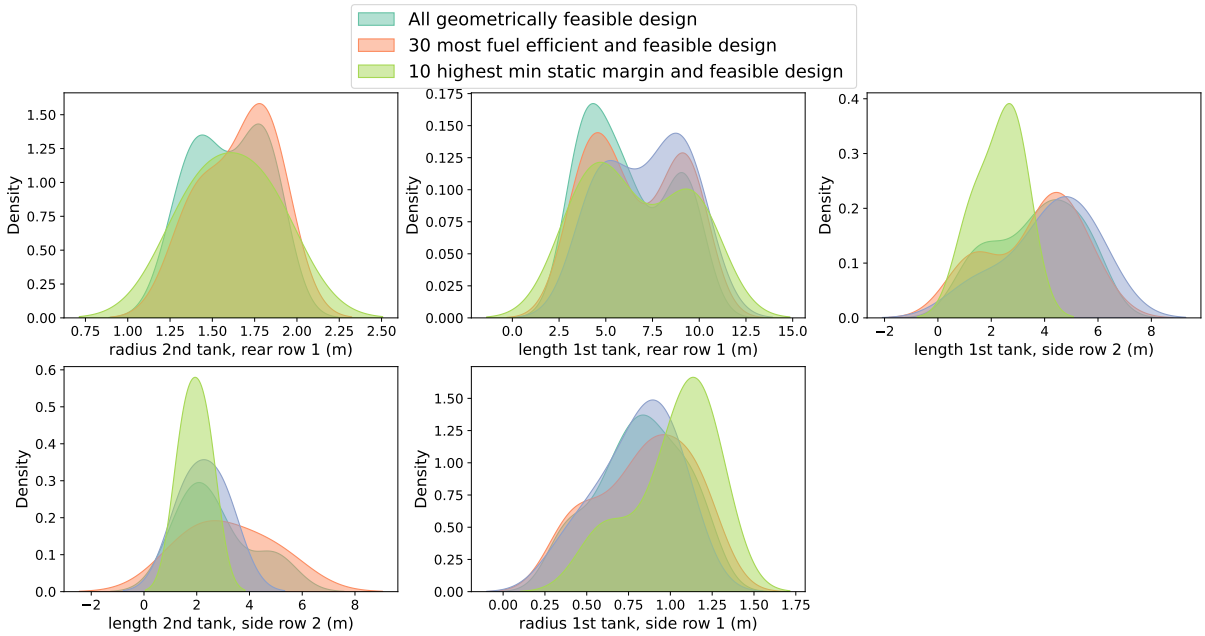

Figure VI.10: Distribution of aircraft characteristics in the geometrically feasible DOE subset

In summary, conducting a design space exploration first demonstrated the capability of the developed method to efficiently size and analyze a wide range of hydrogen-blended wing-body configurations within a reasonable timeframe and with a notable degree of robustness. This process also enabled the identification of the characteristics of various constraints and the boundaries of feasible design regions. The feasible regions appear to be quite limited within the design space: only 57 configurations satisfied all geometric and fuel volume constraints, and none of these met the additional requirement of a positive static margin.

However, given the high dimensionality of the design space, these conclusions must be interpreted with caution. While 18,000 sample points were evaluated, this number may still be insufficient to fully capture the complexity of the space. Furthermore, the observed trends should be considered in light of two key observations:

- **Feasibility does not imply optimality**: Even if more feasible design regions were identified, the global optimum may reside in a highly constrained area that is rarely sampled in a uniformly distributed design of experiments.
- **Sensitivity to fixed design variables**: The identified trends may be influenced by other aircraft design parameters that were held constant in this study. For instance, including the sweep angle in the design space could relax certain constraints, or reducing the 20 cm structural margin between the tank and the aircraft skin might reactivate previously inactive constraints. These considerations, however, underscore the adaptability and scalability of the implemented method, which can be readily extended to explore alternative design spaces.

These findings highlight the value of adopting a Multidisciplinary Design Analysis and Optimization (MDAO) approach. By automating the trade-offs between the objective function—such as achieving an efficient aircraft—and the various constraints—including geometric feasibility and static stability—MDAO provides a robust framework for navigating complex design challenges. Furthermore, with an appropriate optimizer, this approach should be capable of identifying the global optimum, even if it lies within highly constrained or sparsely sampled regions of the design space.
In the subsequent study, however, to streamline the optimization process and accelerate convergence, it was determined—based on the insights gained from the design space exploration—that the constraints V.18 and V.15 could be relaxed without significantly compromising the design integrity.

VI.4 Optimisation of Small-to-Medium-Range Hydrogen-Blended Wing Body

VI.4.1 Establishing a Mixed-Variable Optimization Process

The objective of this section is to execute the optimization outlined in Chapter V.4 to determine an optimized design of a hydrogen-powered **BWB** for a **SMR** mission. While the previous chapter detailed the optimization problem, it did not address the methodology for solving it. Given the complexity of the optimization—particularly due to the presence of discrete and hierarchical design variables—gradient-based approaches are ill-suited. Additionally, the relatively long computational time (approximately 15 minutes for a single **MDA** loop) necessitates an optimization method that minimizes calls to the objective and constraint functions. To address these challenges, a wrapper for **FAST-OAD** was developed within the **SEGOMOE** optimizer.

SEGOMOE is a gradient-free optimizer developed at ONERA and ISAE-SUPAERO[**166**, **167**], based on Bayesian optimization using Gaussian Process surrogate models. The approach involves constructing a Gaussian process surrogate model for the objective function (in this case, the block fuel mass) and each constraint from an initial **DoE**. The optimizer then leverages these surrogate models to identify new enrichment points by maximizing an acquisition function, which balances exploration of unexplored regions in the design space with exploitation—i.e., the minimization of the Gaussian process predictions error. The selected design points are evaluated and used to refine the **DoE**, iteratively improving the surrogate models towards feasible regions of the design space minimizing the objective function. The implemented approach in **SEGOMOE** [**168**] combines continuous relaxation and principal component analysis to reduce the number of hyperparameters, thereby lowering the computational cost associated with the construction of the mixed Gaussian process. For this specific problem, the maximization of the acquisition function within **SEGOMOE** was performed using the **Sequential Least Squares Programming (SLSQP)** optimizer. To ensure that the new enrichment point represents a global maximum, a multistart strategy was employed, limited to six different starting points (instead of twice the problem dimension) to reduce computation time. The previously implemented multiprocessing capability of **FAST-OAD**, adapted for hydrogen **BWB**, enables the parallel convergence of multiple **MDA** loops, facilitating the rapid generation of the initial **DoE**. However, after this step, each iteration depends on the previous one, making parallel computation ineffective. While a potential strategy could involve enriching the **DoE** through batch runs—adding multiple points simultaneously—the current implementation of **SEGOMOE** does not yet support this feature. Given the computationally expensive nature of constructing the Gaussian process, optimization time became a limiting factor. During initial optimization tests, the same design space was indeed used as in the previous section (see table VI.2). However, each optimizer iteration required nearly one hour, making the overall problem resolution impractically lengthy. To mitigate this, the number of points in the initial **DoE** was limited to one hundred, and the number of design variables was reduced from 38 to 17. This reduction was achieved by:

- Limiting the number of rear tank rows to one, with a maximum of 3 tank on that row
- Restricting the number of side tank rows to two, with a maximum of two tanks per side row and three tanks in the last rear row.

These simplifications are justified by the following observations:

- The strict static margin constraint encourages placing as much weight forward as possible, discouraging architectures with multiple rear tank rows.
- During the exploration phase, only a negligible fraction of configurations with three side tank rows were found to be feasible (see figure VI.8) .
- Most geometrically feasible and efficient designs identified in previous analyses do not feature three tanks in the first or second side row (see figure VI.8).

These simplifications result in the following optimization problem (Equation VI.1), which represents a simplified version of the general case presented in Equation V.21. The design variables and their corresponding bounds are detailed in Table VI.4.

$$
\begin{aligned}
\min \quad & m_{blockfuel} \\
\text{w.r.t} \quad & N_{side}, N_{rear}, R_{side}, R_{rear}, L_{side}, L_{rear}, \Delta y_{p1-p2}, \epsilon_{p0} \\
\text{s.t.} \quad & \sum_i V_{tank_i} \geq V_{totalBF} \\
& \sum_i^2 \sum_j^2 a_1 \cap a_{i,j} = 0 \\
& D_{xr2} = 0 \\
& H_{rear} = 0 \\
& H_{srear} = 0 \\
& SM \geq 0
\end{aligned}
\tag{VI.1}
$$

Table VI.4: Design Variables and Bounds for the Optimization of a Hydrogen-Powered **BWB** Aircraft for **SMR** Missions

Design variables				**Lower bound**	**Upper bound**
ϵ_{p0} (marging between cabin height and maximum thickness at plan p_0)				0.4	1
Δy_{p1-p2} (width of the transition zone)				2.5	5
Number of tank	Rear	row 1		1	3
	Side	row 1		1	2
		row 2		0	2
Rear tank	Radius	row 1	$r_{r1,1}$	1	2
			$r_{r1,2}$	1	2
	Length	row 1	$l_{r1,1}$	3	10
			$l_{r1,2}$	3	8
Side tank	Radius	row 1	$r_{s1,1}$	0.3	1.5
			$r_{s1,2}$	0.3	1.5
		row 2	$r_{s2,1}$	0.3	1.1
			$r_{s2,2}$	0.3	1.1
	Length	row 1	$l_{s1,1}$	1.55	8
			$l_{s1,2}$	1.55	5
		row 2	$l_{s2,1}$	1.2	6
			$l_{s2,2}$	1.2	2

VI.4.2 Assessment of Iterative Optimization Behavior

To facilitate convergence of the optimizer, efforts were made to ensure that the initial **DoE** used by **SEGOMOE** included at least one feasible design point. Upon analyzing the **DoE** results, it was observed that several points lay near the feasibility boundary and exhibited clear potential for design improvements that could resolve violated constraints. By applying these improvements, a feasible design was identified and subsequently integrated into the initial **DoE**. A comparison of the initially identified near-feasible design and the adjusted feasible design is presented in Figure VI.11. The near-feasible design already satisfies all geometric constraints, exhibits a fuel margin surplus of 262 kg, and maintains a minimum static margin of -0.4%.

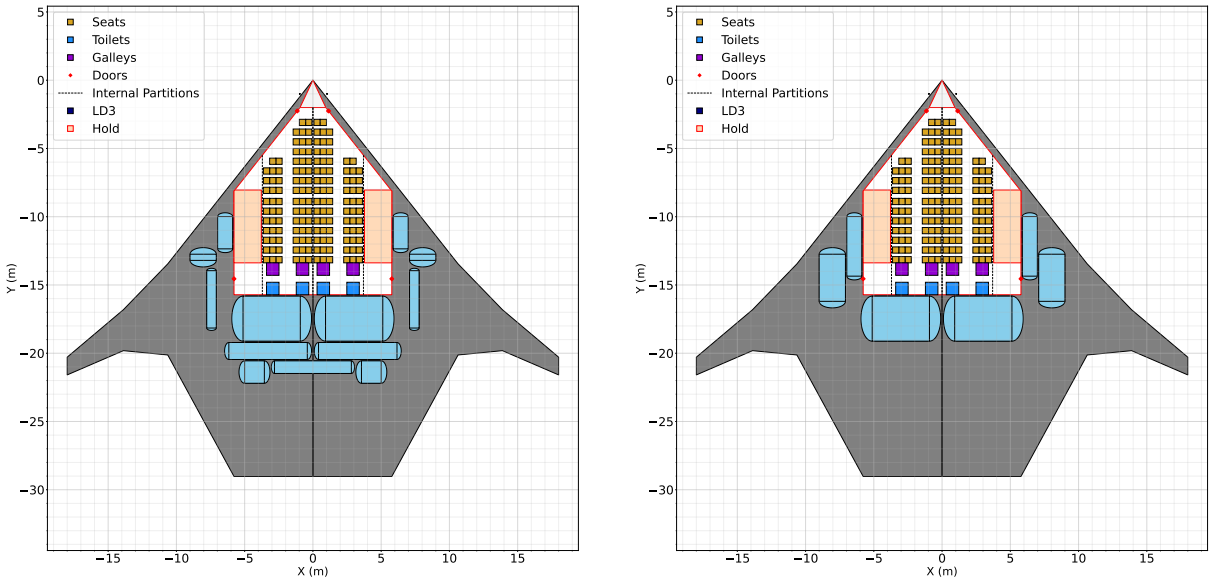

(a) Near-Feasible Design

(b) Adjusted Feasible Design

Figure VI.11: Evolution from Near-Feasible (left) to Feasible Design (right) of the SMR Hydrogen BWB by expert adjustment

As illustrated in Figure VI.11, even the feasible design—which satisfies all constraints—exhibits clear opportunities for architectural optimization. Notably, the excessive space behind the rear tank is significantly larger than necessary, further justifying the need for subsequent optimization.

The optimization was initiated from an initial **DoE** of 100 points, supplemented by one additional point. Each iteration required 20 to 30 minutes on a standard laptop (Intel 12th Gen Core™ i7-1265U, 1.8 GHz), with 10 to 15 minutes dedicated to **DoE** enrichment via **MDA** execution. The optimizer converged to an improved feasible design after approximately 70 iterations, but 100 iterations were made to ensure the robustness of the optimum.

Figures VI.12 and VI.13 depict the convergence history of the optimization process, focusing on the objective function and constraints. Several key observations emerge:

- **SEGOMOE** required around 70 iterations to identify a feasible design, but the result at that stage represents a significant improvement in the objective function and

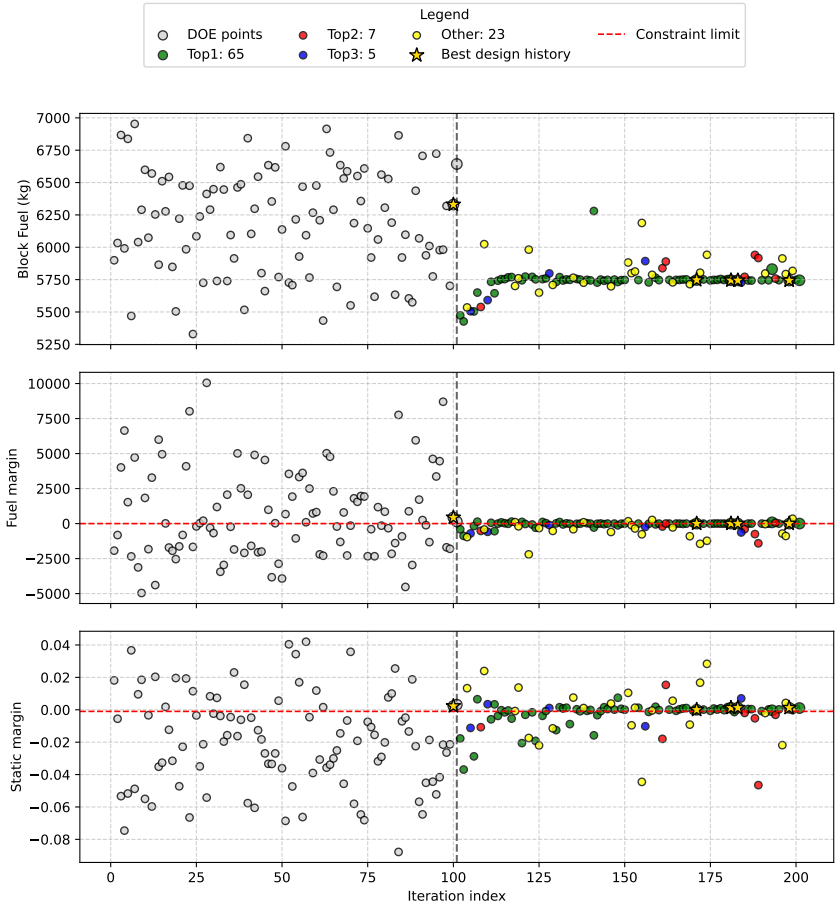

Figure VI.12: Convergence History of Objective and Constraints (Fuel and Static Margin) During Optimization

appears close to the global minimum. Subsequent feasible designs only marginally enhanced the optimum.

- Interestingly, the optimizer approached the optimum by crossing infeasible regions. This behavior may stem from the limited size of the feasible region and the greater complexity of satisfying constraints compared to simply minimizing the objective function. For instance, no feasible iteration resulted in a degraded objective value compared to the previous best design; rather, each feasible iteration consistently improved the block fuel mass. This observation suggests that the feasible design space is not only narrow but also difficult to navigate, compelling the optimizer to cross infeasible regions in order to effectively converge toward the optimal solution.

- In the early iterations, the optimizer prioritized minimizing the objective—often by favoring thin and compact architectures—but these designs strongly violated constraints, particularly those related to tank radius fitting within the available airfoil thickness. The optimizer took approximately 20 iterations to recognize this pattern. In previous tests with a wider design space, this initial phase often extended much longer.

- The rear tank distance constraint was consistently approximated well by the Gaus-

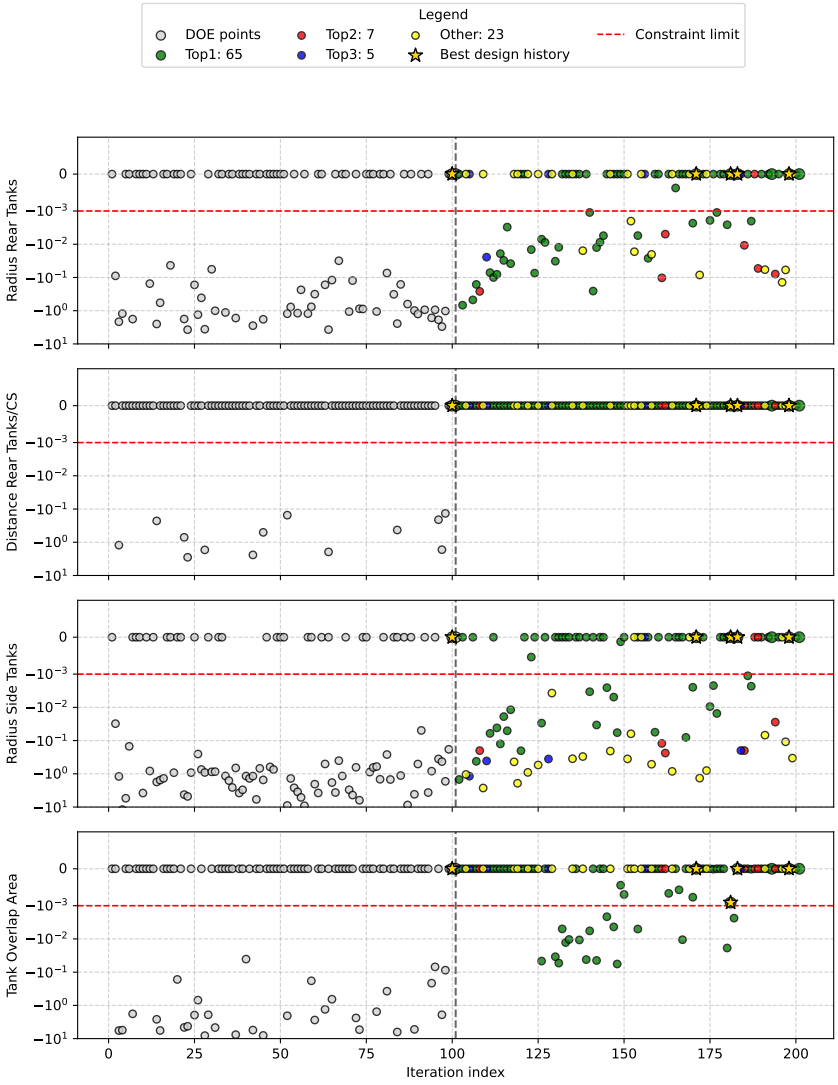

Figure VI.13: Convergence History of Geometrical Constraints During Optimization

sian process, as it was never violated during optimization. This may also suggest that, given the design space constraints (e.g., a 20 cm margin between the tank and airframe) and the possible tank configuration, this constraint cannot be violated in the current setting.

- The designs tested by **SEGOMOE** are categorized based on the tank architecture evaluated. The three most frequently tested architectures (out of thirteen) are represented in green, red, and blue, while the remaining configurations are shown in yellow. The dominant configuration, accounting for 65 out of 100 points, corresponds to the initially identified feasible design in Figure VI.11: a configuration with two rear tanks and one tank in each side row. The next most tested configurations include one rear tank with one tank in each side row (7 occurrences) and two rear tanks, one tank in the first side row, and two in the second (5 occurrences). The remaining ten configurations make up the final 23 points.

  While the optimizer actively explored alternative configurations, those deviating

from the top-ranked class consistently exhibited greater constraint violations—such as side row radius constraints (as shown in Figure VI.13)—or resulted in higher objective function values (e.g., red points frequently appearing above green points in the block fuel monitor). This pattern underscores the robustness of the final optimal design, though it may also indicate that constraints are highly sensitive to configuration changes. In such cases, the surrogate models for constraints may lack precision when applied to configurations outside the top-ranked class, potentially hindering the identification of superior feasible designs. Testing this hypothesis would require additional iterations or a denser initial DOE, both of which would significantly increase optimization time. For this reason, the study was not pursued further in this direction at this stage.

In conclusion, the optimization proved successful within this restricted design space, identifying a feasible design that significantly improved the objective—specifically, the block fuel mass. While there is no guarantee that this solution represents the global optimum, the convergence behavior observed over the subsequent 30 iterations suggests that the identified optimum is robust. Should another global optimum exist, its discovery would likely require substantially longer computational time, potentially yielding only marginal improvements. Regardless, the successful optimization demonstrates the effectiveness of the formulated **MDAO** method in designing a hydrogen-powered blended wing body aircraft. The performance and key characteristics of the optimized aircraft design are detailed in the following section.

VI.4.3 Evaluating the Performance and Key Design Features of an Optimized Hydrogen-Powered Blended Wing Body Aircraft for SMR missions

VI.4.3.1 Presentation of the optimized hydrogen powered Blended Wing Body design

To recap, the final output of the optimization process is a hydrogen-powered Blended Wing Body (BWB) aircraft designed for Small-to-Medium Range (SMR) missions. This aircraft is capable of transporting 150 passengers (or approximately 13.5 metric tons of payload) over a range of 3,050 nautical miles. To enhance visualization of the aircraft design produced by the new **MDAO** sizing methodology, a post-treatment discipline—inspired by prior work in the CICAV project [**104**]—was developed and integrated into **FAST-OAD**. In addition to the previously presented 2D visualizations of the **BWB** aircraft (see Figures VI.6 and VI.11), this post-treatment module automatically converts the **BWB** geometry into an OpenVSP file. Figure VI.15 shows the 2D layout of the optimized aircraft, while Figure VI.14 provides its 3D representation in OpenVSP.

As expected, the final optimized configuration aligns with the most frequently tested layout by the optimizer: two twin tanks in the rear row behind the cabin, one major tank in the first side row, and a smaller tank in the second side row. In terms of fuel storage distribution, the rear tanks dominate, accounting for 62.6% of the total storage capacity.

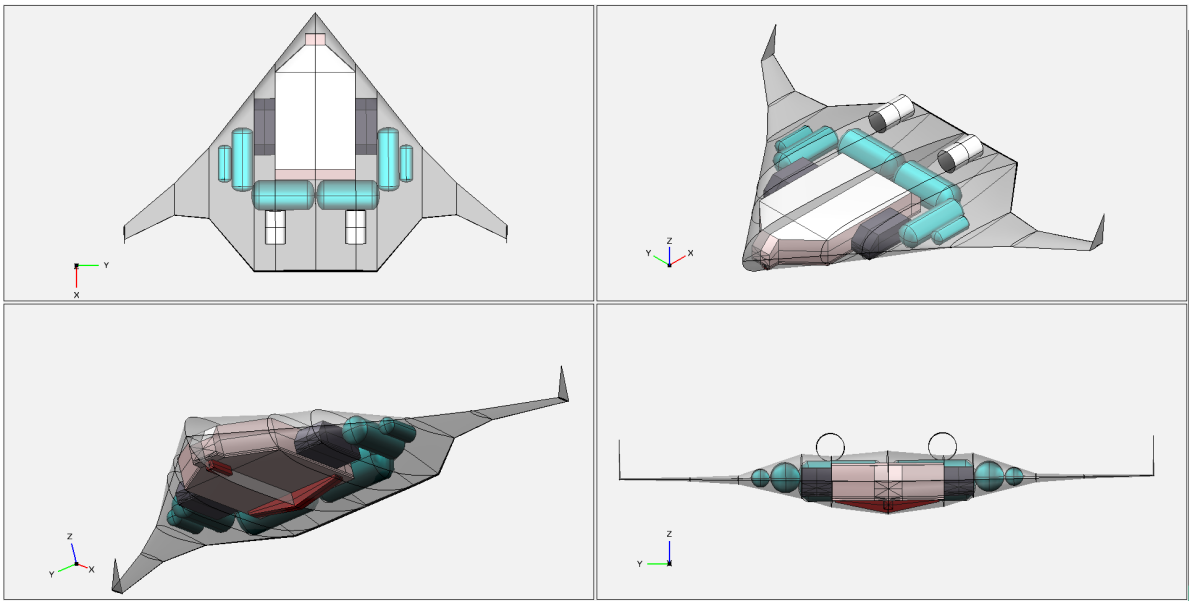

Figure VI.14: 3D Visualisation of the optimized hydrogen **BWB** design on OpenVSP

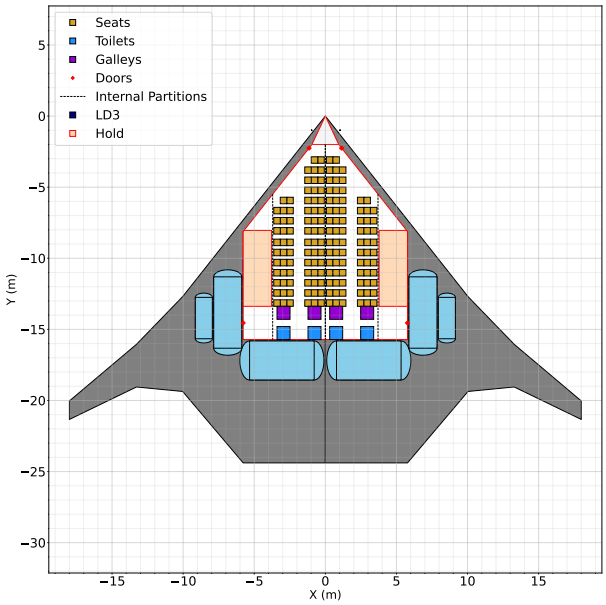

Figure VI.15: 2D Visualisation of the optimized hydrogen **BWB** design

The medium-sized tanks on each side contribute 15.8% each (or 31.6% combined), while the small tanks represent only 2.9% each (5.8% both) of the total capacity.
This fuel distribution is heavily influenced by stability constraints, as illustrated in Figure VI.16 (generated by the post-treatment module in **FAST-OAD**). The figure depicts the shift in the aircraft's center of gravity and the static margin during fuel and passenger loading, unloading, or consumption.
Notably, when the aircraft is fully loaded with fuel and passengers, the static margin—referred to in this study as the minimal static margin—is only slightly above zero. As fuel is consumed during the mission, the static margin gradually improves, reaching a maximum of 1.8% when the tanks are empty, due to the reduction in rearward mass from fuel depletion.
A reduced payload can lead to instability in certain conditions, as the mass of the rear hydrogen tanks shifts the center of gravity backward, insufficiently compensated by passenger weight. Though this issue affects most hydrogen aircraft—not just BWB configurations—it can be mitigated with front ballast, albeit at the cost of performance [**169**]. While incorporating a more sophisticated stability criterion—accounting for various loading configurations—was beyond the scope of this study, it could be readily integrated into the optimization framework.
An analysis was still conducted to evaluate whether prioritizing fuel consumption or refueling from the rear or from the side tanks could yield benefits. The results indicate a variation of approximately 0.5–1% in the static margin, or about 0.15 meters in the global center of gravity. While this adjustment could assist in trimming the aircraft and thus improve efficiency, the range of variation remains limited, primarily due to the low density of hydrogen.

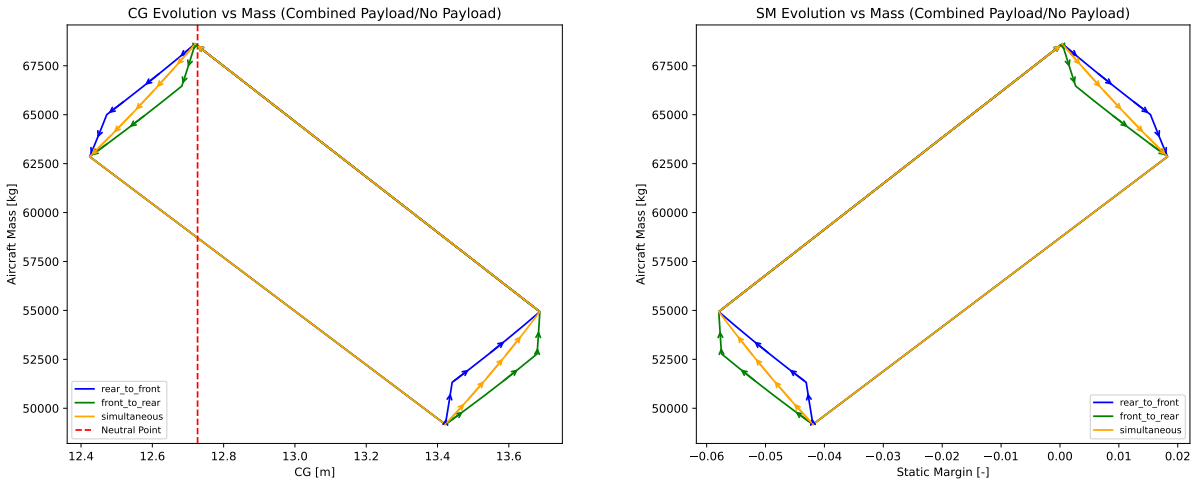

Figure VI.16: Evolution of Aircraft Center of Gravity and Static Margin During Fuel and Payload Loading for Multiple Tank Fueling Strategies (Small segments: fuel mass variation | Long segments: payload loading/unloading)

Regarding emergency exits, this aircraft requires four exits for its intended mission according to current certification norms. Two exits are integrated at the front, just behind

the cockpit, while two additional exits could be positioned aligned with the second seat row. To comply with certification requirements, space is allocated for an emergency exit at the rear of the cabin, positioned aft of the cargo holds—consistent with the approach adopted by Sgueglia in his thesis study [**99**]. However, to avoid obstruction by the hydrogen tanks, such an exit would necessitate repositioning the external wing along the z-axis. For example, if the wing were raised—such as aligning it with the upper surface of the central body—an emergency exit could be created, allowing passengers to pass beneath the external wing and the side tanks (see figure VI.14). Alternatively, the external wing could be aligned with the lower surface (intrados), enabling an exit to open above the wing.
The trade-offs between these options, should rear exits be required, are not addressed in this study and remain a topic for future investigation.

VI.4.3.2 Evaluating Optimization Impact on Hydrogen BWB Performance and Attributes

To assess the performance and characteristics of the optimized hydrogen **BWB** design—and to evaluate the effectiveness of the optimization—several analyses were conducted, comparing this design to both the pre-optimization configuration and a conventional jet-fuel-powered **BWB**.

Figure VI.17 illustrates the evolution of the planform of the hydrogen **BWB**, transitioning from the initial jet-fuel-powered version to the pre-optimization hydrogen configuration and finally to the optimized design. The optimized design is approximately 3 meters longer than the jet-fuel version—a significant reduction from the original 7.7-meter increase in the pre-optimized design. The width of the transition zone between the central body and the external wing was less effectively minimized. This zone was reduced by only 0.6 meters, resulting in a transition zone about 1.8 meters wider in the optimized design. Regarding maximum airfoil thickness, it increased from 3.75 meters in the jet-fuel design to 5.11 meters in the pre-optimized hydrogen design, before being refined to 4.30 meters in the final hydrogen configuration. Given that all remaining design constraints involving tank radius are active, further reduction of the transition zone was not feasible without decreasing the size of the side tanks. Such a reduction would have either compromised storage volume or violated stability constraints. Additionally, as the wingspan is constrained to 36 meters to remain within the same "C" airport category as comparable conventional aircraft, this limitation results in a very short external wing.
The aerodynamic consequences of this planform evolution are evident in the polar curves of the three aircraft configurations, as shown in Figure VI.18. The wide central body of the hydrogen **BWB** generates significant drag, thereby reducing its aerodynamic efficiency compared to the jet-fuel-powered version. In this study, the static margin constraint—given the chosen design parameters—prevented the placement of hydrogen tanks in the rear section of the aircraft, where additional volume was available. Instead, it necessitated an increase in the size and width of the central body, which in turn

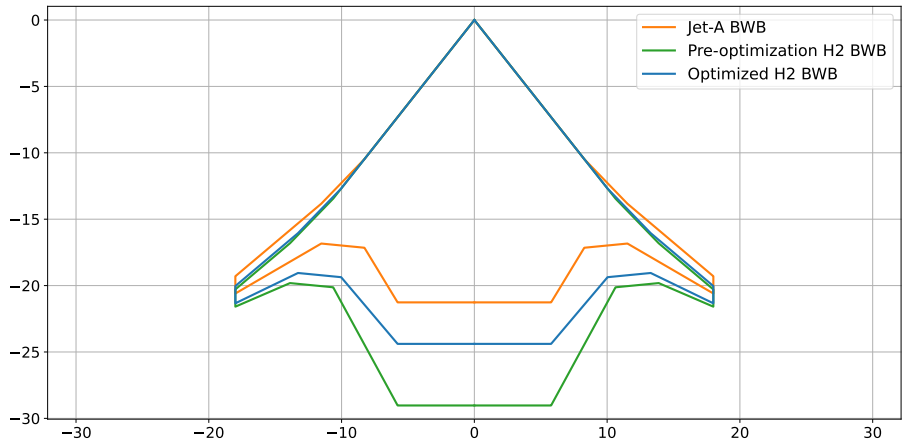

Figure VI.17: Comparison of 2D planform of conventional and hydrogen **BWB**

degraded the maximum lift-to-drag ratio. However, due to the large lifting surface area of these configurations, the peak lift-to-drag ratio occurs at very low lift coefficients C_L, particularly for the larger hydrogen configuration. For example, the optimized hydrogen design reaches its maximum efficiency at a C_L of approximately 0.29.

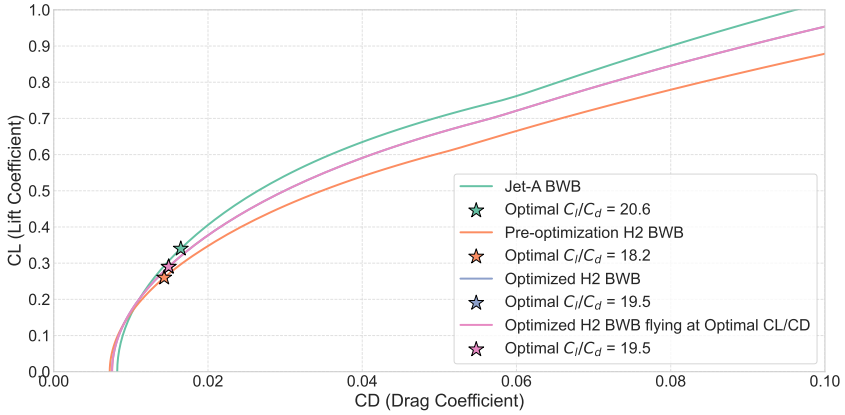

Figure VI.18: Aerodynamic polar curves of different **BWB** design

The drag breakdown comparison in Figure VI.19 shows that the increase in drag stems from both higher zero-lift drag (including friction/form drag and interference drag) and induced drag, with the former being slightly more significant. This trend is logical: a larger airframe naturally boosts friction drag, while the reduced aspect ratio (as seen in Table VI.5) further degrades induced drag performance. It is important to note that the values presented for the H2-powered version have been corrected by the ratio of wing area between the two aircraft configurations (multiplied by a factor of 1.24). This adjustment accounts for the lower maximum cruise lift coefficient (CL) of the H2 version (0.29 vs. 0.34), which is a result of its wider wing area. Without this correction, the total drag coefficient (CD) was originaly equal to 150 drag counts (DC). This normalization ensures a fair comparison of aerodynamic performance between the two configurations.

Through the optimization process, the aerodynamic penalty was still mitigated by mini-

mizing the size increase of the central body. The optimized hydrogen design achieved a maximum $\frac{C_L}{C_D}$ of 19.5, compared to 18.2 for the pre-optimized version and 20.6 for the conventional aircraft.

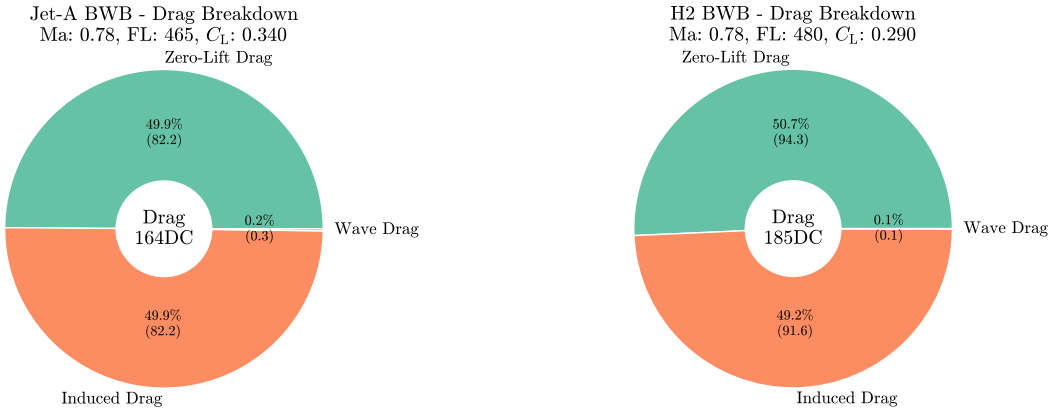

Figure VI.19: Drag Breakdown Comparison Between the Jet-A-Powered **BWB** and the H2-Powered **BWB** at their average cruise lift-to-drag ratio. The drag of the H2 version was corrected by the ratio of surface area to compensate the lower cruise CL

This initial aerodynamic analysis brought attention to the mission profile used in the design of the blended wing body. During the sizing process, the cruise altitude was set to 12,600 meters (41,300 feet) to align with the current cruise altitude of **SMR** flights. However, the low lift coefficient associated with achieving the maximum lift-to-drag ratio suggested that cruising at a higher altitude could be advantageous. Figure VI.20 presents the mission altitude profile, the evolution of the lift-to-drag ratio, and the associated accumulated energy consumption. When the optimized hydrogen **BWB** (blue curve) cruises at 12,600 meters, it operates at a suboptimal lift-to-drag ratio of approximately 18.4–18.3. To explore this further, an additional mission simulation was conducted using the same aircraft, but with the cruise segment parametrized to always target maximum aerodynamic efficiency and not a fixed cruising altitude. The resulting profile (pink curve) transforms the cruise into a continuous climb between 14,000 and 14,600 meters (46,000–48,000 feet). This new mission profile yields a significant reduction in energy consumption compared to the previous profile—without altering the aircraft design. The improvement is particularly notable when contrasted with the energy savings achieved through optimization alone: the modified mission profile delivers an additional 6% reduction in block fuel energy, building on the 14% reduction already attained through optimization.

In the current configuration, the fuel margin in the modified mission is consequently excessively high—approximately 340 kg (6% of the block fuel), equivalent to the volume of the two outermost lateral tanks. Ideally, this finding would have warranted a second optimization cycle, allowing the mission profile to be adjusted for cruising at the optimal lift coefficient. However, due to time constraints, the analysis proceeded with the current optimized hydrogen **BWB** design, now operating under the modified mission profile.
While the design may still be further optimized, this suboptimal approach strengthens

the robustness of the results, mitigating potential overestimations in design assumptions. To ensure consistency and fairness in the subsequent analysis, the reference aircraft—including hydrogen- and jet-fuel-powered **T&W**, as well as jet-fuel-powered **BWB**— were redesigned using this updated mission setting. It should be noted, however, that "optimal" mission setting, though representative of an ideal step-climb profile, is not currently feasible under real-world Air Traffic Management (ATM) constraints.

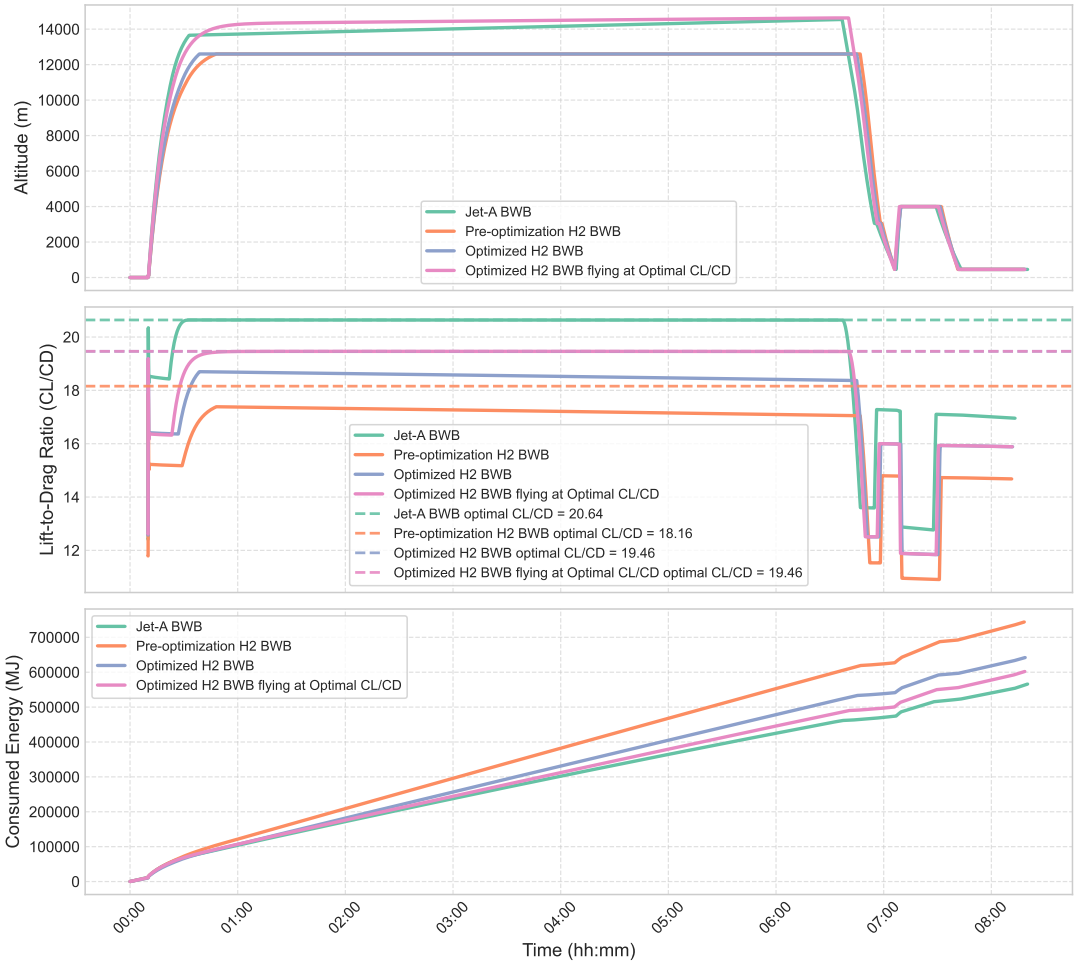

Figure VI.20: Comparative Analysis: Mission Profile, Lift-to-Drag Ratio, and Energy Consumption of Conventional vs. Hydrogen-Powered Blended Wing Body Aircraft

Although the optimization and the subsequent modification of the mission profile significantly improved the fuel efficiency of the hydrogen **BWB**, its energy consumption remains higher than that of a conventional Jet-A-fueled **BWB**. Figure VI.21 provides deeper insight into the origin of this performance difference and the extent to which the optimization reduced it. For further details, Table VI.5 presents a comprehensive overview of the key performance metrics and characteristics of the pre-optimized and optimized hydrogen **BWB**, as well as the reference jet-fuel version.
As previously identified, the primary cause of the reduced energy efficiency is the larger airframe, which adversely affects both the aircraft mass and its aerodynamic efficiency. While the optimization minimized the increase in aircraft size, the hydrogen configuration still requires, for example, a 14% longer body and a 70% wider transition zone.

Table VI.5: Key Characteristics and Performance Metrics of Hydrogen- and Jet-Fuel-Powered Blended Wing Body Aircraft

Category	Variable	Jet-A BWB	H2 BWB pre-optimisation	H2 BWB optimized
Aerodynamic	Optimal C_L	0.34	0.26	0.29
	Optimal C_D	0.016	0.014	0.015
	Max L/D	20.64	18.16	19.46
	MAC [m]	14.03	20.47	16.57
Geometry	Total length [m]	21.3	29.0	24.4
	Wing area [m^2]	314	480	392
	Wing aspect ratio	4.12	2.70	3.30
	Root Sweep angle (p0) [deg]	51.7	51.7	51.7
	Δy_{p1-p2} [m]	2.50	4.85	4.25
	Δy_{p2-p2_1} [m]	3.25	3.25	3.25
	Cabin height [m]	2.1	2.1	2.1
	Cabin length [m]	15.7	15.7	15.7
	Nacelle diameter [m]	2.0	2.0	2.0
	Nacelle length [m]	5.2	5.2	5.2
Weight	MTOW [kg]	70500	72936	67158
	OWE [kg]	43378	52611	48069
	ZFW [kg]	57060	66293	61751
	Payload [kg]	13682	13682	13682
	Central Body mass [kg]	16869	24418	20480
	(External) Wing mass [kg]	1852	1794	1433
	Engine mass [kg]	8215	8197	8202
	Landing gear mass [kg]	3607	3620	3622
	Block Fuel mass [kg]	13439	6643	5407
	Fuel main mission [kg]	10698	5114	4051
	Fuel diversion mission [kg]	1135	544	465
	Fuel holding [kg]	711	338	291
	Fuel Margin [kg]		148	338
	Furniture and system mass [kg]	12834	13050	12927
Hydrogen Tank	Global adjusted gravimetrix index		0.84	0.82
	Global gravimetrix index		0.84	0.83
	Empty mass H2 tanks [kg]		1232	1106
Stability	Minimum Static Margin (%)		0.31	0.04
Propulsion	Thrust at sea level [N]	162472	150204	164648
	Thurst to weight ratio	0.47	0.42	0.50
Performance	Total energy consumed [GJ]	580	798	649

Consequently, the surface area is nearly 25% larger, and the maximum lift-to-drag ratio is reduced by 6%. The impact on aircraft mass is also notable: the optimized hydrogen design achieved a modest 3.6% reduction in **MTOW** compared to the jet-fuel-powered aircraft, down from the pre-optimized design which had shown an increase of nearly 5%. This reduction is relatively small when considering the 57% decrease in fuel weight, attributable to the low density of hydrogen.

Figure VI.22, which presents the mass breakdown of the optimized hydrogen design and the Jet-A-powered **BWB**, reveals that the reduction in fuel mass is largely offset by the increased structural mass of the central body. The central body now accounts for 32% of the **MTOW**, up from 25% in the conventional design. The additional mass of the hydrogen tanks, while contributing to a lesser extent (around 2.2% of **MTOW**), further exacerbates this effect. As a result, the $\frac{OWE}{MTOW}$ ratio increases from 0.62 in the conventional **BWB** to 0.71 in the hydrogen aircraft, corresponding to an 11% increase in **OWE**—or

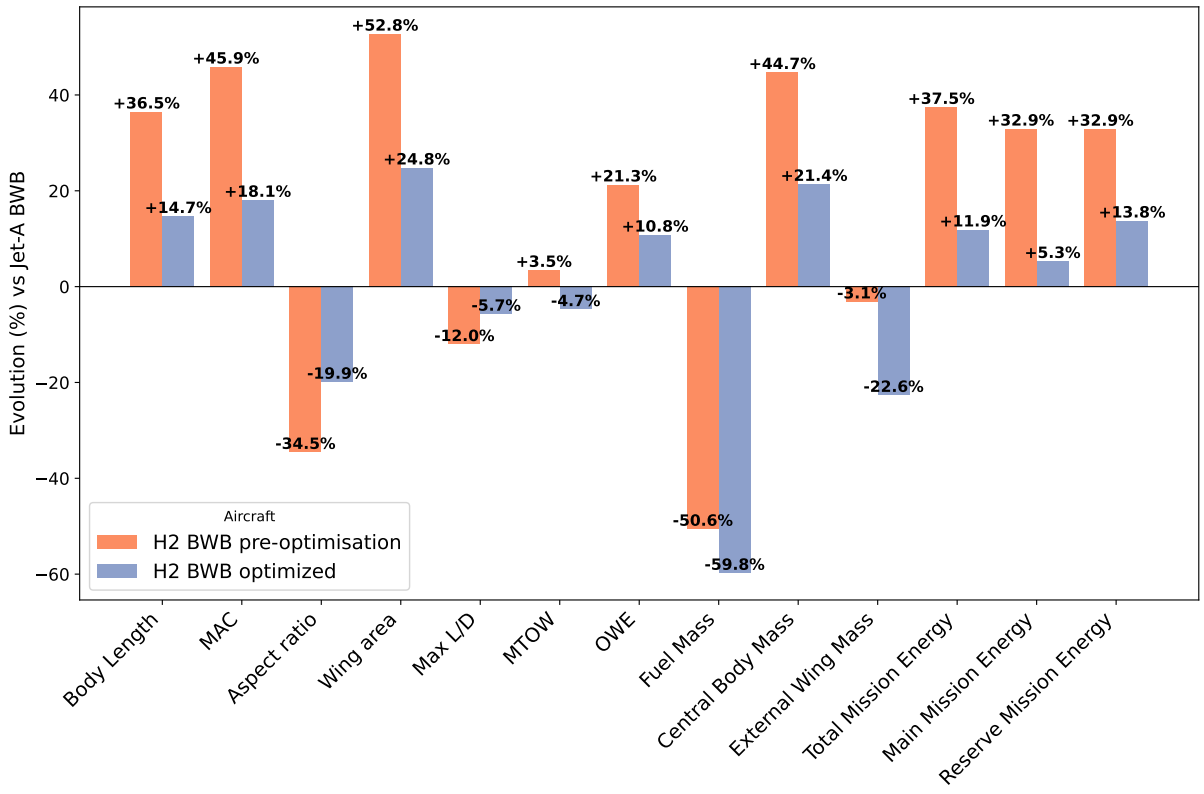

Figure VI.21: Transition Analysis: Changes in Characteristics and Performance from Jet-Fuel to Hydrogen **BWB** Through Optimization

approximately 5 metric tons.

The optimized hydrogen-powered **BWB** experiences a notable increase in mission energy demand, driven by reduced aerodynamic efficiency and a heavier empty weight. Although the maximum takeoff weight (**MTOW**) differs only slightly from the conventional jet-fuel design, the higher operating empty weight (**OWE**) causes the hydrogen aircraft to retain more weight throughout the mission. Unlike jet fuel, which weight onboard decreases rapidly due to its higher density, the hydrogen-powered aircraft's weight decreases more slowly, exacerbating the energy penalty. Combined with a lower lift-to-drag ratio, this effect results in an 11.9% higher energy requirement for the design mission. A closer look at energy distribution reveals that the hydrogen **BWB** consumes only 5.3% more energy than the reference aircraft on the main route, but this gap widens to 13.8% for the reserve mission. This discrepancy occurs because the weight advantage of the jet-fuel aircraft becomes more pronounced as flight duration increases.

It is noteworthy that the weight increase—as well as the aerodynamic degradation—of the hydrogen **BWB** is primarily driven by the larger airframe required to accommodate hydrogen tanks, rather than by the mass of the tanks themselves. This is mainly a consequence of the static margin constraint, which forces most of the tank volume to be placed forward. If alternative solutions—such as relocating the engines under the wings to shift the center of gravity forward—were introduced to alleviate this constraint, the central body would not need to be enlarged to the same extent. In such a scenario, the tanks could make more effective use of the currently unused aft volume,

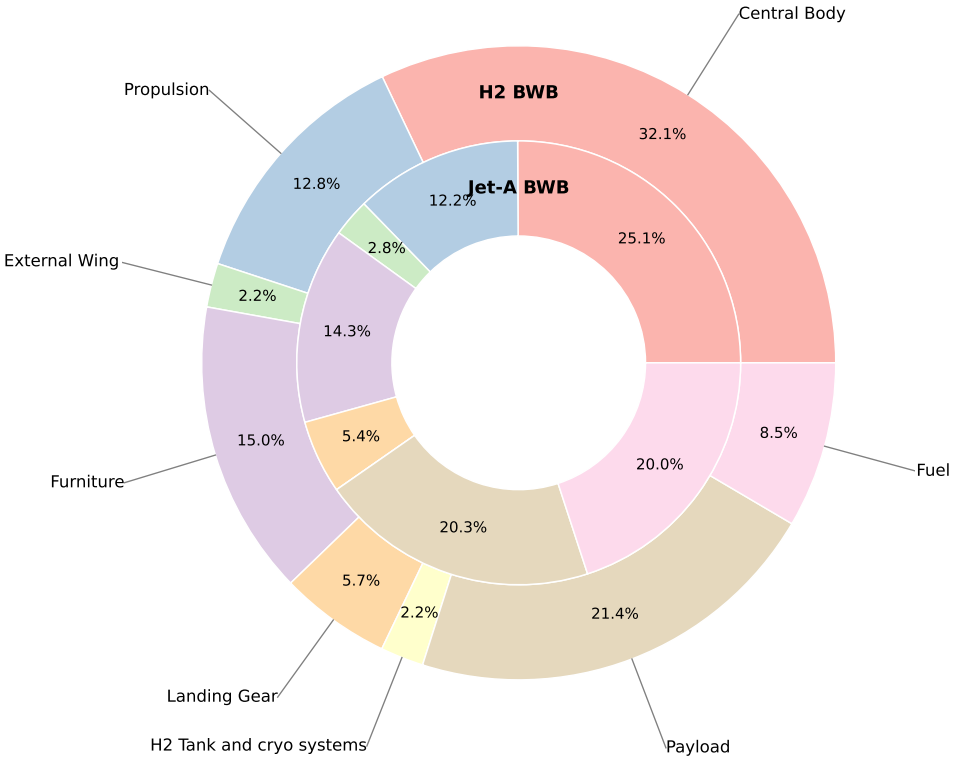

Figure VI.22: Weight Distribution: Jet-Fuel vs. Hydrogen **BWB** Aircraft

enabling configurations that are both lighter and more aerodynamically efficient. In this scenario,the **OWE** of a hydrogen-powered aircraft could potentially be close to that of a jet-fuel-powered equivalent, resulting in a significantly reduced **MTOW**. As the aerodynamic efficiency should remain unchanged, it could potentially lead to highly efficient aircraft.

In conclusion, this study demonstrates that the optimized hydrogen **BWB** aircraft, despite achieving a nearly 25% reduction in energy consumption compared to its pre-optimized design, remains less energy-efficient than the reference jet-fuel-powered **BWB**. However, this disadvantage is somewhat mitigated when considering only the main route segment, which represents the majority of flight operations, as opposed to the reserve mission. This study is also limited in scope, focusing primarily on hydrogen tank configuration as the main design variable, whereas the reference aircraft underwent a more extensive optimization process. This suggests that the gap in energy efficiency could potentially be narrowed in the future through further refinement and optimization. It is important to note that **BWB** architectures, whether hydrogen or jet-fuel-powered, are not currently in operation. Their potential deployment is primarily envisioned as a solution to mitigate the environmental impact of aviation, particularly by facilitating the adoption of hydrogen as an aviation energy source in order to cut carbon emissions. Therefore, the objective of the hydrogen **BWB** is not to consume less energy than a kerosene **BWB**, it is to emit less CO_2, which it achieves. The direct competitor to a hydrogen **BWB** is rather a hydrogen **T&W** aircraft, as both are zero-carbon solutions. To justify its design,

the **BWB** must demonstrate greater energy efficiency compared to its **T&W** alternative. The following section thus presents a comparative analysis of the performance and characteristics of these two hydrogen-powered architectures—**BWB** and **T&W**—in relation to a classical **T&W** aircraft.

VI.4.3.3 Potential of Hydrogen BWB Compared with Hydrogen and Jet-Fuel T&W Aircraft

To assess the viability of introducing a hydrogen **BWB** in achieving the aviation industry's environmental and climate objectives, it must be compared to alternative solutions, such as a conventional hydrogen-powered **T&W** aircraft, and demonstrate its advantages. Additionally, a comparison with a traditional jet-fuel-powered **T&W** aircraft is essential to quantify the potential benefits of this configuration for the future. As previously mentioned, two reference aircraft with a **T&W** architecture were designed for this purpose: one hydrogen-powered and one Jet-A-fueled. The detailed key metrics describing the four aircraft to be compared in this section are presented in Table VI.6.
Figure VI.23 provides a 2D comparison of the planforms of the four aircraft. The conventional jet-fuel **T&W** aircraft has dimensions similar to those of an Airbus A319, with a total length of 31 meters and a wingspan of 31.5 meters. Notably, the wing sizing for this aircraft is constrained by fuel volume storage requirements. Due to its short fuselage length, the horizontal and vertical tails are significantly larger to compensate for the short lever arm relative to the center of gravity.

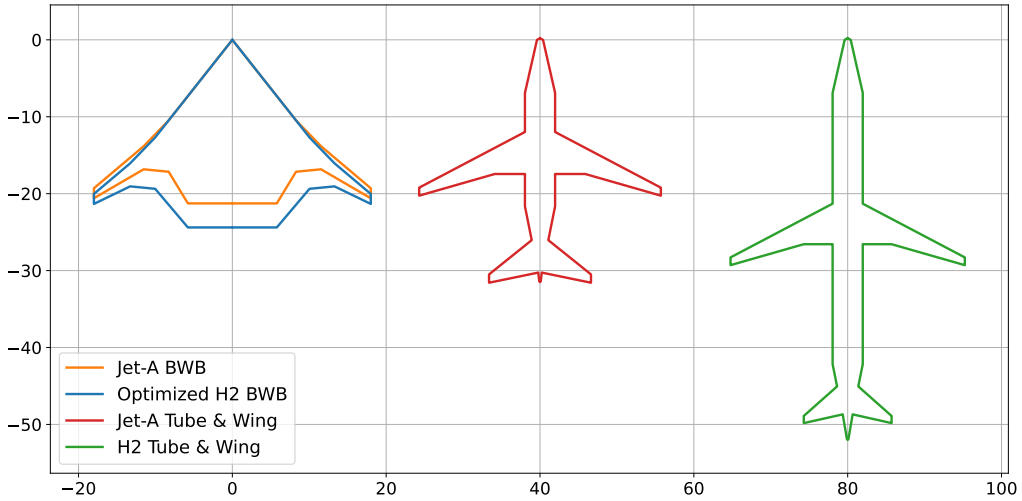

Figure VI.23: Comparison of 2D planform of jet-fuel and hydrogen **BWB** with jet fuel and hydrogen powered **T&W**

In contrast, the hydrogen **T&W** aircraft features a much longer fuselage, measuring around 50 meters in total, with 12 meters dedicated to housing two 6.1-meter-long hydrogen tanks. This configuration aligns with findings from earlier hydrogen aircraft design studies conducted using FAST-OAD. [**170**]. This elongated fuselage allows for a reduction in empennage size. Additionally, due to its lighter **MTOW** thanks to the lighter fuel mass and the absence of fuel storage in the wings, the wings themselves are downsized.

When compared to the hydrogen **BWB** however, the hydrogen **T&W** aircraft is more than twice as long,posing operational challenges at airports and complicating fuselage design due to increased bending moments and structural deformations.
The compact design of the blended wing body, combined with the absence of an empennage, results in a reduced drag coefficient, as shown in Figure VI.24. Due to their wider lifting surface, **BWB** aircraft can operate at lower lift coefficients (0.3–0.35) compared to 0.7–0.8 for **T&W** configurations, and they exhibit an overall superior lift-to-drag ratio.

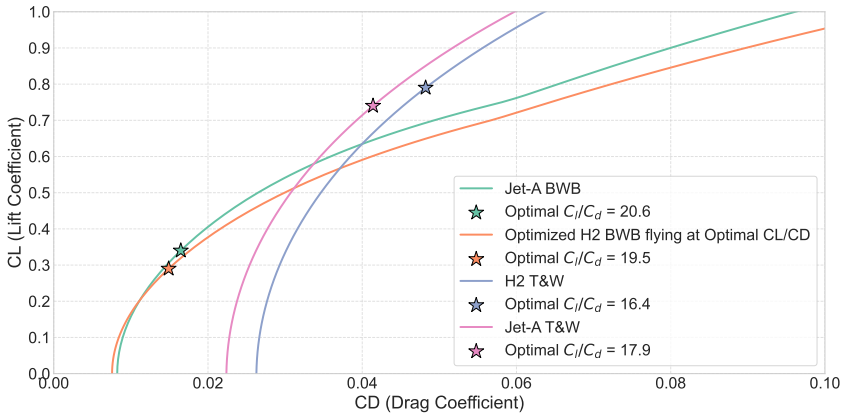

Figure VI.24: Comparison of aerodynamic polar curves of **BWB** and **T&W** design

The hydrogen **T&W** configuration, in particular, suffers from an increased wetted area due to its elongated fuselage, achieving a maximum $\frac{C_l}{C_d}$ of 16.4—significantly lower than the 19.5 attained by the hydrogen **BWB** configuration. Consequently, the mission profile of the **T&W** aircraft differs significantly, as illustrated in Figure VI.25: its cruise must be conducted at lower altitudes (12,000–12,500 meters or 39,000–41,000 feet) to maintain flight at the maximum lift-to-drag ratio.
Figure VI.26 provides a detailed comparison of key performance metrics for the hydrogen **T&W** and **BWB** aircraft, alongside their jet-fuel-powered counterparts. Regarding aircraft masses, the trends observed align with the earlier comparison of hydrogen and Jet-A **BWB** designs: both hydrogen configurations exhibit a substantial reduction in fuel mass, thanks to hydrogen's high specific energy. However, while this reduction enables a lower **MTOW** compared to the reference designs, the improvement is limited—9.3% for the **T&W** and only 0.5% for the **BWB**.
Conversely, the **OWE** increases—by 5.7% for the **T&W** and 20% for the **BWB**. The hydrogen **BWB** is more adversely affected by the need to upsize to accommodate hydrogen tanks. This is primarily due to the structural complexity of pressurizing a non-circular fuselage, which necessitates significant stiffening, thereby increasing structural mass. Additionally, both **BWB** configurations require more powerful—and consequently larger and heavier—engines to reach their cruise altitude, which introduces an additional weight penalty. In contrast, the hydrogen **T&W** benefits from its lower cruise altitude and **MTOW** by requiring a smaller, less powerful and lighter engine.
While the hydrogen **BWB** exhibits a higher **MTOW** (+9.8%) and **OWE** (+13.6%)—as shown in Figure VI.27— than a hydrogen **T&W**, its aerodynamic performance surpasses both **T&W** designs. It achieves a maximum lift-to-drag ratio (at which the aircraft

Table VI.6: Key Characteristics and Performance Metrics of Hydrogen- and Jet-Fuel-Powered **BWB** and **T&W** Aircraft

Category	**Variable**	**H2 T&W**	**Jet-A T&W**	**H2 BWB**	**Jet-A BWB**
Aerodynamic	Optimal C_L	0.79	0.74	0.29	0.34
	Optimal C_D	0.048	0.041	0.015	0.016
	Max L/D	16.40	17.87	19.46	20.64
	MAC [m]	3.65	3.80	16.57	14.03
Geometry	Total length [m]	50	31	24.4	21.3
	Wing area [m^2]	92	100	392	314
	Wing aspect ratio	9.90	9.90	3.30	4.12
	Root Sweep angle (p0) [deg]	27.8	27.8	51.7	51.7
	Vertical Tail area [m^2]	23.1	29.4		
	Vertical Tail span [m]	6.5	7.3		
	Horizontal Tail area [m^2]	26.1	35.1		
	Horizontal Tail span [m]	11.4	13.3		
	Δy_{p1-p2} [m]			4.25	2.50
	Δy_{p2-p2_1} [m]			3.25	3.25
	Cabin height [m]	3.8		2.1	2.1
	Cabin length [m]	20.9	25.4	15.7	15.7
	Cabin width [m]	3.7			
	Nacelle diameter [m]	2.2	2.3	2.0	2.0
	Nacelle length [m]	3.1	3.1	5.2	5.2
Weight	MTOW [kg]	61174	67483	67158	70500
	OWE [kg]	42327	40054	48069	43378
	ZFW [kg]	56009	53736	61751	57060
	Payload [kg]	13682	13682	13682	13682
	Central Body mass [kg]			20480	16869
	Fuselage mass [kg]	9280	7695		
	(External) Wing mass [kg]	6886	7183	1433	1852
	Engine mass [kg]	6682	7366	8202	8215
	Landing gear mass [kg]	2040	2248	3622	3607
	Block Fuel mass [kg]	5517	14029	5407	13439
	Fuel main mission [kg]	4288	11449	4051	10698
	Fuel diversion mission [kg]	402	1031	465	1135
	Fuel holding [kg]	271	685	291	711
	Fuel Margin [kg]			338	
	Furniture and system mass [kg]	12462	11915	12927	12834
Hydrogen Tank	Global adjusted gravimetrix index	0.76		0.82	
	Global gravimetrix index	0.76		0.83	
	Empty mass H2 tanks [kg]	1699		1106	
Stability	Minimum Static Margin (%)	5.0	5.0	0.04	
Propulsion	Thrust at sea level [N]	125982	138975	164648	162472
	Thurst to weight ratio	0.42	0.42	0.50	0.47
Performance	Total energy consumed [GJ]	662	606	649	580

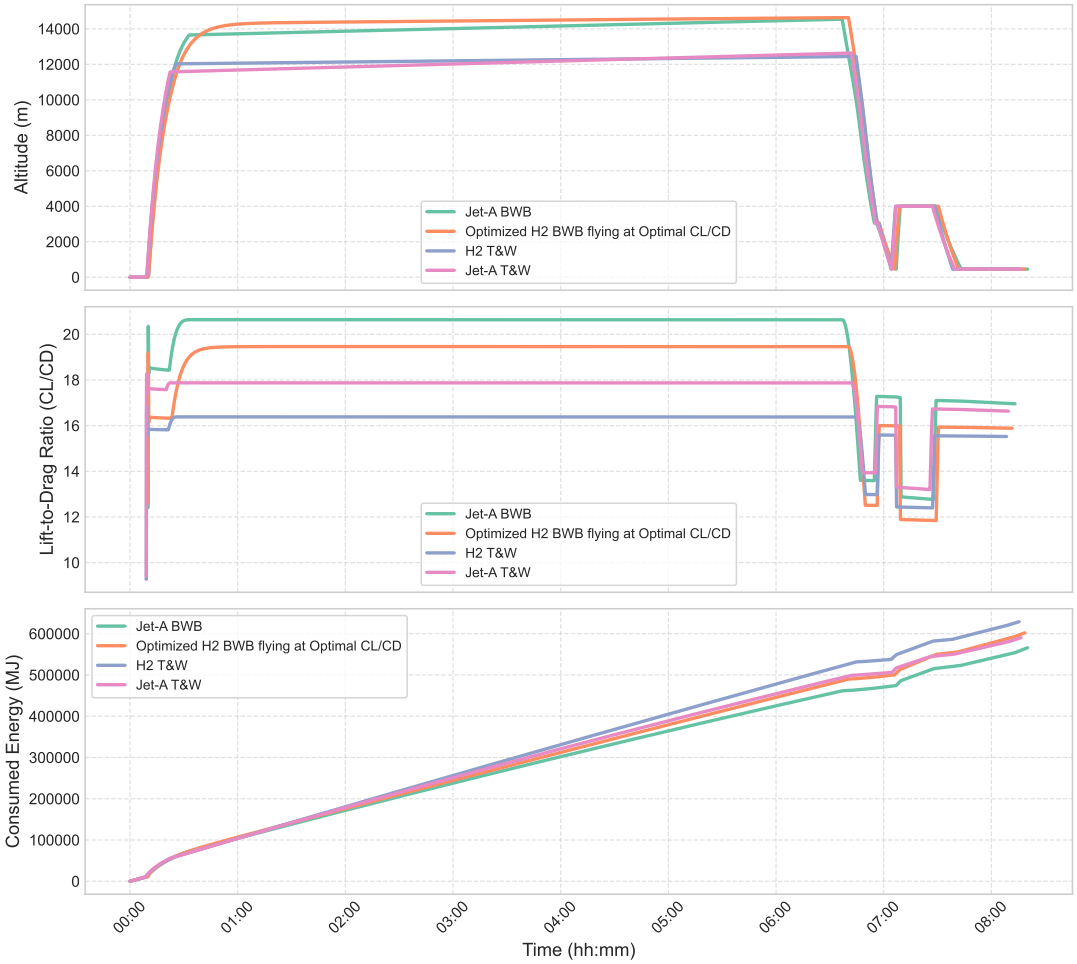

Figure VI.25: Comparative Analysis: Mission Profile, Lift-to-Drag Ratio, and Energy Consumption of Conventional **T&W** vs. **BWB** Aircraft

operates during cruise) that is nearly 19% higher. Consequently, it is approximately 2% more energy-efficient than the hydrogen **T&W** configuration over the entire design mission. If only the main route is considered—as it is the most relevant for assessing the potential of an aircraft that will primarily operate this mission—the reduction in energy consumption reaches 5.5%. From this perspective, the hydrogen **BWB**'s energy requirement is even slightly lower than that of a traditional Jet-A-powered **T&W**, with a 1.6% reduction in energy consumption, as illustrated in Figure VI.26.

The lower performance of the **BWB**—particularly the hydrogen-powered variant—during the reserve mission is clearly illustrated in Figure VI.28, which presents the breakdown of fuel consumption for each mission phase. As expected, both **BWB** designs allocate a greater proportion of their block fuel to the initial climb phase, owing to their higher cruise altitude. But more importantly, they dedicate a larger fraction of their fuel capacity to the diversion mission and holding phase.

The primary reason for this discrepancy lies in the altitude of these flight segments: all aircraft operate at the same altitude during these phases, as dictated by operational and safety regulations rather than efficiency considerations. Consequently, the **BWB** aircraft must operate at an altitude that imposes a lift-to-drag ratio farther from their

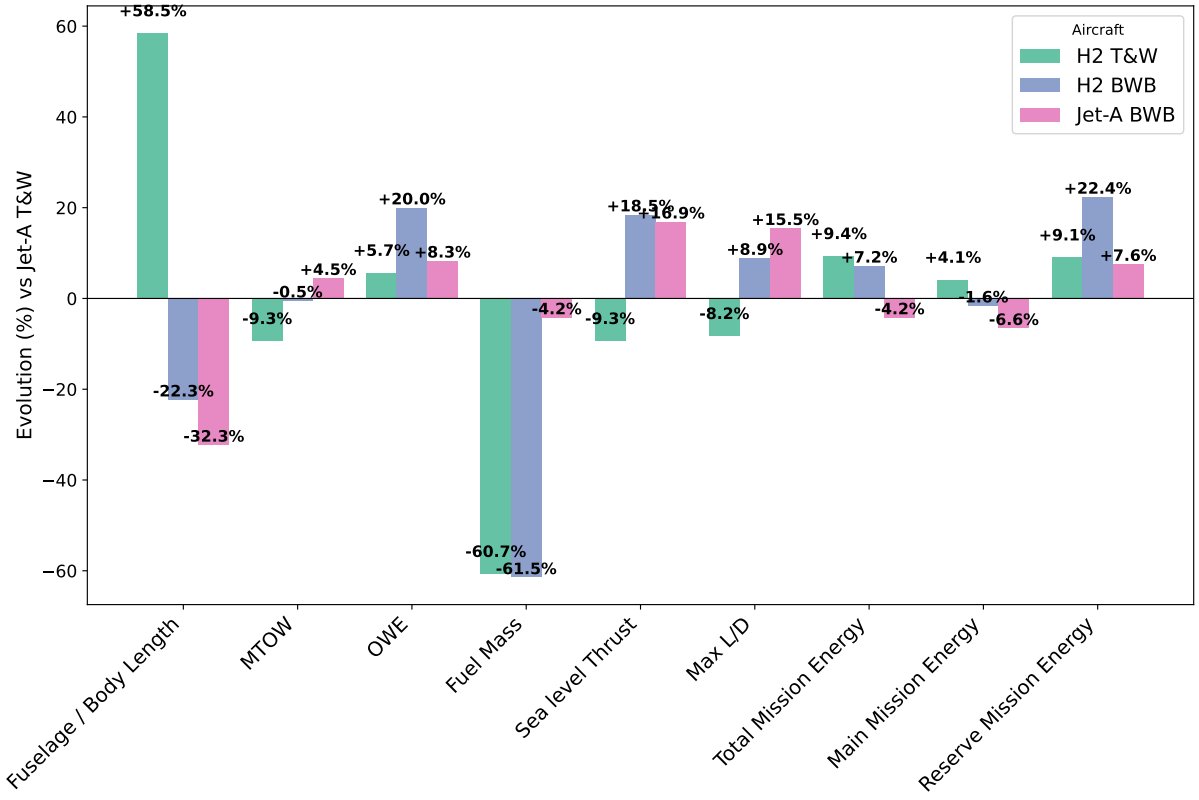

Figure VI.26: Relative Performance and Characteristics of Jet-Fuel **BWB** and Hydrogen-Powered **T&W**/**BWB** Configurations Compared to a Conventional Jet-Fuel **T&W**

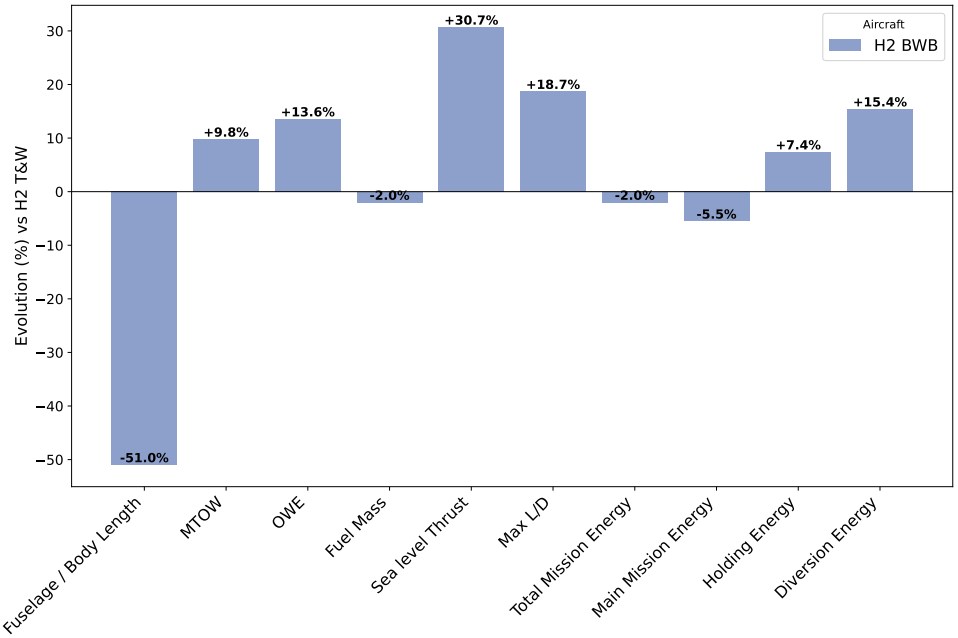

Figure VI.27: Evaluation of the Performance of Hydrogen-Powered **BWB** Compared to Hydrogen-Powered **T&W** Configurations

optimum compared to the **T&W** aircraft. For example, the central graph in Figure VI.25 shows that during the diversion segment, the hydrogen **BWB** operates at $\frac{C_l}{C_d}$ = 12, while the jet-fuel **BWB** operates at 13. Notably, the hydrogen **BWB** reaches the lowest lift-to-drag ratio among all four aircraft. At this stage of the mission, the hydrogen **BWB** is the heaviest: the hydrogen **T&W** is structurally lighter, and the jet-fuel-powered aircraft have already burnt a significant portion of their fuel mass. This higher mass consequently requires greater lift, which in turn increases drag.

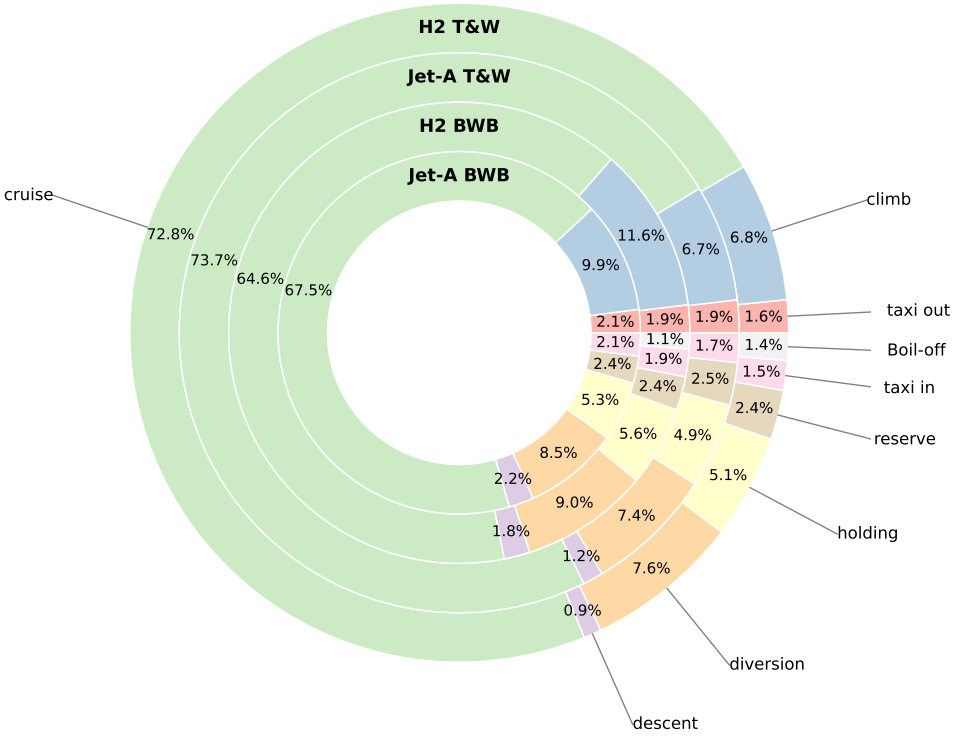

Figure VI.28: Fuel Consumption Breakdown by Mission Segment for Jet-Fuel and Hydrogen **T&W** and **BWB**

In conclusion, the comparison of the optimized hydrogen **BWB** aircraft—sized in this study—with its hydrogen **T&W** equivalent demonstrates superior energy efficiency and a more compact design. Notably, the hydrogen **BWB** also exhibits slightly higher energy efficiency than conventional jet-fuel-powered aircraft currently in operation.
The advantages of the hydrogen **BWB** over both conventional jet-fuel and hydrogen **T&W** configurations could likely be further enhanced through a more comprehensive optimization of the design—including parameters such as airfoil shape, planform, and mission profile—or by relaxing constraints, such as the maximum wingspan. Assuming the use of a robust and efficient optimization algorithm, the implemented **BWB** sizing methodology could readily facilitate such a study. Moreover, it is worth noting that several weight estimates in the BWB configurations are intentionally conservative. For instance, the furniture and equipment weight allocation is approximately 1 ton higher,

and the landing gear is also about 1 ton heavier than for their **T&W** counterparts.
Even without considering more advanced designs, the transition to a **BWB** architecture has demonstrated its potential to surpass hydrogen **T&W** designs and mitigate the energy efficiency disadvantages associated with using hydrogen as an aviation fuel for **SMR** missions. This further validates the necessity and value of the developed sizing and optimization methodology for such aircraft.

VI.5 Conclusion

This chapter demonstrated the capabilities and potential of the hydrogen-powered **BWB** design methodology through the preliminary design of an aircraft optimized for short- to medium-range missions. To this goal, the aircraft design case study is first defined, meaning the **SMR** mission is specified and some design parameters are set and justified. The next step was the construction of the design space for the hydrogen-powered **BWB**, which is notably large (37 design variables) and complex due to the presence of mixed and hierarchical variables. This space is explored through a large-scale Design of Experiments (**DoE**), enabled by the parallelization of the **MDA** loop on high-performance computing servers.

The analysis of the **DoE** provided critical insights into the influence of design constraints, as well as the feasibility and optimal regions within the design space, along with the characteristics of aircraft configurations in these regions. Among the constraints, the minimum static margin requirement emerged as particularly restrictive. Within the defined design space and fixed parameters, two constraints—those governing the front diameter of the lateral tanks and the spacing between the rear tank ends and control surfaces—were deemed redundant and subsequently excluded from the optimization process, as they remained inactive under the given configuration. To enhance feasibility, the analysis revealed that reducing the number of tanks and limiting the number of rows improved design viability. However, it was also determined that satisfying the static margin constraint could negatively impact the objective of maximizing energy efficiency.
The knowledge gained from the **DoE** exploration was then leveraged to simplify the optimization problem. By focusing on feasibility-driven architectures, the number of optimization variables is reduced to 17, limiting the configuration to a single row of rear tanks and two lateral rows, with a maximum of two tanks per lateral row. This simplification enables a complete design loop to be executed, solving the global optimization of the hydrogen-powered **BWB** with reasonable computational efficiency. The optimization was performed using the Bayesian optimizer **SEGOMOE**. The final optimized design is a **BWB** equipped with six hydrogen tanks: two twin rear tanks and four additional tanks distributed in two rows on each side.

The optimized design was compared to a conventional kerosene-powered **BWB**, which revealed that the transition to hydrogen requires a larger central body to accommodate cryogenic tanks, although optimization efforts have minimized this increase. This constraint is primarily driven by stability requirements, which necessitate placing most tanks

forward to balance the aircraft, thereby preventing the use of available rear volume. This results in degraded aerodynamic performance and a substantial increase in structural mass, far exceeding the impact of the tanks' weight alone. Consequently, the hydrogen-powered version exhibits approximately 12% higher energy consumption compared to its kerosene counterpart.

A more relevant comparative analysis was finally conducted between the hydrogen-powered **BWB** and conventional **T&W** configurations, as they represent its primary competitors. Although the hydrogen-powered **BWB** presents a higher empty weight and maximum takeoff mass than a hydrogen-powered **T&W** aircraft, its superior aerodynamic efficiency grants it a 3% energy consumption advantage. When focusing solely on the primary mission (excluding the reserve mission, which is rarely performed and during which the **BWB**—particularly the hydrogen-powered variant—operates less efficiently due to deviation from its aerodynamic optimum and higher mass), the energy savings reach nearly 6%. In this context, the hydrogen-powered **BWB** demonstrates slightly lower energy consumption than a kerosene-powered **T&W** aircraft. It must be noted, however, that while both aircraft rely on identical hydrogen tank models for boil-off and mass estimation, the structural mass uncertainty of the BWB configuration remains higher. Given the narrow performance margin previously noted, further studies are necessary to strengthen the reliability of these results. When compared to previously conducted studies in the litterature, the results remain however consistent. Firstly, Di Summa's [**114**] findings about the potential of 1 to 3% improvement in energy efficiency by playing with the tank arrangements were also confirmed and even reinforced as the optimization of the hydrogen BWB showed a 20% improvement in performance (partly due to the fact that Di Summa limited his comparison to 3 configurations). The superior empty mass of the hydrogen **BWB**, although compensated by a better aerodynamic resulting in similar or slightly better overhaul energy performance was indeed also highlighted by Heinze, Seeckt et al. [**109**, **110**].

Adler and Martins [**115**], who assumed conformal hydrogen tanks integrated within the wing of the **BWB**, also observed that both **BWB** and **T&W** hydrogen aircraft exhibit a modest increase in energy consumption relative to their kerosene counterparts. They noted, however, that the relatively small advantage of the **BWB**—with a 3.1% increase compared to 5% for the **T&W**—does not constitute a decisive benefit for transitioning to hydrogen. A similar conclusion can be drawn from the present study, where the hydrogen **BWB** shows a 12% increase in energy consumption relative to its kerosene equivalent, compared to a 9.5% increase for the **T&W**. The direct comparison between both configurations made in this thesis, however, reveals that the energy consumption of a hydrogen **BWB** can be significantly lower than a hydrogen **T&W** as the Blended-Wing-Body configuration is aerodynamically superior. Nevertheless, the direct comparison conducted in this thesis indicates that a hydrogen **BWB** can achieve significantly lower energy consumption than a hydrogen **T&W**, owing to the superior aerodynamic efficiency of the Blended-Wing-Body configuration. From a broader perspective, this reduction in energy consumption is critical for both operational economics and the environmental impact of aviation, as it implies lower emissions and facilitates the transition to hydrogen by reducing overall fuel requirements.

It should also be noted that these results are derived from a partial optimization and do not encompass the full set of relevant design variables for a hydrogen-powered **BWB**. As such, they suggest considerable potential for further improvement. A more comprehensive optimization, incorporating an expanded design space and with a optimized mission profile, could enable this architecture to substantially surpass the energy performance of current aircraft, thereby contributing to the reduction of the aviation sector's environmental impact. Regardless, these findings demonstrate the robustness, efficiency, and relevance of the sizing and optimization methodology developed for hydrogen-powered **BWB**s. Validated through this study, the methodology provides a solid foundation for conducting further advanced analyses in this field.

Conclusion and perspectives

The Earth's ecosystem is currently experiencing multiple crises driven by human activity, and their consequences pose a serious threat to the long-term sustainability of modern society. The aviation sector contributes significantly to one of these crises—global warming—primarily through the emission of greenhouse gases during flight operations. As could be reasonably expected, and because inaction may ultimately lead to imposed restrictions on the sector, the aviation industry faces not only a strategic imperative but also a moral obligation to eliminate its environmental footprint. While **SAF** may offer a partial short-term solution, most of these fuels do not fully eliminate carbon emissions, have limited impact on non-CO_2 effects such as other pollutants or contrails, and are unlikely to be available in sufficient quantities to supply the global fleet, particularly if the sector continues to grow as projected.
Transitioning to hydrogen-powered aircraft represents, by contrast, a more environmentally favourable solution. Hydrogen combustion emits no carbon dioxide, and current research indicates the potential for substantial reductions in NO_x emissions, as well as a possible mitigation of contrail radiative forcing—an effect that could in any case be further limited through trajectory-management strategies. Hydrogen can also be produced from water using decarbonised electricity, with a higher overall efficiency than that of e-fuel production. While economic and infrastructure challenges lie beyond the scope of this thesis, previous studies have examined hydrogen-powered aircraft and concluded that they are technically feasible. However, the integration of liquid hydrogen tanks, which are essential for achieving acceptable storage density, substantially impacts aircraft performance Studies also suggest that a **BWB** architecture offers both improved aerodynamic efficiency and substantially greater internal volume, making it a promising candidate for accommodating liquid-hydrogen tanks. Conversely, the urgency of hydrogen adoption might finally drive the industry to embrace **BWB** designs, which, despite their long-recognized potential, have been deemed too risky for widespread implementation.

While the hydrogen-powered Blended Wing Body (**BWB**) concept has appeared on sev-

eral occasions in the literature, relatively few studies—particularly before the start of this thesis—attempted to develop a dedicated design methodology to rigorously evaluate its potential. Because this configuration differs fundamentally from conventional kerosene-powered **T&W** aircraft, traditional **Overall Aircraft Design (OAD)** methods and tools are unable to size such an aircraft. Existing approaches addressing hydrogen aircraft or **BWB** architectures typically treat these aspects in isolation and therefore fail to integrate both simultaneously.
Moreover, the few attempts to design hydrogen **BWB** aircraft show significant discrepancies across studies in terms of efficiency, configuration, and overall performance. These inconsistencies arise from heterogeneous assumptions and arbitrary design choices—such as gravimetric indices or tank placement—as well as the use of low-fidelity disciplinary models in parts of the design process. In addition, most existing studies rely on single-point designs tailored to very specific missions, making their methodologies overly specialized and lacking the generality required for broader applicability.

Main achievements

The primary objective of this thesis was therefore to develop a novel overall aircraft design methodology capable of sizing a hydrogen-powered **BWB** aircraft, assessing its performance, and evaluating its potential to reduce aviation's environmental impact. Significant effort was devoted to increasing disciplinary model fidelity whenever feasible and deemed necessary for the robustness of the outcomes, as well as to building a design framework as flexible as possible. In particular, rather than imposing arbitrary design assumptions upfront, critical choices were embedded when possible within the design space, enabling the optimization process to objectively identify the most effective configurations.The newly developed method was integrated into FAST-OAD, the aircraft design tool jointly developed by ONERA and ISAE-SUPAERO, thereby enhancing and contributing to the software's evolving capabilities.

To highlight the significant achievements of this research in more detail, the following notable advancements were made:

- A novel thermodynamic model for hydrogen tanks—capable of explicitly accounting for boil-off losses in aircraft design—has been integrated into the **FAST-OAD** tool. The model employs an electrical resistance analogy to estimate heat flux into the tank's liquid and gaseous phases, with a key innovation: segmenting the tank into multiple sections, each analyzed individually to capture localized thermal variations and enhance accuracy. Additionally, a three-control-volume self-pressurization model, inspired by space industry practices, was developed. This model independently simulates the bulk liquid, ullage, and their interface, representing a significant departure from the traditional homogeneous models previously used in aircraft design.

- Complementary to this thermodynamic model, a new methodology was developed

for sizing cylindrical cryogenic hydrogen tanks with hemispherical or semi-elliptical bulkheads in order to estimate their structural mass. The methodology ensures full compliance with CS-25 regulations for pressurized cylinders and sizes both the tank walls and the associated stiffening structure, explicitly accounting for buckling constraints. Integrated within **FAST-OAD** and coupled with the thermodynamic tank model described previously, this work provides a comprehensive capability for evaluating the performance of hydrogen-powered **T&W** aircraft. In particular, it enables the estimation of tank gravimetric efficiency across a wide range of design hypotheses and architectural choices, such as integral versus non-integral tanks, different insulation technologies, or alternative structural materials. It also allows for meaningful trade-off analyses between insulation strategy, maximum design pressure, structural weight, and overall efficiency.

- The **FAST-OAD** framework was extended to support the design of hydrogen-powered flying-wing aircraft, enabling the exploration and optimization of a large design space for hydrogen tank configurations. The framework was first adapted to flying-wing geometries by replacing its original geometric and structural models with those developed in ONERA's CICAV project, tailored specifically for this configuration, along with targeted modifications to account for hydrogen-specific considerations such as engine and landing-gear placement. Furthermore, a new aerodynamic model based on VSP AERO was integrated to evaluate static margin and longitudinal stability. A dedicated parameterization was then introduced to define the number, location, and geometry of cylindrical hydrogen tanks, allowing for flexible arrangements—including longitudinal side tanks along the cabin and transverse rear tanks positioned aft of the pressurized volume. Each tank family is organized into configurable rows, enabling variations in tank count, dimensions, and placement. The traditional Multidisciplinary Design Analysis process was subsequently expanded into a Multidisciplinary Design Analysis and Optimization (**MDAO**) approach. This enhanced framework incorporates a set of feasibility constraints—such as minimum required hydrogen volume, positive static margin, and geometric integrability—to ensure viable aircraft designs. As a result, the hydrogen-powered flying-wing configuration becomes a constrained optimization problem featuring a combination of mixed and hierarchical design variables.

Overview of key results

With these key advancements in place, a series of studies were conducted on hydrogen-powered aircraft—encompassing both **T&W** and **BWB** configurations—leading to the following conclusions:

- The **DoE** and parametric analyses conducted with the hydrogen-enhanced **FAST-OAD** tool for **T&W** aircraft confirmed both the robustness of the updated framework and several key design trends. In particular, they revealed that optimizing in-flight performance systematically favors minimizing structural mass—primarily

through low pressure differentials—rather than increasing insulation thickness to reduce boil-off. Moreover, zero-venting missions are achievable with only moderate foam insulation thicknesses (150–200 mm) provided that the tank operates under low pressure differentials.

- Dormancy periods during which zero venting may be required could significantly affect overall fuel efficiency, as meeting such constraints demands substantially thicker insulation. With foam-based insulation technologies, maintaining strict zero-venting conditions becomes impractical beyond a few hours. A pragmatic approach would therefore be to limit zero-venting requirements to short durations—on the order of one hour—while allowing the aircraft to vent into the airport's hydrogen distribution system for longer ground periods.

- For **T&W** configurations, integral tanks were found to offer slightly higher efficiency, whereas increasing tank width—although beneficial for gravimetric performance—necessitated a larger fuselage cross-section, ultimately degrading the aircraft's overall fuel efficiency.

- For a typical **SMR** mission (2,500 NM design range and 239 passengers), the optimal hydrogen **T&W** aircraft configuration identified in this work exhibits roughly a 10% increase in total mission energy consumption (falling to about 3.5% when considering only the main mission, excluding reserves). This rise is primarily driven by the higher empty weight and the aerodynamic penalties associated with the elongated fuselage required to accommodate the hydrogen tanks—effects that are not fully offset by the reduction in fuel mass.

- The exploration of the extensive and complex design space for hydrogen-powered **BWB**—made possible by high-performance computing at ONERA—highlighted the critical influence of stability constraints, identified redundant geometric limitations, and pinpointed the most feasible architectures region and the main characteristics. These insights allowed for a significant simplification of the optimization problem, enabling an efficient, full **MDAO** loop to be solved using the **SEGOMOE** optimizer.

- The optimized design incorporates six hydrogen tanks within the blended-wing body: two twin rear tanks and two pairs of side tanks. Compared to a kerosene-powered **BWB**, the hydrogen variant demands a larger central body to accommodate cryogenic tanks while ensuring stability. Placing too many tanks in the unused rear volume compromised stability, necessitating side tanks that widened the airframe. This results in degraded aerodynamics, higher structural weight, and approximately 12% greater energy consumption.

- A more meaningful comparison with hydrogen-powered **T&W** aircraft shows that, despite a higher empty and takeoff mass, the hydrogen **BWB** benefits from superior aerodynamic efficiency, reducing energy consumption by about 3% over the full mission and nearly 6% on the primary mission alone—performances that even slightly outperform a kerosene **T&W**.

In conclusion, the methodology developed for the overall aircraft design of hydrogen-powered **BWB**s has demonstrated strong robustness and flexibility, both through the thousands of feasible configurations examined during the **DoE** exploration and through its capacity to identify viable and efficient designs in the subsequent optimization phase with reasonable computational time despite the complexity of the problem addressed. The hydrogen **BWB** concept itself exhibits notable potential in terms of energy efficiency when compared with hydrogen or kerosene **T&W** configurations, suggesting that it could offset—or even eliminate—the energy penalty typically associated with transitioning to hydrogen for **SMR** missions. This potential is further reinforced by the improvement opportunities identified in this work: broader optimizations, expanded design spaces, and refined mission modelling could enable hydrogen-powered **BWB**s to surpass current aircraft in energy efficiency by an even greater margin.

Perspectives for future research

The key findings presented earlier underscore the relevance of developing a dedicated methodology for sizing hydrogen-powered **BWB** aircraft and evaluating their performance. While the approach developed in this thesis represents a significant advancement over existing methods, there remain numerous opportunities to further refine and expand the methodology:

- As discussed in Chapter II, the thermodynamic model used to estimate hydrogen boil-off losses could be further improved by incorporating more detailed bulk-boiling and film-boiling correlations, particularly if design with thin insulation layers are envisioned.

- Additionally, access to experimental data on cryogenic hydrogen tanks would enable validation of the thermodynamic model, helping to refine boil-off estimates and reduce uncertainty. Likewise, validating the structural model would further strengthen the reliability of the results.

- Although the thermal model can accommodate MLI insulation technologies, no corresponding structural-sizing module was implemented. This is primarily due to the complexity of modeling double-wall structures subjected to internal and external pressure loads and because the literature indicates that foam-based insulation remains more effective. Extending the structural-sizing methodology to support **MLI** (or hybrid foam–MLI solutions) would enable more accurate trade-offs between insulation technology, tank mass, and allowable dormancy times.

- Developing a dedicated module for sizing tank fixation and support systems—together with the loads transmitted through them—would make it possible to explicitly compare integral and non-integral tank integration strategies for **T&W** configurations. Although more challenging, a similar approach could be envisaged for **BWB** architectures, where cylindrical tanks might contribute to overall airframe stiffness through their attachment points, potentially enabling lighter structural designs.

- Although hydrogen tanks represent the most impactful modification when transitioning from kerosene to hydrogen-powered aircraft at the pre-conceptual design stage, other hydrogen-related subsystems should also be modeled to obtain a more accurate mass estimation. This includes the sizing of the fuel delivery system, heat exchangers, refueling and venting systems, and potentially a fuel-cell-based APU, among others. Integrating these subsystems into the design framework would provide a more comprehensive assessment of the mass and system-level implications of hydrogen propulsion. An effort to expand FAST-OAD in that direction is already under way at ISAE-SUPAERO through the work of Sarr et al. [**156**]

- For the **BWB** configuration, this study highlighted the strong influence of static-stability constraints on the achievable design space. Investigating alternative engine placements—such as under-wing positions—could help relax these constraints. However, such an analysis would greatly benefit from integrating a noise-assessment module, as noise emissions remain the primary limitation of under-wing propulsion. If other means of relaxing this constraint are found, the integration of boundary layer ingestion engines on the top of the aircraft could represent another interesting solution to improve **BWB** performance [**171**].

- The stability module developed in this study represents an initial assessment and should be expanded to incorporate lateral and dynamic stability analyses. Ideally, it would also be integrated with a control-surface sizing capability for a more comprehensive evaluation. While this enhancement is not yet implemented, it is currently under consideration within the European project EXAELIA, where both ONERA and ISAE-SUPAERO are actively involved.

- To further refine the optimization of the **BWB** configuration, a geometric parameterization of the airfoils used in each aircraft section could be introduced and incorporated into the set of optimization variables. This would enable a more accurate coupling between aerodynamic performance, structural considerations, and tank integration, potentially unlocking additional performance improvements.

- The optimization process in the final chapter for designing a hydrogen **BWB** was constrained by the computational limits of the SEGOMOE optimizer, restricting the number of design variables and constraints. Adopting a more flexible optimizer or optimization strategy—for example by exploring the potential combination of global Bayesian optimization with gradient-based optimization of some differentiable design disciplines—could broaden the design space, incorporating additional geometric parameters for the BWB and expanded tank design variables. This approach would facilitate the exploration of more optimal aircraft configurations.

- In a longer-term perspective, it would be valuable to use the developed optimization framework to identify distinct classes of optimal tank configurations, potentially tailored to specific mission types (e.g., short-haul, medium-range, or long-haul). This classification could pave the way for defining specialized tank sizing methodologies for each class, allowing these configurations to be resolved directly within the **MDA**.

By doing so, the time-consuming optimization phase could be streamlined or bypassed, enabling a greater focus on broader design exploration and accelerating the overall design process.

- To further refine the design and performance of the hydrogen BWB, a more detailed engineering phase would be essential. This phase would focus on optimizing the layout, positioning, and interconnections of all major subsystems (such as cables, pipes, and ducts). An effective approach could involve adopting a framework like the "Overall Systems Design Framework" proposed by Bielsky et al. [**172**], which links conceptual OAD results with high-fidelity subsystem architecture tools to achieve a more precise and mature aircraft design.

If future research were to focus specifically on advancing environmentally sustainable aircraft, the following research directions could be pursued:

- Expansion to Other Aircraft Segments: The same methodology applied to short-to-medium-range (SMR) hydrogen **BWB** could be extended to regional and long-range aircraft to evaluate the potential of the **BWB** concept across different classes. Additionally, a fleet-level analysis—where the global aircraft distribution shifts toward the most energy-efficient classes per kilometer—could be conducted to quantify the potential reduction in aviation's environmental footprint.

- Reevaluating **TLARs** for Sustainability: The studies in this thesis are based on current **TLARs**, but these could be reassessed to prioritize environmental impact. For example, trade-offs could be explored between cruise speed, altitude, range, and emissions. For example, reducing cruise speed to Mach 0.6 might enable thicker airfoils, which could benefit **BWB** design and potentially improve fuel efficiency, for a reasonable increase in travel time, especially on short to medium range mission.

- Integration of Innovative Technologies into the **BWB** Concept: To further enhance the fuel efficiency of hydrogen-powered **BWB** aircraft, additional technological innovations could be incorporated. These may include:

  - Distributed propulsion systems, as explored by Sguelia [**99**],
  - Partial hybridization with batteries or fuel cells,
  - Hydrogen engines actively cooled by liquid hydrogen, as proposed by Brewer [**24**],
  - A radical redesign of the **BWB** structure using modular, lattice-based, ultralight materials, as investigated by Cramer et al. in collaboration with **Massachusetts Institute of Technology (MIT)** and NASA [**173**].

  These advancements could significantly improve the performance and sustainability of the **BWB** concept.

Overall, the results obtained throughout this thesis confirm both the relevance and the significance of the proposed design and optimization methodology, in part by highlighting

the promising role that hydrogen **BWB** architectures could play in the future of aviation as the sector moves toward more environmentally responsible operations. The work conducted over these three years lays the foundation for more detailed and accurate overall aircraft design methodologies tailored to hydrogen blended wing bodies, and it emphasizes the need for a broader exploration of this concept to fully assess its potential in meeting the demanding objectives of net-zero aviation.

Annexes

A.1 Production pathways for alternative aviation fuels

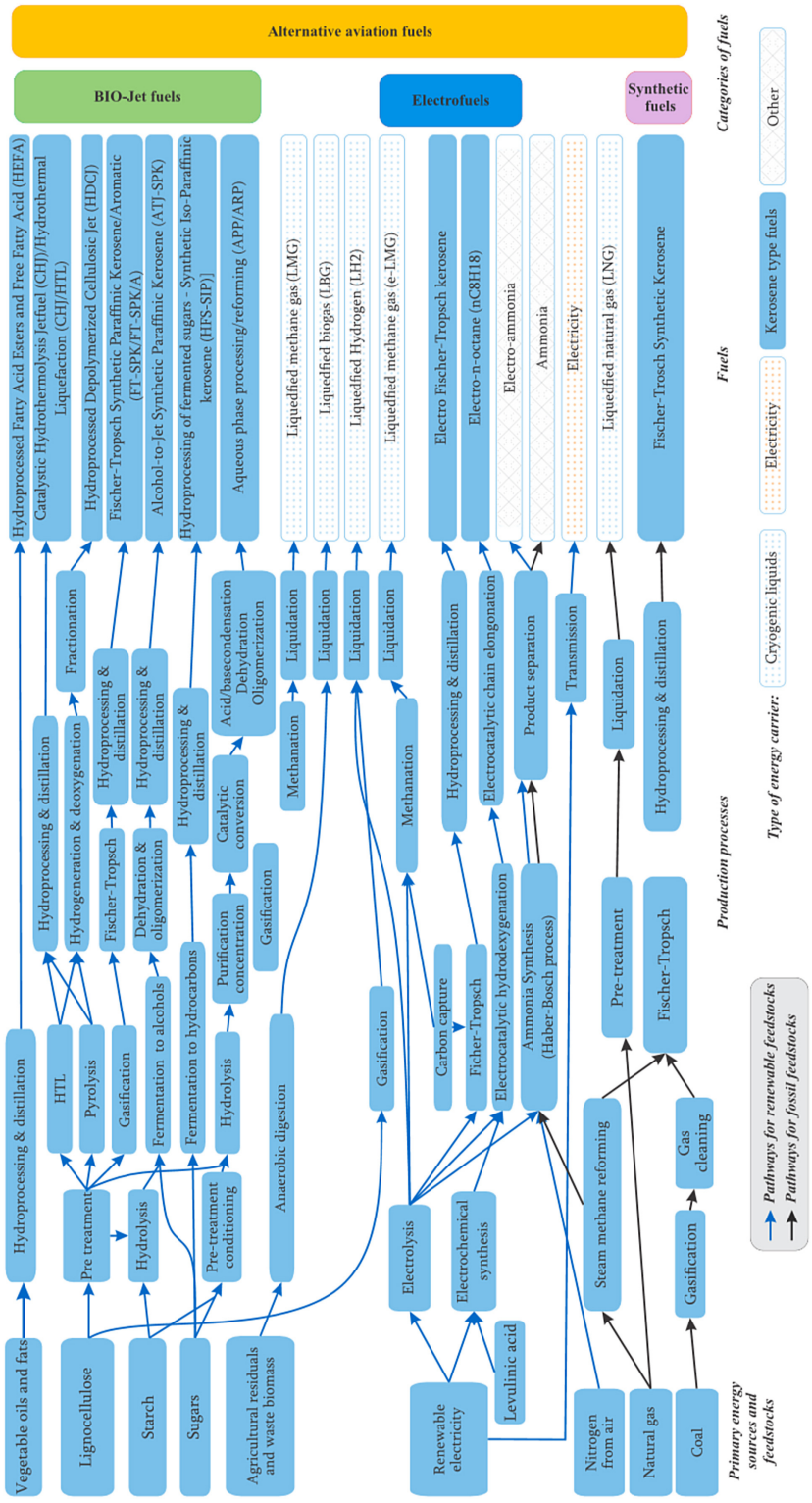

Figure A.29: Schematic Overview of Alternative Aviation Fuel Pathways: From Biomass to Electric-Based Fuels [**174**]

A.2 A Review of Materials for Cryogenic Hydrogen Storage: Properties and Challenges

The selection of materials for hydrogen tanks requires careful consideration, as cryogenic hydrogen storage presents unique challenges. Materials in direct contact with hydrogen must be impermeable to prevent leakage, a difficult requirement given hydrogen's small molecular size, which allows it to penetrate many materials. Additionally, hydrogen can diffuse into materials, leading to hydrogen embrittlement—a process that degrades mechanical properties and structural integrity over time.

Hydrogen tanks are also exposed to extreme thermal cycles, transitioning between ambient and cryogenic temperatures, which can cause thermal fatigue in the tank structure. To mitigate this, the chosen materials must exhibit high resistance to thermal fatigue, or alternative strategies must be implemented. These may include maintaining the tank at a constant cryogenic temperature or placing insulation inside the tank to shield the structural components from thermal stress. Such measures are essential to ensure the long-term durability and safety of the tank system.

For the tank structure, two primary material options are considered: metals and composites [**175**]. Among metals, stainless steel, titanium, and aluminum are common candidates. However, aluminum is often preferred due to its advantageous balance between weight and cost compared to steel and titanium. Aluminum is already widely used in launchers, as it is impermeable to hydrogen and not susceptible to hydrogen embrittlement. Consequently, most of the studies referenced earlier have adopted aluminum for tank construction.

Composite materials offer the significant benefit of reduced weight, but their use is complicated by poor hydrogen permeation resistance. As noted by Mital et al. [**176**], "for advanced fiber-reinforced composites, even the state-of-the-art resin systems may be too permeable to contain liquid and gaseous hydrogen when subjected to high strains resulting from mechanical and thermal loads that are characteristic of efficient tanks." One potential solution to this issue is the use of a metallic liner within the composite tank [**177**]. Additionally, differences in thermal expansion coefficients between composite components can lead to structural failure, as seen in the NASA X-33 reusable spacecraft concept [**178**]. Despite these challenges, the weight savings offered by composites—approximately 25% lighter than metal [**39**]—justifies their higher cost and ongoing research efforts to address these issues. While composites have long been a focus in the space industry, their relevance for aircraft applications is now gaining attention [**179**].
Beyond the structural material, the insulation for cryogenic tanks must also be carefully selected. Mital et al. [**176**] conducted a comprehensive review of insulation strategies and materials for long-term cryogenic applications. Effective insulation must be lightweight, possess high thermal resistance, and exhibit a low radiation heat transfer coefficient.

It should also prevent condensation or ice formation on the tank surface, necessitating waterproof and airtight properties if placed externally. The ratio between thermal conductivity and diffusivity is critical, as diffusivity affects the rate of heat ingress, while conductivity determines the total heat entering the tank.

Mital et al. provide a comprehensive summary of the benefits and drawbacks of various tank insulation methods in Table A.32. While authors such as Brewer and Verstraete typically focus on Multi-Layer Insulation (MLI) or foam, aerogel is recognized as a promising future option—provided its fragility can be addressed [**39**].

Brewer conducted an extensive experimental comparison of different foam types before selecting the insulation for his design [**24**]. Similarly, Verstraete compared two insulation types (see Figures A.30 and A.31). His analysis revealed that, although MLI offers lower thermal conductivity, the additional weight required for a double-walled structure results in a poorer gravimetric index compared to foam-based insulation. Thus, foam-based solutions often prove more advantageous in terms of overall weight efficiency for hydrogen tank applications.

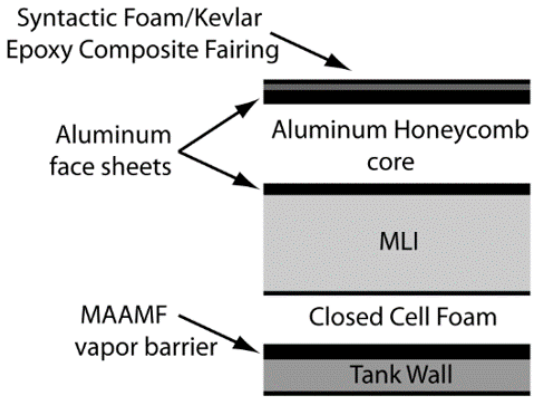

Figure A.30: Foam-based insulation [**32**], derived from Brewer [**24**]

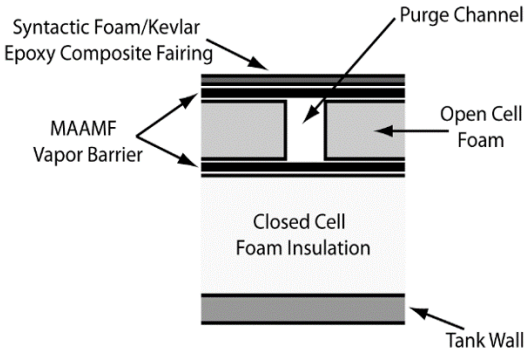

Figure A.31: Multi-layer insulation [**32**], derived from Brewer [**24**]

Location		Discriminators
		Foam
Outside	Advantages	Currently in use, well established Low cost, easy to implement Light weight and low density
	Disadvantages	Limited to short duration missions because of excessive thermal conductivity Low resistance to thermal radiation Potential damage from environmental hazards
Inside	Advantages	Low cost Structural wall not exposed to cryogenic conditions Reduced CTE mismatch issues of composite constituents, resulting in reduced microcracking
	Disadvantages	Necessitates larger structural tank wall, resulting in increased mass Difficult to seal from cryogenic fluid • Fluid infiltration leads to increased thermal conductivity • Potential loss of structural wall integrity May interfere with fluid management upon failure
		Perlite
Between walls	Advantages	Low cost, well established Some compressive load-bearing capability Resistance against thermal conductivity and radiation
	Disadvantages	Limited to short duration due to excessive thermal conductivity Excessive mass for aerospace applications
		Aerogel
Between walls	Advantages	Extremely low thermal conductivity[a]
	Disadvantages	New material, not well characterized Limited mechanical properties
		Vacuum
Between walls	Advantages	Near zero thermal conductivity Well established
	Disadvantages	Heavier tank walls required Costly to implement and maintain No resistance to radiation heat transfer Near catastrophic failure upon loss of vacuum
		MLI
Between walls	Advantages	Very low thermal conductivity and radiation heat transfer[b] Extremely low density Well established
	Disadvantages	High vacuum required Heavier tank walls required Costly to implement and maintain Near catastrophic failure upon loss of vacuum

[a]The balance between the structural and thermal properties can be altered to optimize for the application.
[b]MLI is available in graded form to improve thermal properties and to reduce the density, but at a higher cost.

Figure A.32: Advantages and disadvantages of various insulation methods (listed in order of increasing thermal insulation performance) [**176**]

A.3 Effect of Tank Dimensions on the Hydrogen BWB Feasible Design Space

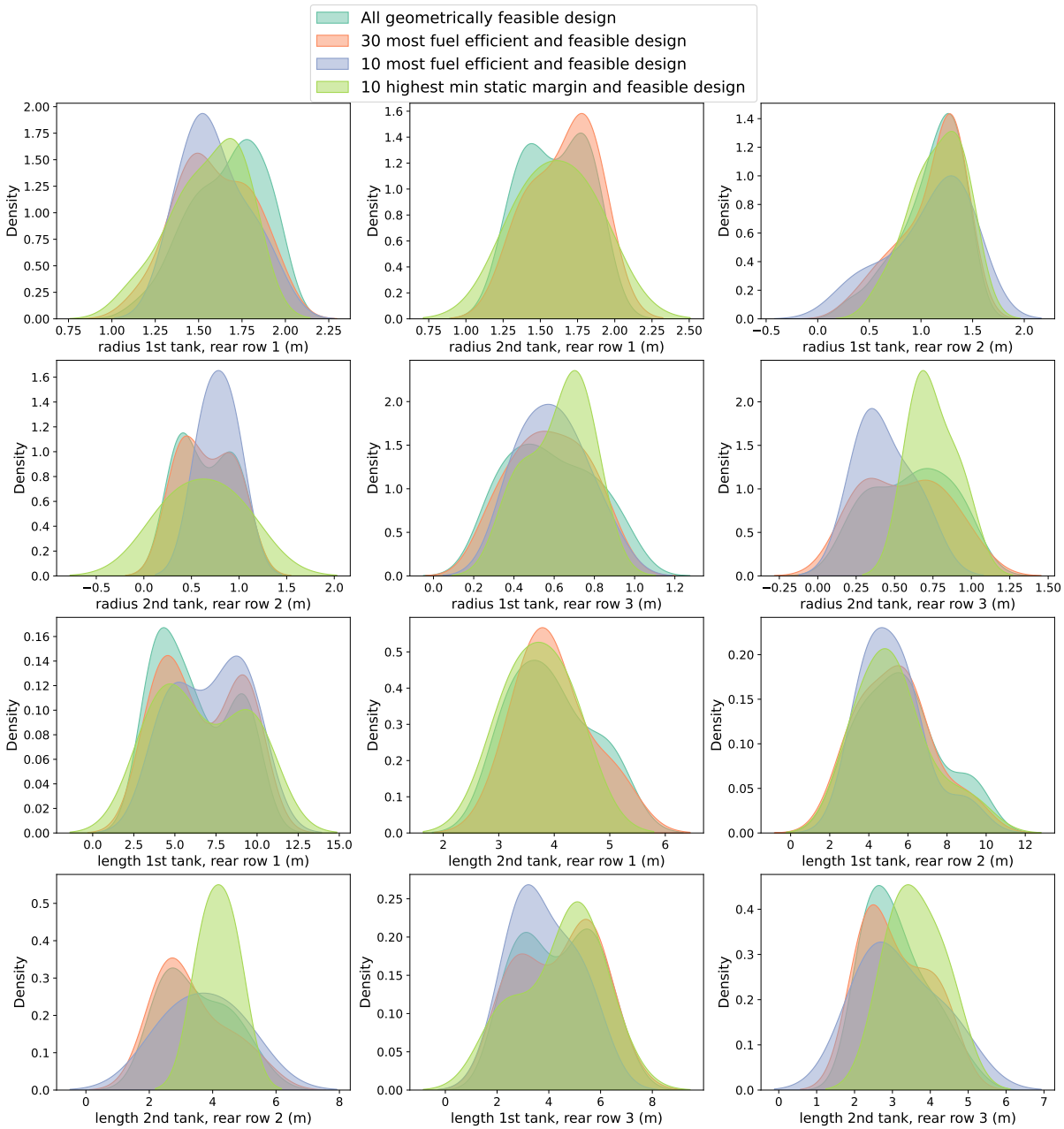

Figure A.33: Influence of Rear Tank Dimensions on Geometric Feasibility and Stability Constraints

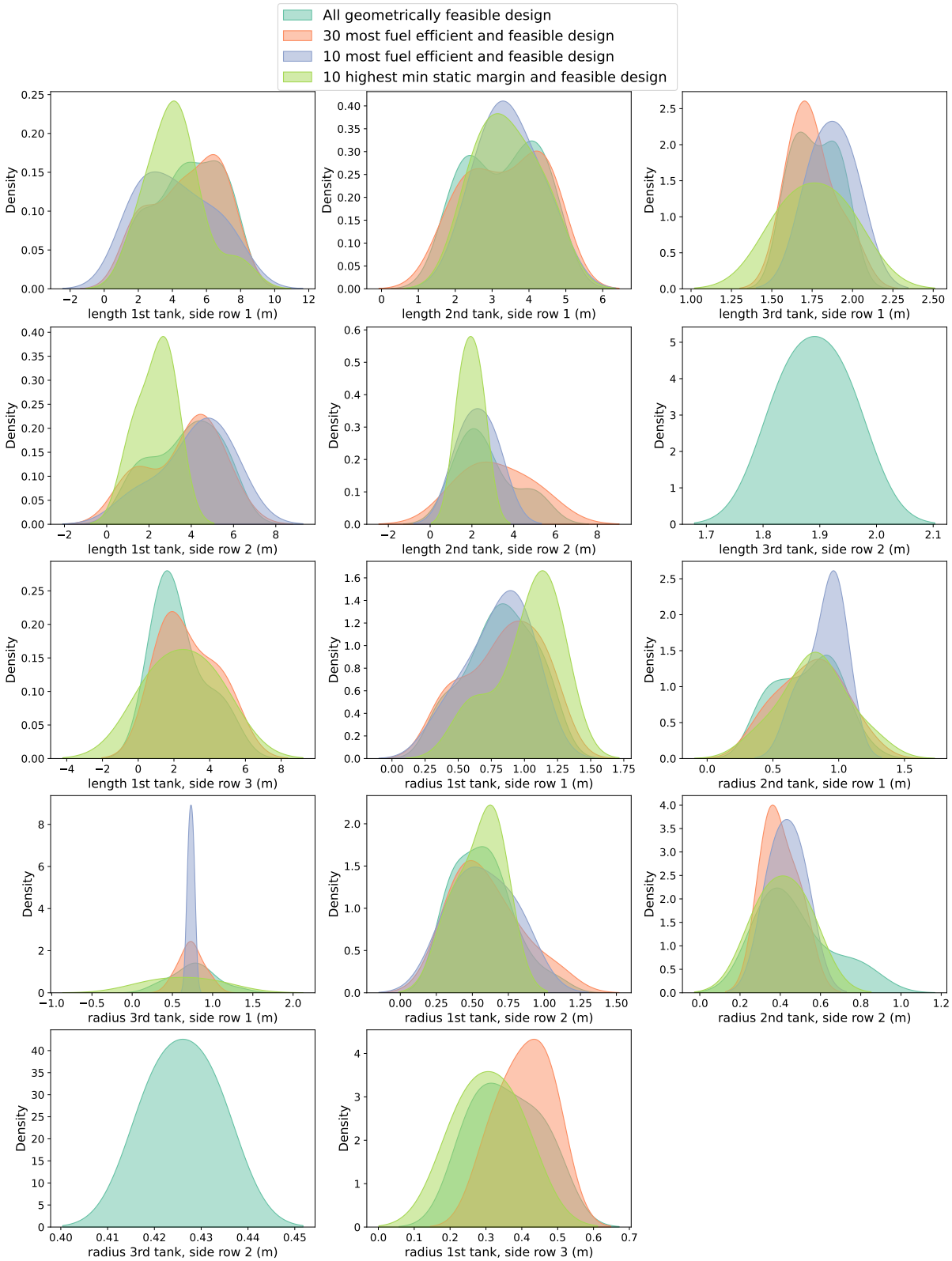

Figure A.34: Influence of Side Tank Dimensions on Geometric Feasibility and Stability Constraints

Bibliography

1 Intergovernmental Panel On Climate Change (Ipcc). *Climate Change 2021 – The Physical Science Basis: Working Group I Contribution to the Sixth Assessment Report of the Intergovernmental Panel on Climate Change*. 1st ed. Cambridge University Press, July 2023. ISBN: 978-1-009-15789-6. DOI: 10.1017/9781009157896.

2 P. M. Forster et al. "Indicators of Global Climate Change 2023: annual update of key indicators of the state of the climate system and human influence". English. In: *Earth System Science Data* 16 (6) (June 2024), pp. 2625–2658. ISSN: 1866-3508. DOI: 10.5194/essd-16-2625-2024.

3 Intergovernmental Panel On Climate Change (Ipcc). *Summary for Policymakers*. 1st ed. Climate Change 2021 – The Physical Science Basis: Working Group I Contribution to the Sixth Assessment Report of the Intergovernmental Panel on Climate Change. Cambridge University Press, July 2023. ISBN: 978-1-009-15789-6. DOI: 10.1017/9781009157896.

4 Intergovernmental Panel On Climate Change (Ipcc), ed. *Climate Change 2022 - Mitigation of Climate Change: Working Group III Contribution to the Sixth Assessment Report of the Intergovernmental Panel on Climate Change*. 1st ed. Cambridge University Press, Aug. 2023. ISBN: 978-1-009-15792-6. DOI: 10.1017/9781009157926.

5 Hannah Ritchie. "Global inequalities in CO emissions from aviation". In: *Our World in Data* (2020).

6 D. S. Lee, D. W. Fahey, A. Skowron, M. R. Allen, U. Burkhardt, Q. Chen, S. J. Doherty, S. Freeman, P. M. Forster, J. Fuglestvedt, A. Gettelman, R. R. De León, L. L. Lim, M. T. Lund, R. J. Millar, B. Owen, J. E. Penner, G. Pitari, M. J. Prather, R. Sausen, and L. J. Wilcox. "The contribution of global aviation to anthropogenic climate forcing for 2000 to 2018". en. In: *Atmospheric Environment* 244 (Jan. 2021), p. 117834. ISSN: 1352-2310. DOI: 10.1016/j.atmosenv.2020.117834.

7 *Airbus Global Market Forecast 2025 | Airbus*. en. June 2025.

8 O. Rech and H. Duterne. *The Future of Oil Supply in the European Union: State of Reserves and Production Prospects for Major Suppliers (english summary)*. English. Tech. rep. Shift Project, 2021.

9 ICAO. *REPORT ON THE FEASIBILITY OF A LONG-TERM ASPIRATIONAL GOAL*. English. Tech. rep. Mar. 2022.

10 P. Kurzawska-Pietrowicz. "Life Cycle emission of selected Sustainable Aviation Fuels – A review". en. In: *Transportation Research Procedia* 75 (2023), pp. 77–85. ISSN: 23521465. DOI: 10.1016/j.trpro.2023.12.010.

11 M. Prussi, U. Lee, M. Wang, R. Malina, H. Valin, F. Taheripour, C. Velarde, M. Staples, L. Lonza, and J. Hileman. "CORSIA: The first internationally adopted approach to calculate life-cycle GHG emissions for aviation fuels". In: *Renewable and Sustainable Energy Reviews* 150 (Aug. 2021). DOI: 10.1016/j.rser.2021.111398.

12 X. Zhao, F. Taheripour, R. Malina, M. Staples, and W. Tyner. "Estimating induced land use change emissions for sustainable aviation biofuel pathways". In: *Science of The Total Environment* 779 (Mar. 2021), p. 146238. DOI: 10.1016/j.scitotenv.2021.146238.

13 D. Evridiki and L. Corey. *Long-term demand for SAF could run into supply constraints*. en. Mar. 2022.

14 M. F. Rojas-Michaga, S. Michailos, E. Cardozo, M. Akram, K. J. Hughes, D. Ingham, and M. Pourkashanian. "Sustainable aviation fuel (SAF) production through power-to-liquid (PtL): A combined techno-economic and life cycle assessment". In: *Energy Conversion and Management* 292 (Sept. 2023), p. 117427. ISSN: 0196-8904. DOI: 10.1016/j.enconman.2023.117427.

15 P Meyer. *Is there any available source of heat lighter than gasoline*. English. Technical Note 136. NASA, 1923.

16 J. L. Sloop. *Liquid Hydrogen as a Propulsion Fuel, 1945-1959*. English. The NASA History Series NASA SP 4404. US: National Aeronautics and Space Administration, 1978.

17 A. Silverstein and E. W. Hall. *Liquid Hydrogen as a Jet Fuel for High-Altitude Aircraft*. Research Memorandum. Cleveland, Ohio US: Lewis Flight Propulsion Laboratory, NACA, Apr. 1955.

18 D. R. Mulholland, L. W. Acker, H. H. Christenson, and W. V. Gough. *Flight Investigation of a Liquid-Hydrogen Fuel Sytem*. en. Research Memorandum E57F19a. Cleveland, Ohio US: NACA, Aug. 1957.

19 D. B. Fenn, L. W. Acker, and J. S. Algranti. *Flight Operation of a Pump-Fed Liquid-Hydrogen Fuel System*. Tech. rep. NASA-TM-X-252. NTRS Author Affiliations: NASA Lewis Research Center NTRS Document ID: 19680068699 NTRS Research Center: Glenn Research Center (GRC). Apr. 1960.

20 G. D. Brewer and G. Brewer. "AVIATION USAGE OF LIQUID HYDROGEN FUEL – PROSPECTS AND PROBLEMS". In: *International Journal of Hydrogen Energy* 1 (1) (Jan. 1976). MAG ID: 2101207070, pp. 65–88. DOI: 10.1016/0360-3199(76)90011-2.

21 G. D. Brewer, G. D. Brewer, Robert E. Morris, R. E. Morris, Roy H Lange, R. H. Lange, Jason W. Moore, and J. W. Moore. "Study of the application of hydrogen fuel to long-range subsonic transport aircraft. Volume 1: Summary". In: (Jan. 1975). MAG ID: 1505868120.

22 G. D. Brewer, R. E. Morris, G. W. Davis, E. F. Versaw, G. R. Cunnington, J. C. Riple, C. F. Baerst, and G. Garmong. *Study of fuel systems for LH2-fueled subsonic transport aircraft, volume 1*. Tech. rep. LR-28384-VOL-1. NTRS Author Affiliations: Lockheed-California Co., Lockheed Missiles and Space Co., Inc., AiResearch Mfg. Co., Rocketdyne NTRS Document ID: 19780023142 NTRS Research Center: Legacy CDMS (CDMS). July 1978.

23 G. D. Brewer and G. Brewer. "The prospects for liquid hydrogen fueled aircraft". In: *International Journal of Hydrogen Energy* 7 (1) (Jan. 1982). MAG ID: 2072429941, pp. 21–41. DOI: 10.1016/0360-3199(82)90205-1.

24 G. D. Brewer. *Hydrogen Aircraft Technology*. en. 1st ed. New York: Routledge, 1991. ISBN: 978-0-203-75148-0. DOI: 10.1201/9780203751480.

25 W. Mikolowsky, L. Noggle, W. Hederman, and R. Horvath. *An Evaluation of Very Large Airplanes and Alternative Fuels*. Tech. rep. R-1889-AF. The Rand Corporation: Santa Monica, California, USA: US Air Force, Dec. 1976, p. 402.

26 J. Muehlbauer. "Very large aircraft with alternate fuels - LH2 most promising". In: *2nd International Very Large Vehicles Conference*. Meeting Paper Archive. American Institute of Aeronautics and Astronautics, May 1982. DOI: 10.2514/6.1982-813.

27 R. D. Witcofski. *Alternate aircraft fuels: Prospects and operational implications*. Technical Memorandum NASA-TM-X-74030. NTRS Author Affiliations: NASA Langley Research Center NTRS Document ID: 19770021378 NTRS Research Center: Legacy CDMS (CDMS). Langley Research Center, Hampton, VA, USA: NASA, May 1977.

28 K. Fulton. "Cryogenic-Fueled Turbofans". In: *Aircraft Engineering and Aerospace Technology* 65 (11) (Jan. 1993), pp. 8–11. ISSN: 0002-2667. DOI: 10.1108/eb037431.

29 V. Sosounov and V. Orlov. "Experimental turbofan using liquid hydrogen and liquid natural gas as fuel". In: *26th Joint Propulsion Conference*. Joint Propulsion Conferences. American Institute of Aeronautics and Astronautics, July 1990. DOI: 10.2514/6.1990-2421.

30 J. Ziemann, F. Shum, M. Moore, D. Kluyskens, D. Thomaier, N. Zarzalis, and H. Eberius. "Low-NOx combustors for hydrogen fueled aero engine". In: *International Journal of Hydrogen Energy* 23 (4) (Apr. 1998), pp. 281–288. ISSN: 0360-3199. DOI: 10.1016/S0360-3199(97)00054-2.

31 J. Brand, S. Sampath, F. Shum, R. Bayt, and J. Cohen. "Potential Use of Hydrogen In Air Propulsion". en. In: *AIAA International Air and Space Symposium and Exposition: The Next 100 Years*. Dayton, Ohio: American Institute of Aeronautics and Astronautics, July 2003. ISBN: 978-1-62410-165-6. DOI: 10.2514/6.2003-2879.

32 D. Verstraete. "The Potential of Liquid Hydrogen for long range aircraft propulsion". en. PhD thesis. Crandfield, Apr. 2009.

33 A. Westenberger. *Liquid Hydrogen Fuelled Aircraft – System Analysis (CRYOPLANE)*. en. Technical. Airbus Deutschland GmbH, Sept. 2003.

34 D Guynn and E. D. Oison. *Evaluation of an Aircraft Concept With Over-Wing, Hydrogen-Fueled Engines for Reduced Noise and Emissions*. en. Technical Memorandum TM-2002-211926. Langley Research Center, Hampton, Virginia, USA: NASA, 2002.

35 M. D. Guynn, J. E. Freeh, and E. D. Olson. *Evaluation of a Hydrogen Fuel Cell Powered Blended-Wing-Body Aircraft Concept for Reduced Noise and Emissions*. en. Technical Memorandum TM-2004-2 12989. Langley Research Center, Hampton, Virginia, USA: NASA, 2004.

36 M. J. Sefain. "Hydrogen aircraft concepts and ground support". en. Accepted: 2008-10-08T16:08:58Z. PhD thesis. Cranfield University, Nov. 2005.

37 F. Svensson. "Potential of Reducing the Environmental Impact of Civil Subsonic Aviation by Using Liquid Hydrogen". English. PhD thesis. Swedish Energy Agency, Eskilstuna (Sweden): Crandfield University, June 2005.

38 D. Maniaci. "Relative Performance of a Liquid Hydrogen-Fueled Commercial Transport". en. In: *46th AIAA Aerospace Sciences Meeting and Exhibit*. Reno, Nevada: American Institute of Aeronautics and Astronautics, Jan. 2008. ISBN: 978-1-62410-128-1. DOI: 10.2514/6.2008-152.

39 D. Verstraete, P. Hendrick, P. Pilidis, and K. Ramsden. "Hydrogen fuel tanks for subsonic transport aircraft". In: *International Journal of Hydrogen Energy* 35 (20) (Oct. 2010). MAG ID: 2022361019, pp. 11085–11098. DOI: 10.1016/j.ijhydene.2010.06.060.

40 Dries Verstraete and D. Verstraete. "Long range transport aircraft using hydrogen fuel". In: *International Journal of Hydrogen Energy* 38 (34) (Nov. 2013). MAG ID: 1972012714, pp. 14824–14831. DOI: 10.1016/j.ijhydene.2013.09.021.

41 U. Nations. *Paris Agreement*. Dec. 2015.

42 Clean Sky and Fuel Cells and Hydrogen 2 Joint Undertaking. *Hydrogen-Powered Aviation: A Fact-Based Study of Hydrogen Technology, Economics, and Climate Impact by 2035*. Tech. rep. 2020.

43 D. Debney, B. Simon, F. Malcom, J. Darren, K. Edward, K. Oliver, S. Karim, S. Emma, T. Deborah, W. Karen, and W. Richard. *FlyZero-Zero Carbon Emission Aircraft Concepts*. Tech. rep. FZO-AIN-REP-0007. Aerospace Technology Institute, Mar. 2022.

44 J. R. Smith and E. Mastorakos. "An energy systems model of large commercial liquid hydrogen aircraft in a low-carbon future". In: *International Journal of Hydrogen Energy* 52 (Jan. 2024), pp. 633–654. ISSN: 0360-3199. DOI: 10.1016/j.ijhydene.2023.04.039.

45 *Performance analysis of evolutionary hydrogen-powered aircraft*. Jan. 2022.

46 E. J. Adler and J. R. R. A. Martins. "Hydrogen-Powered Aircraft: Fundamental Concepts, Key Technologies, and Environmental Impacts". en. In: *Progress in Aerospace Sciences* (2023).

47 D Silberhorn, G Atanasov, J.-N. Walther, and T Zill. "Assessment of hydrogen Fuel Tank Integration at Aircraft Level". en. In: German Aerospace Center (DLR), Hamburg, Sept. 2019.

48 C. Winnefeld, T. Kadyk, B. Bensmann, U. Krewer, and R. Hanke-Rauschenbach. "Modelling and Designing Cryogenic Hydrogen Tanks for Future Aircraft Applications". en. In: *Energies* 11 (1) (Jan. 2018). Number: 1, p. 105. ISSN: 1996-1073. DOI: 10.3390/en11010105.

49 J. Huete and P. Pilidis. "Parametric study on tank integration for hydrogen civil aviation propulsion". en. In: *International Journal of Hydrogen Energy* 46 (74) (Oct. 2021), pp. 37049–37062. ISSN: 0360-3199. DOI: 10.1016/j.ijhydene.2021.08.194.

50 J. Huete, D. Nalianda, and P. Pilidis. "Impact of tank gravimetric efficiency on propulsion system integration for a first-generation hydrogen civil airliner". en. In: *The Aeronautical Journal* 126 (1302) (Aug. 2022), pp. 1324–1332. ISSN: 0001-9240, 2059-6464. DOI: 10.1017/aer.2022.60.

51 G. Onorato, P. Proesmans, and M. F. M. Hoogreef. "Assessment of hydrogen transport aircraft: Effects of fuel tank integration". en. In: *CEAS Aeronautical Journal* 13 (4) (Oct. 2022), pp. 813–845. ISSN: 1869-5582, 1869-5590. DOI: 10.1007/s13272-022-00601-6.

52 S. S. Jagtap, P. R. N. Childs, and M. E. J. Stettler. "Energy performance evaluation of alternative energy vectors for subsonic long-range tube-wing aircraft". In: *Transportation Research Part D: Transport and Environment* 115 (Feb. 2023), p. 103588. ISSN: 1361-9209. DOI: 10.1016/j.trd.2022.103588.

53 V. Cipolla, D. Zanetti, K. Abu Salem, V. Binante, and G. Palaia. "A Parametric Approach for Conceptual Integration and Performance Studies of Liquid Hydrogen Short–Medium Range Aircraft". en. In: *Applied Sciences* 12 (14) (Jan. 2022). Number: 14, p. 6857. ISSN: 2076-3417. DOI: 10.3390/app12146857.

54 G. Palaia, K. Abu Salem, and E. Carrera. "Preliminary Performance Analysis of Medium-Range Liquid Hydrogen-Powered Box-Wing Aircraft". en. In: *Aerospace* 11 (5) (May 2024). Number: 5, p. 379. ISSN: 2226-4310. DOI: 10.3390/aerospace11050379.

55 C. Van Woensel. "Integration of a Liquid Hydrogen Fuel Tank into the Concept of the Flying-V". en. MA thesis. TU Delft, June 2021.

56 V. Palladino, N. Bartoli, V. Pommier-budinger, E. Benard, P. Schmollgruber, and A. Jordan. "Optimization of a hydrogen-based hybrid propulsion system under aircraft performance constraints". In: *Chinese Journal of Aeronautics* 36 (5) (May 2023), pp. 41–56. ISSN: 1000-9361. DOI: 10.1016/j.cja.2023.02.019.

57 M. Soleymani, V. Mostafavi, M. Hebert, S. Kelouwani, and L. Boulon. "Hydrogen propulsion systems for aircraft, a review on recent advances and ongoing challenges". In: *International Journal of Hydrogen Energy* 91 (Nov. 2024), pp. 137–171. ISSN: 0360-3199. DOI: 10.1016/j.ijhydene.2024.10.131.

58 S. Nicolay, S. Karpuk, Y. Liu, and A. Elham. "Conceptual design and optimization of a general aviation aircraft with fuel cells and hydrogen". In: *International Journal of Hydrogen Energy* 46 (64) (Sept. 2021), pp. 32676–32694. ISSN: 0360-3199. DOI: 10.1016/j.ijhydene.2021.07.127.

59 R. Wood and S. Bauer. "Flying Wings/Flying Fuselages". In: Reno, Nevada, Feb. 2001. DOI: 10.2514/6.2001-311.

60 A. Penaud and Gauchot. "Un aéroplane ou appareil aérien volant". Français. Pat. 111.574 (Paris).

61 K. Munson and J. W. Wood. *Pioneer aircraft, 1903-1914*. The Pocket encyclopaedia of world aircraft in colour. London: Blandford, 1969. ISBN: 978-0-7137-0500-3.

62 E. P. A. Heinze. *The Dreieck I Tailless Airplane (German) : A Low-Wing Cantilever Monoplane*. English. NTRS Author Affiliations: NTRS Report/Patent Number: NACA-AC-159 NTRS Document ID: 19930090268 NTRS Research Center: Legacy CDMS (CDMS). Mar. 1932.

63 A. Shepelev and H. Ottens. *Horten Ho 229: spirit of Thuringia: the Horten all-wing jet fighter*. eng. Classic Publications. Hersham: Classic, 2014. ISBN: 978-1-903223-66-6.

64 K. Thompson. "Northrop Grumman and the US Air Force Introduce the B-21 Raider, the World's First Sixth-Generation Aircraft". en. In: *Northrop Grumman Newsroom* (Feb. 2022).

65 R. Liebeck, M. Page, and B. Rawdon. "Blended-wing-body subsonic commercial transport". en. In: *36th AIAA Aerospace Sciences Meeting and Exhibit*. Reno,NV,U.S.A.: American Institute of Aeronautics and Astronautics, Jan. 1998. DOI: 10.2514/6.1998-438.

66 R. H. Liebeck. "Design of the Blended Wing Body Subsonic Transport". en. In: *Journal of Aircraft* 41 (1) (Jan. 2004), pp. 10–25. ISSN: 0021-8669, 1533-3868. DOI: 10.2514/1.9084.

67 *X-48 Research All good things must come to an end*. en-US. Section: Armstrong Flight Research Center. Apr. 2013.

68 E. M. Greitzer, P. A. Bonnefoy, E. DelaRosaBlanco, C. S. Dorbian, M. Drela, D. K. Hall, R. J. Hansman, J. I. Hileman, R. H. Liebeck, J. Levegren, P. Mody, J. A. Pertuze, S. Sato, Z. S. Spakovszky, C. S. Tan, J. S. Hollman, J. E. Duda, N. Fitzgerald, J. Houghton, J. L. Kerrebrock, G. F. Kiwada, D. Kordonowy, J. C. Parrish, J. Tylko, and E. A. Wen. *N+3 Aircraft Concept Designs and Trade Studies*. Tech. rep. E-17419-1. NTRS Author Affiliations: Massachusetts Inst. of Tech., Aurora Flight Sciences, Inc. NTRS Document ID: 20100042401 NTRS Research Center: Glenn Research Center (GRC). Dec. 2010.

69 A. Morris. "MOB A European Distributed Multi-Disciplinary Design and Optimisation Project". en. In: *9th AIAA/ISSMO Symposium on Multidisciplinary Analysis and Optimization*. Atlanta, Georgia: American Institute of Aeronautics and Astronautics, Sept. 2002. ISBN: 978-1-62410-120-5. DOI: 10.2514/6.2002-5444.

70 A Morris, P Arendsen, G LaRocca, M Laban, R Voss, and H Hönlinger. "MOB – a European Project on Multidisciplinary Design Optimisation". en. In: Yokohoma, Japan, 2004.

71 M. Kozek and A. Schirrer, eds. *Modeling and Control for a Blended Wing Body Aircraft: A Case Study*. en. Advances in Industrial Control. Cham: Springer International Publishing, 2015. ISBN: 978-3-319-10791-2 978-3-319-10792-9. DOI: 10.1007/978-3-319-10792-9.

72 J. Frota, Kevin Nicholls, J. Whurr, M. Müller, P.-E. Gall, J. Loerke, K. Macgregor, P. Schmollgruber, Jacqueline Russell, M. Hepperle, S. Rodriguez, K. Taupin, J.-L. Godard, S. Dron, K. Plötner, and G. Gallant. *NACRE Final Activity Report 2005-2010*. Tech. rep. FP6-2003-AERO-1. SIXTH FRAMEWORK PROGRAMME PRIORITY 4 Aeronautics and Space, 2011, p. 182.

73 P. Okonkwo and H. Smith. "Review of evolving trends in blended wing body aircraft design". en. In: *Progress in Aerospace Sciences* 82 (Apr. 2016), pp. 1–23. ISSN: 0376-0421. DOI: 10.1016/j.paerosci.2015.12.002.

74 AIRBUS. *Airbus reveals its blended wing aircraft demonstrator*. 2020.

75 N. Qin, A. Vavalle, A. Le Moigne, M. Laban, K. Hackett, and P. Weinerfelt. "Aerodynamic considerations of blended wing body aircraft". en. In: *Progress in Aerospace Sciences* 40 (6) (Aug. 2004), pp. 321–343. ISSN: 0376-0421. DOI: 10.1016/j.paerosci.2004.08.001.

76 N. Qin, A. Vavalle, and A. Le Moigne. "Spanwise Lift Distribution for Blended Wing Body Aircraft." en. In: *Journal of Aircraft* 42 (2) (Mar. 2005), pp. 356–365. ISSN: 0021-8669, 1533-3868. DOI: 10.2514/1.4229.

77 A. L. Moigne and N. Qin. "Aerofoil profile and sweep optimisation for a blended wing-body aircraft using a discrete adjoint method". en. In: *The Aeronautical Journal* 110 (1111) (Sept. 2006), pp. 589–604. ISSN: 0001-9240, 2059-6464. DOI: 10.1017/S0001924000001457.

78 S. Peigin and B. Epstein. "Computational Fluid Dynamics Driven Optimization of Blended Wing Body Aircraft". en. In: *AIAA Journal* 44 (11) (Nov. 2006), pp. 2736–2745. ISSN: 0001-1452, 1533-385X. DOI: 10.2514/1.19757.

79 Z. Lyu and J. R. R. A. Martins. "Aerodynamic Design Optimization Studies of a Blended-Wing-Body Aircraft". In: *Journal of Aircraft* 51 (5) (Sept. 2014), pp. 1604–1617. ISSN: 0021-8669. DOI: 10.2514/1.C032491.

80 N. B. Kuntawala. "Aerodynamic Shape Optimization of a Blended-Wing-Body Aircraft Configuration". en. MA thesis. Toronto, Canada: University of Toronto, 2011.

81 N. Kuntawala, J. Hicken, and D. Zingg. "Preliminary Aerodynamic Shape Optimization of a Blended-Wing-Body Aircraft Configuration". en. In: *49th AIAA Aerospace Sciences Meeting including the New Horizons Forum and Aerospace Exposition*. Orlando, Florida: American Institute of Aeronautics and Astronautics, Jan. 2011. ISBN: 978-1-60086-950-1. DOI: 10.2514/6.2011-642.

82 M. Meheut, A. Arntz, and G. Carrier. "Aerodynamic Shape Optimizations of a Blended Wing Body Configuration for Several Wing Planforms". en. In: *30th AIAA Applied Aerodynamics Conference*. New Orleans, Louisiana: American Institute of Aeronautics and Astronautics, June 2012. ISBN: 978-1-62410-185-4. DOI: 10.2514/6.2012-3122.

83 T. A. Reist and D. W. Zingg. "Optimization of the Aerodynamic Performance of Regional and Wide-Body-Class Blended Wing-Body Aircraft". en. In: *33rd AIAA Applied Aerodynamics Conference*. Dallas, TX: American Institute of Aeronautics and Astronautics, June 2015. ISBN: 978-1-62410-363-6. DOI: 10.2514/6.2015-3292.

84 T. A. Reist and D. W. Zingg. "Aerodynamic Design of Blended Wing-Body and Lifting-Fuselage Aircraft". en. In: *34th AIAA Applied Aerodynamics Conference*. Washington, D.C.: American Institute of Aeronautics and Astronautics, June 2016. ISBN: 978-1-62410-437-4. DOI: 10.2514/6.2016-3874.

85 T. A. Reist and D. W. Zingg. "High-Fidelity Aerodynamic Shape Optimization of a Lifting-Fuselage Concept for Regional Aircraft". en. In: *Journal of Aircraft* 54 (3) (May 2017), pp. 1085–1097. ISSN: 0021-8669, 1533-3868. DOI: 10.2514/1.C033798.

86 T. A. Reist, D. W. Zingg, M. Rakowitz, G. Potter, and S. Banerjee. "Multifidelity Optimization of Hybrid Wing–Body Aircraft with Stability and Control Requirements". en. In: *Journal of Aircraft* 56 (2) (Mar. 2019), pp. 442–456. ISSN: 0021-8669, 1533-3868. DOI: 10.2514/1.C034703.

87 V. Mukhopadhyay. "Structural Concepts Study of Non-circular Fuselage Configurations". In: Oct. 1996, p. 965561. DOI: 10.4271/965561.

88 V. Mukhopadhyay, J. Sobieszczanski-Sobieski, I. Kosaka, G. Quinn, and G. N. Vanderplaats. "Analysis, Design, and Optimization of Noncylindrical Fuselage for Blended-Wing-Body Vehicle". en. In: *Journal of Aircraft* 41 (4) (July 2004), pp. 925–930. ISSN: 0021-8669, 1533-3868. DOI: 10.2514/1.417.

89 V. Mukhopadhyay. "Blended Wing Body (BWB) Fuselage Structural Design for Weight Reduction". In: _eprint: https://arc.aiaa.org/doi/pdf/10.2514/6.2005-2349. Austin, Texas: American Institute of Aeronautics and Astronautics, Apr. 2005. DOI: 10.2514/6.2005-2349.

90 K. R. Bradley. "A Sizing Methodology for the Conceptual Design of Blended-Wing-Body Transports." In: Sept. 2004.

91 T. Laughlin. "A Parametric and Physics-Based Approach to Structural Weight Estimation of the Hybrid Wing Body Aircraft". en. PhD thesis. ATLANTA, United States: Georgia Institute of Technology, Jan. 2013.

92 R. Vos, F. Geuskens, and M. Hoogreef. "A New Structural Design Concept for Blended Wing Body Cabins". en. In: *53rd AIAA/ASME/ASCE/AHS/ASC Structures, Structural Dynamics and Materials Conference
20th AIAA/ASME/AHS Adaptive Structures Conference
14th AIAA*. Honolulu, Hawaii: American Institute of Aeronautics and Astronautics, Apr. 2012. ISBN: 978-1-60086-937-2. DOI: 10.2514/6.2012-1998.

93 R. K. Schmidt. "A Semi-Analytical Weight Estimation Method for Oval Fuselages in Novel Aircraft Configurations". en. In: (2013).

94 M. Voskuijl, G. L. Rocca, and F. Dircken. "CONTROLLABILITY OF BLENDED WING BODY AIRCRAFT". en. In: Anchorage, Sept. 2008.

95 M Meheut, R Grenon, G. Carrier, M Defos, and M Duffau. "Aerodynamic Design of Transonic Flying Wing Configurations". In: Jan. 2009.

96 Y. Denieul. "Preliminary Design of Control Surfaces and Laws for Unconventional Aircraft Configurations". Theses. INSTITUT SUPERIEUR DE L'AERONAUTIQUE ET DE L'ESPACE (ISAE), Dec. 2016.

97 D. Vicroy. "Blended-Wing-Body Low-Speed Flight Dynamics: Summary of Ground Tests and Sample Results (Invited)". In: *47th AIAA Aerospace Sciences Meeting including The New Horizons Forum and Aerospace Exposition*. Aerospace Sciences Meetings. American Institute of Aeronautics and Astronautics, Jan. 2009. DOI: 10.2514/6.2009-933.

98 M. A. Sargeant, T. P. Hynes, W. R. Graham, J. I. Hileman, M. Drela, and Z. S. Spakovszky. "Stability of Hybrid-Wing-Body-Type Aircraft with Centerbody Leading-Edge Carving". en. In: *Journal of Aircraft* 47 (3) (May 2010), pp. 970–974. ISSN: 0021-8669, 1533-3868. DOI: 10.2514/1.46544.

99 A. Sgueglia. "Methodology for sizing and optimising a Blended Wing-Body with distributed electric ducted fans". en. Mechanical Engineering. ISAE-SUPAERO, Toulouse, France: Université de Toulouse, 2019.

100 A. Ko, L. Leifsson, J. Schetz, W. Mason, B. Grossman, and R. Haftka. "MDO of a Blended-Wing-Body Transport Aircraft with Distributed Propulsion". en. In: *AIAA's 3rd Annual Aviation Technology, Integration, and Operations (ATIO) Forum*. Denver, Colorado: American Institute of Aeronautics and Astronautics, Nov. 2003. ISBN: 978-1-62410-104-5. DOI: 10.2514/6.2003-6732.

101 Y.-Y. A. Ko. "The Multidisciplinary Design Optimization of a Distributed Propulsion Blended-Wing-Body Aircraft". fr. PhD thesis. Virginia Tech, Apr. 2003.

102 R Martínez-Val, E Pérez, P Alfaro, and J Pérez. "Conceptual design of a medium size flying wing". In: *Proceedings of the Institution of Mechanical Engineers, Part G: Journal of Aerospace Engineering* 221 (1) (Jan. 2007), pp. 57–66. ISSN: 0954-4100. DOI: 10.1243/09544100JAERO90.

103 M. Brown and R. Vos. "Conceptual Design and Evaluation of Blended-Wing Body Aircraft". In: *2018 AIAA Aerospace Sciences Meeting*. AIAA SciTech Forum. American Institute of Aeronautics and Astronautics, Jan. 2018. DOI: 10.2514/6.2018-0522.

104 J. Gauvrit-Ledogar, S. Defoort, A. Tremolet, and F. Morel. "Multidisciplinary Overall Aircraft Design Process Dedicated to Blended Wing Body Configurations". In: *AIAA AVIATION 2018*. ATLANTA, United States, June 2018.

105 A. TREMOLET, J. GAUVRIT-LEDOGAR, L. BREVAULT, S. DEFOORT, and F. MOREL. "Multidisciplinary Overall Aircraft Design and Optimization of Blended Wing Body Configurations". In: (2019). Artwork Size: 15 pages Medium: PDF, 15 pages. DOI: 10.13009/EUCASS2019-900.

106 J. Gauvrit-Ledogar, A. Tremolet, F. Moens, M. Méheut, S. Defoort, R. Liaboeuf, F. Morel, and B. Paluch. "Multidisciplinary Design Analysis and Optimization Process Dedicated to Blended Wing Body Configurations". In: *ICAS 2022*. Stockholm, Sweden, Sept. 2022.

107 J. Gauvrit-Ledogar, A. Tremolet, S. Defoort, F. Morel, R. Liaboeuf, and M. Méheut. "Multidisciplinary Design and Optimization of the Blended Wing Body Configuration SMILE". en. In: June 2022.

108 P. P. C. Okonkwo. "Conceptual Design Methodology for Blended Wing Body Aircraft". en. P.h.D Thesis. Cranfield, England: School of Aerospace, Transport and Manufacturing · Cranfield University, May 2016.

109 W Heinze, L. Hansen, C Werner-Spatz, and P Horst. "Gesamtentwurfsuntersuchungen zu BWB-Frachtflugzeugen mit Alternaiven Treibstoffen". German. In: Aachen, Sept. 2009.

110 K. Seeckt, W. Heinze, and D. Scholz. "Hydrogen Powered Freighter Aircraft – The Final Results of the Green Freighter Project". English. In: Nice, France, 2010.

111 C. Werner-Westphal, W. Heinze, and P. Horst. "Multidisciplinary Integrated Preliminary Design Applied to Unconventional Aircraft Configurations". en. In: *Journal of Aircraft* 45 (2) (Mar. 2008), pp. 581–590. ISSN: 0021-8669, 1533-3868. DOI: 10.2514/1.32138.

112 P. Rompokos, A. Rolt, D. Nalianda, A. T. Isikveren, C. Senné, T. Gronstedt, and H. Abedi. "Synergistic Technology Combinations for Future Commercial Aircraft Using Liquid Hydrogen". In: *Journal of Engineering for Gas Turbines and Power* 143 (7) (Mar. 2021). ISSN: 0742-4795. DOI: 10.1115/1.4049694.

113 S. Karpuk, Y. Ma, and A. Elham. "Design Investigation of Potential Long-Range Hydrogen Combustion Blended Wing Body Aircraft with Future Technologies". en. In: *Aerospace* 10 (6) (June 2023). Number: 6, p. 566. ISSN: 2226-4310. DOI: 10.3390/aerospace10060566.

114 G. Di Summa. "The Effect of the Internal Layout of Hydrogen Combustion Blended Wing Body Concepts on Performance". en. MA thesis. Delt, Netherlands: TU Delft, 2025.

115 E. Adler and J. R. R. A. Martins. "Blended wing body configuration for hydrogen-powered aviation". en. In: *AIAA AVIATION 2023 Forum*. San Diego, CA and Online: American Institute of Aeronautics and Astronautics, June 2023. ISBN: 978-1-62410-704-7. DOI: 10.2514/6.2023-4020.

116 J. P. Jasa, J. T. Hwang, and J. R. R. A. Martins. "Open-source coupled aerostructural optimization using Python". en. In: *Structural and Multidisciplinary Optimization* 57 (4) (Apr. 2018), pp. 1815–1827. ISSN: 1615-1488. DOI: 10.1007/s00158-018-1912-8.

117 S. Patel, E. Ragauss, J. Ahuja, J. C. Gladin, and D. N. Mavris. "Development of a Regional Blended Wing Body Aircraft with Distributed Hybrid Hydrogen-Electric Propulsion". en. In: *AIAA SCITECH 2024 Forum*. Orlando, FL: American Institute of Aeronautics and Astronautics, Jan. 2024. ISBN: 978-1-62410-711-5. DOI: 10.2514/6.2024-0282.

118 O. C. V. Chung, K. AlSamri, J. Huynh, and J. Brouwer. "Design of Hydrogen Solid Oxide Fuel Cells in Blended-Wing–Body Aircraft". en. In: *Journal of Aircraft* 62 (4) (July 2025), pp. 816–834. ISSN: 0021-8669, 1533-3868. DOI: 10.2514/1.C038174.

119 A. B. Lambe and J. R. R. A. Martins. "Extensions to the design structure matrix for the description of multidisciplinary design, analysis, and optimization processes". en. In: *Structural and Multidisciplinary Optimization* 46 (2) (Aug. 2012), pp. 273–284. ISSN: 1615-1488. DOI: 10.1007/s00158-012-0763-y.

120 C. David, S. Delbecq, S. Defoort, P. Schmollgruber, E. Benard, and V. Pommier-Budinger. "From FAST to FAST-OAD: An open source framework for rapid Overall Aircraft Design". In: *IOP Conference Series: Materials Science and Engineering* 1024 (1) (Jan. 2021), p. 012062. ISSN: 1757-8981, 1757-899X. DOI: 10.1088/1757-899X/1024/1/012062.

121 J. Roskam. *Airplane design*. Lawrence, Kan: DARcorporation, 1986. ISBN: 978-1-884885-42-6 978-1-884885-43-3 978-1-884885-53-2 978-1-884885-50-1 978-1-884885-52-5.

122 D. P. Raymer. *Aircraft design: a conceptual approach*. eng. Seventh edition. Reston, Virginia: The American Institute of Aeronautics and Astronautics, Inc, 2024. ISBN: 978-1-62410-715-3 978-1-62410-729-0.

123 W. P. Dupont and C. Colongo. *PRELIMINARY DESIGN OF A COMMERCIAL TRANSPORT AIRCRAFT*. en. 2012.

124 F. Moëns. "A Fast Aerodynamic Model for Aircraft Multidisciplinary Design and Optimization Process". en. In: *Aerospace* 10 (1) (Dec. 2022), p. 7. ISSN: 2226-4310. DOI: 10.3390/aerospace10010007.

125 E. Roux. "Modèles Moteur . . . Réacteurs double flux civils et réacteurs militaires à faible taux de dilution avec PC". Français. PhD thesis. Toulouse, France, 2002.

126 J. S. Gray, J. T. Hwang, J. R. R. A. Martins, K. T. Moore, and B. A. Naylor. "OpenMDAO: an open-source framework for multidisciplinary design, analysis, and optimization". en. In: *Structural and Multidisciplinary Optimization* 59 (4) (Apr. 2019), pp. 1075–1104. ISSN: 1615-147X, 1615-1488. DOI: 10.1007/s00158-019-02211-z.

127 S. S. Jagtap, P. R. N. Childs, and M. E. J. Stettler. "Performance sensitivity of subsonic liquid hydrogen long-range tube-wing aircraft to technology developments". In: *International Journal of Hydrogen Energy* 50 (Jan. 2024), pp. 820–833. ISSN: 0360-3199. DOI: 10.1016/j.ijhydene.2023.07.297.

128 H. S. Carslaw and J. C. Jaeger. *Conduction of heat in solids*. eng. 2. ed., repr. Oxford: Clarendon Pr, 1980. ISBN: 978-0-19-853303-0.

129 P. Raja Sekaran, A. S. Gohardani, G. Doulgeris, and R. Singh. "Liquid hydrogen tank considerations for turboelectric distributed propulsion". en. In: *Aircraft Engineering and Aerospace Technology* 86 (1) (Dec. 2013), pp. 67–75. ISSN: 0002-2667. DOI: 10.1108/AEAT-12-2011-0195.

130 A. Gomez and H. Smith. "Liquid hydrogen fuel tanks for commercial aviation: Structural sizing and stress analysis". en. In: *Aerospace Science and Technology* 95 (Dec. 2019), p. 105438. ISSN: 12709638. DOI: 10.1016/j.ast.2019.105438.

131 M. Shi, I. Chakraborty, J. C. Tai, and D. N. Mavris. "Integrated Gas Turbine and Environmental Control System Pack Sizing and Analysis". en. In: *2018 AIAA Aerospace Sciences Meeting*. Kissimmee, Florida: American Institute of Aeronautics and Astronautics, Jan. 2018. ISBN: 978-1-62410-524-1. DOI: 10.2514/6.2018-1748.

132 L. G. Bolshinskiy, A Hedayat, L. J. Hastings, and J. P. Moder. *Tank System Integrated Model: A Cryogenic Tank Performance Prediction Program*. en. Technical Memorandum. Marshall Space Flight Center, Huntsville, Alabama: NASA, Apr. 2017.

133 C. Lin, N. Van Dresar, and M. Hasan. "A pressure Control Analysis Of Cryogenic Storage Systems". en. In: June 1991.

134 G. D. Brewer, R. E. Morris, R. H. Lange, and J. W. Moore. *Study of the application of hydrogen fuel to long-range subsonic transport aircraft, volume 2*. Tech. rep. LR-26752-2. NTRS Author Affiliations: Lockheed-California Co. NTRS Document ID: 19750022090 NTRS Research Center: Legacy CDMS (CDMS). Jan. 1975.

135 M. Sielemann, J. Huete, D. Andersson, A. Nguyen, and C. Coïc. "Case study in design and transient analysis of hydrogen-propelled aircraft using direct combustion". en. In: *AIAA AVIATION 2023 Forum*. San Diego, CA and Online: American Institute of Aeronautics and Astronautics, June 2023. ISBN: 978-1-62410-704-7. DOI: 10.2514/6.2023-3230.

136 A. Majumdar, J. Bailey, B. Sarkar, A. Majumdar, J. Bailey, and B. Sarkar. "A generalized fluid system simulation program to model flow distribution in fluid networks". en. In: *33rd Joint Propulsion Conference and Exhibit*. Seattle,WA,U.S.A.: American Institute of Aeronautics and Astronautics, July 1997. DOI: 10.2514/6.1997-3225.

137 A. Majumdar, J. Valenzuela, A. LeClair, and J. Moder. "Numerical modeling of self-pressurization and pressure control by a thermodynamic vent system in a cryogenic tank". en. In: *Cryogenics* 74 (Mar. 2016), pp. 113–122. ISSN: 00112275. DOI: 10.1016/j.cryogenics.2015.12.001.

138 E. Ring. *Rocket Propellant and Pressurization Systems*. en. US: Prentice-Hall, 1964.

139 P. N. Estey, D. H. Lewis, and M. Connor. "Prediction of a propellant tank pressure history using state space methods". en. In: *Journal of Spacecraft and Rockets* 20 (1) (Jan. 1983), pp. 49–54. ISSN: 0022-4650, 1533-6794. DOI: 10.2514/3.28355.

140 E. Mendez Ramos. "Enabling Conceptual Design and Analysis of Cryogenic In-Space Vehicles through the Development of an Extensible Boil-Off Model". en. PhD thesis. ATLANTA, US: Georgia Institute of Technology, May 2021.

141 I. H. Bell, J. Wronski, S. Quoilin, and V. Lemort. "Pure and Pseudo-pure Fluid Thermophysical Property Evaluation and the Open-Source Thermophysical Property Library CoolProp". In: *Industrial & Engineering Chemistry Research* 53 (6) (Feb. 2014), pp. 2498–2508. ISSN: 0888-5885. DOI: 10.1021/ie4033999.

142 D. Verstraete. "On the energy efficiency of hydrogen-fuelled transport aircraft". en. In: *International Journal of Hydrogen Energy* 40 (23) (June 2015), pp. 7388–7394. ISSN: 03603199. DOI: 10.1016/j.ijhydene.2015.04.055.

143 L. J. Hastings, R. H. Flachbart, J. J. Martin, A Hedayat, M Fazah, T Lak, H Nguyen, J. W. Bailey, and S. Technology. *Spray Bar Zero-Gravity Vent System for On-Orbit Liquid Hydrogen Storage*. en. Tech. rep. NASA, Oct. 2003.

144 L. J. Hastings, A Hedayat, and T. M. Brown. *Analytical Modeling and Test Correlation of Variable Density Multilayer Insulation for Cryogenic Storage*. en. Tech. rep. Marshall Space Flight Center, Alabama, USA: NASA, May 2004.

145 R. Doane. "Engineering practice: Accurate wetted areas for partially filled vessels". In: 114 (Dec. 2007).

146 R. F. Barron and G. F. Nellis. *Cryogenic Heat Transfer*. en. Google-Books-ID: exRjDAAAQBAJ. CRC Press, Dec. 2017. ISBN: 978-1-4822-2745-1.

147 R. Parello, S. Defoort, E. Benard, and Y. Gourinat. "Design and Integration of a Liquid Hydrogen Tank on an Aircraft". en. In: *AIAA SCITECH 2024 Forum*. Orlando, FL: American Institute of Aeronautics and Astronautics, Jan. 2024. ISBN: 978-1-62410-711-5. DOI: 10.2514/6.2024-2638.

148 K. Stephan. *Heat transfer in condensation and boiling*. eng. International series in heat and mass transfer. Berlin: Springer, 1992. ISBN: 978-3-642-52459-2 978-3-540-52203-4 978-0-387-52203-6.

149 E. J. Adler and J. R. R. A. Martins. "Liquid Hydrogen Tank Boil-off Model for Design and Optimization". en. In: *Journal of Thermophysics and Heat Transfer* 39 (3) (July 2025), pp. 505–519. ISSN: 0887-8722, 1533-6808. DOI: 10.2514/1.T7005.

150 R. F. Barron. *Cryogenic systems*. 2nd ed. Monographs on cryogenics 3. New York : Oxford [Oxfordshire]: Oxford University Press ; Clarendon Press, 1985. ISBN: 978-0-19-503567-4.

151 K.-H. Grote and J. Feldhusen, eds. *Dubbel: Taschenbuch für den Maschinenbau*. de. Berlin, Heidelberg: Springer Berlin Heidelberg, 2014. ISBN: 978-3-642-38890-3 978-3-642-38891-0. DOI: 10.1007/978-3-642-38891-0.

152 S. Schwaigerer and G. Mühlenbeck. *Festigkeitsberechnung: im Dampfkessel-, Behälter-und Rohrleitungsbau*. de. Google-Books-ID: g_egBgAAQBAJ. Springer-Verlag, Mar. 2013. ISBN: 978-3-642-59090-0.

153 R. G. Budynas and A. M. Sadegh. *Roark's Formulas for Stress and Strain, Ninth Edition*. eng. Ninth edition. New York, N.Y: McGraw-Hill Education, 2020. ISBN: 978-1-260-45375-1 978-1-260-45376-8.

154 *Certification Specifications and Acceptable Means of Compliance for Large Aeroplanes (CS-25)*. Nov. 2021.

155 Y. GOURINAT. "Charges structurales en vol Dimensionnement de panneaux fuselage". fr. In: *Techniques de l'ingénieur: Systèmes aéronautiques et spatiaux* (TRP 4033 V1) (Aug. 2017). Editions T.I. DOI: 10.51257/a-v1-trp4033.

156 A. Sarr, J. Jézégou, and P. de Saqui-Sannes. "Sizing of Fuel Distribution and Thermopropulsion Systems for Liquid-Hydrogen-Powered Aircraft Using an MBSE Approach". en. In: *Aerospace* 12 (6) (June 2025), p. 554. ISSN: 2226-4310. DOI: 10.3390/aerospace12060554.

157 M. D. McKay, R. J. Beckman, and W. J. Conover. "A Comparison of Three Methods for Selecting Values of Input Variables in the Analysis of Output from a Computer Code". In: *Technometrics* 21 (2) (May 1979), p. 239. ISSN: 00401706. DOI: 10.2307/1268522.

158 R Parello, S Defoort, E Benard, and Y Gourinat. "Integrating Cryogenic Tanks Model in Hydrogen Aircarft Design for Parametric Performance Analysis". en. In: *ICAS 2024*. Florance, Italy: International Concil of the Aeronautical Science, Sept. 2024.

159 R Parello, Y Gourinat, E Benard, and S Defoort. "Structural sizing of a hydrogen tank for a commercial aircraft". In: *Journal of Physics: Conference Series* 2716 (1) (Mar. 2024), p. 012040. ISSN: 1742-6588, 1742-6596. DOI: 10.1088/1742-6596/2716/1/012040.

160 R. Liebeck. "Blended Wing Body Design Challenges". In: *AIAA International Air and Space Symposium and Exposition: The Next 100 Years*. International Air and Space Symposium (Evolution of Flight). American Institute of Aeronautics and Astronautics, July 2003. DOI: 10.2514/6.2003-2659.

161 R. A. McDonald and J. R. Gloudemans. "Open Vehicle Sketch Pad: An Open Source Parametric Geometry and Analysis Tool for Conceptual Aircraft Design". en. In: *AIAA SCITECH 2022 Forum*. San Diego, CA & Virtual: American Institute of Aeronautics and Astronautics, Jan. 2022. ISBN: 978-1-62410-631-6. DOI: 10.2514/6.2022-0004.

162 S. Santilli, P. Ramsey, D. Baston, M. Łoskot, M. Davis, R. Obe, C. Savage, Y. Bychkov, E. Rouault, and M. Toews. *GEOS (Geometry Engine, Open Source)*. Nov. 2023. DOI: 10.5281/ZENODO.11396894.

163 Clean Sky 2 joint Undertaking and F. C. a. H. joint undertaking. *Hydrogen-powered aviation: a fact based study of hydrogen technology, economics, and climate impact by 2050*. eng. Publications Office of the European Union, 2020. ISBN: 978-92-9246-342-7.

164 M. A. Bouhlel, J. T. Hwang, N. Bartoli, R. Lafage, J. Morlier, and J. R. R. A. Martins. "A Python surrogate modeling framework with derivatives". en. In: *Advances in Engineering Software* 135 (Sept. 2019), p. 102662. ISSN: 09659978. DOI: 10.1016/j.advengsoft.2019.03.005.

165 P. Saves, R. Lafage, N. Bartoli, Y. Diouane, J. Bussemaker, T. Lefebvre, J. T. Hwang, J. Morlier, and J. R. R. A. Martins. "SMT 2.0: A Surrogate Modeling Toolbox with a focus on hierarchical and mixed variables Gaussian processes". en. In: *Advances in Engineering Software* 188 (Feb. 2024), p. 103571. ISSN: 09659978. DOI: 10.1016/j.advengsoft.2023.103571.

166 R. Priem, N. Bartoli, Y. Diouane, and A. Sgueglia. "Upper trust bound feasibility criterion for mixed constrained Bayesian optimization with application to aircraft design". In: *Aerospace Science and Technology* 105 (Oct. 2020), p. 105980. ISSN: 1270-9638. DOI: 10.1016/j.ast.2020.105980.

167 N. Bartoli, T. Lefebvre, S. Dubreuil, R. Olivanti, R. Priem, N. Bons, J. R. R. A. Martins, and J. Morlier. "Adaptive modeling strategy for constrained global optimization with application to aerodynamic wing design". en. In: *Aerospace Science and Technology* 90 (July 2019), pp. 85–102. ISSN: 12709638. DOI: 10.1016/j.ast.2019.03.041.

168 P. Saves, N. Bartoli, Y. Diouane, T. Lefebvre, J. Morlier, C. David, E. N. Van, and S. Defoort. "Constrained bayesian optimization over mixed categorical variables, with application to aircraft design". In: *AeroBest 2021*. Lisbonne, Portugal, July 2021.

169 A. Antonakis and D. Glenis. "Conceptual Co-Design of Cryogenic Storage and Ballast Systems for a Hydrogen Airliner". In: *AIAA SCITECH 2025 Forum*. AIAA SciTech Forum. American Institute of Aeronautics and Astronautics, Jan. 2025. DOI: 10.2514/6.2025-1245.

170 M. Oak, A. Fabre, M. Delavenne, E. N. Van, E. Benard, and S. Defoort. "Spectral project - application of FAST-OAD code to the conceptual design of a hydrogen fuelled commercial aircraft". In: *IOP Conference Series: Materials Science and Engineering* 1226 (1) (Feb. 2022), p. 012027. ISSN: 1757-8981, 1757-899X. DOI: 10.1088/1757-899X/1226/1/012027.

171 B. Coyle. "Fully coupled analysis of a conceptual blended wing body aircraft with ultra high bypass ratio engine installation effects". fr. thesis. Toulouse, ISAE, Jan. 2025.

172 T. Bielsky, F. Thielecke, G. Atanasov, T. Burschyk, and B. Nagel. "Collaborative Parametric Overall Aircraft and Systems Design to Evaluate Hydrogen-Powered Regional Aircraft". en. In: (Oct. 2024). Artwork Size: 9 pages Medium: application/pdf Version Number: 1.0, 9 pages. DOI: 10.25967/630123.

173 N. B. Cramer, D. W. Cellucci, O. B. Formoso, C. E. Gregg, B. E. Jenett, J. H. Kim, M. Lendraitis, S. S. Swei, G. T. Trinh, K. V. Trinh, and K. C. Cheung. "Elastic shape morphing of ultralight structures by programmable assembly". en. In: *Smart Materials and Structures* 28 (5) (Apr. 2019), p. 055006. ISSN: 0964-1726. DOI: 10.1088/1361-665X/ab0ea2.

174 K. Dahal, S. Brynolf, C. Xisto, J. Hansson, M. Grahn, T. Grönstedt, and M. Lehtveer. "Techno-economic review of alternative fuels and propulsion systems for the aviation sector". In: *Renewable and Sustainable Energy Reviews* 151 (Nov. 2021), p. 111564. ISSN: 1364-0321. DOI: 10.1016/j.rser.2021.111564.

175 Y. Qiu, H. Yang, L. Tong, and L. Wang. "Research Progress of Cryogenic Materials for Storage and Transportation of Liquid Hydrogen". en. In: *Metals* 11 (7) (July 2021). Number: 7, p. 1101. ISSN: 2075-4701. DOI: 10.3390/met11071101.

176 S. K. Mital, J. Z. Gyekenyesi, R Engineering, S. M. Arnold, R. M. Sullivan, J. M. Manderscheid, and P. L. N. Murthy. *Review of Current State of the Art and Key Design Issues With Potential Solutions for Liquid Hydrogen Cryogenic Storage Tank Structures for Aircraft Applications*. en. Tech. rep. NASA, 2006.

177 R Heydenreich. "Cryotanks in future vehicles". In: *Cryogenics* 38 (1) (Jan. 1998), pp. 125–130. ISSN: 0011-2275. DOI: 10.1016/S0011-2275(97)00122-7.

178 E. H. Glaessgen, J. R. Reeder, D. W. Sleight, J. T. Wang, I. S. Raju, and C. E. Harris. "Debonding Failure of Sandwich-Composite Cryogenic Fuel Tank with Internal Core Pressure". en. In: *Journal of Spacecraft and Rockets* 42 (4) (July 2005), pp. 613–627. ISSN: 0022-4650, 1533-6794. DOI: 10.2514/1.5567.

179 C. Gebhardt. *With all-composite cryogenic tank, Boeing eyes mass-reducing space, aviation applications*. en-US. Mar. 2022.